2016

Physics Based Modeling Of Guided Waves For Detection And Characterization Of Structural Damage In NDE and SHM

Banibrata Poddar
University of South Carolina

PHYSICS BASED MODELING OF GUIDED WAVES FOR DETECTION AND CHARACTERIZATION OF STRUCTURAL DAMAGE IN NDE AND SHM

By

Banibrata Poddar

Bachelor of Technology
Indian Institute of Technology Bombay, 2007

Master of Engineering
University of South Carolina, 2014

Submitted in Partial Fulfillment of the Requirements

For the Degree of Doctor of Philosophy in

Mechanical Engineering

College of Engineering and Computing

University of South Carolina

2016

Accepted by:

Victor Giurgiutiu, Major Professor

Sourav Banerjee, Committee Member

Paul Ziehl, Committee Member

Lingyu Yu, Committee Member

Jingjing Bao, Committee Member

Cheryl L. Addy, Vice Provost and Dean of The Graduate School

ACKNOWLEDGEMENTS

I would like to acknowledge my academic advisor, Dr. Victor Giurgiutiu, for his kind support and genial guidance. It has been a fulfilling experience to be his student. His unique outlook for science and teaching has helped me grow and will guide me in future. His kind help and clear guidance have helped me successfully overcome many difficult times during my research.

I would also like to thank Dr. Jingjing Bao, Dr. Sourav Banerjee, Dr. Lingyu Yu and Dr. Paul Ziehl for being part of my Committee and for their invaluable guidance. I want to thank my dear colleagues for their friendship and company during this difficult journey, especially Dr. Jingjing Bao, and Dr. Bin Lin for their help in my research. I would like to express my gratitude to Dr. Mira Mitra from Department of Aerospace Engineering, Indian Institute of Technology Bombay (IITB) for her guidance during my research at IITB which motivated me to pursue a career in research.

I would like to acknowledge my loving wife Anna-Marie for her patience and support. Without her this journey would not be possible. I would also like to acknowledge my father, Bikash Chandra and my mother Mira for their love and guidance of a life time.

The following funding supports are thankfully acknowledged: Office of Naval Research #N000141110271, N000141410655, Dr. Ignacio Perez, Program Officer; Air Force Office of Scientific Research #FA9550-11-1-0133, Dr. David Stargel, Program Manager.

ABSTRACT

Guided waves based damage detection techniques are popular for their ease of generation and detection along with their ability to travel long distances. Accurate and efficient modeling is a key for successful implementation of guided waves for NDE/SHM. However, efficient prediction of scattering from various damage is challenging due to the complex nature of these guided waves.

This dissertation presents as physics based efficient and accurate modeling techniques to predict ultrasonic wave propagation and their interaction with various damage. Detection and characterization of damage in structures can typically be divided into two categories, active and passive. This research is aimed towards detection and characterization of damage in thin walled structures. Therefore, the type of guided wave that we discussed is plate guided waves. For active detection, our focus is to develop an efficient analytical predictive simulation of scattered wave field and extract the damage characteristics based on physics of Lamb wave propagation. For passive characterization, our focus is on detection of acoustic emission caused by fatigue-crack growth. The scope of this research is to develop a predictive simulation method for acoustic emission signals and extract the damage related information from acoustic emission signals based on physics of material. This approach is in contrast with the traditional approach involving statistics of acoustic emissions and their relation with damage criticality. We present our unique method to extract fatigue crack length information from acoustic emission signals recorded during fatigue crack growth.

TABLE OF CONTENTS

LIST OF TABLES

LIST OF FIGURES

CHAPTER 1
INTRODUCTION

1.1 MOTIVATION

In the field of non-destructive evaluation (NDE) and structural health monitoring (SHM), methods based on ultrasonic guided waves are most popular for their ability to inspect large structures. Due to this popularity, interaction of guided waves with damage has been a major preoccupation among researchers. However, modeling of guided waves is challenging due to their multi-modal and dispersive nature. To complicate the matter even further, upon interaction with damage, guided waves like Lamb waves undergo mode conversion and scattering. Because of these complications most of the researchers have adopted some numerical techniques, such as FEM or BEM, to solve this problem. Although these approaches produce good results, the process can be described as numerical experimentation because various factors affecting the study cannot be fully understood by these kinds of simulations. Also, as these techniques are not tailored for complex phenomena like guided wave propagation, the solutions obtained by these techniques are typically computationally expensive and cannot be performed in real time.

The motivation for this research is to develop physical understanding on the effects of damage on Lamb wave propagation. We aim is to use this understanding to develop efficient predictive methodology for damage detection and characterization.

Therefore, in one part of this research, we focus on creating analytical tools to tackle the complex phenomena like Lamb waves interaction with damage using physical

understanding of Lamb wave propagation. This would achieve two main objectives. First, the analytical modeling of the interaction process will help us develop unique insight of the problem which can be extended to modeling of other complex physical phenomena. Two the created fully analytical models will be able to predict a phenomenon like scattering of Lamb waves from damage in real time with full control over all of the parameters involved in the process. This would give us capability to design complex experiments more efficiently.

In another part of this research, a similar approach is taken towards understanding the phenomenon of acoustic emission. For most of the thin walled engineering structures, the acoustic emission detection through sensor network has been well established. However, the majority of the research is focused on prediction of the acoustic emission due to fatigue crack growth using stochastic methods. Where, stochastic models are used to predict the criticality of the damage. However, these models cannot predict the physical characteristics of the damage. In our approach, first, our aim is to understand fatigue crack growth as source of acoustic emission using physics of guided wave propagation. Then our aim is to investigate detectability of crack lengths directly from crack-generated acoustic emission (AE) signals using this physical understanding of acoustic emissions due to fatigue crack growth.

1.2 RESEARCH GOAL, SCOPE AND OBJECTIVE

The scope of this research is to develop physics base prediction methodologies for active and passive damage detection and characterization in structures. This dissertation is focused on thin walled structures such as aircraft, ships and many other modern structures. Because of its intended application we focused on plate guided waves such as Lamb waves.

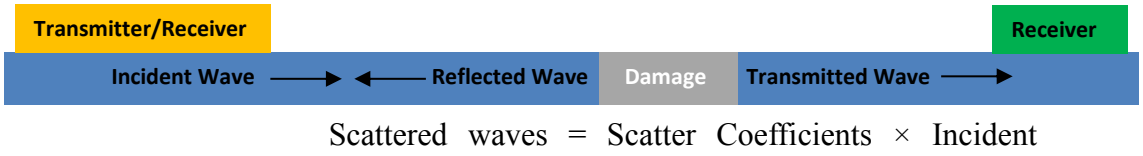

Figure 1.1: Schematic diagram of active damage detection

In general, damage detection can be divided into two main groups; active and passive detection. In active detection energy is imparted in the structure using transducers to created elastic waves. These incident waves then travel in the structure and they are scattered when they encounter a damage or sudden change in the geometry or material properties. The scatter field is sensed using various types of strain or velocity sensors. The scatter fields are then compared with the incident waves to calculated scatter coefficients (Figure 1.1). In a typical SHM or NDE system, these scatter coefficients are analyzed to detect and characterize the damage. However, to identify damage using scatter coefficients we need to understand the effects of different types of damage on these scatter coefficients.

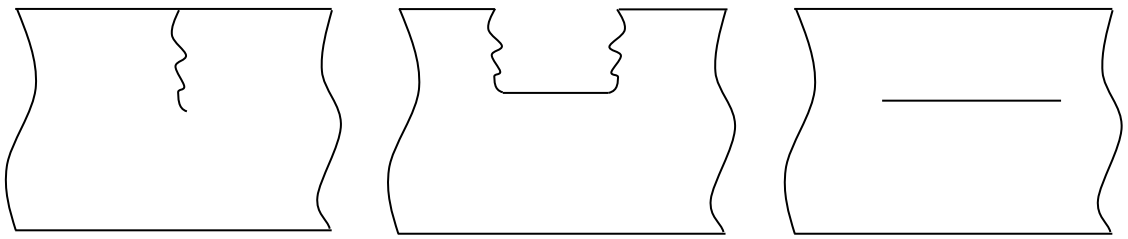

Figure 1.2: Typical types of damage in plate structure

In plate structures, typically, there are three main types of damage; surface breaking cracks, corrosions, and horizontal cracks or disbonds (Figure 1.2). To successfully identify these types of damage we need to understand their unique characteristics (if any) represented by the scatter coefficients. Also, each of these types of

damage has specific features such as, their depth, inclination of surface angle, width, surface roughness, etc. Ideally, the goal of a SHM or NDE system is to identify these characteristics too. Therefore, to successfully detect and characterize these types of damage we also need to understand the effects (if any) of each of these features on scatter coefficients.

Figure 1.3 shows examples of several different cracks with different features and the corresponding scatter coefficients generated using FE simulations. In Figure 1.3 (a) we can see the variation of scatter coefficients for surface breaking vertical cracks with different depths (solid lines) along with corresponding inclined cracks with the same depths (dashed lines). We can observe that, as the depths of the vertical cracks increase, so does scatter coefficients.

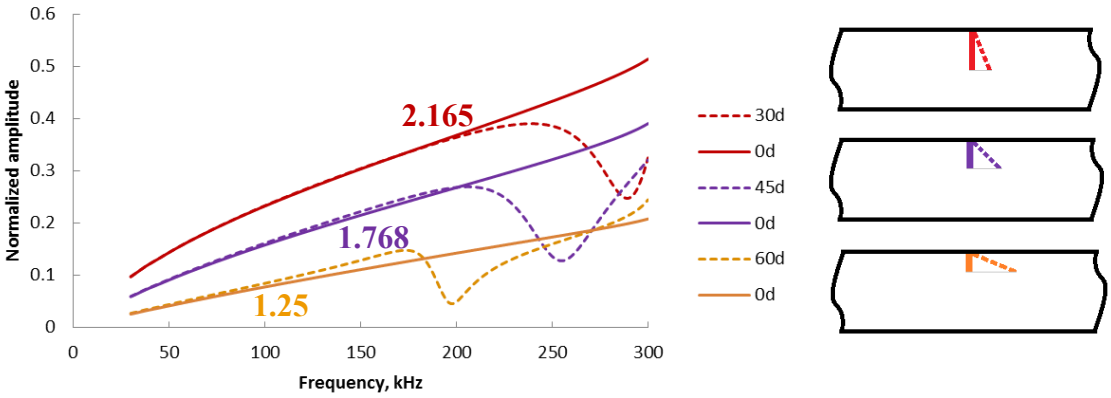

(a) (b)

Figure 1.3: (a) Forward scatter coefficient of S0 with incident S0 for surface breaking cracks with different geometric features, (b) diagram of surface breaking cracks with different geometric features

From the same figure we can also see that, for an inclined crack of the same vertical depth the scatter coefficient remains same at low frequencies; but as the frequency increases a dip appears in the scatter coefficient plot. Also, the frequency

corresponding to this dip decreases as the inclination angle increases. Therefore, depths and inclination angles are distinguishable clearly from these scatter coefficients.

Similar plots can be seen in Figure 1.4 (a) for a crack with smooth surfaces vs a crack with rough surfaces. We can see, for the crack with smooth surface, the scatter coefficient varies with frequency quite smoothly with monotonic increasing trend. However, as we introduced surface roughness, this trend changed. Though the behavior remains very similar al low frequencies, there appears a distinctive hump at higher frequency. Therefore, the scatter coefficient carries the information related to the major features of a surface breaking crack.

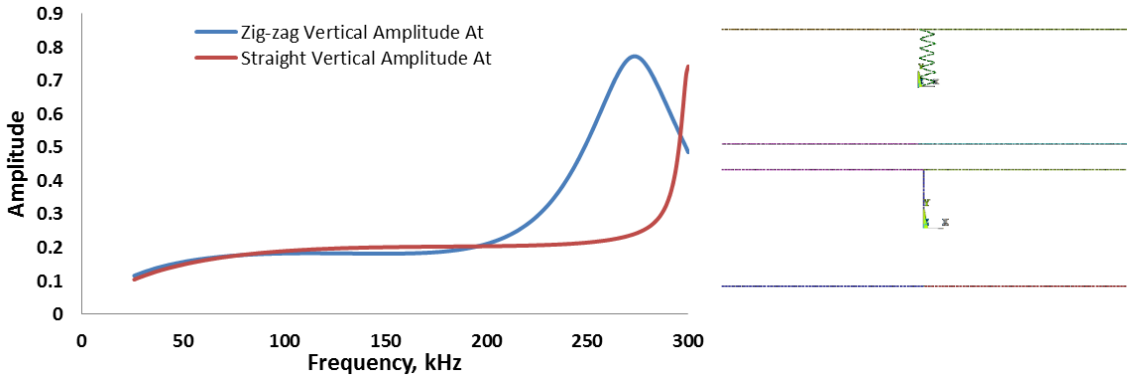

(a) (b)

Figure 1.4: (a) Scatter coefficient for a crack with smooth surface vs. rough surface, (b) diagram of cracks with smooth and rough surfaces

Although the scatter coefficients carry specific features corresponding to the each of the features of damage, so far, we have presented scatter coefficients calculated using a forward problem solver. A forward solver typically uses a predefined mathematical model of the system of interest. Then different input parameters are simulated using this model to predict the output (Figure 1.5 (a)). In our examples, we used a mathematical model constructed using finite element analysis for this purpose. Then, we introduced

incident wave field in the model which, using predefined formulation, predicted the scattered wave field.

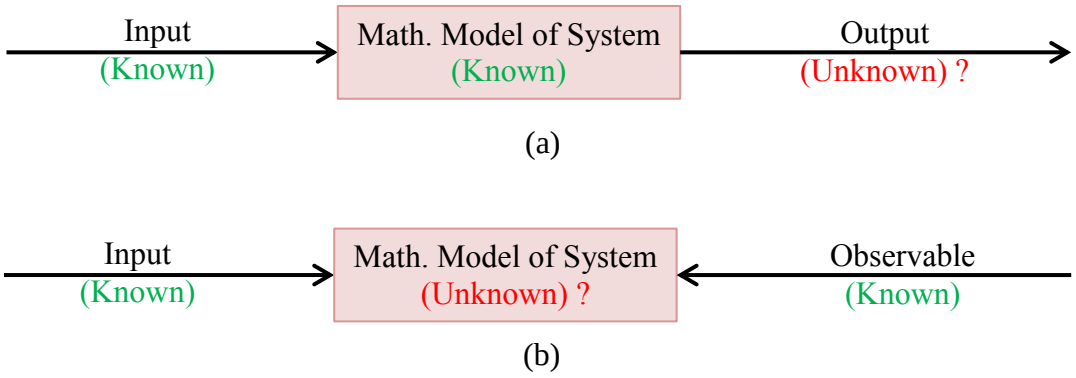

Figure 1.5: (a) Forward problem, (b) inverse problem

However, in reality, the problem is quite different from a typical forward problem. In SHM or NDE systems we do not know the mathematical or physical model of the system, at least not fully. We know the input to the structure in the form of excited waves and we know the output in the form of sensed scattered waves; our aim is to predict the material and physical state of the structure (Figure 1.5 (b)).

To solve an inverse problem, we first need to ensure that the problem in well-posed. There are three conditions for an inverse problem to be well-posed. Since the system of interest has distinctive physical properties that can be mathematically define, we may assume that the problem has a solution that we are looking for. But, for us to obtain the solution, it has to be unique. For example, as shown in Figure 1.6, for identifying the surface roughness of a crack, we need to gather data corresponding to a wider frequency of excitation because at lower frequencies, the scatter coefficient may not be distinguishable from that of a crack with smooth surfaces. This means, we need to collect more information to clearly identify the differences in the physical system. But,

the solution must also be stable in the sense a small disturbance of the measured data should only cause a small deviation in the solution of the inverse problem. The stability of the solution may be compromised by more information because more information will also bring in more stochastic variations.

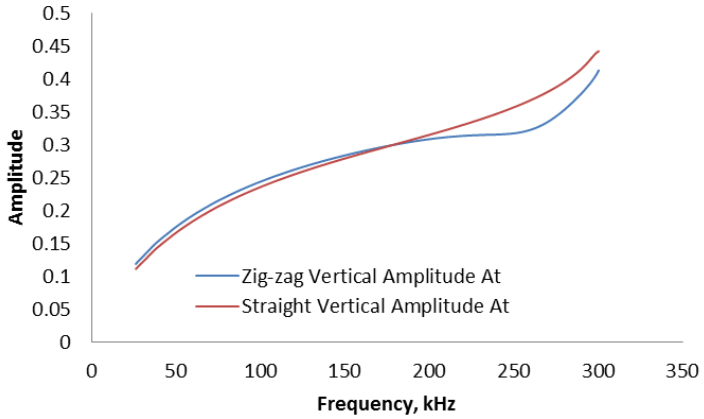

Figure 1.6: Detectability of surface roughness of a crack using scatter coefficients

Therefore, as we can see that, the real problem of damage detection and characterization is a lot more complex that just simulation the effects of a damage using a forward problem solver or simulator. In fact, the solution of the inverse problem completely independent of the forward problem is impossible as we will not be able to interpret the scatter coefficients obtained from the tests.

Therefore, the solution process of a problem of this complexity typically involves both predictors (forward problem solver or simulator) and detectors (inverse problem solver) as shown in Figure 1.7. However, for a detector the problem of detection and characterization of damage is obscured by stochastic confounding factor such as variation in the physical geometric, material, and physical systems. Also, as discussed earlier, to identify the damage, the sensitivity of these scatter coefficients to specific features have to be high. Therefore, to maximize the probability of success using this process of

damage detection and characterization, a predictor is used to predict distinguishable outcomes of a test for various situations possible. We can also use the predictor to design our tests such that the sensitivity of the scatter coefficients to the features of damage is maximum and the sensitivity to the confounding factors is minimum.

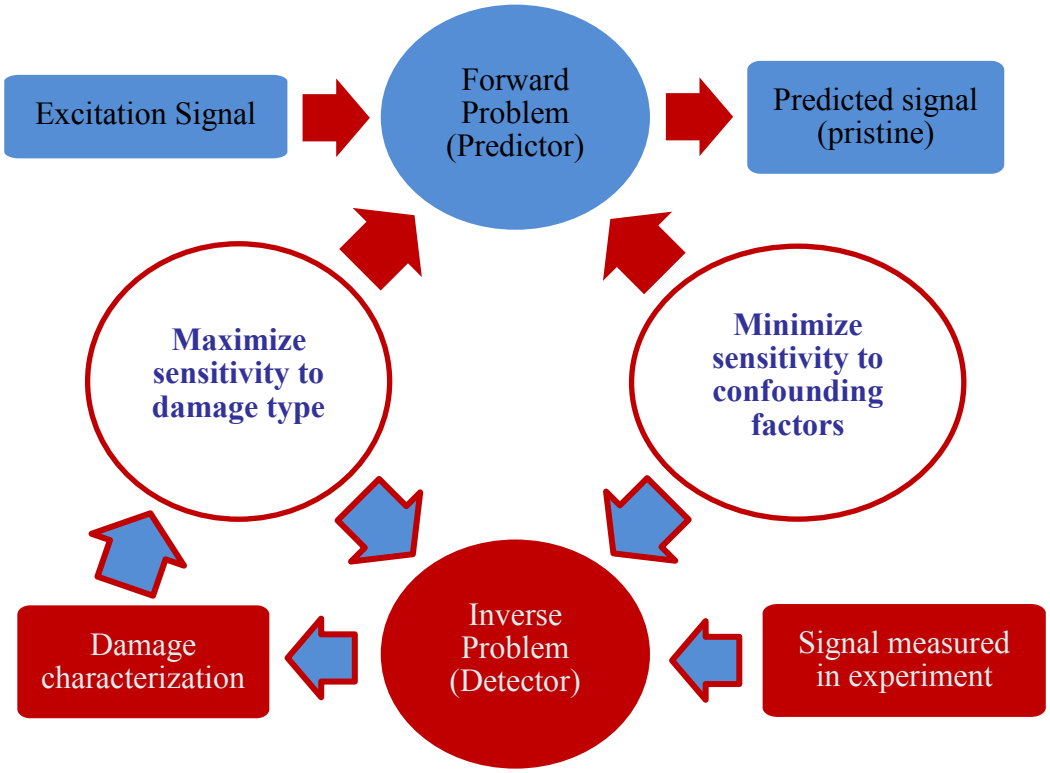

Figure 1.7: Efficient physics based predictor and its use in the solution of inverse problem for in-situ damage detection and characterization

However, the execute the process in a very short time, if not in real time, we need a very fast predictor. Especially for SHM systems which aim toward detecting damage in real time in-situ. But, due to the complexity associated with the mathematical and physical model of guided wave propagation in plate structures, researchers rely on numerical solvers as predictor. Though robust and generic, the popular numerical techniques such as FEM and BEM are slow. Therefore, an accurate and efficient predictor is desirable. In the first part of this dissertation we present our research to

develop a fast and accurate predictor using an analytical model based on physics of Lamb wave propagation and interaction with damage.

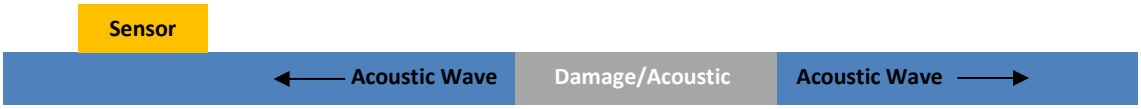

Figure 1.8: Schematic diagram of passive damage detection

In the second part of this dissertation we present our research to detect and characterize damage in passive detection technique. As shown in Figure 1.8, in passive detection, sensors are used to sense an acoustic event. This acoustic event could be caused by various environmental sources of by events of damage. One of the main challenges of passive detection is to identify the damage events from the environmental sources and predict the criticality of damage. Traditionally, various stochastic models have been used for this purpose. Typically, a stochastic model is used to predict the criticality of the damage based on rate of emission, energy of emission, etc. Although, this method is useful to predict the critical conditions of the structure, it is not very useful for pre-critical damage characterization. In our research, we focused on acoustic emission due to fatigue crack growth; we focused on developing physical understanding of fatigue crack as acoustic emission source and use this understanding to extract the features of the fatigue crack such as the size of the crack. Therefore, the scope of this research is to develop a predictive method for acoustic emission signals and extract the damage related information from acoustic emission signals based on physics of material.

1.3 ORGANIZATION OF THE DISSERTATION

This dissertation is divided into total eight chapters including the current chapter. Chapter two present theoretical background of guided waves in plate and physical understanding of the Lamb wave modes in plates.

Chapter three and four presents an analytical model based on the physics of the Lamb wave modes to predict the scattering of them from various types of damage. This chapter also presents their validation using finite element models.

Chapter five presents an experimental method to verify theoretical models predicting Lamb wave propagation in plates. We also present the verification of the analytical model using this experimental method for most fundamental damage type.

Chapter six presents our experimental and numerical study to understand fatigue crack growth as a source of acoustic emissions. We also present a method invented to detect fatigue crack length from the acoustic emissions along with its experimental verification.

Finally, chapter seven presents conclusions from our research and recommended future work along with the major contributions of this research.

CHAPTER 2
FUNDAMENTALS OF GUIDED WAVES

2.1 THEORY OF GUIDED WAVES

Guided waves are elastic waves carrying energy confined near the boundary or between the boundaries separating different materials. Guided waves propagate parallel to these boundaries. The guided waves are created by interactions of bulk waves and the boundaries. These interactions create standing wave modes perpendicular to the boundaries and these standing modes propagate parallel to the boundaries. There are three major guided wave types; Rayleigh waves (known as surface acoustic waves, SAW) which exists near the traction free boundary of a semi-infinite solid; shear horizontal (SH) waves and Lamb waves (Achenbach 1973; Giurgiutiu 2014; Graff 1991; Viktorov 1967) which exist in plate structure between two traction free boundaries. In this dissertation, our focus will be on Lamb waves.

2.1.1 LAMB WAVES

Lamb waves or plate guided waves, are a type of stress waves that remain confined between two parallel traction free plate surfaces. For brief introduction of the Lamb wave theory we consider the Navier-Lame equations in vector form for Cartesian coordinates given as

$$(\lambda+\mu)\vec{\nabla}\left(\vec{\nabla}\cdot\vec{u}\right)+\mu\nabla^2\vec{u}=\rho\ddot{\vec{u}} \tag{2.1}$$

where, $\vec{u}=u_x\hat{i}+u_y\hat{j}+u_z\hat{k}$, with $\hat{i}$, $\hat{j}$, $\hat{k}$ being unit vectors in the x, y, z directions respectively. Following the formulation proposed by Helmholtz (Helmholtz 1867) we

express the displacement vector $\vec{u}$ as summation of dilatational and rotational motion, i.e.,

$$\vec{u} = \text{dilatational motion + rotational motion} = \vec{u}_d + \vec{u}_r \tag{2.2}$$

On one hand, we express the dilatational motion as

$$\vec{u}_d = \vec{\nabla}\Phi \tag{2.3}$$

where, Φ is a *scalar potential* and $\vec{u}_d$ represents irrotational motion because curl of a gradient vector field is zero, i.e.,

$$\vec{\nabla} \times \vec{u}_d = \vec{\nabla} \times \left(\vec{\nabla}\Phi\right) = 0 \tag{2.4}$$

On the other hand, we express the rotational motion as

$$\vec{u}_r = \vec{\nabla} \times \vec{H} \tag{2.5}$$

where, $\vec{H}$ is a *vector potential* defined as

$$\vec{H} = H_x\vec{i} + H_y\vec{j} + H_z\vec{k} \tag{2.6}$$

The displacement field, $\vec{u}_r$ represents only rotation motion because divergence of curl of any vector field is zero, i.e.,

$$\vec{\nabla} \cdot \vec{u}_r = \vec{\nabla} \cdot \left(\vec{\nabla} \times \vec{H}\right) = 0 \tag{2.7}$$

Therefore, we express the displacement field as sum of dilatational and rotational motion in the form

$$\vec{u} = \vec{u}_d + \vec{u}_r = \vec{\nabla}\Phi + \vec{\nabla} \times \vec{H} \tag{2.8}$$

Using equation (2.8), we write the components of the equations (2.1) as

$$\vec{\nabla}\left(\vec{\nabla} \cdot \vec{u}\right) = \vec{\nabla}\left(\vec{\nabla} \cdot (\vec{\nabla}\Phi + \vec{\nabla} \times \vec{H})\right) = \vec{\nabla}(\nabla^2\Phi) + \vec{\nabla}\left(\vec{\nabla} \cdot (\vec{\nabla} \times \vec{H})\right) = \vec{\nabla}\left(\nabla^2\Phi\right) \tag{2.9}$$

$$\nabla^2\vec{u} = \nabla^2(\vec{\nabla}\Phi + \vec{\nabla} \times \vec{H}) = \vec{\nabla}\nabla^2\Phi + \vec{\nabla} \times \nabla^2\vec{H} \tag{2.10}$$

Note that the outcome of equation (2.9) is independent of the divergence field of $\vec{H}$ and this property is known as “gauge invariance”. The gauge invariance is evident as, in equation (2.9),

$$\vec{\nabla}\left(\vec{\nabla} \cdot (\vec{\nabla} \times \vec{H})\right) = \vec{\nabla} \times \left(\vec{\nabla}\left(\vec{\nabla} \cdot \vec{H}\right)\right) = \vec{\nabla} \times \left(\vec{\nabla}\vartheta\right) = 0 \tag{2.11}$$

where, $\vartheta = \vec{\nabla} \cdot \vec{H}$ is a scalar field known as "gauge condition". Therefore, we may assume ϑ to be any scalar function. However, following Helmholtz (Helmholtz 1867), we assume $\vec{H}$ to be a vector field related to only rotational displacements with zero divergence. Therefore,

$$\vartheta = \vec{\nabla} \cdot \vec{H} = 0 \tag{2.12}$$

Upon substitution of equations (2.9), (2.10) into equation (2.1) yields

$$\vec{\nabla}\left((\lambda + 2\mu)\nabla^2\Phi - \rho\ddot{\Phi}\right) + \vec{\nabla} \times \left(\mu\nabla^2\vec{H} - \rho\ddot{\vec{H}}\right) = \vec{0} \tag{2.13}$$

If we perform divergence operation on equation (2.13), we obtain

$$\begin{aligned} &\vec{\nabla} \cdot \left(\vec{\nabla}\left((\lambda + 2\mu)\nabla^2\Phi - \rho\ddot{\Phi}\right) + \vec{\nabla} \times \left(\mu\nabla^2\vec{H} - \rho\ddot{\vec{H}}\right)\right) = 0 \\ &\Rightarrow \vec{\nabla} \cdot \vec{\nabla}\left((\lambda + 2\mu)\nabla^2\Phi - \rho\ddot{\Phi}\right) + \vec{\nabla} \cdot \vec{\nabla} \times \left(\mu\nabla^2\vec{H} - \rho\ddot{\vec{H}}\right) = 0 \\ &\Rightarrow \vec{\nabla} \cdot \vec{\nabla}\left((\lambda + 2\mu)\nabla^2\Phi - \rho\ddot{\Phi}\right) = 0 \end{aligned} \tag{2.14}$$

From equation (2.14), we can see that the only surviving term related to the dilatational motion on the left hand side is the first term of equation (2.13). Similarly, if we perform curl operation on equation (2.13), we obtain

$$\begin{aligned} &\vec{\nabla} \times \left(\vec{\nabla}\left((\lambda + 2\mu)\nabla^2\Phi - \rho\ddot{\Phi}\right) + \vec{\nabla} \times \left(\mu\nabla^2\vec{H} - \rho\ddot{\vec{H}}\right)\right) = 0 \\ &\Rightarrow \vec{\nabla} \times \vec{\nabla}\left((\lambda + 2\mu)\nabla^2\Phi - \rho\ddot{\Phi}\right) + \vec{\nabla} \times \vec{\nabla} \times \left(\mu\nabla^2\vec{H} - \rho\ddot{\vec{H}}\right) = 0 \\ &\Rightarrow \vec{\nabla} \times \vec{\nabla} \times \left(\mu\nabla^2\vec{H} - \rho\ddot{\vec{H}}\right) = 0 \end{aligned} \tag{2.15}$$

We see that the only surviving term related to the rotational motion on the left hand side is the second term of equation (2.13). The equation (2.13) holds at any place and time only when

$$\begin{aligned} &(\lambda + 2\mu)\nabla^2\Phi - \rho\ddot{\Phi} = 0 \\ &\Rightarrow c_p^2\nabla^2\Phi = \ddot{\Phi} \end{aligned} \tag{2.16}$$

and

$$\begin{aligned} &\mu\nabla^2\vec{H} - \rho\ddot{\vec{H}} = \vec{0} \\ &\Rightarrow c_S^2\nabla^2\vec{H} = \ddot{\vec{H}} \end{aligned} \tag{2.17}$$

where, c_P and c_S are the wave speeds of pressure wave and shear waves, respectively. From equations (2.14) and (2.15) we can conclude that equation (2.16) is related to the dilatational motion and equation (2.17) is related to the rotational motion. Therefore, equations (2.16) and (2.17) represent the governing system of equations for elastodynamic field at any location at any time in an isotropic solid. Using equation (2.8), we can express the displacement vector as

$$\begin{aligned} \vec{u} &= u_x\hat{i} + u_y\hat{j} + u_z\hat{k} \\ &= \left(\frac{\partial\Phi}{\partial x} + \frac{\partial H_z}{\partial y} - \frac{\partial H_y}{\partial z}\right)\hat{i} + \left(\frac{\partial\Phi}{\partial y} + \frac{\partial H_x}{\partial z} - \frac{\partial H_z}{\partial x}\right)\hat{j} + \left(\frac{\partial\Phi}{\partial z} + \frac{\partial H_y}{\partial x} - \frac{\partial H_x}{\partial y}\right)\hat{k} \end{aligned} \tag{2.18}$$

The stresses can be expressed in terms of the displacements in Cartesian coordinates as

$$\begin{aligned} \sigma_{xx} &= (\lambda + 2\mu)\frac{\partial u_x}{\partial x} + \lambda\frac{\partial u_y}{\partial y} + \lambda\frac{\partial u_z}{\partial z}; & \tau_{xy} &= \mu\left(\frac{\partial u_x}{\partial y} + \frac{\partial u_y}{\partial x}\right) \\ \sigma_{yy} &= \lambda\frac{\partial u_x}{\partial x} + (\lambda + 2\mu)\frac{\partial u_y}{\partial y} + \lambda\frac{\partial u_z}{\partial z}; & \tau_{yz} &= \mu\left(\frac{\partial u_y}{\partial z} + \frac{\partial u_z}{\partial y}\right) \\ \sigma_{zz} &= \lambda\frac{\partial u_x}{\partial x} + \lambda\frac{\partial u_y}{\partial y} + (\lambda + 2\mu)\frac{\partial u_z}{\partial z}; & \tau_{zx} &= \mu\left(\frac{\partial u_z}{\partial x} + \frac{\partial u_x}{\partial z}\right) \end{aligned} \tag{2.19}$$

In this dissertation we consider straight crested Lamb waves in plane strain condition. We assume the wave propagation direction is aligned with the unit vector $\hat{i}$ along x axis and the plate thickness direction is aligned with the unit vector $\hat{j}$ along y axis. We also assume the plate is infinitely wide in the $\hat{k}$ direction along z axis. Therefore the problem becomes z-invariant. Using equations (2.18) and (2.19) the

displacements and stresses for z-invariant elastodynamic field are expressed as (Giurgiutiu 2014)

$$u_x = \frac{\partial \Phi}{\partial x} + \frac{\partial H_z}{\partial y}; \qquad u_y = \frac{\partial \Phi}{\partial y} - \frac{\partial H_z}{\partial x}; \qquad u_z = \frac{\partial H_y}{\partial x} - \frac{\partial H_x}{\partial y} \tag{2.20}$$

$$\begin{aligned} \sigma_{xx} &= (\lambda + 2\mu)\frac{\partial^2 \Phi}{\partial x^2} + \lambda \frac{\partial^2 \Phi}{\partial y^2} + 2\mu \frac{\partial^2 H_z}{\partial x \partial y}; & \tau_{xy} &= \mu\left(2\frac{\partial^2 \Phi}{\partial x \partial y} - \frac{\partial^2 H_z}{\partial x^2} + \frac{\partial^2 H_z}{\partial y^2}\right) \\ \sigma_{yy} &= \lambda \frac{\partial^2 \Phi}{\partial x^2} + (\lambda + 2\mu)\frac{\partial^2 \Phi}{\partial y^2} - 2\mu \frac{\partial^2 H_z}{\partial x \partial y}; & \tau_{yz} &= \mu\left(\frac{\partial^2 H_y}{\partial x \partial y} - \frac{\partial^2 H_x}{\partial y^2}\right) \\ \sigma_{zz} &= \lambda\left(\frac{\partial^2 \Phi}{\partial x^2} + \frac{\partial^2 \Phi}{\partial y^2}\right); & \tau_{zx} &= \mu\left(\frac{\partial^2 H_y}{\partial x^2} - \frac{\partial^2 H_x}{\partial x \partial y}\right) \end{aligned} \tag{2.21}$$

Also, the equations (2.16) and (2.17) become

$$\left.\begin{aligned} c_P^2 \nabla^2 \Phi = \ddot{\Phi} &\Rightarrow \frac{\partial^2 \Phi}{\partial x^2} + \frac{\partial^2 \Phi}{\partial y^2} = \frac{1}{c_P^2}\ddot{\Phi} \\ c_S^2 \nabla^2 \vec{H}_z = \ddot{\vec{H}}_z &\Rightarrow \frac{\partial^2 H_z}{\partial x^2} + \frac{\partial^2 H_z}{\partial y^2} = \frac{1}{c_S^2}\ddot{H}_z \end{aligned}\right\} \text{Equations for } u_x \text{ and } u_y \tag{2.22}$$

$$\left.\begin{aligned} c_S^2 \nabla^2 \vec{H}_x = \ddot{\vec{H}}_x &\Rightarrow \frac{\partial^2 H_x}{\partial x^2} + \frac{\partial^2 H_x}{\partial y^2} = \frac{1}{c_S^2}\ddot{H}_x \\ c_S^2 \nabla^2 \vec{H}_y = \ddot{\vec{H}}_y &\Rightarrow \frac{\partial^2 H_y}{\partial x^2} + \frac{\partial^2 H_y}{\partial y^2} = \frac{1}{c_S^2}\ddot{H}_y \end{aligned}\right\} \text{Equations for } u_z \tag{2.23}$$

From equation (2.20), we can see that equations (2.22) govern u_x and u_y displacements and equations (2.23) govern u_z displacement. Equations (2.22) contain both dilatational and rotational terms and describe pressure wave and shear vertical wave; equations (2.23) contain only rotational term and describes shear horizontal waves. This decoupling of u_z displacement component from u_x and u_y displacement components is possible because of the z-invariance condition. This makes it possible for us to split the governing equation of the elastodynamic field into two as shown in equations (2.22) and (2.23).

For a plate with thickness $2d$ the wave is confined between two traction free plate surfaces at $y = \pm d$. Therefore, the boundary conditions for a plate are

$$\sigma_{yy}\big|_{y=\pm d} = 0; \qquad \tau_{xy}\big|_{y=\pm d} = 0 \tag{2.24}$$

$$\tau_{yz}\big|_{y=\pm d} = 0 \tag{2.25}$$

If we assume standing wave modes in plate thickness direction y, then the solutions of equations (2.22) and (2.23) take the general form

$$\begin{aligned} \Phi &= f(y)e^{i(\xi x-\omega t)}; \qquad H_z = h_z(y)e^{i(\xi x-\omega t)} \\ H_x &= h_x(y)e^{i(\xi x-\omega t)}; \quad H_y = h_y(y)e^{i(\xi x-\omega t)} \end{aligned} \tag{2.26}$$

Using equations (2.26) in equations (2.22) and (2.23) gives

$$\begin{aligned} \Phi &= \left(A\cos\eta_P y + B\sin\eta_P y\right)e^{i(\xi x-\omega t)} \\ H_x &= \left(C\cos\eta_S y + D\sin\eta_S y\right)e^{i(\xi x-\omega t)} \\ H_y &= \left(E\cos\eta_S y + F\sin\eta_S y\right)e^{i(\xi x-\omega t)} \\ H_z &= \left(G\cos\eta_S y + H\sin\eta_S y\right)e^{i(\xi x-\omega t)} \end{aligned} \tag{2.27}$$

where, ξ is the wave number in x direction with $\eta_P^2 = \frac{\omega^2}{c_P^2} - \xi^2$ and $\eta_S^2 = \frac{\omega^2}{c_S^2} - \xi^2$ and A, B, C, D, E, F, G, H are unknown coefficients. To obtain these unknowns, we use the boundary conditions given in equations (2.24) and (2.25). However the six boundary conditions are not sufficient for the eight unknown coefficients in equations (2.27). The additional conditions are obtained from the gauge condition of equation (2.12). Meeker and Meitzler (Meeker and Meitzler 1964) used this condition at the top and bottom surfaces of the plate to obtain two additional boundary conditions to solve for the unknown coefficients in equations (2.27) directly. The method is also described by Graff (Graff 1991). Another method for solving the wave equations for a plate is to solve for system of equations (2.22) and (2.23) separately. In this method, to solve equations (2.22)

, we assume the solution to be of similar general form as given in equations (2.26). This will result in four unknowns, A, B, G, H, i.e.,

$$\begin{aligned} \Phi &= \left(A\cos\eta_P y + B\sin\eta_P y\right)e^{i(\xi x-\omega t)} \\ H_z &= \left(G\cos\eta_S y + H\sin\eta_S y\right)e^{i(\xi x-\omega t)} \end{aligned} \tag{2.28}$$

These four unknowns are directly obtained by using the four boundary conditions given by equations (2.24). Next, we solve for u_x, u_y using Φ, H_z into equation (2.20). To find u_z, which is uncoupled from u_x, u_y, we solve the Navier-Lame equations considering only u_z, which results in the wave equation for u_z, i.e.,

$$\nabla^2 u_z = \frac{1}{c_S^2}\ddot{u}_z \Rightarrow \frac{\partial^2 u_z}{\partial x^2} + \frac{\partial^2 u_z}{\partial y^2} = \frac{1}{c_S^2}\ddot{u}_z \tag{2.29}$$

Note that we avoid solving equation (2.23) because it contains two unknown fields H_x and H_y. To solve equation (2.29), we assume u_z to have similar general form as equations (2.26). This will result in two unknowns which can be obtained using two boundary conditions given by equation (2.25). This method is elaborated by both Graff (Graff 1991) and Giurgiutiu (Giurgiutiu 2014).

In this dissertation we focus only on Lamb waves in plane strain condition; application of boundary conditions (2.24) yields the well-known Rayleigh-Lamb equations.

$$\frac{\tan\eta_P d}{\tan\eta_S d} = \left[-\frac{(\xi^2-\eta_S^2)^2}{4\xi^2\eta_P\eta_S}\right]^{\pm 1} \tag{2.30}$$

Lamb waves exist in plate structures in two basic types of modes, symmetric and antisymmetric modes. The power of the right hand side of equation (2.30) changes sign for symmetric and antisymmetric modes; $+1$ is for symmetric modes and -1 is for antisymmetric modes. Equation (2.30) can also be expressed as

$$\left(\xi^2-\eta_S^2\right)^2\cos\eta_P d\sin\eta_S d+4\xi^2\eta_P\eta_S\sin\eta_P d\cos\eta_S d=0 \qquad \text{(Symmetric)}$$
$$\left(\xi^2-\eta_S^2\right)^2\sin\eta_P d\cos\eta_S d+4\xi^2\eta_P\eta_S\cos\eta_P d\sin\eta_S d=0 \qquad \text{(AntiSymmetric)} \tag{2.31}$$

The equations (2.31) are transcendental equations in complex domain. The only way to obtain the roots of these equations is by numerical techniques. To our knowledge, there is no standard method to obtain all possible complex roots of a transcendental equation in the complex domain. Therefore the complete solution of Rayleigh-Lamb equations is quite challenging.

2.1.1.1 Complete Solution of the Rayleigh-Lamb Equation

Numerical root finding methods typically fall into two categories; bracketing methods and open methods (Burden and Faires 2011; Kreyszig 1997). Open methods such as Newton Raphson method, are faster than the bracketing methods but requires an initial guess. These methods make use of the slope of the curve at different points. Therefore, if the function is non differentiable at a point or has a point of inflexion, the method may not be able to find a root. Also, if the function changes its slope very quickly or is discontinuous, then it cannot be solved by this type of methods. Also there is no straightforward way to find all the roots in an interval or even ascertain the number of roots in the interval. Hence, the open methods are faster but not robust. Also they are not able to deal with the points of bifurcation in the locus of the solution. Therefore open methods may not be successful in solving complex transcendental equations such as equations (2.31).

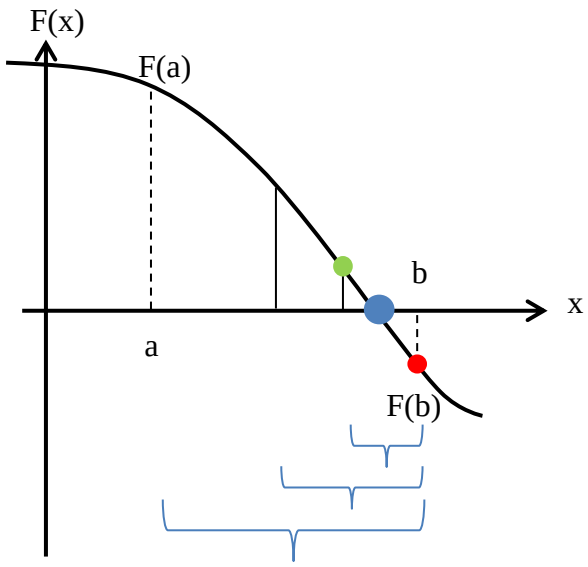

Figure 2.1: Illustration of bisection method

Bracketing methods are slower but robust. Amongst all the bracketing methods, the bisection method is guaranteed to find a solution in a given domain if a solution exists in that domain. In this method, a domain is selected for root search where the function of interest is monotonic (Figure 2.1). If the function changes its sign across the domain, then there is a root in that domain and subsequently the domain is bisected. Since the function is monotonic, it must change sign across one of these two halves. The same operation is continued on the subdomain where the function changes sign until the subdomain size is smaller than the required accuracy, i.e., a zero of the function is found. For the method to work, the initial domain should be small enough to assume monotonicity of the function. However, there is no straightforward analytical method to find these domains. Nonetheless, if such monotonicity is ensured, then the method is guaranteed to find the root in the domain.

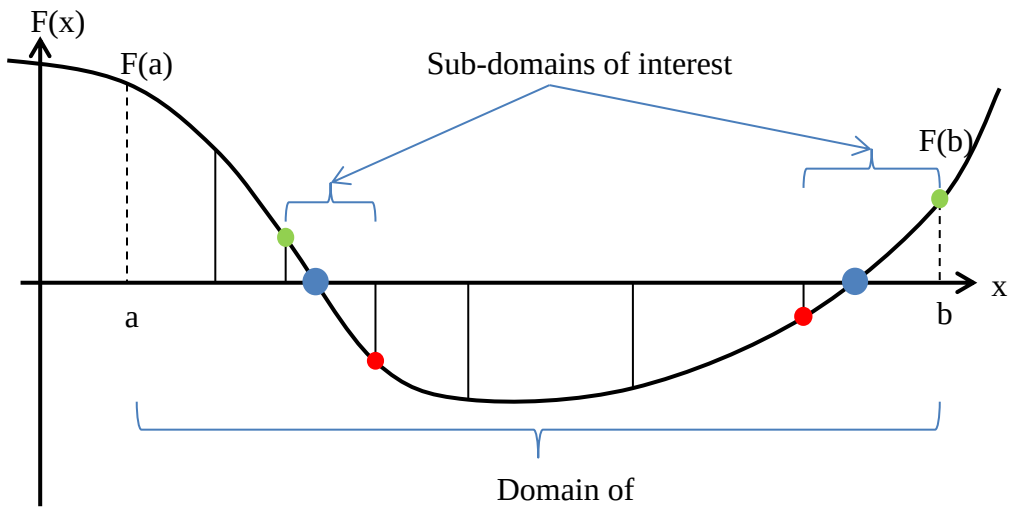

Figure 2.2: Illustration of modified bracketing method

In modified bracketing method, the domain of interest is subdivided into subdomains where the function is monotonic (Press et al. 1987). These subdivisions can be more than two and need not be of the same size. If the function changes sign across one or more of these subdivisions then there are roots of the function in these subdivisions. The same sub-dividing operation is repeated until the subdivisions where the function changes sign are smaller than the required accuracy, i.e., the zeroes of the function are obtained. The advantage of this method over bisection method is that the domain of interest need not be a region where the function is monotonic. Also, since the number of subdomains can be more than two this method is faster than the bisection method. However, the size of subdomains in the first iteration should be small enough such that the function of interest is monotonic in these subdomains. If this is ensured then the method is guaranteed to find multiple roots in a given domain to an accuracy limited only by the computer.

In 1957 Mindlin described the behavior of the roots of Rayleigh-Lamb equations but with limited numerical investigation (Mindlin 1957). The earliest work on application of numerical method to find the complex roots of Rayleigh-Lamb is by Torvik in 1966 (Torvik 1966). Torvik used Newton iteration method to find first few complex Lamb wave modes. Later Gregory and Gladwell in 1981 (Gregory and Gladwell 1983) and Scandrett and Vasudevan (Scandrett and Vasudevan 1991) in 1991 used similar method to find the complex roots of Rayleigh-Lamb waves in limited numbers for eigen modes expansion. All these methods depended on the initial guess of the roots starting with the analytical solution at zero frequency or zero wave number. In 2001 Pagneux and Maurel (Pagneux and Maurel 2001) proposed an alternate method for initial guesses used by transforming the transcendental equation to a traditional eigen value problem. They used direct projection of the ordinary differential equation governing the Lamb modes on a spectral basis of orthogonal functions. However, the initial guesses are only possible for a homogeneous plate medium. To obtain the eigen values corresponding to a layered or anisotropic plate guide, the initial guess is not possible and therefore the Newton iteration method is not suitable. Recently Quintanilla et al. have also demonstrated the use of spectral collocation method to compute complex roots for plates of highly anisotropic materials with damping (Hernando Quintanilla, Lowe, and Craster 2015).

We used modified bracketing method to solve the equation $D(k,\omega)=0$ directly and found all possible roots of the Rayleigh-Lamb equation. This method is applicable for any system of equations governing the behavior of the eigen values of the plate guide without any initial guess. To find complex roots of any system of equations, we find the

roots of the real and imaginary parts separately and then the common roots of these two parts are the complex eigen values, i.e.,

$$f(z) = f_R(z) + if_I(z) = 0; \qquad z = x + iy \in \mathbb{C}; \qquad x,\ y \in \mathbb{R}$$
$$\Rightarrow f_R(x+iy) = 0; \qquad f_I(x+iy) = 0 \tag{2.32}$$

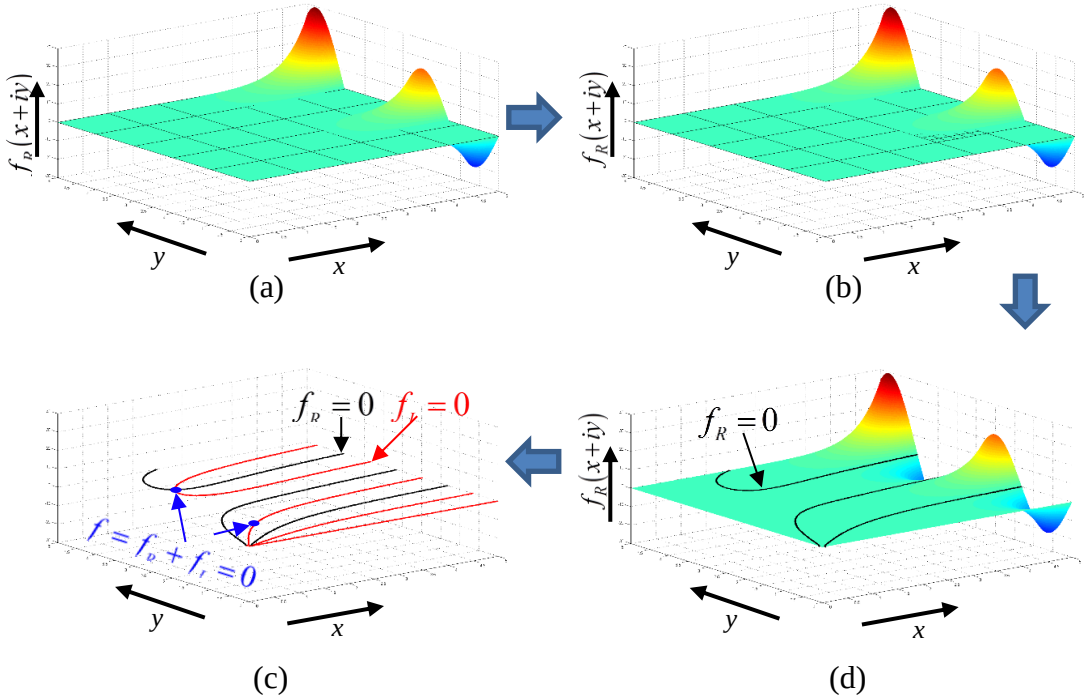

Figure 2.3: Application of modified bracketing method to find complex roots; (a) initial mesh to find sign change, (b) refined mesh to find sign change, (c) intersection of real and imaginary loci of zero crossings , (d) finding locus of zero crossings

This method is illustrated in Figure 2.3. Figure 2.3 (a) and (b) show how the initial sub-domain is further divided and checked for monotonicity. Also the subdomain is divided again if the real part of the function changes sign in it. This operation is repeated until the required accuracy is achieved and results in the curve correspond to zeroes of the real part of the function as shown in Figure 2.3 (d). Same operation is performed on the imaginary part of the functions also. The intersections of these curves corresponding to the real part and imaginary part give us the roots of the complex equation (Figure 2.3 (c)).

The method was implemented in a Matlab program. In this program, the subdomains are further divided only if both the imaginary and real parts of the function change sign or have encountered an exact zeros in that subdomain. The program uses recursive algorithm to progressively refine the subdomains where the roots exist. This results in a fractal like self-similar structure of the algorithm. This recursion is implemented by a self-calling of functions; this makes the algorithm efficient. The algorithmic structure of the program is shown in Figure 2.4.

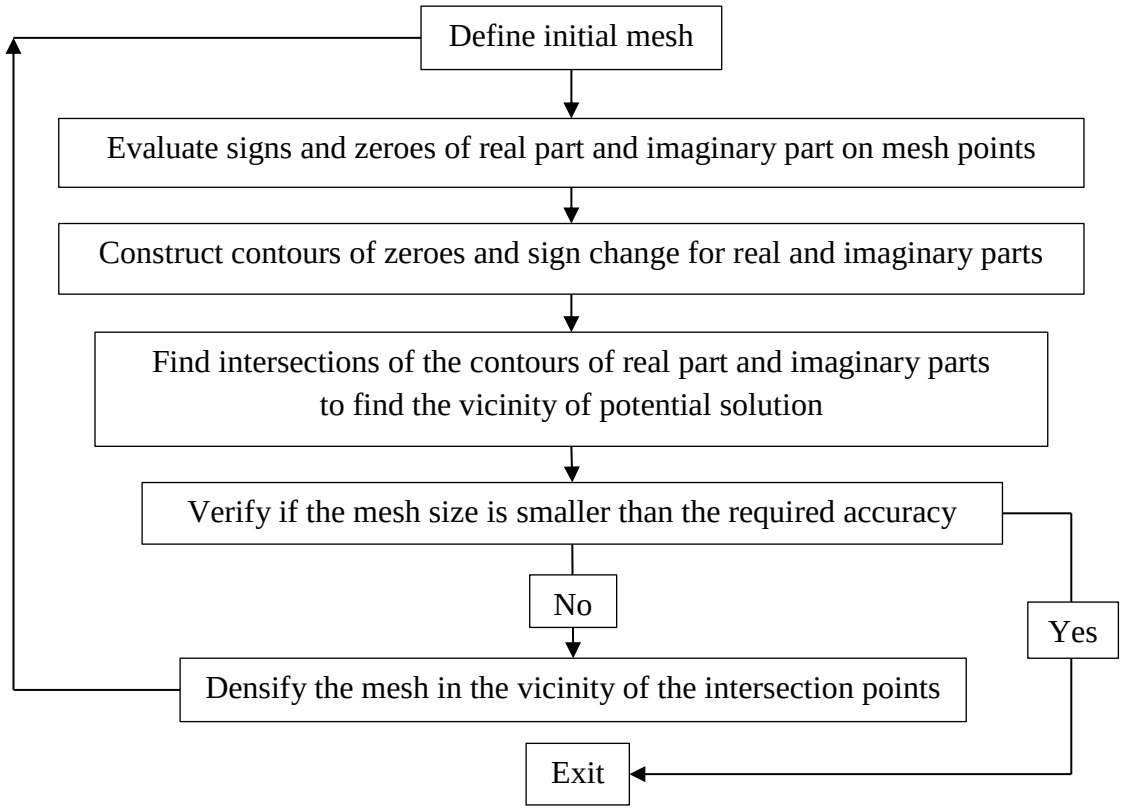

Figure 2.4: Algorithm to find complex root using modified bracketing method

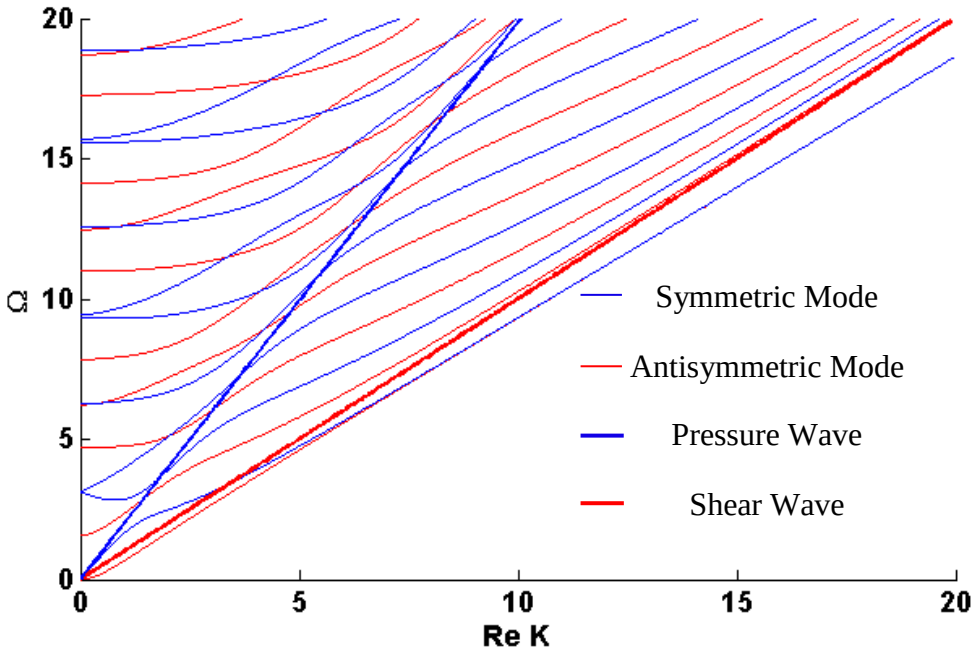

Figure 2.5: Real roots of the Rayleigh-Lamb equations

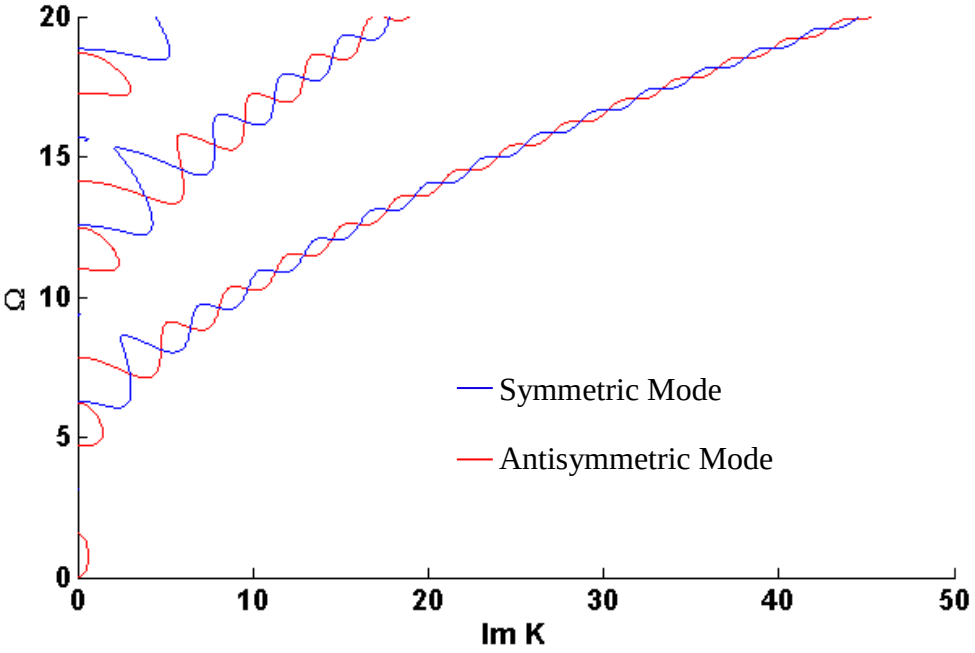

Figure 2.6: Imaginary roots of the Rayleigh-Lamb equations

To find the complex roots of Rayleigh-Lamb equations first we expressed equations (2.31) in terms of the dimensionless wavenumber $K = \xi d$ and the dimensionless frequency $\Omega = \omega d / c_S$ as

$$f_S(K,\Omega) = \left(K^2 - a^2\right)^2 \sin a \cos b + 4abK^2 \cos a \sin b = 0 \quad \text{(Symmetric)}$$
$$f_A(K,\Omega) = \left(K^2 - a^2\right)^2 \sin b \cos a + 4abK^2 \cos b \sin a = 0 \quad \text{(Antisymmetric)} \tag{2.33}$$

where, $a = \left(\Omega^2 - K^2\right)^{1/2}$, $b = \left(\Omega^2/\kappa^2 - K^2\right)^{1/2}$, $\kappa = c_P/c_S$ and c_P, c_S are pressure and shear wave speeds respectively.

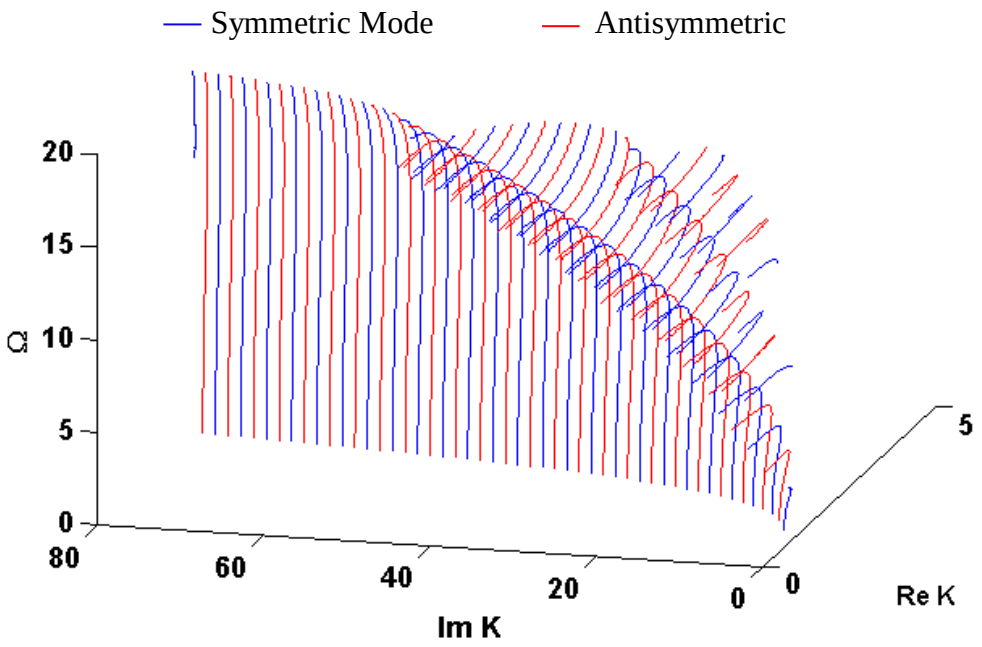

Figure 2.7: Complex roots of the Rayleigh-Lamb equations

Since κ is a function of Poisson's ration (ν), equations (2.33) are also functions of ν. We assumed $\nu = 0.33$ as it is most common among metals such as aluminum. Then we solved functions f_S and f_A separately for symmetric and antisymmetric modes. The algorithm searches for complex values of K for a given real value of Ω in the first quadrant of the complex plane. Although, for any given value of Ω, equations (2.33) have infinite number of roots for K, we limited our search for roots only in a large complex plane in the first quadrant. The initial mesh size was determined based on the monotonicity of the real part and imaginary part of the two functions. An initial discretization of 0.1 in both real and imaginary parts on the complex K plane was

chosen. This was sufficient to ensure monotonicity of the real and imaginary parts of both the functions f_S and f_A. Then the mesh was progressively densified in the regions where the complex roots existed, until, the mesh size was smaller than 10^{-5}. Therefore, the roots obtained have errors less than $\sqrt{2}\times10^{-5}$ .in magnitude. The roots were obtained for a non-dimensional frequency range of $0 \le \Omega \le 20$ with a step of 0.01.

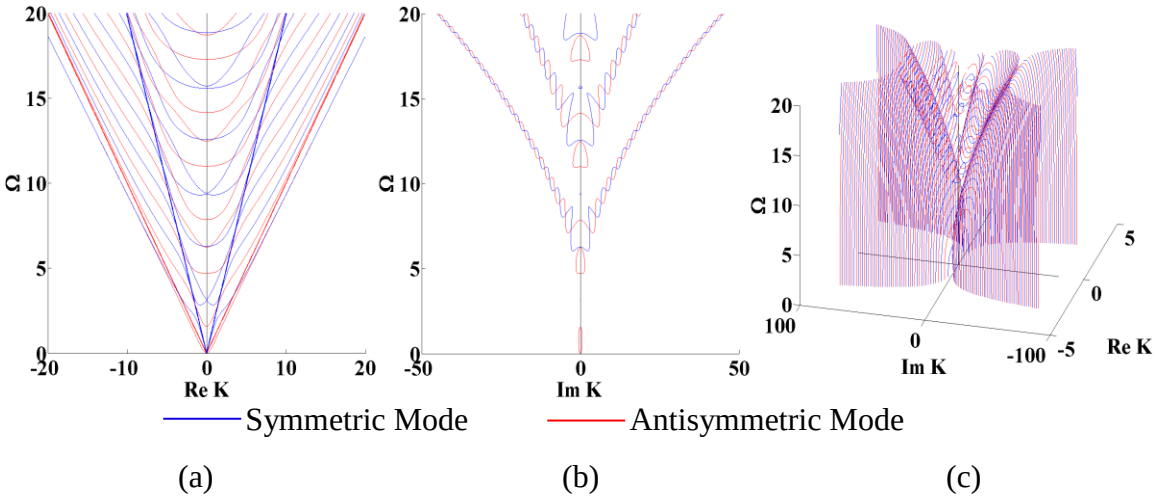

Figure 2.8: All possible roots of the Rayleigh-Lamb equations in all four quadrants of a large complex plane (ν = 0.33); (a) real roots, (b) imaginary roots, and (c) complex roots

The complete solution of Rayleigh-Lamb equations has three distinctive groups: real solutions, imaginary solutions, and complex solutions as shown in Figure 2.5, Figure 2.6, and Figure 2.7 respectively. It is important to mention that the K values corresponding to the pressure wave (P wave) and shear vertical wave (SV wave) are also part of the solution, as can be seen from Figure 2.5. We can notice in Figure 2.5 and Figure 2.6 that there are only a finite number of real and imaginary Lamb wave roots for a given frequency. Also, note that there is no imaginary root for frequencies between 1.57 and 4.7. From Figure 2.7 we notice that the complex Lamb wave roots exist for all the frequencies and that there is an infinite number of them at any given frequency. These

roots shown in Figure 2.5, Figure 2.6, and Figure 2.7 are solutions in the first quadrant of the complex planes only. It can be easily verified that if K is a solution of equations (2.33), so are $-K$, $\bar{K}$, $-\bar{K}$, where $\bar{K}$ is the conjugate of K. Therefore we obtain all possible solutions of the Rayleigh-Lamb equations for $\mu = 0.33$ in a large domain as shown in Figure 2.8.

2.1.1.2 Behavior of Lamb Wave Modes

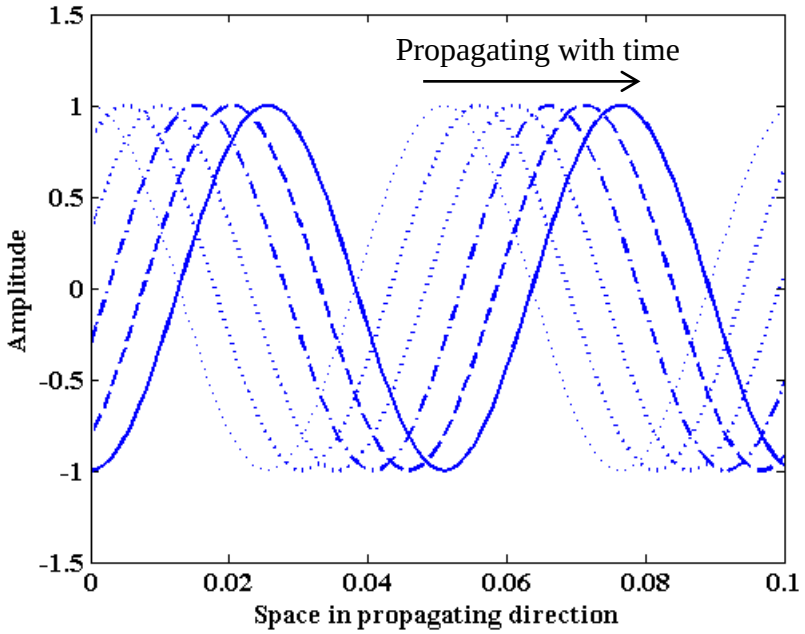

Figure 2.9: Propagating modes from real roots of the Rayleigh-Lamb equations

The three different groups of solution have very different physical behavior despite of them being solutions of the same elastodynamic problem. Assume a generic wave field of the form

$$f(y)e^{i(\xi x-\omega t)} = f(y)e^{i((\xi_R+i\xi_I)x-\omega t)} = f(y)e^{-\xi_I x}e^{i(\xi_R x-\omega t)} \tag{2.34}$$

with complex wavenumber $\xi = \xi_R + i\xi_I$. In general, a complex valued wave number will result in a harmonic wave field as represented in equation (2.34); we can see that the

imaginary part represents decay in amplitude in the positive x propagation direction and the real part dictates the harmonic motion in space along the propagating direction.

Therefore, as shown in Figure 2.9, the real solutions of the Rayleigh-lamb equations represent wave modes that are purely harmonic in space-time. These modes propagate in the space and carry power along the direction of propagation; they are called propagating modes and the wave fields associated with them can be expresses as

$$\begin{aligned} f(y)e^{i(\xi x-\omega t)} &= f(y)e^{i(\xi_R x-\omega t)} \in x \geq 0 \quad \text{with} \quad \xi = \xi_R \\ f(y)e^{i(\xi x-\omega t)} &= f(y)e^{i(-\xi_R x-\omega t)} \in x \leq 0 \ \text{with} \quad \xi = -\xi_R \end{aligned} \tag{2.35}$$

Note that the positive value of the wave number results in power flow in the $+\text{ve}\,x$ direction.

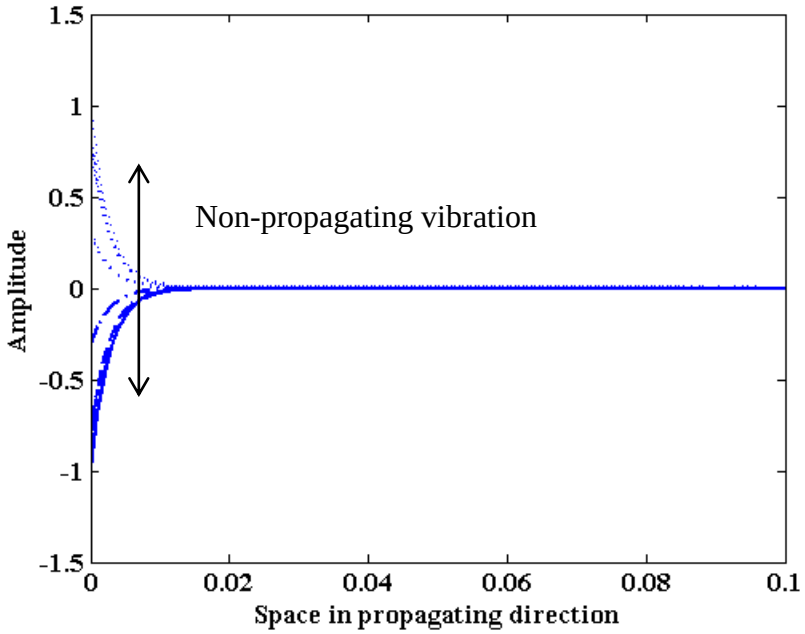

Figure 2.10: Non-propagating (evanescent) modes from imaginary roots of the Rayleigh-Lamb equations

However, for imaginary solutions, equation (2.34) is no longer harmonic in space; it becomes pure exponential in space while being harmonic in time. These modes can be represented as motions that exponentially vary with space but do not propagate in space

as the time passes. This is depicted in Figure 2.10. Since the motion stays trapped in space there is no power flow associated with these modes. These modes are called non-propagating (evanescent) modes and the motion can be expresses as

$$\begin{aligned} f(y)e^{i(\xi x-\omega t)} &= f(y)e^{-\xi_I x}e^{-i\omega t} \in x \geq 0 \text{ with} \quad \xi = i\xi_I \\ f(y)e^{i(\xi x-\omega t)} &= f(y)e^{\xi_I x}e^{-i\omega t} \in x \leq 0 \quad \text{with} \quad \xi = -i\xi_I \end{aligned} \tag{2.36}$$

It is important to note that, the negative imaginary value of the wave number cannot be associated with the positive x direction because it will result in absurd physical situation of exponentially increasing amplitude in the positive x direction with unlimited amount of energy, i.e., violates the radiation condition.

For complex roots equation (2.34) stays unchanged and the motion associated with these wave modes appear as a decaying harmonic motion in space and pure harmonic in time.

$$\begin{aligned} f(y)e^{i(\xi x-\omega t)} &= f(y)e^{i((\xi_R+i\xi_I)x-\omega t)} = f(y)e^{-\xi_I x}e^{i(\xi_R x-\omega t)} \\ f(y)e^{i(\xi x-\omega t)} &= f(y)e^{i((-\xi_R+i\xi_I)x-\omega t)} = f(y)e^{-\xi_I x}e^{i(-\xi_R x-\omega t)} \end{aligned} \Big\} \in x \geq 0$$
$$\begin{aligned} f(y)e^{i(\xi x-\omega t)} &= f(y)e^{i((-\xi_R-i\xi_I)x-\omega t)} = f(y)e^{\xi_I x}e^{i(-\xi_R x-\omega t)} \\ f(y)e^{i(\xi x-\omega t)} &= f(y)e^{i((\xi_R-i\xi_I)x-\omega t)} = f(y)e^{\xi_I x}e^{i(\xi_R x-\omega t)} \end{aligned} \Big\} \in x \leq 0 \tag{2.37}$$

Note that for all the complex roots, K, $-K$, $\bar{K}$, $-\bar{K}$, the associated motions are different. To avoid physically implausible condition of exponentially increasing amplitude, the roots with +ve imaginary part are associated with the positive x direction and vice versa as shown in equations (2.37). Another interesting fact is that these modes do carry power in the propagating direction because they are harmonic in space. Interestingly, on one hand, for the roots those lie in the first and third quadrant of the complex plane, the complex modes look like propagating modes with damping (Figure 2.11). However, no material damping or other energy dissipative mechanism was assumed in the elastodynamic system. On the other hand, for the roots those lie in the

second and fourth quadrant of the complex plane, the complex modes appear to be propagating modes emanating from within the material and exponentially increasing in amplitude without any assumption of energy source in the elastodynamic system (Figure 2.12). Though these modes are eigen modes, it seems implausible for them to exist on their own without energy dissipative or additive mechanisms in the elastodynamic system.

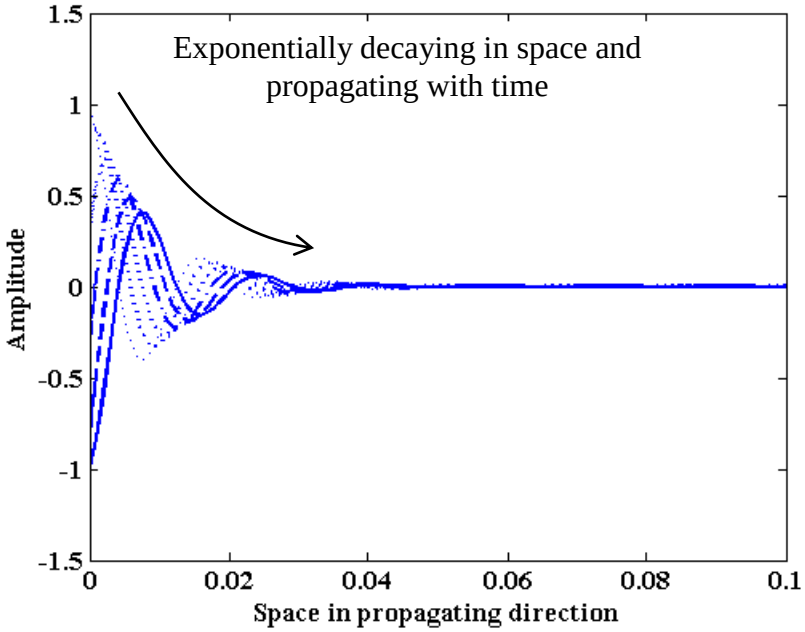

Figure 2.11: Forward propagating modes from complex roots of the Rayleigh-Lamb equations in first and third quadrant

This apparent paradox is resolved by the fact that the complex roots may appear in conjugate pair. So, if we consider these modes as coexisting pairs then the equation of motion becomes

$$\begin{aligned} f(y)e^{i((\xi_R+i\xi_I)x-\omega t)} + f(y)e^{i((-\xi_R+i\xi_I)x-\omega t)} &= 2f(y)e^{-\xi_I x}\cos\xi_R x e^{-i\omega t} \in x \geq 0 \\ f(y)e^{i((-\xi_R-i\xi_I)x-\omega t)} + f(y)e^{i((\xi_R-i\xi_I)x-\omega t)} &= 2f(y)e^{\xi_I x}\cos\xi_R x e^{-i\omega t} \in x \leq 0 \end{aligned} \quad (2.38)$$

From equations (2.38) we can see that if we consider a coexisting pair of these complex modes then the wave modes become exponentially decaying cosine function of

space while being harmonic in time. These complex mode pairs do not have any power flow associated with them as they do not propagate in space. Similar to the imaginary, these complex mode pairs also represent non-propagating local vibrations as shown in Figure 2.13.

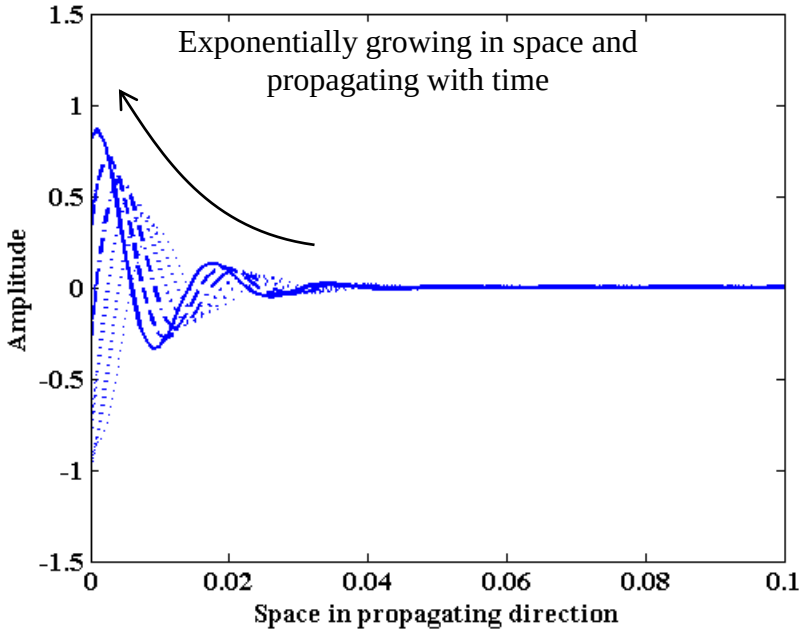

Figure 2.12: Backward propagating modes from complex roots of the Rayleigh-Lamb equations in the second and fourth quadrant

In general a wave field contains a large number of complex modes corresponding to these complex roots. These complex modes, in aggregate, will not carry any power. However, for this zero power flow, two complex modes corresponding to a complex root pair may not have equal amplitudes and may not represent a non-propagating vibration. The elastodynamic field corresponding to sum of these complex modes will represent a local vibration field and will not carry any power.

So, according to the solution of equations (2.33), for a given frequency of excitation, infinite number of wave modes may exists in a plate. Based on the inherent assumption made in the solution process of the general elastodynamic system (recall

equations (2.26)), these modes are standing wave modes across the plate thickness but, in general, are bi-harmonic along the plane of the plate and time. Thus, the solutions of Rayleigh-Lamb equation are the eigen values of the elastodynamic system defined by the equations (2.22), (2.23), and (2.24), (2.25) and the corresponding eigen vectors are standing waves in the thickness direction and propagating in the plane of the plate with time. Also, these eigen vectors form the basis vector space of the displacement field in an isotropic plate. Therefore, at this point it is important to note that, in a plate structure, any general displacement in xy plane can be represented as the linear combination of these eigen vectors.

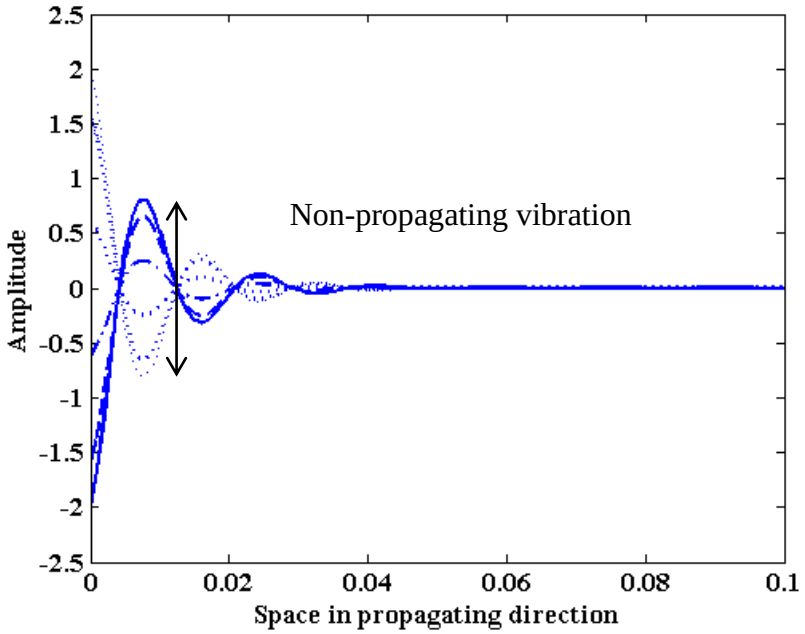

Figure 2.13: Non-propagating modes from a complex root pair of the Rayleigh-Lamb equations

In general, the displacement field can be depicted as shown in Figure 2.14; the local non-propagating and exponentially decaying vibrations corresponding to imaginary and complex modes disappear very quickly as we move away from the source with only

the propagating wave modes surviving to carry power through space in the propagating direction away from the source.

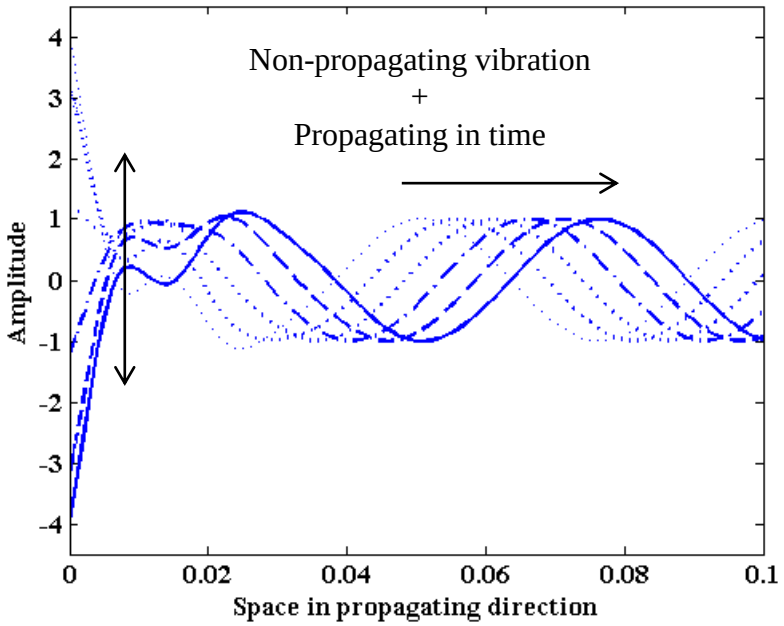

Figure 2.14: Total wave field wave field for real, imaginary and complex roots of the Rayleigh-Lamb equations

So far, to characterize displacements in xy plane for z-invariant condition in an elastodynamic field bounded by two traction free parallel surfaces, we have assumed standing wave modes across the field perpendicular to the surfaces. This assumption resulted in infinite number of eigen vectors in the form of propagating and non-propagating Lamb wave modes that are needed to represent any displacements in xy plane in this elastodynamic field at any frequency. However, any elastodynamic field has only two fundamental eigen vectors, namely, pressure wave and shear wave. Therefore, it should be possible to represent the Lamb wave modes in terms of these two waves in a plate. Also, for displacements in xy plane, we need pressure wave (P wave) and shear vertical wave (SV wave) only.

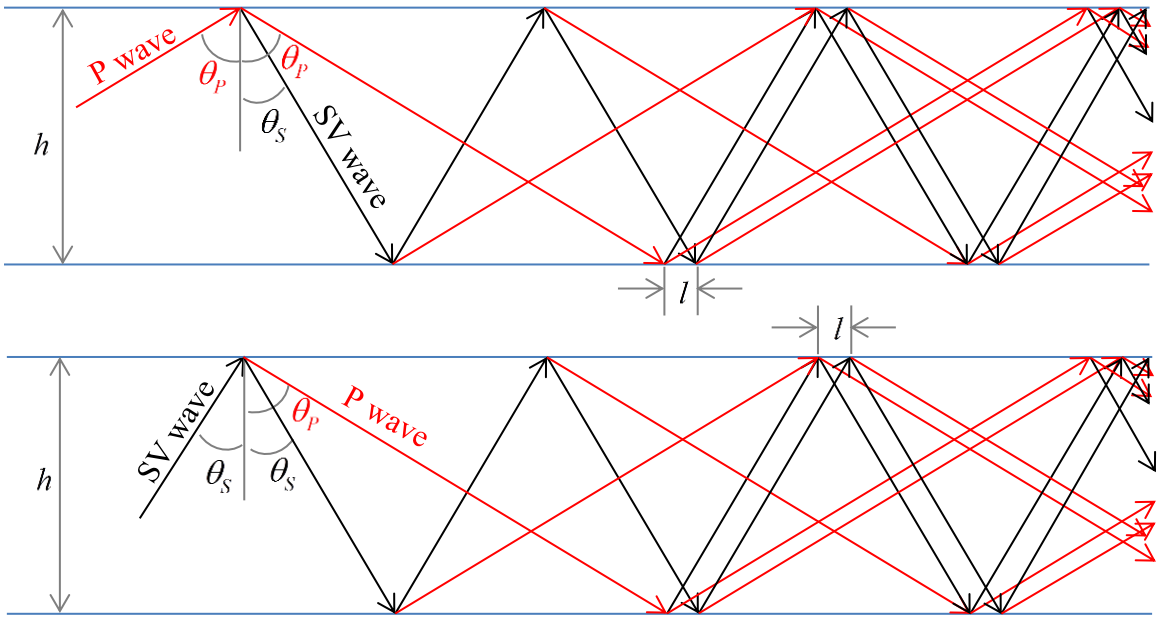

Figure 2.15: Multiple reflections of pressure and shear vertical waves in a plate

As shown in Figure 2.15, if we assume a P wave or SV wave travelling in a plate with traction free surfaces, then the resulting wave field will consist of multiple reflection patterns between the two surfaces. These reflected waves can also be assumed to be emanating from point sources distributed on the free surfaces with the distribution and the reflection angles being functions of the angle of incidence (θ_P or θ_S in Figure 2.15).

However, there are infinite such possible angles of incidences; but only a finite number of them will form a sustained reflection pattern between the two surfaces and others will disappear due to the destructive interferences with each other. For example, for some angles of incidences, when the distance l in Figure 2.15 vanishes, the reflections will be repeated identically along the plate and will form a standing wave mode across the thickness of the plate propagating along the plate in time. However, for others, the reflections will undergo progressive phase shift and decay as it travels due to destructive interference with each other.

Thus, the relative phases of the reflection patterns will dictate the resultant wave filed. Therefore, we will need only two wave modes as eigen vectors to characterize the displacement field; but, there are infinite such possible reflection patterns which make it difficult to analyze. The solutions of Rayleigh-Lamb equation give us these thickness wise standing modes created by the interactions of P and SV weaves with the plate boundaries.

Therefore, the propagating Lamb wave modes are reflection patterns of P and SV waves sustained along the plate and the non-propagating modes are decaying reflection patterns due to the destructive interferences cause by the changing phases of these reflections. Also, it can be understood from Figure 2.15 that, this phase change will depend on the thickness h of the plate and frequency. Thus, the Lamb wave modes are functions of both frequency and thickness.

2.2 CONCLUSION AND FUTURE WORK

In this chapter we have explained the theoretical background of plate guided waves. We have illustrated an algorithm to solve for complex roots of a transcendental equation in a large complex domain. We have also applied this algorithm to obtain all complex roots of the Rayleigh-Lamb equations in a large complex domain containing several hundreds of complex Lamb wave modes. We have also explained the physical behaviors of these Lamb wave modes and how they appear in an elastodynamic field in a plate. We have also illustrated the physical behavior of Lamb wave modes in terms of fundamental pressure wave and shear wave.

The algorithm described in this chapter uses modified bracketing method for the entire complex domain. However, this method can be improved; based on the roots already obtained we can predict the roots along the direction of increasing Ω. This will

improve the speed by narrowing the region for root search and follow the modes as they appear.

CHAPTER 3
CMEP: A NEW ANALYTICAL MODEL FOR SCATTERING OF STRAIGHT CRESTED LAMB WAVES FROM DAMAGE

3.1 STATE OF THE ART

In the field of non-destructive evaluation (NDE) and structural health monitoring (SHM), methods using ultrasonic plate guided waves are popular for their potential use in the inspection of large structures. Due to this popularity, the prediction of the scattering of Lamb waves from damage has been a major focus for researchers in NDE and SHM. Damage characterization in particular, as an inverse problem, requires fast and accurate prediction of scattered waves. But the solution of the scattering problem is highly challenging because of the existence of multiple dispersive modes of Lamb waves at any frequency along with mode conversion at the damage location. Therefore, well-developed numerical methods such as the finite element method (FEM) and the boundary element method (BEM) have been popular (Cho and Rose 2000; Galán and Abascal 2005; Mackerle 2004; Moser, Jacobs, and Qu 1999). However commercial FEM codes are time consuming and they do not provide much insight of the wave field in the structure, especially near the damage location. Therefore, for efficiency of simulation, researchers developed hybrid methods using FEM, BEM, and normal mode expansion (Cho and Rose 2000; Galán and Abascal 2005; Gunawan and Hirose 2004; Terrien et al. 2007). Glushkov et al. proposed the layered element method (LEM) which, unlike BEM, satisfies the plate boundary conditions by formulation (Y. V. Glushkov et al. 2009). They also proposed a simplified analytical model based on Kirchhoff plate theory for fast

simulation (E. Glushkov et al. 2015). However, the prospect of developing analytical models based on normal mode expansion has also attracted attention for possible speed and accuracy(Castaings, Le Clezio, and Hosten 2002; Feng, Shen, and Lin 2012; Feng, Shen, and Shen 2016; Flores-López and Douglas Gregory 2006; Grahn 2003; Gregory and Gladwell 1983; Gunawan and Hirose 2007; Moreau et al. 2011, 2012; Torvik 1966). Gunawan et al. (Gunawan and Hirose 2007) developed a semi analytical solution to the reflection of an oblique guided wave from the free edge of a plate by substituting the stress free edge boundary conditions into the complex orthogonality relations. However, this approach was not applied to a geometric discontinuity problem such as the step problem. Feng et al. (Feng, Shen, and Lin 2012), (Feng, Shen, and Shen 2016) used the normal mode expansion method to analyze thickness discontinuities in a plate under the plane strain condition. They split the initial plate into layers of real and virtual subplates in order to achieve the step discontinuity. Then, free-end reflection conditions were imposed on some of the subplates to generate a system of algebraic equations which yielded the modal expansion coefficient.

One of the main challenges of the scattering problem is to satisfy the thickness dependent boundary conditions at the discontinuity (Castaings, Le Clezio, and Hosten 2002; Terrien et al. 2007). Gregory et al. (Gregory and Gladwell 1982, 1983) developed the ‘projection method’ to satisfy these thickness dependent boundary conditions. This method was developed to predict the singularity in stresses in the case of geometric discontinuities (Flores-López and Douglas Gregory 2006). A scalar form of the projection method was also used by Grahn (Grahn 2003); though simple, this approach proved to be not very stable and to have slow convergence due to the use of simple sine

and cosine functions (Moreau et al. 2012). Moreau et al. (Moreau et al. 2011) used the displacement components of the complex Lamb wave modeshapes instead of simple sine and cosine functions and attained a faster convergence in the projection method.

3.2 ANALYTICAL MODEL FOR LOW FREQUENCIES: THE STEP PROBLEM

At first, to understand the modal expansion for guided wave, we apply this method on the simplest of the plate guided wave formulation, axial-flexural waves. Also, we use the simplest of the geometric discontinuities, a step in plate thickness, to demonstrate the application of modal expansion to calculate unknown scatter fields of guided waves. In terms of analytical modeling, a step involves challenges same as a realistic damages in very simple form. Therefore, for any new method aiming to solve the scattering problem, the step problem becomes a benchmark problem even though it may lack practical importance.

In this dissertation we present the formulation of axial and flexural waves in brief (Giurgiutiu 2014). For straight crested axial waves the motion is assumed to be uniform across the thickness for the plate and parallel to the mid plane. The governing equation of motion for axial wave is

$$c_L^2 \frac{\partial^2 u}{\partial x^2} = \ddot{u} \tag{3.1}$$

where, $c_L = \sqrt{\frac{1}{1-\nu^2}\frac{E}{\rho}}$ is the phase velocity of axial wave in plate. The solution of equation (3.1) is

$$u(x,t) = A_1 e^{-i(\gamma_L x - \omega t)} + A_2 e^{i(\gamma_L x - \omega t)} \tag{3.2}$$

where $\gamma_L = \frac{\omega}{c_L}$ is the wavenumber for axial plate waves with $+\gamma_L$ is the velocity in the positive x direction and $-\gamma_L$ being in the negative x direction.

For straight crested flexural waves in plate, we assume Kirchhoff plate theory. The governing equation is

$$a^4 w'''' + \ddot{w} = 0 \tag{3.3}$$

$$\text{with, } a = \left(\frac{Ed^2}{3\rho(1-\nu^2)} \right)^{1/4} \text{ and}$$

$$c_F = \sqrt{\omega}\left(\frac{D}{\rho h} \right)^{1/4} = \sqrt{\omega}\left(\frac{Ed^2}{3\rho(1-\nu^2)} \right)^{1/4} \tag{3.4}$$

being the flexural wave speed and d being the plate half thickness. Equation (3.3) accepts solution of type

$$w(x,t) = A_1 e^{i(\gamma_F x - \omega t)} + A_2 e^{\gamma_F x} e^{-i\omega t} + A_3 e^{-i(\gamma_F x + \omega t)} + A_4 e^{-\gamma_F x} e^{-i\omega t} \tag{3.5}$$

where, $\gamma_F = \dfrac{\omega}{c_F}$ is the wavenumber for axial plate waves with $+\gamma_F$ is the velocity in the positive x direction and $-\gamma_F$ being in the negative x direction. Note that in equation (3.5) the wave field of flexural waves contains propagating wave modes along with non-propagating wave modes which decay exponentially with space.

3.2.1 SCATTERING OF AXIAL-FLEXURAL WAVES FROM A STEP

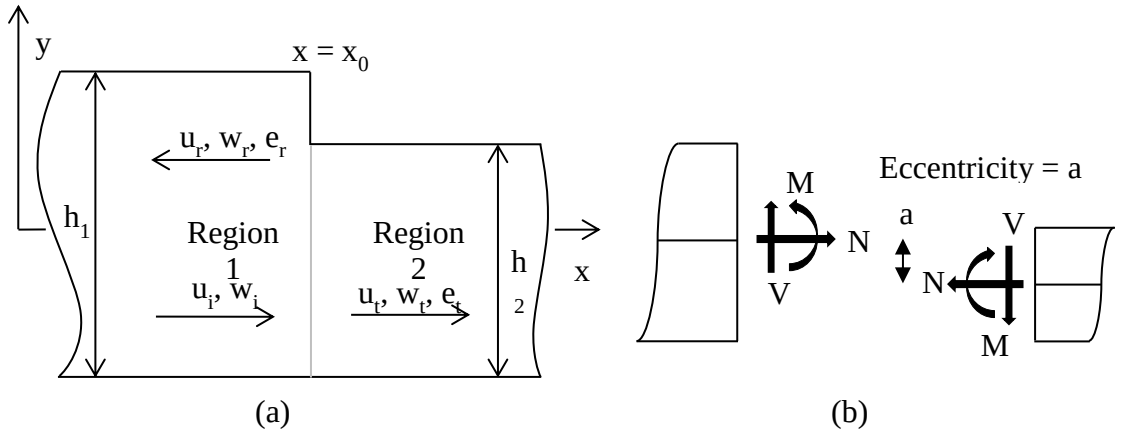

Figure 3.1: Schematic of the axial-flexural waves interacting with a step: (a) incident, transmitted, and reflected waves (b) boundary conditions at the step

Recall the axial-flexural wave solutions for a plate [15]. To begin our analysis, let us assume a step of depth d in a plate of thickness h at a distance $x = x_0$ as shown in Figure 3.1 (a). The region before the step is named Region 1 and after the step is named Region 2. The eccentricity between the Region 1 and the Region 2 is $a = \left(h_1 - h_2\right)/2$ and the depth ratio of the step is defined as $R = \left(h_1 - h_2\right)/h_1$. Also, consider a straight-crested axial-flexural 1D wave travelling in the +ve x direction in the Region 1. Let us define these waves considering the origin at $x = 0$ as,

$$\begin{aligned} {}_1u_i(x,t) &= {}_1\hat{u}_i e^{i(\gamma_1^u x - \omega t)} \\ {}_1w_i(x,t) &= {}_1\hat{w}_i e^{i(\gamma_1^w x - \omega t)} \end{aligned} \tag{3.6}$$

where, ${}_1\hat{u}_i$ and ${}_1\hat{w}_i$ are known amplitudes of the incident waves.

After interacting with the step, the incident waves result in a scattered field. This scattered field is assumed to be originating from the location of the step. For the sake of complete representation, the scattered field is expressed in terms of all possible modes including the evanescent modes. Therefore the scattered field is expressed as the combination of reflected and transmitted waves with unknown complex amplitudes as

$$\begin{aligned} {}_1u_r(x,t) &= {}_1\hat{u}_r e^{i[-\gamma_1^u (x-x_0) - \omega t]} & {}_2u_t(x,t) &= {}_2\hat{u}_t e^{i[\gamma_2^u (x-x_0) - \omega t]} \\ {}_1w_r(x,t) &= {}_1\hat{w}_r e^{i[-\gamma_1^w (x-x_0) - \omega t]} & {}_2w_t(x,t) &= {}_2\hat{w}_t e^{i[\gamma_2^w (x-x_0) - \omega t]} \\ {}_1e_r(x,t) &= {}_1\hat{e}_r e^{\gamma_1^w (x-x_0) - i\omega t} & {}_2e_t(x,t) &= {}_2\hat{e}_t e^{-\gamma_2^w (x-x_0) - i\omega t} \end{aligned} \tag{3.7}$$

where, the subscript *t* stands for the transmitted wave and the subscript *r* stands for the reflected waves. The scattered waves have unknown complex amplitudes which we want to obtain by applying the boundary conditions at the location of the step. We consider the boundary conditions to be continuities of slope and displacements with force and moment balance at the neutral axis (Figure 3.1 (b)). This leads us to a set of linear equations which can be expressed as

$$[A]\{X\} = \{B\} \tag{3.8}$$

where, $\{X\} = \left[{}_1\hat{u}_r \;\; {}_1\hat{w}_r \;\; {}_1\hat{e}_r \;\; {}_2\hat{u}_t \;\; {}_2\hat{w}_t \;\; {}_2\hat{e}_t \right]^T$ is the vector containing unknown amplitudes of the scattered waves,

$$[A] = \begin{bmatrix} 0 & -1 & -1 & 0 & 1 & 1 \\ 0 & i\gamma_1^w & -\gamma_1^w & 0 & i\gamma_2^w & -\gamma_2^w \\ -1 & ia\gamma_1^w & -a\gamma_1^w & 1 & 0 & 0 \\ E_1A_1\gamma_1^u & 0 & 0 & E_2A_2\gamma_2^u & 0 & 0 \\ 0 & iE_1I_1\left(\gamma_1^w\right)^3 & E_1I_1\left(\gamma_1^w\right)^3 & 0 & iE_2I_2\left(\gamma_2^w\right)^3 & E_2I_2\left(\gamma_2^w\right)^3 \\ 0 & -E_1I_1\left(\gamma_1^w\right)^2 & E_1I_1\left(\gamma_1^w\right)^2 & -iaE_2A_2\gamma_2^u & E_2I_2\left(\gamma_2^w\right)^2 & -E_2I_2\left(\gamma_2^w\right)^2 \end{bmatrix}$$ is

related to the known geometric and material properties and $\{B\} = \begin{bmatrix} {}_1\hat{w}_i e^{i\gamma_1^w x_0} \\ i\gamma_1^w \, {}_1\hat{w}_i e^{i\gamma_1^w x_0} \\ {}_1\hat{u}_i e^{i\gamma_1^u x_0} + ia\gamma_1^w \, {}_1\hat{w}_i e^{i\gamma_1^w x_0} \\ E_1A_1\gamma_1^u \, {}_1\hat{u}_i e^{i\gamma_1^u x_0} \\ iE_1I_1\left(\gamma_1^w\right)^3 \, {}_1\hat{w}_i e^{i\gamma_1^w x_0} \\ E_1I_1\left(\gamma_1^w\right)^2 \, {}_1\hat{w}_i e^{i\gamma_1^w x_0} \end{bmatrix}$ is

related to the known incident wave field. Equation (3.8) can be solved for $\{X\}$ as,

$$\{X\} = [A]^{-1}\{B\} \tag{3.9}$$

3.2.2 NUMERICAL RESULTS FOR THE AXIAL-FLEXURAL WAVES MODEL

Assuming $u_i = 1$ and $w_i = 0$ we obtained the unknown complex amplitudes by solving Equation (3.9). Figure 3.2 shows the result from the axial-flexural wave model for a step. We can see how the displacement field varies for scattered axial-flexural waves for $0 \le R \le 1$. We can notice that for free end $(R = 1)$ the net axial wave amplitude is doubled $(u_t = 2)$ and the reflected wave amplitude is same as the incident wave amplitude $(u_r = 1)$; the amplitude of the flexural waves also vanish at the free end ($w_t = w_r = 0$). It can also be seen that the calculated displacement fields are accurate for

the continuous plate case $(R=0)$. From Figure 3.3 we can see that the power flow through the step is balanced as power flow through the Region 1 and the Region 2 are identical. Therefore from Figure 3.2 and Figure 3.3 we can conclude that the axial-flexural wave model is correct.

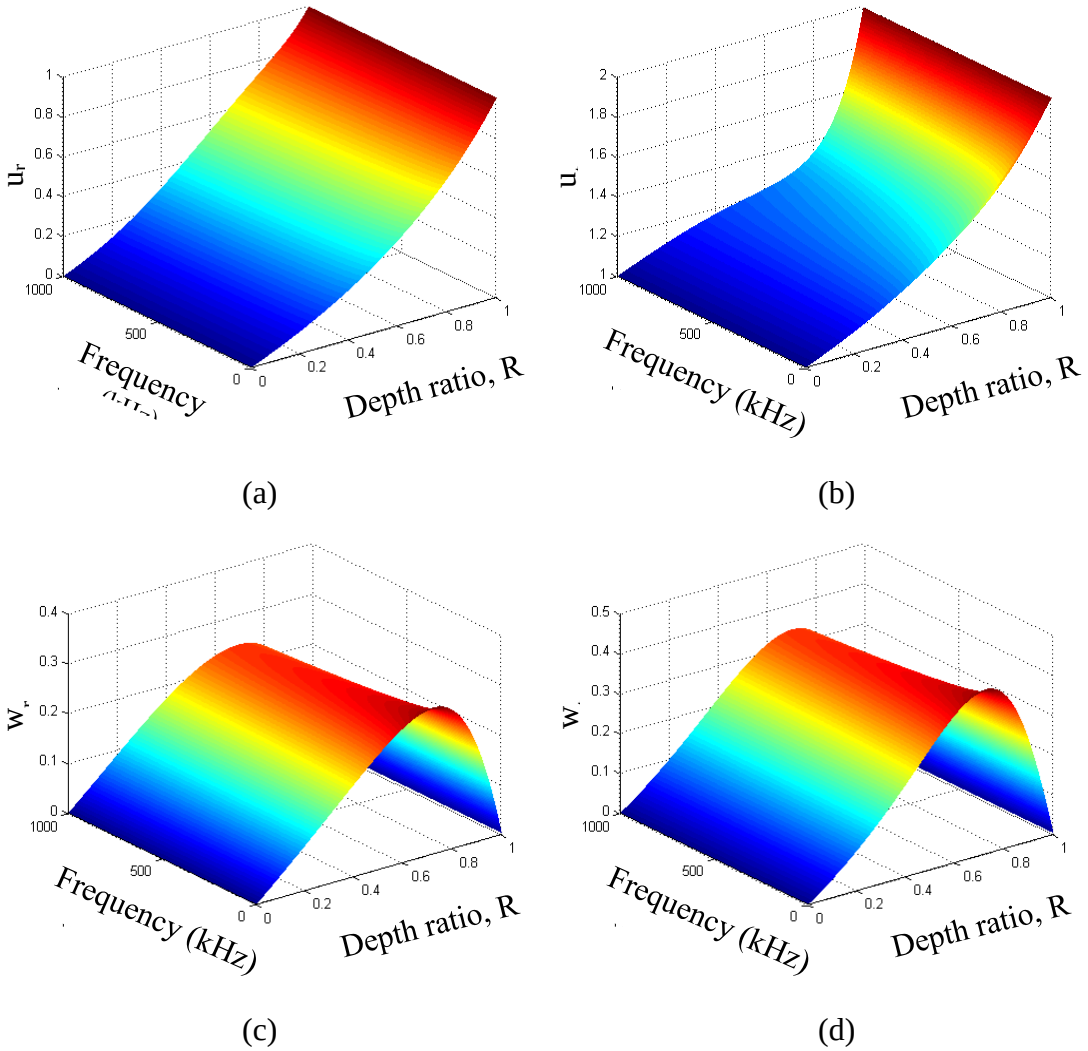

Figure 3.2: Variation with frequency and depth-ratio of the axial-flexural reflected and transmitted waves for incident axial wave (a) reflected axial (b) transmitted axial (c) reflected flexural (d) transmitted flexural

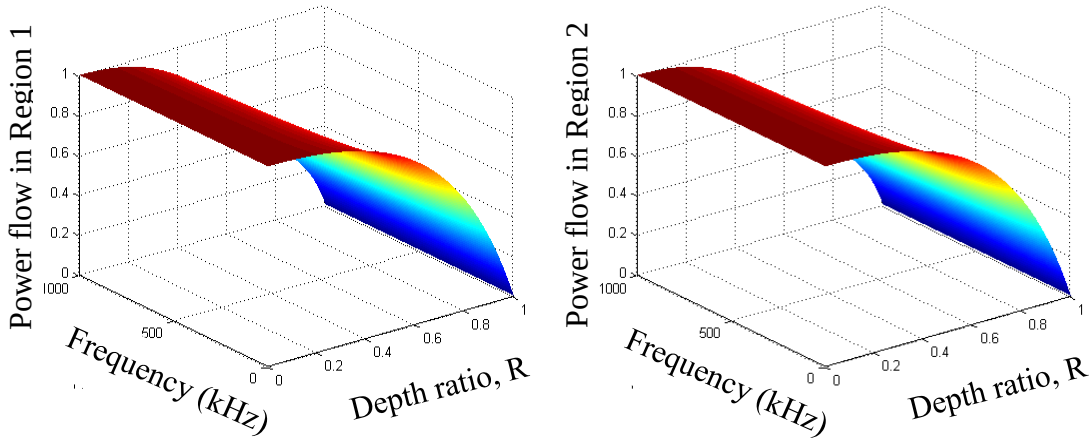

(a) (b)

Figure 3.3: Total axial-flexural wave power flow for incident axial wave through, (a) Region 1 and (b) Region 2

Analytically, the power flow through the step can be expressed as,

$$\langle P_1 \rangle = \omega \frac{E_1}{\left(1-\nu^2\right)} \left(\frac{1}{2} A_1 \gamma_1^u \operatorname{Re}\left({}_1u_{i\,1}\overline{u_i} - {}_1u_{r\,1}\overline{u_r} \right) + I_1 \left(\gamma_1^w\right)^3 \operatorname{Re}\left({}_1w_{i\,1}\overline{w_i} - {}_1w_{r\,1}\overline{w_r} \right) \right)$$
$$\langle P_2 \rangle = \omega \frac{E_2}{\left(1-\nu^2\right)} \left(\frac{1}{2} A_2 \gamma_{2\,2}^u \operatorname{Re}\left({}_2u_{t\,2}\overline{u_t} \right) + I_2 \left(\gamma_1^w\right)^3 \operatorname{Re}\left({}_2w_{t\,2}\overline{w_t} \right) \right) \tag{3.10}$$

It should be noted that in Equation (3.10) there is no contribution of the evanescent modes to the power flow. However it is very important to consider them for the modal expansion as they are solutions of the governing equation of the wave field (Giurgiutiu 2014).

3.3 ANALYTICAL MODEL FOR ALL FREQUENCIES: THE STEP PROBLEM

In this section, we present an efficient analytical method for the prediction of Lamb wave scattered field using complex mode expansion and vector projection. We improved in several ways upon previous authors. One improvement is that we modified the projection method to take advantage of the power flow associated with Lamb wave modes. As different from the references (Grahn 2003), (Moreau et al. 2011), the stress boundary conditions are projected onto the conjugate of the displacement modeshapes

and the displacement boundary conditions are projected onto the conjugate of the stress modeshapes. Therefore this method transforms stress and displacement equations into the power equations. Another improvement is that we applied the projection to all the unknown wave fields. Our approach leads to fast convergence in terms of the number of complex modes needed in the modal expansion because it creates dominant diagonal terms in the matrix equation. It also ensures that, when the method has converged, the power balance is automatically satisfied. We call this method complex modes expansion with vector projection (CMEP). It is a Galerkin type approach where we implemented vector projection of the boundary conditions directly using the power flow expression.

Other approaches exist in the literature using the orthogonality between modal stresses and displacements (Feng, Shen, and Lin 2012), (Feng, Shen, and Shen 2016) but they are different from our method because they need to assume virtual wave guides and vertical free-ends to implement the orthogonality relations.

In this paper, we demonstrate the CMEP method using the step problem which is one of the simplest forms of plate discontinuities. However, in terms of analytical modeling, the step problem poses the same challenges as a realistic damage. Therefore, for any new method aiming to solve the scattering problem, the step problem can be used as a benchmark problem even though it may lack a direct practical relevance.

3.3.1 Problem Setup for a Step

To begin our analysis, let us consider a plate with a cross section as shown in Figure 3.4. We assume that there is an incident straight-crested Lamb wave mode travelling from the left towards the step. Upon interacting with the step, it will result in reflected wave modes and transmitted wave modes.

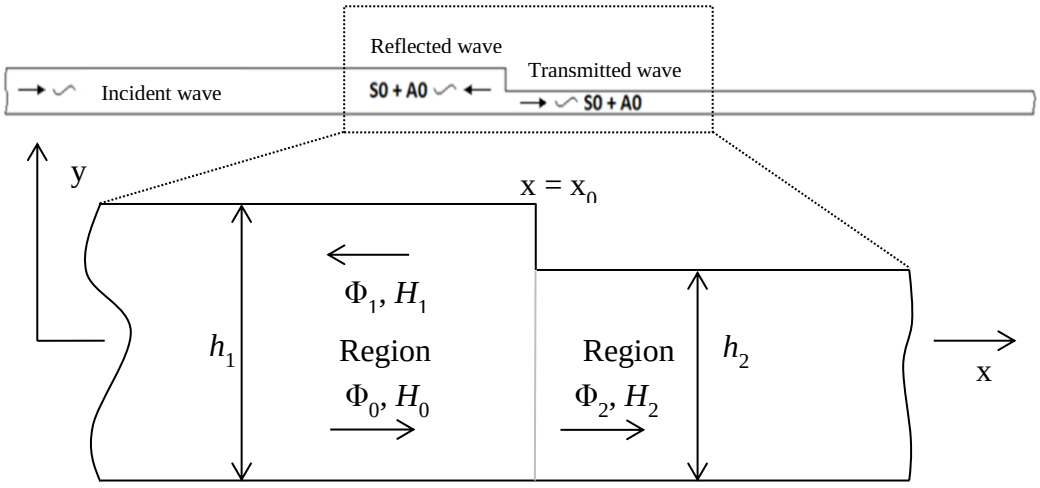

Figure 3.4: Schematic of Lamb waves interacting with a step

As shown in Figure 3.4, the step is located at a distance $x = x_0$ with the thickness of the plate being h_1 before the step and h_2 after the step. Also, let us imagine that the incident wave field is represented by (Φ_0, H_0), travelling in the $+ve$ x direction in the Region 1. We define the reflected wave field as (Φ_1, H_1) and the transmitted wave field as (Φ_2, H_2). The incident and scattered wave fields satisfy the generic wave equations

$$\begin{aligned} \frac{\partial^2 \Phi}{\partial x^2} + \frac{\partial^2 \Phi}{\partial y^2} &= \frac{1}{C_P^2} \ddot{\Phi} \\ \frac{\partial^2 H}{\partial x^2} + \frac{\partial^2 H}{\partial y^2} &= \frac{1}{C_S^2} \ddot{H} \end{aligned} \tag{3.11}$$

These must satisfy the zero-stress boundary conditions at the top and the bottom of the plate,

$$\sigma_{yy}\Big|_{\left(x<x_0;\, y=\pm\frac{h_1}{2}\right),\ \left(x>x_0;\, y=h_2-\frac{h_1}{2},-\frac{h_1}{2}\right)} = 0 \qquad \sigma_{xy}\Big|_{\left(x<x_0;\, y=\pm\frac{h_1}{2}\right),\ \left(x>x_0;\, y=h_2-\frac{h_1}{2},-\frac{h_1}{2}\right)} = 0 \tag{3.12}$$

The boundary conditions at the traction free vertical step are,

$$\sigma_{xx,0} + \sigma_{xx,1} = \begin{cases} 0, & x = x_0, \quad h_2 - h_1/2 \le y \le h_1/2 \\ \sigma_{xx,2}, & x = x_0, \quad -h_1/2 \le y \le h_2 - h_1/2 \end{cases} \tag{3.13}$$

$$\sigma_{xy,0}+\sigma_{xy,1}=\begin{cases}0, & x=x_0, \quad h_2-h_1/2\le y\le h_1/2\\ \sigma_{xy,2}, & x=x_0, \quad -h_1/2\le y\le h_2-h_1/2\end{cases} \tag{3.14}$$

$$\left.\begin{aligned}u_{x,0}+u_{x,1}&=u_{x,2}\\ u_{y,0}+u_{y,1}&=u_{y,2}\end{aligned}\right\} \quad x=x_0, \quad -h_1/2\le y\le h_2-h_1/2 \tag{3.15}$$

where, the subscript 0 stands for incident waves in Region 1, the subscript 1 stands for reflected waves in Region 1 and the subscript 2 stands for transmitted waves in Region 2. We assume the incident wave field to be time harmonic of the form

$$\Phi_0=f_n(y)e^{i(\xi_n x-\omega t)} \qquad H_0=ih_n(y)e^{i(\xi_n x-\omega t)} \tag{3.16}$$

Assuming ξ_n to be one of the roots of the Rayleigh-Lamb equation for the plate in the Region 1, Equations (3.11) and (3.12) are satisfied by the definition of Lamb waves and the incident wave becomes one of the modes of Lamb waves.

3.3.2 Complex Modes Expansion of the Scattered Wave Field for a Step

In this section, we present the general concept of CMEP algorithm. We assume the scattered wave field to consist of a reflected wave field (Φ_1, H_1) and a transmitted wave field (Φ_2, H_2) having harmonic expressions similar to the incident wave field (Φ_0, H_0) given by Equation (3.16). Since the boundary conditions at the step cannot be satisfied by assuming any finite number of Lamb wave modes (Torvik 1966), we expand these reflected and transmitted wave fields in terms of all possible complex Lamb wave modes corresponding to the complex roots of Rayleigh-Lamb frequency equation. Therefore, the scattered wave field is expressed as

$$\begin{aligned}
&\Phi_1=\sum_{n_1=1}^{\infty}C_{1,n_1}\Phi_{n_1}=\sum_{n_1=1}^{\infty}C_{1,n_1}f_{n_1}(y_1)e^{i(\xi_{n_1}x-\omega t)} && \Phi_2=\sum_{n_2=1}^{\infty}C_{2,n_2}\Phi_{n_2}=\sum_{n_2=1}^{\infty}C_{2,n_2}f_{n_2}(y_2)e^{i(\xi_{n_2}x-\omega t)}\\
&H_1=\sum_{n_1=1}^{\infty}C_{1,n_1}H_{n_1}=\sum_{n_1=1}^{\infty}C_{1,n_1}ih_{n_1}(y_1)e^{i(\xi_{n_1}x-\omega t)} && H_2=\sum_{n_2=1}^{\infty}C_{2,n_2}H_{n_2}=\sum_{n_2=1}^{\infty}C_{2,n_2}ih_{n_2}(y_2)e^{i(\xi_{n_2}x-\omega t)}\\
&n_1=1,2,3,... && n_2=1,2,3,...
\end{aligned} \tag{3.17}$$

where, y_1 and y_2 are connected by the expression $y_2 = y_1 + a$ with $a = (h_1 - h_2)/2$ being the eccentricity between the Region 1 and the Region 2. The wavenumber ξ_{n_1} is the n_1 th complex root of the Rayleigh-Lamb equation in the Region 1 and the wavenumber ξ_{n_2} is the n_2 th complex root of the Rayleigh-Lamb equation in the Region 2. The coefficient $C_{n_1,1}$ is the unknown amplitude of the n_1 th mode of Lamb waves in the Region 1 whereas $C_{n_2,2}$ is the unknown amplitude of the n_2 th mode of Lamb waves in the Region 2. Equation (3.17) expresses the scattered wave field as the summation of all possible complex Lamb wave modes at a given frequency. The amplitudes $C_{n_1,1}$, $C_{n_2,2}$ of these modes have to be determined through the boundary matching process. Recall the boundary conditions at the step $x = x_0$ as given by Equations (3.13), (3.14) and (3.15). Also note that the plate boundary conditions given by Equations (3.11) and (3.12) are satisfied by the definition of Lamb waves. We express stress and displacement fields from Equations (3.13), (3.14) and (3.15) using the complex Lamb wave mode expansion of Equation (3.17), i.e.,

$$\begin{aligned} \vec{u}_1 &= \begin{bmatrix} u_{x,1} \\ u_{y,1} \end{bmatrix} = \sum_{n_1=1}^{\infty} C_{n_1,1} \begin{bmatrix} u_x \\ u_y \end{bmatrix}_{n_1,1} & \vec{\sigma}_1 &= \begin{bmatrix} \sigma_{xx,1} \\ \sigma_{xy,1} \end{bmatrix} = \sum_{n_1=1}^{\infty} C_{n_1,1} \begin{bmatrix} \sigma_{xx} \\ \sigma_{xy} \end{bmatrix}_{n_1,1} \\ \vec{u}_2 &= \begin{bmatrix} u_{x,2} \\ u_{y,2} \end{bmatrix} = \sum_{n_2=1}^{\infty} C_{n_2,2} \begin{bmatrix} u_x \\ u_y \end{bmatrix}_{n_2,2} & \vec{\sigma}_2 &= \begin{bmatrix} \sigma_{xx,2} \\ \sigma_{xy,2} \end{bmatrix} = \sum_{n_2=1}^{\infty} C_{n_2,2} \begin{bmatrix} \sigma_{xx} \\ \sigma_{xy} \end{bmatrix}_{n_2,2} \end{aligned} \tag{3.18}$$

where, for the displacement vectors, subscripts *x* and *y* indicate the directions of the displacement. For stresses, the subscript *xx* stands for the normal stress in the *x* direction and subscript *xy* stands for the shear stress. The notations $C_{n_1,1}$, $C_{n_2,2}$ are the unknown amplitudes of the complex Lamb wave modes in Regions 1 and 2, respectively. In the same vein, the incident wave field uses the subscript 0, i.e.,

$$\vec{u}_0 = \begin{bmatrix} u_{x,0} \\ u_{y,0} \end{bmatrix} = \begin{bmatrix} u_x \\ u_y \end{bmatrix}_0 \qquad \vec{\sigma}_0 = \begin{bmatrix} \sigma_{xx,0} \\ \sigma_{xy,0} \end{bmatrix} = \begin{bmatrix} \sigma_{xx} \\ \sigma_{xy} \end{bmatrix}_0 \tag{3.19}$$

Using Equations (3.18), (3.19) into Equations (3.13), (3.14) and (3.15) yields

$$\vec{\sigma}_0 + \vec{\sigma}_1 = \begin{cases} 0, & x = x_0, \quad h_2 - h_1/2 \le y \le h_1/2 \\ \vec{\sigma}_2, & x = x_0, \quad -h_1/2 \le y \le h_2 - h_1/2 \end{cases} \tag{3.20}$$

$$\vec{u}_0 + \vec{u}_1 = \vec{u}_2, \qquad x = x_0, \qquad -h_1/2 \le y \le h_2 - h_1/2 \tag{3.21}$$

Therefore, Equations (3.20), and (3.21) represent the thickness dependent boundary conditions at the step location.

3.3.3 Vector Projection of the Boundary Conditions for a Step

To make Equations (3.20), (3.21) independent of y, we follow Grahn (Grahn 2003) and project them onto appropriate complete orthogonal vector spaces as described. But, different from (Grahn 2003), we do not use generic sine and cosine functions, instead, we use the time averaged power flow expression which uses the stress-velocity product (Auld 1973). Thus, in the Region 1, we project the stress boundary conditions onto the conjugate displacement vector space of the complex Lamb wave modes. By the same token, in the Region 2, we project the displacement boundary conditions onto the conjugate stress vector space of the complex Lamb wave modes. By doing so, the CMEP formulation automatically incorporates the average power flow associated with both the reflected and the transmitted wave fields. This approach has two main advantages: first, following the time averages power flow associated with the modes, it creates dominant diagonal terms in the final matrix equation which leads to fast convergence; second, it transforms the stress and displacement equations at the interface into the equations representing the power flow balance across the interface between the two separate wave fields. In short, this approach incorporates the balance of power flow across the interface achieving fast convergence.

The projection vector space for the Equation (3.20) is

$$\vec{\bar{u}}_1 = \text{conj}\begin{bmatrix} u_x \\ u_y \end{bmatrix}_{\bar{n}_1,1} = \begin{bmatrix} \bar{u}_x \\ \bar{u}_y \end{bmatrix}_{\bar{n}_1,1} \quad ; \quad \bar{n}_1 = 1,2,3,... \tag{3.22}$$

After projecting Equation (3.20) onto Equation (3.22), the stress boundary conditions in Equation (3.20) take the form

$$\int_{-h_1/2}^{h_1/2} \left(\vec{\sigma}_0 + \vec{\sigma}_1\right) \cdot \vec{\bar{u}}_1 dy = \int_{-h_1/2}^{h_2-h_1/2} \vec{\sigma}_2 \cdot \vec{\bar{u}}_1 dy$$

$$\Rightarrow \sum_{n_2=1}^{\infty} C_{n_2,2} \left\langle \begin{bmatrix} \sigma_{xx} \\ \sigma_{xy} \end{bmatrix}_{n_2,2}, \begin{bmatrix} \bar{u}_x \\ \bar{u}_y \end{bmatrix}_{\bar{n}_1,1} \right\rangle_{-h_1/2}^{h_2-h_1/2} - \sum_{n_1=1}^{\infty} C_{n_1,1} \left\langle \begin{bmatrix} \sigma_{xx} \\ \sigma_{xy} \end{bmatrix}_{n_1,1}, \begin{bmatrix} \bar{u}_x \\ \bar{u}_y \end{bmatrix}_{\bar{n}_1,1} \right\rangle_{-h_1/2}^{h_1/2} = \left\langle \begin{bmatrix} \sigma_{xx} \\ \sigma_{xy} \end{bmatrix}_0, \begin{bmatrix} \bar{u}_x \\ \bar{u}_y \end{bmatrix}_{\bar{n}_1,1} \right\rangle_{-h_1/2}^{h_1/2} \tag{3.23}$$

where, $\int_a^b P \cdot Q\, dy = \langle P, Q \rangle_a^b$ represents the inner product. The projection vector space for Equation (3.21) is

$$\vec{\bar{\sigma}}_2 = \text{conj}\begin{bmatrix} \sigma_{xx} \\ \sigma_{xy} \end{bmatrix}_{\bar{n}_2,2} = \begin{bmatrix} \bar{\sigma}_{xx} \\ \bar{\sigma}_{xy} \end{bmatrix}_{\bar{n}_2,2} \quad ; \quad \bar{n}_2 = 1,2,3,... \tag{3.24}$$

After projecting Equation (3.21) onto Equation (3.24), the displacement boundary conditions in Equation (3.21) take the form

$$\int_{-h_1/2}^{h_2-h_1/2} \left(\vec{u}_0 + \vec{u}_1\right) \cdot \vec{\bar{\sigma}}_2 dy = \int_{-h_1/2}^{h_2-h_1/2} \vec{u}_2 \cdot \vec{\bar{\sigma}}_2 dy$$

$$\Rightarrow \sum_{n_2=1}^{\infty} C_{n_2,2} \left\langle \begin{bmatrix} u_x \\ u_y \end{bmatrix}_{n_2,2}, \begin{bmatrix} \bar{\sigma}_{xx} \\ \bar{\sigma}_{xy} \end{bmatrix}_{\bar{n}_2,2} \right\rangle_{-h_1/2}^{h_2-h_1/2} - \sum_{n_1=1}^{\infty} C_{n_1,1} \left\langle \begin{bmatrix} u_x \\ u_y \end{bmatrix}_{n_1,1}, \begin{bmatrix} \bar{\sigma}_{xx} \\ \bar{\sigma}_{xy} \end{bmatrix}_{\bar{n}_2,2} \right\rangle_{-h_1/2}^{h_2-h_1/2} \tag{3.25}$$

$$= \left\langle \begin{bmatrix} u_x \\ u_y \end{bmatrix}_0, \begin{bmatrix} \bar{\sigma}_{xx} \\ \bar{\sigma}_{xy} \end{bmatrix}_{\bar{n}_2,2} \right\rangle_{-h_1/2}^{h_2-h_1/2}$$

3.3.4 NUMERICAL SOLUTION FOR A STEP

For numerical calculation we consider finite values for the indices $n_1, n_2, \bar{n}_1, \bar{n}_2$. We assume, $n_1 = 1,2,3,...,N_1$, $n_2 = 1,2,3,...,N_2$, $\bar{n}_1 = 1,2,3,...,\bar{N}_1$, $\bar{n}_2 = 1,2,3,...,\bar{N}_2$. Then, Equation (3.23) contains $\bar{N}_1$ linear equations with $\left(N_1 + N_2\right)$ unknowns and

Equation (3.25) contains $\bar{N}_2$ linear equations with $\left(N_1+N_2\right)$ unknowns. Recall that the $\left(N_1+N_2\right)$unknowns are the complex Lamb wave mode amplitudes $\left(C_{n_1,1},\, C_{n_2,2}\right)$. Thus, Equations (3.23), (3.25) combined are a set of $\left(\bar{N}_1+\bar{N}_2\right)$linear algebraic equations in $\left(N_1+N_2\right)$ unknowns. Equations (3.23) and (3.25) can be written together in matrix form as

$$\begin{bmatrix} \langle [\ ],[\ ] \rangle & \cdots & \cdots & \cdots & \cdots & \langle [\ ],[\ ] \rangle \\ \vdots & \ddots & & & & \vdots \\ \vdots & & \ddots & & & \vdots \\ \vdots & & & \ddots & & \vdots \\ \vdots & & & & \ddots & \vdots \\ \langle [\ ],[\ ] \rangle & \cdots & \cdots & \cdots & \cdots & \langle [\ ],[\ ] \rangle \end{bmatrix}_{\left(\bar{N}_1+\bar{N}_2\right)\times\left(N_1+N_2\right)} \begin{bmatrix} {}_1C_1 \\ \vdots \\ {}_1C_{n_1} \\ {}_2C_1 \\ \vdots \\ {}_2C_{n_2} \end{bmatrix}_{\left(N_1+N_2\right)\times 1} = \begin{bmatrix} \langle [\ ],[\ ] \rangle \\ \vdots \\ \vdots \\ \vdots \\ \langle [\ ],[\ ] \rangle \end{bmatrix}_{\left(\bar{N}_1+\bar{N}_2\right)\times 1}$$

$$\Rightarrow [A]\{C\} = \{B\} \tag{3.26}$$

where, [*A*] and [*B*] are known entities and {*C*} contains the $\left(N_1+N_2\right)$ unknowns $\left(C_{n_1,1},\, C_{n_2,2}\right)$. The unknown {*C*} can be calculated as

$$\{C\} = [A]^{-1}\{B\} \tag{3.27}$$

As a test case we consider aluminum as the material of the plate with $E_1 = E_2 = 70$ GPa, $\rho = 2780$ kg/m^3 and $\nu = 0.33$ with $h_1 = 2$ mm and $h_2 = 1$ mm. We also consider $N_1 = N_2 = \bar{N}_1 = \bar{N}_2$ with S0 as the incident Lamb wave mode. We use a frequency-thickness range of up to 2.75 MHz-mm. We perform convergence studies to determine the maximum number of complex roots of the Rayleigh-Lamb equation needed to calculate the first three scattered Lamb wave modes, S0, A0 and A1 with high accuracy. Figure 3.5 shows the convergence study for the amplitudes of the first three modes of Lamb waves, S0, A0 and A1. From Figure 3.5 we can also see that the

convergence of the A1 mode does not change much as it goes from being an evanescent mode (0.2 and 1.5 MHz-mm) to being a propagating mode (2.75 MHz-mm).

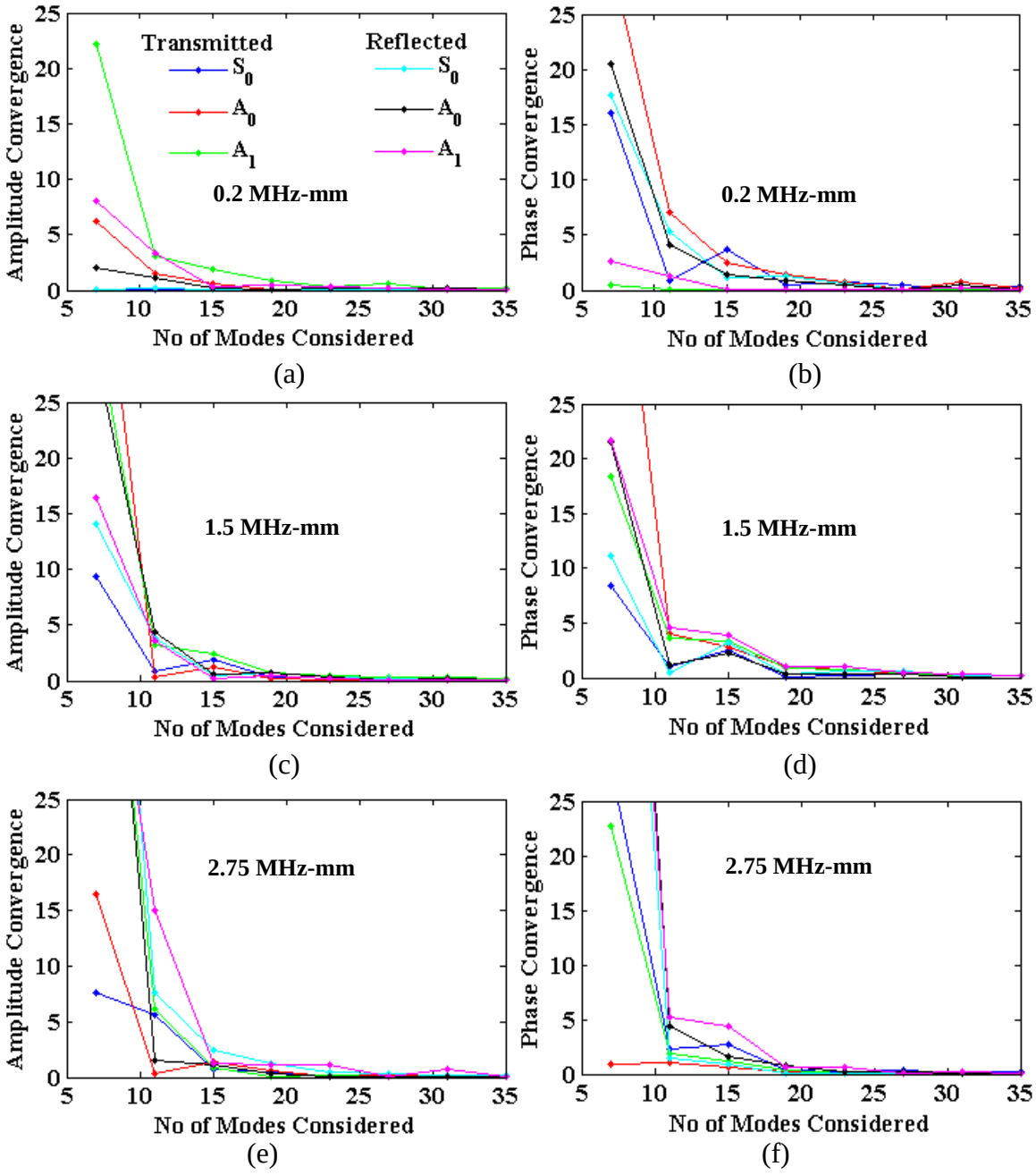

Figure 3.5: Convergence of (a) amplitude at 0.2 MHz-mm, (b) phase at 0.2 MHz-mm, (c) amplitude at 1.5 MHz-mm, (d) phase at 1.5 MHz-mm, (e) amplitude at 2.75 MHz-mm, (f) phase at 2.75 MHz-mm of scattered Lamb wave modes for S0 mode incident on half thickness step

Considering 27 modes in the expansion ensured convergence of S0, A0 and A1 modes close to 0.5% error up to 2.75 MHz-mm. However, at even higher frequencies when the propagating S1 mode appears, we may need to consider a higher number of Lamb wave modes for proper convergence of the complex amplitudes. This is because the S1 mode does not exist below 2.75 MHz-mm, neither as complex mode nor as evanescent mode; this changes the structure of the wave field.

Another important verification of convergence is the power flow balance. Figure 3.6 shows that a 27-mode expansion gave a balanced average power flow though the step over the whole frequency range up to 2.75 MHz. It is apparent that power flow balance requirements are met since the "P_{av} incident" line overlaps with the "P_{av} Scattered (Reflected + Transmitted)" line.

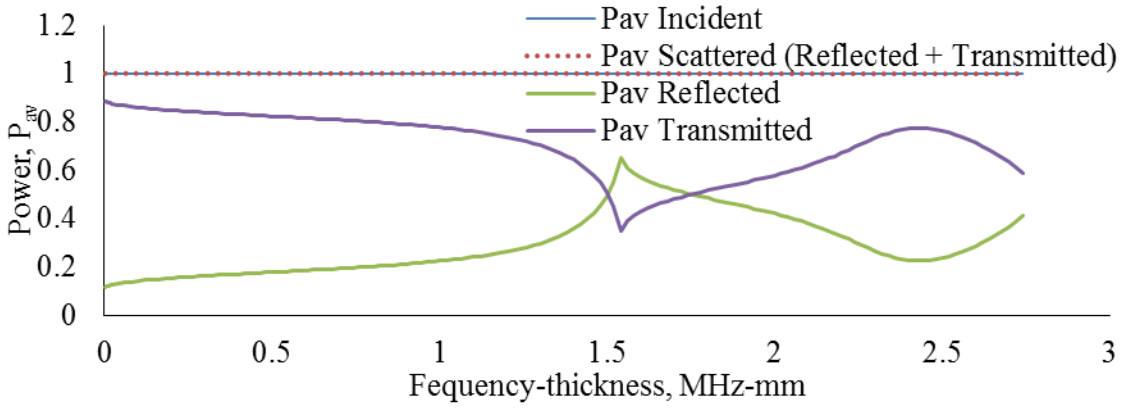

Figure 3.6: Variation of time average power flow P_{av} through the step as calculated using CMEP with a 27-mode expansion for S0 mode incident on half thickness step

3.3.5 Asymptotic Behavior of Lamb Waves at Low Frequencies

We consider again the test case of an aluminum plate having $E_1 = E_2 = 70$ GPa, $\rho = 2780$ kg/m^3 and $\nu = 0.33$ with $h_1 = 2$ mm and $h_2 = 1$ mm. For simplicity, we consider $N_1 = N_2 = \bar{N}_1 = \bar{N}_2$. We then solve Equation (3.27) for $\{C\}$ with S0 as the incident wave.

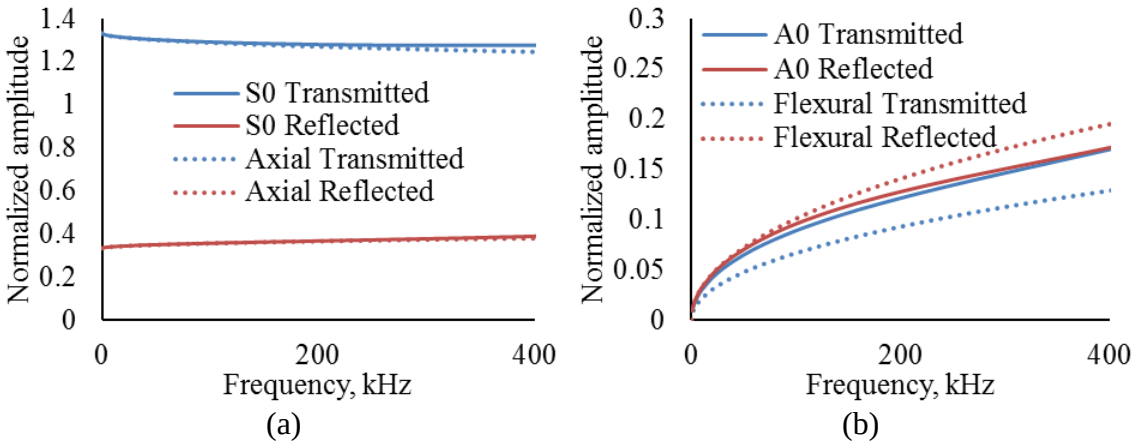

Figure 3.7: Comparison between the displacement amplitudes of the Lamb-wave CMEP solution and axial-flexural solution: (a) symmetric mode (b) antisymmetric mode waves

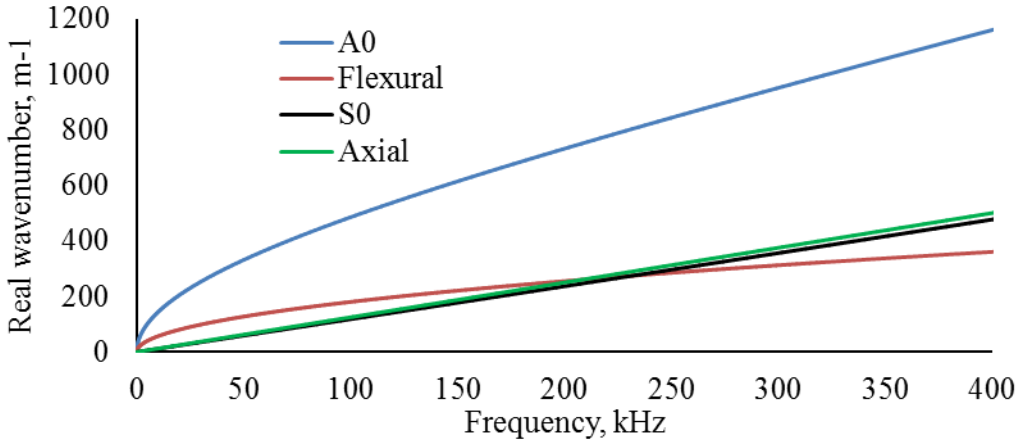

Figure 3.8: Frequency-wavenumber plot: axial-flexural waves vs. Lamb waves

We compare the results from the axial-flexural wave solution with the Lamb wave CMEP solutions for its validity as frequency $\rightarrow 0$. Figure 3.7 shows the comparison of the scattered wave amplitudes from the axial-flexural model and the CMEP with 27 modes expansion. We can see that the scattered wave amplitudes from these two models converge at low frequencies. However the results diverge as the frequency increases. This divergence happens quickly for the A0 wave (Figure 3.7 (b)) and a little slower for the S0 wave (Figure 3.7 (a)). Figure 3.8 explains this clearly by showing that the A0 wavenumber diverges very quickly from the flexural wavenumber as the frequency

increases whereas the S0 wavenumber takes a little longer. This shows that the simplified assumption of no shear deformation for the flexural waves is valid only as frequency $\rightarrow 0$.

3.4 VERIFICATION OF CMEP FOR A STEP USING FEM

For the validation of the results from CMEP at higher frequencies, we made finite element models (FEM) using the commercial software ANSYS. The dimensions and the material properties were chosen as described in section 3.3.4. To ensure accuracy of the FEM results we follow Moser et al. (Moser, Jacobs, and Qu 1999). We used PLANE182 elements in ANSYS multi physics. We ensured the value of λ / l_{FEM} to be at least 30 (Figure 3.9) which is higher than the recommended value for an accurate result. We also performed convergence study with progressively smaller element sizes with the value of λ / l_{FEM} to be up to 40.

3.4.1 FEM MODELING STRATEGY

We consider again the test case of an aluminum plate having $E = 70$ GPa, $\rho = 2780$ kg/m3 and $\nu = 0.33$ with $h_1 = 2$ mm and $h_2 = 1$ mm being the thicknesses of the plate at region 1 and 2 respectively. The frequency range for comparison was chosen to be 50 kHz to 750 kHz to avoid exciting the propagating A1 mode. The S0 Lamb wave mode was excited by applying force at the top and bottom node of the plate in phase at the transmission location. However, at the specified frequencies, this type of excitation will create the S0 Lamb wave mode along with large number of non-propagating evanescent modes. Therefore, for successful simulation of the S0 mode incident on the step, the distance between the transmission location and the step should be sufficiently large for the evanescent modes to die out.

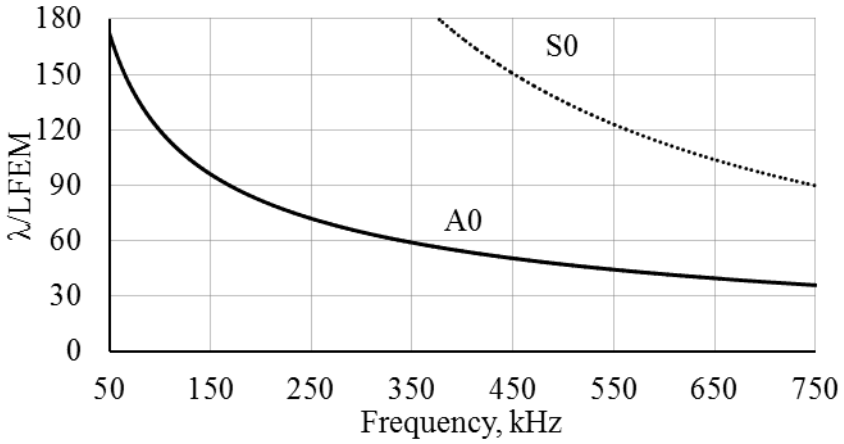

Figure 3.9: Variation of λ / l_{FEM} with frequency

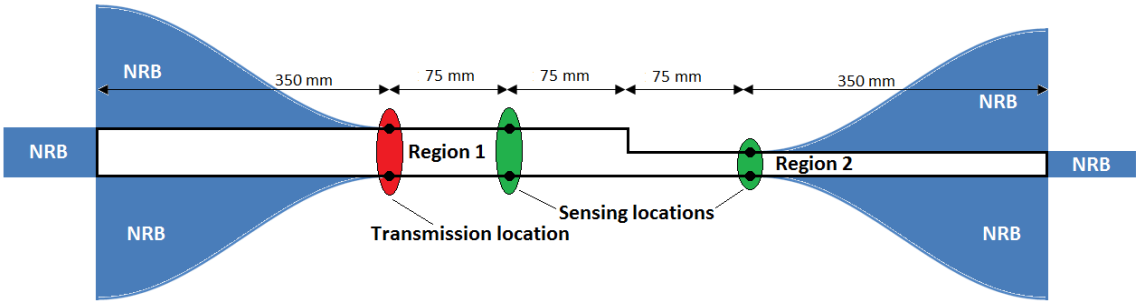

Figure 3.10: Schematics of the finite element model with nonreflecting boundary for harmonic analysis

From chapter 2, section 2.1.1.2 we know that the decay of evanescent modes depend on the imaginary part of their complex wave numbers as $e^{-\xi_I x}$. Therefore, for the above frequencies, A1 mode is the slowest decaying evanescent mode with the smallest imaginary part of its wavenumber among all the evanescent Lamb modes (Figure 3.11(a)). Figure 3.11 (b) shows the distance travelled by A1 mode in both regions 1 and 2 for 99% decay of its amplitude. Therefore, in our FEM model, the distances between sources and sensors were chosen to be larger than that shown in Figure 3.11 Similarly, as shown in Figure 3.10, for sensing of scattered waves, we recorded the displacements at the top and bottom nodes at the sensing locations sufficient distances from the step.

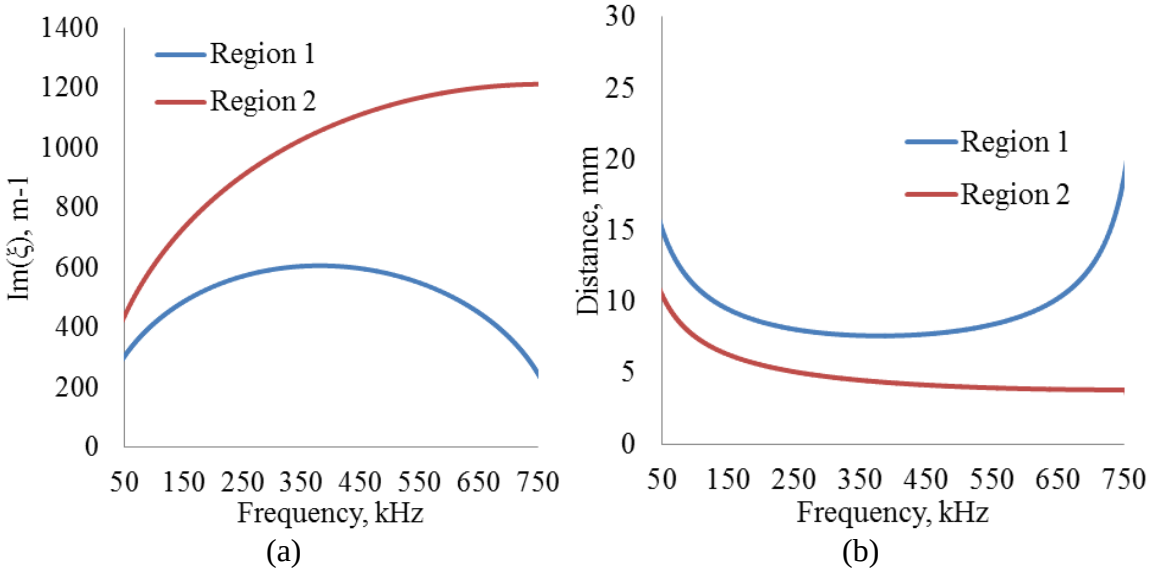

Figure 3.11: (a) Travel distance of A1 evanescent mode for 99% amplitude decay; (b) wavenumber of A1 mode in regions 1 and 2.

We performed a harmonic analysis in ANSYS to verify the CMEP results in the frequency domain. To achieve a transient response from a finite dimensional model from the harmonic analysis, we introduced non-reflective boundaries (NRB) at both the ends of the model to eliminate the boundary reflections and thereby eliminating standing waves. The NRBs were created using the COMBIN14 spring damper element (Shen and Giurgiutiu 2015). These elements were arranged at the top and the bottom surfaces of the NRBs and also at both the ends. The damping coefficients of the elements were varied gradually in a sinusoidal pattern starting from zero (Figure 3.10). This eliminated any reflection from the edge of the NRB itself.

A similar model was created without the step to capture the incident wave field only. We subtracted the incident wave field from the wave field in the Region 1 obtained from the step model to get the reflected wave fields. The transmitted wave field was obtained directly from the Region 2. The symmetric and the antisymmetric modes were

separated by averaging the summation and by subtraction of displacements at the top and the bottom nodes.

3.4.2 CMEP VS. FEM FOR A STEP

Table 3.1: Computational advantages of CMEP over FEM

FEM						CMEP/FEM Comparative Run Time (%)
	Amplitude		Phase			
λ/l_{FEM} (Min.)	% Diff. with CMEP (Max.)	Convergence	% Diff. with CMEP (Max.)	Convergence	Run Time (Sec.)	
30	1.2	Yes	63	No	5000	0.5%
35	0.6	Yes	2.1	Yes	5400	0.46%
40	0.7	Yes	2.2	Yes	6000	0.42%

Figure 3.12 shows a comparison of CMEP, FEM and axial-flexural results over a wide range of frequencies. It is apparent that the axial-flexural results only apply for frequency $\rightarrow 0$. Regarding FEM vs. CMEP, the amplitudes and the phases of the reflected and the transmitted waves obtained from the CMEP analysis are in perfect agreement with the FEM results. However, from Table 3.1 we can see that the convergence of the FEM model was quite expensive in terms of computational time and it took 200 times more computational time than the CMEP code to obtain the same results. The disparity in computational time was because the FEM model required a very high level of discretization with more than 30 elements per wavelength to obtain convergence of the phase (Table 3.1).

This confirms that the CMEP method is a reliable and accurate method for predicting the scattering of Lamb waves. It is very important to obtain correct scatter coefficients quickly for NDE and SHM. This can be done easily by using the specialized

analytical model, CMEP which can predict the scatter coefficients in seconds instead of hours.

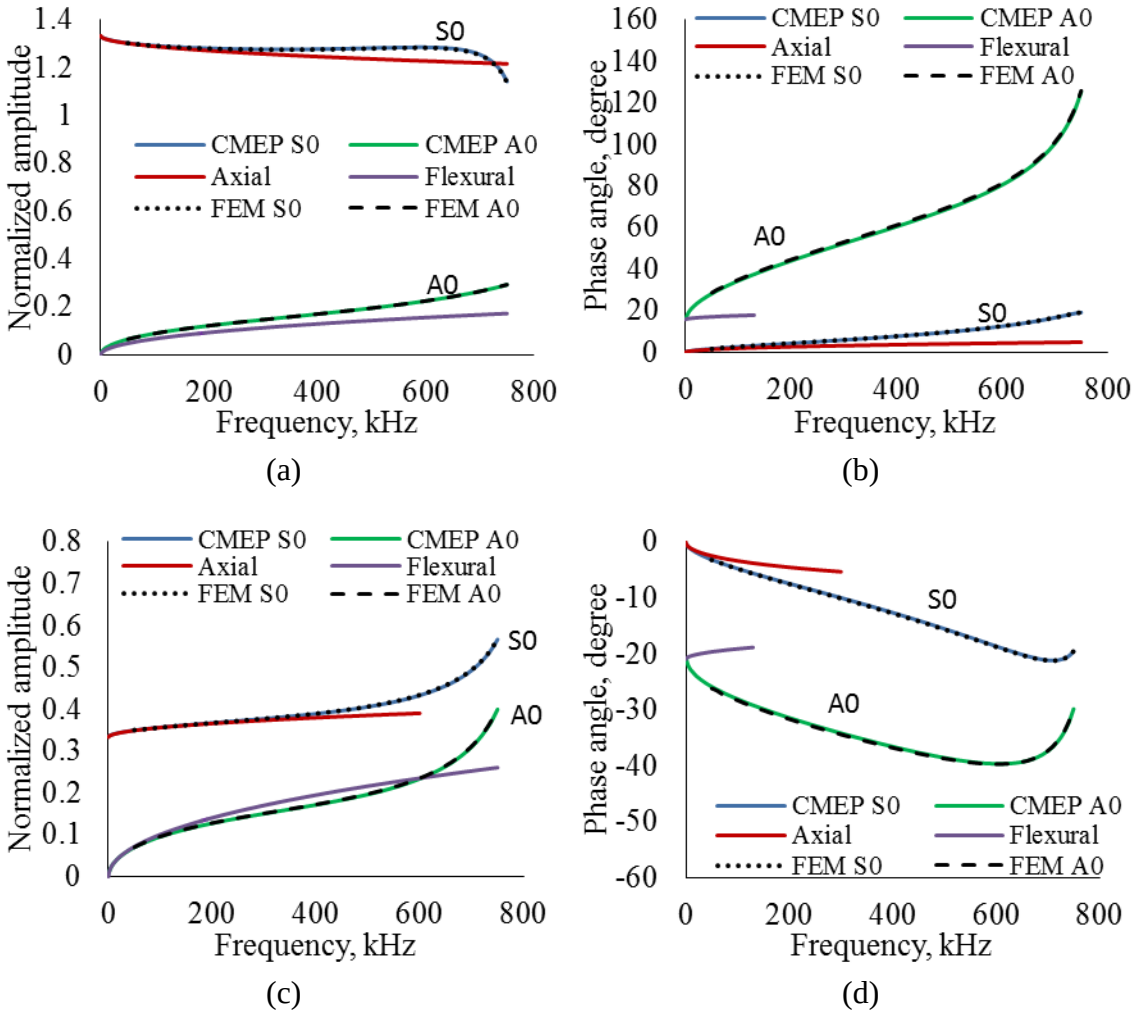

Figure 3.12: Comparison of u_x displacement of transmitted wave (a) amplitudes and (b) phases; reflected wave (c) amplitudes and (d) phases

3.5 CONCLUSION AND FUTURE WORK

This chapter has illustrated how the Lamb wave complex eigen space can be used efficiently to project the thickness dependent boundary conditions encountered in the Lamb wave scatter problem. The convergence and accuracy of the CMEP method was verified over a wide range of frequency-thickness values up to 1.5 MHz-mm. It was found that the CMEP method is more than two orders of magnitude faster than FEM for

the same accuracy. As a byproduct, the CMEP method also yields the local vibration field near the damage which is dominated by the evanescent and complex wave modes. The CMEP method is different from other methods (Feng, Shen, and Lin 2012), (Feng, Shen, and Shen 2016) which use the orthogonality between modal stresses and displacements. Unlike these methods, CMEP does not need to assume virtual wave guides and vertical free-ends to implement the orthogonality relations.

The CMEP method was demonstrated for straight crested Lamb waves which exist in z invariant condition. Similar approach can be taken to analyze interactions of non-straight crested Lamb waves with damages. However, in addition to Lamb waves, we need to consider shear horizontal waves for such analysis in non z invariant elastodynamic field.

CHAPTER 4

CMEP FOR LAMB WAVES SCATTERING FROM VARIOUS DAMAGE TYPES

4.1 STATE OF THE ART

As discussed in section 3.1, the full analytical solution of scattering of Lamb waves from various types of damage is rare due to the complexity associated with the physical phenomenon. Earlier analytical work focused on the free edge problem and prediction of the associated stress singularities using a projection method (Gregory and Gladwell 1982, 1983). Flores-López et al. have used this method to predict scattering from non-resonating type damage, a vertical crack. Feng et al. (Feng, Shen, and Lin 2012), (Feng, Shen, and Shen 2016) used the normal mode expansion method to analyze thickness discontinuities in a plate. They split the initial plate into layers of real and virtual subplates and vertical free-ends to implement the orthogonality relations. Then, free-end reflection conditions were imposed on some of the subplates to generate a system of algebraic equations which yielded the modal expansion coefficient. They have applied this method for either resonating or non-resonating type damage. However, this method requires virtual wave guides and is complex in its application. For notch like resonating damage, Grahn (Grahn 2003) used a scalar projection method to predict the scattered Lamb wave modes. He used simple sine and cosine function as basis vectors which resulted in slow convergence (Moreau et al. 2012). Moreau et al. (Moreau et al. 2011) have used harmonic functions as projection vector space for similar problem. They have also used displacement components of complex Lamb wave modeshapes instead of simple sine and cosine functions and attained a faster convergence in the projection

method (Moreau et al. 2012). These studies focused on notch like damage because of the similarity of a notch with corrosion type damage. Similarly, the interaction with horizontal cracks is also important not only in the case of disbonds in layered media, but also in the case of forging and diffusion bonding of isotropic materials (Lampman, Zorc, and Ronke 1992). For interaction with horizontal cracks, Karim et al. (Karim, Awal, and Kundu 1992) and Gunawan et al. (Gunawan and Hirose 2004) combined FEM with analytical approach for faster prediction of the scatter field of Lamb waves. Full analytical approaches such as Wiener-Hopf technique and higher order plate theories were also used by Rocklin (Rokhlin 1980) and Wang et al. (Wang and Rose 2003) to solve this problem. Glushkov et al. have proposed the layered element method (LEM) which, unlike BEM, satisfies the plate boundary conditions by formulation (Y. V. Glushkov et al. 2009).

In section 3.3, we have demonstrated modal expansion of complex Lamb wave modes and its effective use to express unknown scattered wave fields. We have also demonstrated the use of vector projection of the associated thickness dependent boundary conditions onto the complex eigen vector space of the Lamb modes. We have shown that, this vector projection can utilize power flow associated with each of the wave guides and ensures power flow balance and the convergence of the predicted scattered wave amplitudes. The method was demonstrated using the step problem. In this chapter we will extend the CMEP method to more realistic damage in a plate structure, such as a horizontal crack, a vertical crack and a vertical notch. These damages can be grouped in to two main types; resonating and non-resonating.

4.2 ANALYTICAL MODEL OF SCATTERING FROM RESONANT TYPE DAMAGE

Resonance in an elastodynamic field is typically associated with finite geometric dimensions like finite width of a plate. Damage with finite width creates two different boundary conditions at the ends. This creates a finite geometric effect causing standing wave field confined along the damage. This standing wave field resonates with the width of the damage. Examples of this type of damage are a horizontal crack, a vertical notch, etc.

4.2.1 CMEP FOR A NOTCH

4.2.1.1 Problem Setup for a Notch

To begin our analysis, let us consider a plate with a cross section as shown in Figure 4.1. We assume that there is an incident straight-crested Lamb wave mode travelling from the left towards a notch. Upon interacting with the notch, it will result in reflected wave modes, transmitted wave modes, and wave modes trapped in the notch. As shown in Figure 4.1, the notch is located at a distance $x = x_0$ with the thickness of the plate being h_1. At the notch the plate has been corroded to a thickness h_2 with the width of the notch being $L = 2b$. At the notch, we define depth ration as $R_d = (h_1 - h_2)/h_1$ and width ratio as $R_w = 2b/h_1$. Also, let us imagine that the incident wave field is represented by (Φ_0, H_0), travelling in *+ve* x direction in the Region 1. We define the reflected wave field as (Φ_1, H_1) and the transmitted wave field in Region 3 as (Φ_3, H_3). We also define the trapped wave field inside the notch in Region 2 as (Φ_2, H_2).

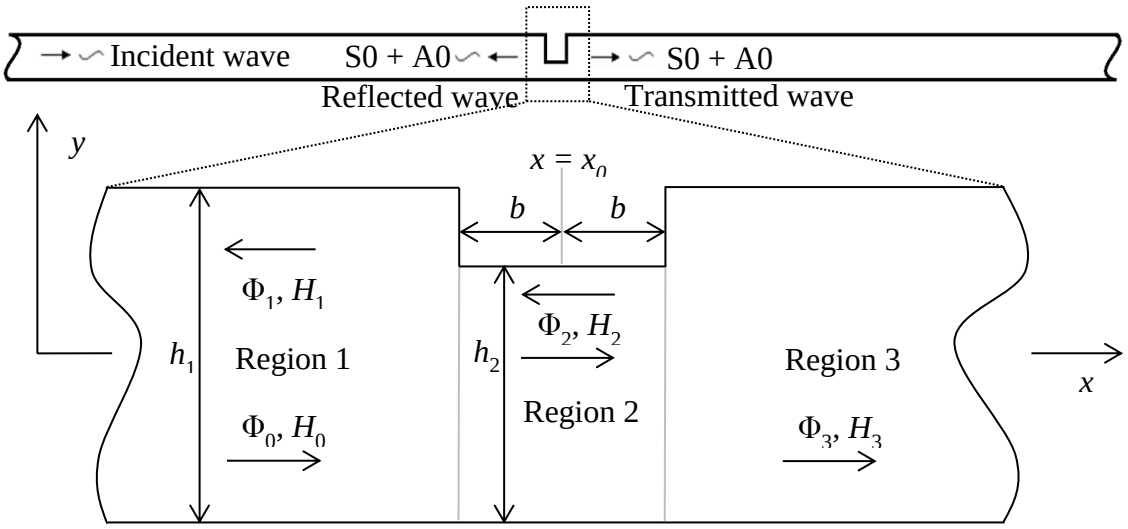

Figure 4.1: Schematic of Lamb waves interacting with a notch

The incident and scattered wave fields satisfy the generic wave equations

$$\frac{\partial^2 \Phi}{\partial x^2} + \frac{\partial^2 \Phi}{\partial y^2} = \frac{1}{C_P^2}\ddot{\Phi}$$
$$\frac{\partial^2 H}{\partial x^2} + \frac{\partial^2 H}{\partial y^2} = \frac{1}{C_S^2}\ddot{H} \qquad (4.1)$$

where, C_P and C_S are the wave speeds of pressure wave and shear waves, respectively.

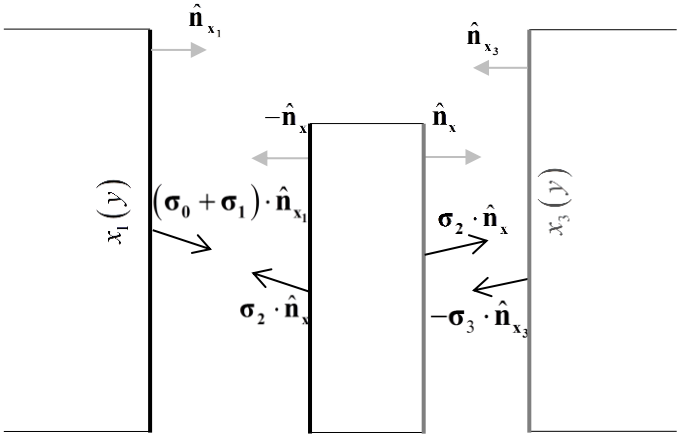

Figure 4.2: Boundary conditions at the notch

These must satisfy the zero-stress boundary condition at the top and bottom of the plate,

$$\sigma_{yy}\Big|_{\left(x<x_0-b;\ y=\pm\frac{h_1}{2}\right),\ \left(x>x_0+b;\ y=\pm\frac{h_1}{2}\right),\ \left(x_0+b>x>x_0-b;\ y=h_2-\frac{h_1}{2},-\frac{h_1}{2}\right)}=0$$
$$\tau_{xy}\Big|_{\left(x<x_0-b;\ y=\pm\frac{h_1}{2}\right),\ \left(x>x_0+b;\ y=\pm\frac{h_1}{2}\right),\ \left(x_0+b>x>x_0-b;\ y=h_2-\frac{h_1}{2},-\frac{h_1}{2}\right)}=0 \tag{4.2}$$

The stress and displacement fields associated with the wave fields are expressed as

$$\boldsymbol{\sigma}=\begin{bmatrix}\sigma_{xx} & \tau_{xx}\\ \tau_{xy} & \sigma_{yy}\end{bmatrix};\quad \vec{\sigma}=\begin{bmatrix}\sigma_{xx}\\ \tau_{xy}\end{bmatrix};\quad \vec{u}=\begin{bmatrix}u_x\\ u_y\end{bmatrix} \tag{4.3}$$

where, $\boldsymbol{\sigma}$ is stress tensor, $\vec{\boldsymbol{\sigma}}$ is stress vector, and $\vec{\mathbf{u}}$ is displacement vector. For the displacements, subscripts x and y indicate the directions of the displacement. For stresses, the subscripts xx, yy stand for the normal stress in x, y directions, respectively and the subscript xy stands for the shear stress. The boundary conditions at the notch are illustrated in Figure 4.2. The boundary conditions at the interface at $x=x_0-b$ are,

$$\left(\boldsymbol{\sigma_0}+\boldsymbol{\sigma_1}\right)\cdot\hat{n}_{x_1}=\begin{cases}0, & x_1(y)=x_0-b,\quad h_2-h_1/2\le y\le h_1/2\\ \boldsymbol{\sigma_2}\cdot-\hat{n}_x, & x=x_0-b,\quad -h_1/2\le y\le h_2-h_1/2\end{cases} \tag{4.4}$$

$$\vec{u}_0+\vec{u}_1=\vec{u}_2,\qquad x=x_0-b,\quad -h_1/2\le y\le h_2-h_1/2 \tag{4.5}$$

The boundary conditions at the interface at $x=x_0+b$ are,

$$\boldsymbol{\sigma_3}\cdot\hat{n}_{x_3}=\begin{cases}0, & x_3(y)=x_0-b,\quad h_2-h_1/2\le y\le h_1/2\\ \boldsymbol{\sigma_2}\cdot\hat{n}_x, & x=x_0+b,\quad -h_1/2\le y\le h_2-h_1/2\end{cases} \tag{4.6}$$

$$\vec{u}_3=\vec{u}_2,\qquad x=x_0+b,\quad -h_1/2\le y\le h_2-h_1/2 \tag{4.7}$$

where $\hat{n}_{x_1}$, $\hat{n}_{x_3}$ are the unit surface normal vectors of the interface surfaces represented by $x_1(y)$, $x_3(y)$ and $\hat{n}_x$ is the unit vector in +ve x direction as shown in Figure 4.2. Also, note that for a vertical notch, $\hat{n}_{x_1}=\hat{n}_x$ and $\hat{n}_{x_3}=-\hat{n}_x$. The subscript 0 stands for incident waves in Region 1, subscript 1 stands for reflected waves in Region 1, subscript 2 stands for the trapped waves in Region 2 and subscript 3 stands for transmitted waves in Region 3. Let us assume the incident wave field to be a harmonic wave field of the form

$$\Phi_0 = f_0(y)\mathrm{e}^{\mathrm{i}(\xi_0 x-\omega t)} \qquad H_0 = \mathrm{i}h_0(y)\mathrm{e}^{\mathrm{i}(\xi_0 x-\omega t)} \tag{4.8}$$

Assuming ξ_0 to be one of the roots of Rayleigh-Lamb equation for the plate in Region 1, Eq. (4.1) and (4.2) are satisfied by definition of Lamb waves and the incident wave becomes one of the modes of Lamb waves.

4.2.1.2 Complex Modes Expansion of the Scattered Wave Field for a Notch

In this section, we present the general concept of our CMEP algorithm. We assume that the transmitted, reflected, and trapped wave fields to have harmonic expressions similar to the incident wave field (Φ_0, H_0) given by Eq. (4.8). Since the boundary conditions at the notch cannot be satisfied by assuming any finite number of Lamb wave modes (Torvik 1966), we expand these transmitted, reflected, and trapped wave fields in terms of all possible complex Lamb wave modes corresponding to the complex roots of Rayleigh-Lamb frequency equation. Therefore, the scattered wave fields are expressed as

$$\begin{aligned}
\Phi_1 &= \sum_{n_1=1}^{\infty} C_{1B,n_1}\Phi_{1B,n_1} = \sum_{n_1=1}^{\infty} C_{1B,n_1} f_{n_1}(y_1)\mathrm{e}^{\mathrm{i}\left(\xi_{1B,n_1}x-\omega t\right)} \\
H_1 &= \sum_{n_1=1}^{\infty} C_{1B,n_1}H_{1B,n_1} = \sum_{n_1=1}^{\infty} C_{1B,n_1}\mathrm{i}h_{n_1}(y_1)\mathrm{e}^{\mathrm{i}\left(\xi_{1B,n_1}x-\omega t\right)} \\
\Phi_2 &= \sum_{n_2=1}^{\infty}\left(C_{2F,n_2}\Phi_{2F,n_2} + C_{2B,n_2}\Phi_{2B,n_2}\right) \\
&= \sum_{n_2=1}^{\infty}\left(C_{2F,n_2} f_{n_2}(y_2)\mathrm{e}^{\mathrm{i}\left(\xi_{2F,n_2}x-\omega t\right)} + C_{2B,n_2} f_{n_2}(y_2)\mathrm{e}^{\mathrm{i}\left(\xi_{2B,n_2}x-\omega t\right)}\right) \\
H_2 &= \sum_{n_2=1}^{\infty}\left(C_{2F,n_2}H_{2F,n_2} + C_{2B,n_2}H_{2B,n_2}\right) \\
&= \sum_{n_2=1}^{\infty}\left(C_{2F,n_2}\mathrm{i}h_{n_2}(y_2)\mathrm{e}^{\mathrm{i}\left(\xi_{2F,n_2}x-\omega t\right)} + C_{2B,n_2}\mathrm{i}h_{n_2}(y_2)\mathrm{e}^{\mathrm{i}\left(\xi_{2B,n_2}x-\omega t\right)}\right) \\
\Phi_3 &= \sum_{n_3=1}^{\infty} C_{3F,n_3}\Phi_{3F,n_3} = \sum_{n_3=1}^{\infty} C_{3F,n_3} f_{n_3}(y_3)\mathrm{e}^{\mathrm{i}\left(\xi_{3F,n_3}x-\omega t\right)} \\
H_3 &= \sum_{n_3=1}^{\infty} C_{3F,n_3}H_{3F,n_3} = \sum_{n_3=1}^{\infty} C_{3F,n_3}\mathrm{i}h_{n_3}(y_3)\mathrm{e}^{\mathrm{i}\left(\xi_{3F,n_3}x-\omega t\right)}
\end{aligned} \tag{4.9}$$

where, y_1 and y_2 are connected by the expression $y_2 = y_1 + a$ with $a = (h_1 - h_2)/2$ being the eccentricity between Region 1 and Region 2 and $y_1 = y_3$. The wavenumber ξ_{1B,n_1} is the n_1th complex root of the Rayleigh-Lamb equation corresponding to backward propagating Lamb waves in Region 1 and the wavenumbers ξ_{2F,n_2} and ξ_{2B,n_2} are n_2th complex root of the Rayleigh-Lamb equation corresponding to forward and backward propagating waves in Region 2, respectively. Similarly, wavenumber ξ_{3F,n_3} is the n_3th complex root of the Rayleigh-Lamb equation corresponding to forward propagating waves in Region 3. The coefficient C_{1B,n_1} is the unknown amplitude of the n_1th mode of backward propagating Lamb waves in Region 1 whereas C_{2F,n_2} and C_{2B,n_2} are the unknown amplitudes of the n_2th mode of forward and backward propagating Lamb waves in Region 2, respectively. Similarly, the coefficient C_{3F,n_3} is the unknown amplitude of the n_3th mode of forward propagating Lamb waves in Region 3. Eq. (4.9) expresses the scattered wave field as the summation of all possible complex Lamb wave modes at a given frequency. The amplitudes C_{1B,n_1}, C_{2F,n_2}, C_{2B,n_2} and C_{3F,n_3} of these modes have to be determined through the boundary matching process. Recall the boundary conditions at the interfaces at $x = x_0 - b$ and $x = x_0 + b$ are given by Eq. (4.4), (4.5), (4.6), and.(4.7). Also, note that the plate boundary conditions given by Eq. (4.1) and (4.2) are satisfied by the definition of Lamb waves. We express the stress and displacement fields of Eq. (4.4), (4.5), (4.6), and (4.7) using the complex Lamb wave mode expansion of Eq. (4.9), i.e.,

$$
\begin{aligned}
\vec{u}_1 &= \sum_{n_1=1}^{\infty} C_{1B,n_1} \begin{bmatrix} u_x \\ u_y \end{bmatrix}_{1B,n_1} ; \boldsymbol{\sigma_1} = \sum_{n_1=1}^{\infty} C_{1B,n_1} \begin{bmatrix} \sigma_{xx} & \tau_{xx} \\ \tau_{xy} & \sigma_{yy} \end{bmatrix}_{1B,n_1} \\
\vec{u}_2 &= \sum_{n_2=1}^{\infty} \left(C_{2F,n_2} \begin{bmatrix} u_x \\ u_y \end{bmatrix}_{2F,n_2} + C_{2B,n_2} \begin{bmatrix} u_x \\ u_y \end{bmatrix}_{2F,n_2} \right) \\
\boldsymbol{\sigma_2} &= \sum_{n_2=1}^{\infty} \left(C_{2F,n_2} \begin{bmatrix} \sigma_{xx} & \tau_{xx} \\ \tau_{xy} & \sigma_{yy} \end{bmatrix}_{2F,n_2} + C_{2B,n_2} \begin{bmatrix} \sigma_{xx} & \tau_{xx} \\ \tau_{xy} & \sigma_{yy} \end{bmatrix}_{2F,n_2} \right) \\
\vec{u}_3 &= \sum_{n_3=1}^{\infty} C_{3F,n_3} \begin{bmatrix} u_x \\ u_y \end{bmatrix}_{3F,n_3} ; \boldsymbol{\sigma_3} = \sum_{n_3=1}^{\infty} C_{3F,n_3} \begin{bmatrix} \sigma_{xx} & \tau_{xx} \\ \tau_{xy} & \sigma_{yy} \end{bmatrix}_{3F,n_3}
\end{aligned}
\tag{4.10}
$$

In the same vein, the incident wave field uses subscript 0, i.e.,

$$
\vec{u}_0 = \begin{bmatrix} u_x \\ u_y \end{bmatrix}_0 \qquad \boldsymbol{\sigma}_0 = \begin{bmatrix} \sigma_{xx} & \tau_{xy} \\ \tau_{xy} & \sigma_{yy} \end{bmatrix}_0 \tag{4.11}
$$

Therefore, for a vertical notch, using Eq. (4.10), (4.11) into Eq. (4.4), (4.5), (4.6) and (4.7) yields

$$
\vec{\sigma}_0 + \vec{\sigma}_1 = \begin{cases} 0, & x = x_0 - b, \quad h_2 - h_1/2 \le y \le h_1/2 \\ \vec{\sigma}_2 & x = x_0 - b, \quad -h_1/2 \le y \le h_2 - h_1/2 \end{cases} \tag{4.12}
$$

$$
\vec{u}_0 + \vec{u}_1 = \vec{u}_2, \quad x = x_0 - b, \quad -h_1/2 \le y \le h_2 - h_1/2 \tag{4.13}
$$

$$
\vec{\sigma}_3 = \begin{cases} 0, & x = x_0 + b, \quad h_2 - h_1/2 \le y \le h_1/2 \\ \vec{\sigma}_2 & x = x_0 + b, \quad -h_1/2 \le y \le h_2 - h_1/2 \end{cases} \tag{4.14}
$$

$$
\vec{u}_3 = \vec{u}_2, \quad x = x_0 + b, \quad -h_1/2 \le y \le h_2 - h_1/2 \tag{4.15}
$$

Therefore, Eq. (4.12), (4.13), (4.14), and (4.15) represent the thickness dependent boundary conditions at the notch.

4.2.1.3 Vector Projection of the Boundary Conditions for a Notch

To make Eq. (4.12), (4.13), (4.14), and (4.15) independent of y, we follow Grahn (Grahn 2003) and project them onto appropriate complete orthogonal vector spaces as described. But, different from (Grahn 2003), we do not use generic sine and cosine functions, instead, we use the time averaged power flow expression which uses stress-velocity product (Auld 1973). Thus, in Region 1, we project the stress boundary conditions onto the conjugate displacement vector space of the complex Lamb wave

modes; in Region 2, we project the displacement boundary conditions onto the conjugate stress vector space of the complex Lamb wave modes. By the same token, in Region 3, we project the stress boundary conditions onto the conjugate displacement vector space of the complex Lamb wave modes. By doing so, the CMEP formulation automatically incorporates the average power flow associated with the reflected, transmitted, and trapped wave fields. This approach has two main advantages: first, following the time averages power flow associated with the modes, it creates dominant diagonal terms in the final matrix equation which leads to fast convergence; second, it transforms the stress and displacement equations at the interface into the equations representing the power flow balance across the interface between the two separate wave fields. In short, this approach incorporates the balance of power flow across the interface achieving fast convergence.

The projection vector space for Eq. (4.12) is

$$\vec{\bar{u}}_{1B} = \text{conj}\begin{bmatrix} u_x \\ u_y \end{bmatrix}_{1B,\bar{n}_1} = \begin{bmatrix} \bar{u}_x \\ \bar{u}_y \end{bmatrix}_{1B,\bar{n}_1}, \quad \bar{n}_1 = 1,2,3,... \tag{4.16}$$

After projecting Eq. (4.12) onto Eq. (4.16), the stress boundary conditions in Eq. (4.12) take the form,

$$\begin{aligned} &\int_{-h_1/2}^{h_1/2} \left(\vec{\sigma}_0 + \vec{\sigma}_1\right) \cdot \vec{\bar{u}}_{1B} \mathrm{d}y = \int_{-h_1/2}^{h_2-h_1/2} \vec{\sigma}_2 \cdot \vec{\bar{u}}_{1B} \mathrm{d}y \\ &\Rightarrow \sum_{n_2=1}^{\infty} \left(C_{2F,n_2} \left\langle \begin{bmatrix} \sigma_{xx} \\ \tau_{xy} \end{bmatrix}_{2F,n_2}, \begin{bmatrix} \bar{u}_x \\ \bar{u}_y \end{bmatrix}_{1B,\bar{n}_1} \right\rangle_{-h_1/2}^{h_2-h_1/2} + C_{2B,n_2} \left\langle \begin{bmatrix} \sigma_{xx} \\ \tau_{xy} \end{bmatrix}_{2B,n_2}, \begin{bmatrix} \bar{u}_x \\ \bar{u}_y \end{bmatrix}_{1B,\bar{n}_1} \right\rangle_{-h_1/2}^{h_2-h_1/2} \right) \\ &- \sum_{n_1=1}^{\infty} C_{1B,n_1} \left\langle \begin{bmatrix} \sigma_{xx} \\ \tau_{xy} \end{bmatrix}_{1B,n_1}, \begin{bmatrix} \bar{u}_x \\ \bar{u}_y \end{bmatrix}_{1B,\bar{n}_1} \right\rangle_{-h_1/2}^{h_1/2} = \left\langle \begin{bmatrix} \sigma_{xx} \\ \tau_{xy} \end{bmatrix}_{0}, \begin{bmatrix} \bar{u}_x \\ \bar{u}_y \end{bmatrix}_{1B,\bar{n}_1} \right\rangle_{-h_1/2}^{h_1/2}; \; n_1, \, n_2 = 1,2,3,... \end{aligned} \tag{4.17}$$

where, $\int_a^b P \cdot Q dy = \langle P, Q \rangle_a^b$ represents the inner product. Similarly, the projection vector space for Eq. (4.14) is

$$\vec{\bar{u}}_{3F} = \text{conj}\begin{bmatrix} u_x \\ u_y \end{bmatrix}_{3F,\bar{n}_3} = \begin{bmatrix} \bar{u}_x \\ \bar{u}_y \end{bmatrix}_{3F,\bar{n}_3}, \quad \bar{n}_3 = 1,2,3,... \tag{4.18}$$

Upon projecting Eq. (4.14) onto Eq. (4.18), the stress boundary conditions in Eq. (4.14) take the form,

$$\begin{aligned} &\int_{-h_1/2}^{h_1/2} \vec{\sigma}_3 \cdot \vec{\bar{u}}_{3F} \mathrm{d}y = \int_{-h_1/2}^{h_2-h_1/2} \vec{\sigma}_2 \cdot \vec{\bar{u}}_{3F} \mathrm{d}y \\ &\Rightarrow \sum_{n_2=1}^{\infty} \left(C_{2F,n_2} \left\langle \begin{bmatrix} \sigma_{xx} \\ \tau_{xy} \end{bmatrix}_{2F,n_2}, \begin{bmatrix} \bar{u}_x \\ \bar{u}_y \end{bmatrix}_{3F,\bar{n}_3} \right\rangle_{-h_1/2}^{h_2-h_1/2} + C_{2B,n_2} \left\langle \begin{bmatrix} \sigma_{xx} \\ \tau_{xy} \end{bmatrix}_{2B,n_2}, \begin{bmatrix} \bar{u}_x \\ \bar{u}_y \end{bmatrix}_{3F,\bar{n}_3} \right\rangle_{-h_1/2}^{h_2-h_1/2} \right) \\ &= \sum_{n_3=1}^{\infty} C_{3F,n_3} \left\langle \begin{bmatrix} \sigma_{xx} \\ \tau_{xy} \end{bmatrix}_{3F,n_3}, \begin{bmatrix} \bar{u}_x \\ \bar{u}_y \end{bmatrix}_{3F,\bar{n}_3} \right\rangle_{-h_1/2}^{h_1/2} \end{aligned} \tag{4.19}$$

$$n_2,\ n_3 = 1,2,3,...$$

The projection vector space for Eq. (4.13) is,

$$\vec{\bar{\sigma}}_{2F} = \text{conj}\begin{bmatrix} \sigma_{xx} \\ \tau_{xy} \end{bmatrix}_{2F,\bar{n}_2} = \begin{bmatrix} \bar{\sigma}_{xx} \\ \bar{\tau}_{xy} \end{bmatrix}_{2F,\bar{n}_2}, \quad \bar{n}_2 = 1,2,3,... \tag{4.20}$$

After projecting Eq. (4.13) onto Eq. (4.20), the displacement boundary conditions in Eq. (4.13), take the form,

$$\begin{aligned} &\int_{-h_1/2}^{h_2-h_1/2} \left(\vec{u}_0 + \vec{u}_1\right) \cdot \vec{\bar{\sigma}}_{2F} \mathrm{d}y = \int_{-h_1/2}^{h_2-h_1/2} \vec{u}_2 \cdot \vec{\bar{\sigma}}_{2F} \mathrm{d}y \\ &\Rightarrow \sum_{n_2=1}^{\infty} \left(C_{2F,n_2} \left\langle \begin{bmatrix} u_x \\ u_y \end{bmatrix}_{2F,n_2}, \begin{bmatrix} \bar{\sigma}_{xx} \\ \bar{\tau}_{xy} \end{bmatrix}_{2F,\bar{n}_2} \right\rangle_{-h_1/2}^{h_2-h_1/2} + C_{2B,n_2} \left\langle \begin{bmatrix} u_x \\ u_y \end{bmatrix}_{2B,n_2}, \begin{bmatrix} \bar{\sigma}_{xx} \\ \bar{\tau}_{xy} \end{bmatrix}_{2F,\bar{n}_2} \right\rangle_{-h_1/2}^{h_2-h_1/2} \right) \\ &\quad - \sum_{n_1=1}^{\infty} C_{1B,n_1} \left\langle \begin{bmatrix} u_x \\ u_y \end{bmatrix}_{1B,n_1}, \begin{bmatrix} \bar{\sigma}_{xx} \\ \bar{\tau}_{xy} \end{bmatrix}_{2F,\bar{n}_2} \right\rangle_{-h_1/2}^{h_2-h_1/2} = \left\langle \begin{bmatrix} u_x \\ u_y \end{bmatrix}_0, \begin{bmatrix} \bar{\sigma}_{xx} \\ \bar{\tau}_{xy} \end{bmatrix}_{2F,\bar{n}_2} \right\rangle_{-h_1/2}^{h_2-h_1/2} \end{aligned} \tag{4.21}$$

$$n_1,\ n_2 = 1,2,3,...$$

The projection vector space for Eq. (4.15) is,

$$\vec{\bar{\sigma}}_{2B} = \text{conj}\begin{bmatrix} \sigma_{xx} \\ \tau_{xy} \end{bmatrix}_{2B,\bar{n}_2} = \begin{bmatrix} \bar{\sigma}_{xx} \\ \bar{\tau}_{xy} \end{bmatrix}_{2B,\bar{n}_2}, \quad \bar{n}_2 = 1,2,3,... \tag{4.22}$$

Upon projecting Eq. (4.15) onto Eq. (4.22), the displacement boundary conditions in Eq. (4.15) take the form,

$$\int_{-h_1/2}^{h_2-h_1/2} \vec{u}_3 \cdot \vec{\bar{\sigma}}_{2B} \mathrm{d}y = \int_{-h_1/2}^{h_2-h_1/2} \vec{u}_2 \cdot \vec{\bar{\sigma}}_{2B} \mathrm{d}y$$

$$\Rightarrow \sum_{n_2=1}^{\infty} \left(C_{2F,n_2} \left\langle \begin{bmatrix} u_x \\ u_y \end{bmatrix}_{2F,n_2}, \begin{bmatrix} \bar{\sigma}_{xx} \\ \bar{\tau}_{xy} \end{bmatrix}_{2B,\bar{n}_2} \right\rangle_{-h_1/2}^{h_2-h_1/2} + C_{2B,n_2} \left\langle \begin{bmatrix} u_x \\ u_y \end{bmatrix}_{2B,n_2}, \begin{bmatrix} \bar{\sigma}_{xx} \\ \bar{\tau}_{xy} \end{bmatrix}_{2B,\bar{n}_2} \right\rangle_{-h_1/2}^{h_2-h_1/2} \right) \quad (4.23)$$

$$= \sum_{n_3=1}^{\infty} C_{3F,n_3} \left\langle \begin{bmatrix} u_x \\ u_y \end{bmatrix}_{3F,n_3}, \begin{bmatrix} \bar{\sigma}_{xx} \\ \bar{\tau}_{xy} \end{bmatrix}_{2B,\bar{n}_2} \right\rangle_{-h_1/2}^{h_2-h_1/2}$$

$$n_2,\ n_3 = 1,2,3,...$$

4.2.1.4 Numerical Solution for a Notch

For numerical calculation we consider finite values for the indices $n_1, n_2, n_3, \bar{n}_1, \bar{n}_2, \bar{n}_3$. We assume, $n_1 = 1,2,3,...,N_1$, $n_2 = 1,2,3,...,N_2$, $n_3 = 1,2,3,...,N_3$, $\bar{n}_1 = 1,2,3,...,\bar{N}_1$, $\bar{n}_2 = 1,2,3,...,\bar{N}_2$, $\bar{n}_3 = 1,2,3,...,\bar{N}_3$. Then, Eq. (4.17) contains $\bar{N}_1$ linear equations with $\left(N_1 + 2N_2\right)$ unknowns and Eq. (4.19) contains $\bar{N}_3$ linear equations with $\left(N_3 + 2N_2\right)$. Also Eq. (4.21) contains $\bar{N}_2$ linear equations with $\left(N_1 + 2N_2\right)$ and Eq. (4.23) contains $\bar{N}_2$ linear equations with $\left(N_3 + 2N_2\right)$ unknowns. Recall that the $\left(N_1 + 2N_2 + N_3\right)$ unknowns are the complex Lamb wave mode amplitudes $\left(C_{1B,n_1}, C_{2F,n_2}, C_{2B,n_2}, C_{3F,n_3}\right)$. Thus, Eq. (4.17), (4.19), (4.21), (4.23) combined are a set of $\left(\bar{N}_1 + 2\bar{N}_2 + \bar{N}_3\right)$ linear algebraic equations in $\left(N_1 + 2N_2 + N_3\right)$ unknowns C_{1B,n_1}, C_{2F,n_2}, C_{2B,n_2}, and C_{3F,n_3}. By assuming $N_1 = N_2 = N_3 = \bar{N}_1 = \bar{N}_2 = N$, we get $4N$ equations in $4N$ unknowns. Then Eq. (4.17) and (4.19) can be written as

$$[A]_{N\times N} \begin{Bmatrix} C_{2F,1} \\ \vdots \\ C_{2F,N} \end{Bmatrix}_{N\times 1} + [B]_{N\times N} \begin{Bmatrix} C_{2B,1} \\ \vdots \\ C_{2B,N} \end{Bmatrix}_{N\times 1} - [D]_{N\times N} \begin{Bmatrix} C_{1B,1} \\ \vdots \\ C_{1B,N} \end{Bmatrix}_{N\times 1} + [0]_{N\times N} \begin{Bmatrix} C_{3F,1} \\ \vdots \\ C_{3F,N} \end{Bmatrix}_{N\times 1} = \{E\}_{N\times 1} \quad (4.24)$$

$$[F]_{N\times N}\begin{Bmatrix} C_{2F,1} \\ \vdots \\ C_{2F,N} \end{Bmatrix}_{N\times 1} + [G]_{N\times N}\begin{Bmatrix} C_{2B,1} \\ \vdots \\ C_{2B,N} \end{Bmatrix}_{N\times 1} + [0]_{N\times N}\begin{Bmatrix} C_{1B,1} \\ \vdots \\ C_{1B,N} \end{Bmatrix}_{N\times 1} - [H]_{N\times N}\begin{Bmatrix} C_{3F,1} \\ \vdots \\ C_{3F,N} \end{Bmatrix}_{N\times 1} = \{0\}_{N\times 1} \quad (4.25)$$

Similarly from Eq. (4.21) and (4.23) can be written as

$$[J]_{N\times N}\begin{Bmatrix} C_{2F,1} \\ \vdots \\ C_{2F,N} \end{Bmatrix}_{N\times 1} + [K]_{N\times N}\begin{Bmatrix} C_{2B,1} \\ \vdots \\ C_{2B,N} \end{Bmatrix}_{N\times 1} - [L]_{N\times N}\begin{Bmatrix} C_{1B,1} \\ \vdots \\ C_{1B,N} \end{Bmatrix}_{N\times 1} + [0]_{N\times N}\begin{Bmatrix} C_{3F,1} \\ \vdots \\ C_{3F,N} \end{Bmatrix}_{N\times 1} = \{M\}_{N\times 1} \quad (4.26)$$

$$[N]_{N\times N}\begin{Bmatrix} C_{2F,1} \\ \vdots \\ C_{2F,N} \end{Bmatrix}_{N\times 1} + [O]_{N\times N}\begin{Bmatrix} C_{2B,1} \\ \vdots \\ C_{2B,N} \end{Bmatrix}_{N\times 1} + [0]_{N\times N}\begin{Bmatrix} C_{1B,1} \\ \vdots \\ C_{1B,N} \end{Bmatrix}_{N\times 1} - [P]_{N\times N}\begin{Bmatrix} C_{3F,1} \\ \vdots \\ C_{3F,N} \end{Bmatrix}_{N\times 1} = \{0\}_{N\times 1} \quad (4.27)$$

In Eq. (4.24), (4.25), (4.26) and (4.27) the coefficient matrices $[A]$, $[B]$, $[D]$, $[E]$, $[F]$, $[G]$, $[H]$, $[J]$, $[K]$, $[L]$, $[M]$, $[N]$, $[O]$ and $[P]$ are known matrices containing the vector projected boundary conditions. Combining them we get

$$\begin{bmatrix} A & B & -D & 0 \\ F & G & 0 & -H \\ J & K & -L & 0 \\ N & O & 0 & -P \end{bmatrix}_{4N\times 4N}\begin{Bmatrix} C_{2F,1} \\ \vdots \\ C_{2F,N} \\ C_{2B,1} \\ \vdots \\ C_{2B,N} \\ C_{1B,1} \\ \vdots \\ C_{1B,N} \\ C_{3F,1} \\ \vdots \\ C_{3F,N} \end{Bmatrix}_{4N\times 1} = \begin{Bmatrix} E \\ 0 \\ M \\ 0 \end{Bmatrix}_{4N\times 1} \Rightarrow [Q]_{4N\times 4N}\{C\}_{4N\times 1} = \{R\}_{4N\times 1} \quad (4.28)$$

Eq. (4.28) can be solved for the unknown amplitudes of the reflected and transmitted Lamb wave modes as

$$\{C\}_{4N\times 1} = [Q]^{-1}_{4N\times 4N}[R]_{4N\times 1} \tag{4.29}$$

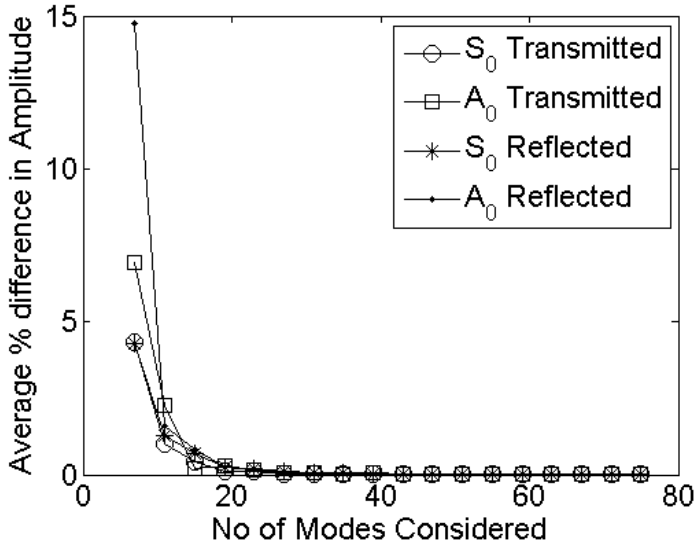

(a)

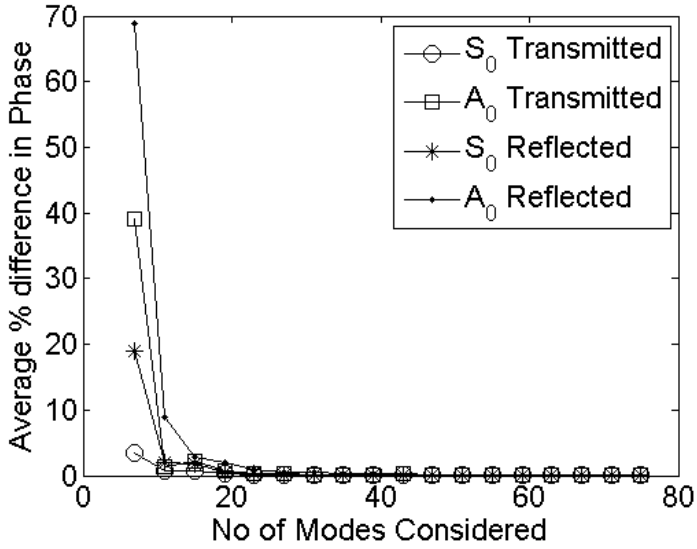

(b)

Figure 4.3: Convergence of (a) amplitudes, (b) phases of scattered Lamb wave modes for S0 mode incident on a vertical notch with R_d=0.5 and R_w=0.5 over a wide frequency range of 200 kHz.mm to 1.5 MHz.mm.

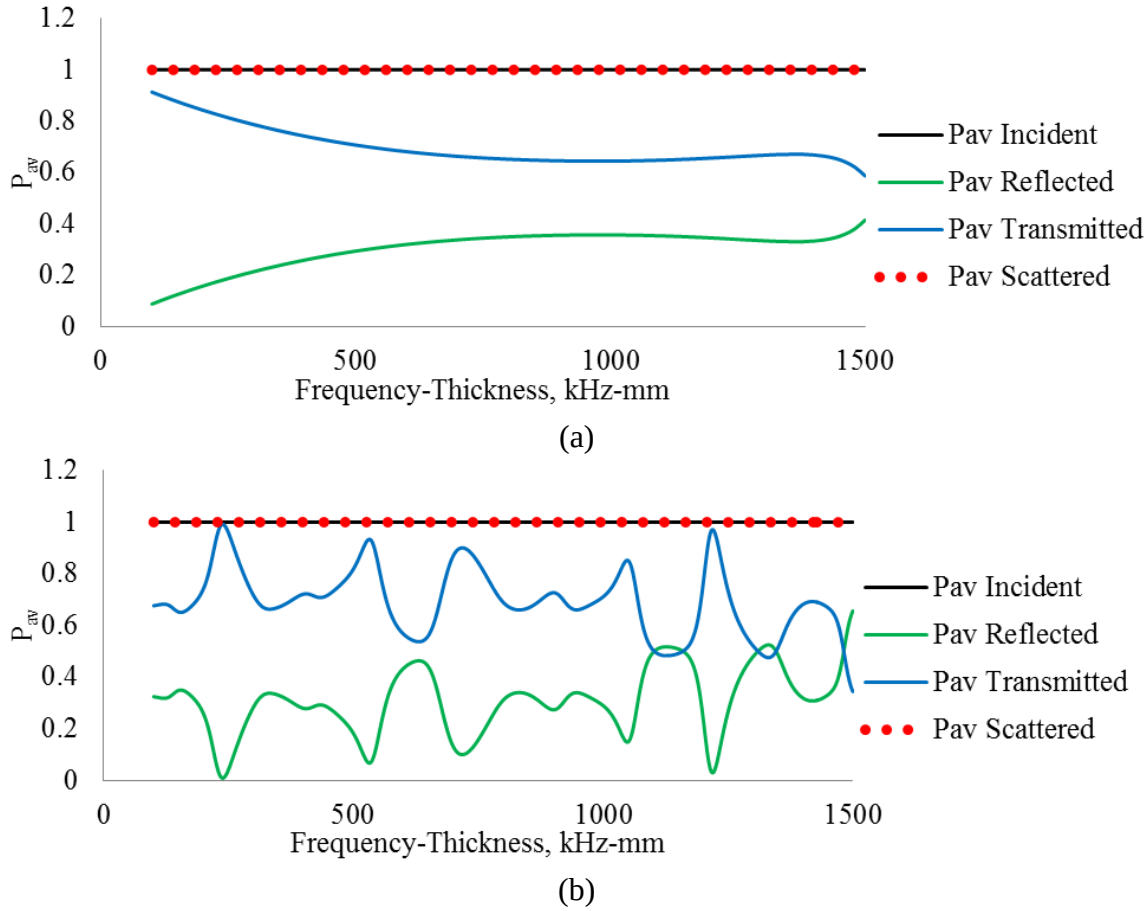

Figure 4.4: Variation of time average power flow P_{av} through the notch as calculated using CMEP with a 27-mode expansion for S0 mode incident on a notch with R_d=0.5 and (a) R_w=0.5, (b) R_w=10.

As a test case we consider a vertical notch in an aluminum plate with $E = 70$ GPa, $\rho = 2780$ kg/m^3, $\nu = 0.33$, $h_1 = 2$ mm, $h_2 = 1$ mm, and $b = 0.5$ mm. This results in depth ratio $R_d = (h_1 - h_2)/h_1 = 0.5$, and width ratio $R_w = 2b/h_1 = 0.5$. We also consider S0 as the incident Lamb wave mode. We use a frequency-thickness range of up to 1.5 MHz-mm for its relevance to practical applications. We perform convergence studies to determine the maximum number of complex roots of the Rayleigh-Lamb equation needed to calculate the first two scattered Lamb wave modes S0 and A0 with high accuracy. Figure 4.3 shows the convergence study for the amplitudes of the first two modes of

Lamb waves, S0 and A0. Considering 27 modes in the expansion ensured convergence to less than 0.5% error. Another important verification of convergence is the power flow balance. Figure 4.4 (a) and (b) show that a 27-mode expansion gave a balanced average power flow though the vertical notches with different widths over the whole frequency-thickness range up to 1.5 MHz. It is apparent that power flow balance requirements are met since the "P_{av} incident" line exactly overlaps with the "P_{av} Scattered (Reflected + Transmitted)" line.

4.2.2 VERIFICATION OF CMEP FOR A NOTCH USING FEM

For the validation of the results from CMEP for a notch, we made finite element models (FEM) using the commercial software ANSYS. The dimensions and the material properties were chosen as described in sections 4.2.1.4 with $R_d = 0.5$ and $R_w = 10$.

4.2.2.1 FEM Modeling Strategy

The modeling strategy was same as described in section 3.4.1 for a step. The element size and the model sizes were same except, instead of a step, a notch was modeled in the 2D FEM model. The range of frequencies was also same along with the thickness of the plate modeled.

4.2.2.2 CMEP vs. FEM for A Notch

Figure 4.5 shows that the amplitudes and phases of the scattered waves obtained from FEM are convergent with the CMEP results for a wide range of frequencies; this confirms that the complex modes expansion with vector projection method is a reliable and accurate method for predicting the scattering of Lamb waves from a notch like discontinuity. We can also see that both CMEP and FEM results predicted resonance frequencies associated with the notch in the form of peaks in amplitude and phases of the scattered waves. These frequencies depend on the depth and width ratios of the notch.

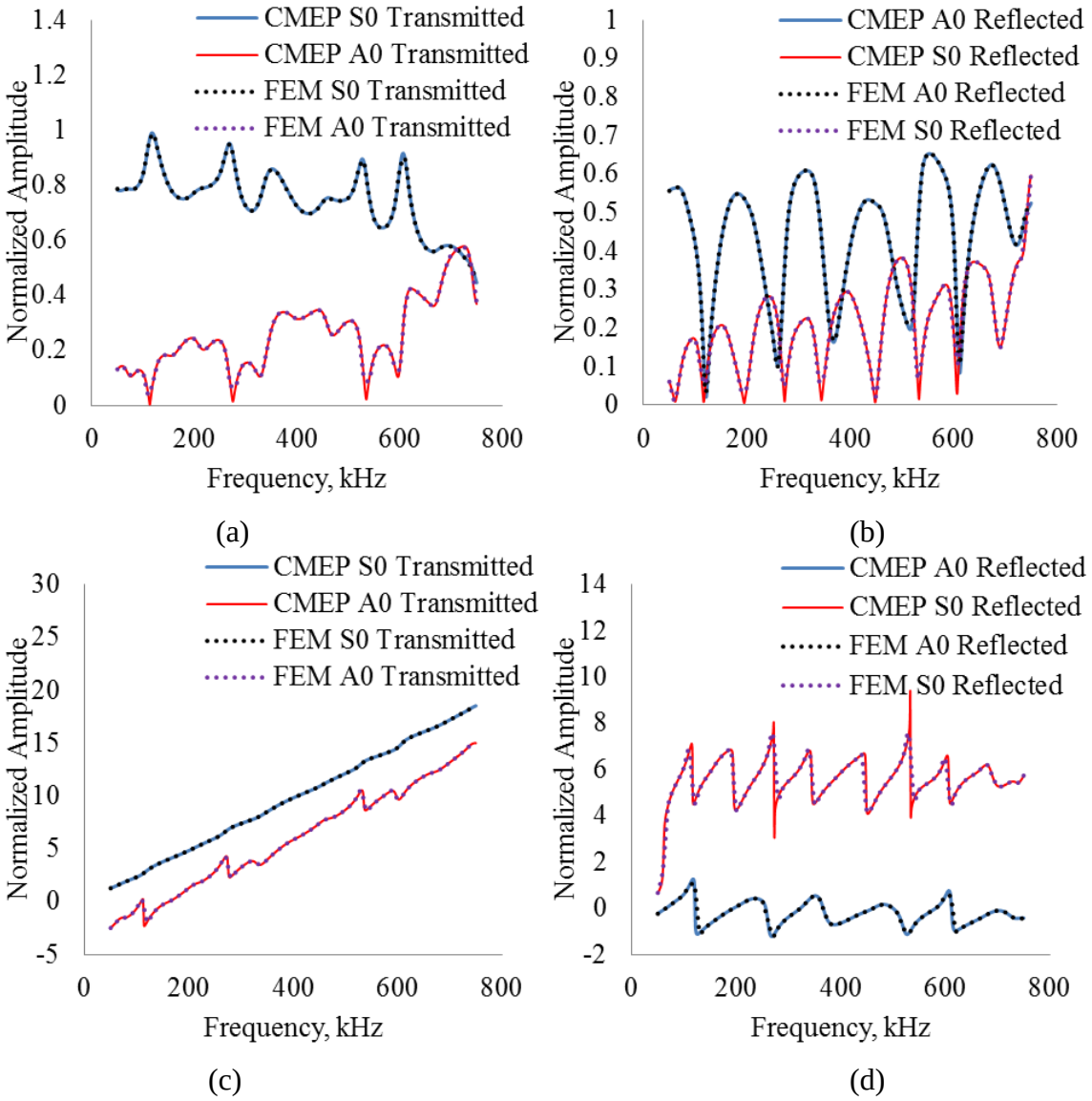

Figure 4.5: Comparison of u_x displacement of scattered waves for incident S0 mode, (a) amplitude of transmitted modes; (b) amplitude of reflected modes; (c) phase of transmitted modes and (b) phase of reflected modes

Therefore, by detecting these resonance frequencies we can estimate the notch dimensions. However, the convergence of FE models is quite expensive in terms of computational time. The reported FE analysis took about 6000 seconds computational time but the CMEP code took only about 26 seconds to compute the same results.

Therefore, CMEP is an accurate and efficient tool to predict scattering from notch type damage; CMEP can be an effective tool for NDE and SHM.

4.2.3 CMEP FOR A HORIZONTAL CRACK

4.2.3.1 Problem Setup for a Horizontal Crack

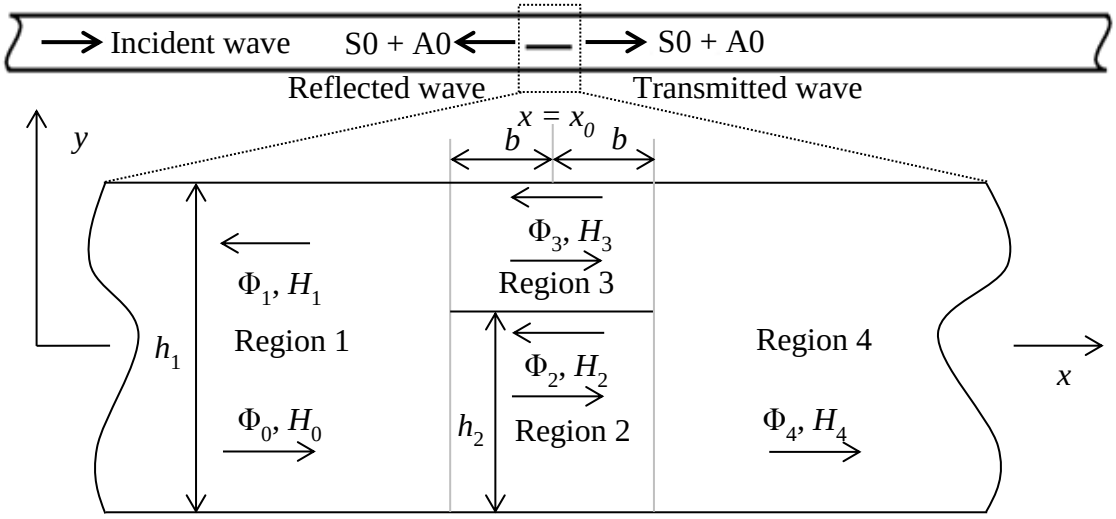

Figure 4.6: Schematic of Lamb waves interacting with a horizontal crack

To begin our analysis, let us consider a plate with a cross section as shown in Figure 4.6. We assume that there is an incident straight-crested Lamb wave mode travelling from the left towards a horizontal crack in the form of a horizontal crack. Upon interacting with the horizontal crack, it will result in reflected wave modes, transmitted wave modes, and wave modes trapped in the horizontal crack. As shown in Figure 4.6, the horizontal crack is located at a distance $x = x_0$ in a plate with thickness h_1. The horizontal crack has a width $W = 2b$ and is located at height h_2 from the bottom of the plate. At the horizontal crack, we define depth ration as $R_d = (h_1 - h_2)/h_1$ and width ratio as $R_w = 2b/h_1$.

Also, let us imagine that the incident wave field is represented by (Φ_0, H_0), travelling in *+ve* x direction in the Region 1. We define the reflected wave field as

(Φ_1, H_1) and the transmitted wave field in Region 4 as (Φ_4, H_4). We also define the trapped wave field in the horizontal crack area as (Φ_2, H_2) and (Φ_3, H_3) in Regions 2 and 3, respectively.

The incident and scattered wave fields satisfy the generic wave equations (4.1). Equations (4.1) must satisfy the zero-stress boundary condition at the top and bottom of the plate,

$$\left.\begin{aligned}\sigma_{yy}\Big|_{\left(x<x_0-b;\ y=\pm\frac{h_1}{2}\right)}&=0\\ \tau_{xy}\Big|_{\left(x<x_0-b;\ y=\pm\frac{h_1}{2}\right)}&=0\end{aligned}\right\}\ (\text{Region 1});\qquad \left.\begin{aligned}\sigma_{yy}\Big|_{\left(x_0+b>x>x_0-b;\ y=h_2-\frac{h_1}{2},-\frac{h_1}{2}\right)}&=0\\ \tau_{xy}\Big|_{\left(x_0+b>x>x_0-b;\ y=h_2-\frac{h_1}{2},-\frac{h_1}{2}\right)}&=0\end{aligned}\right\}(\text{Region 2})$$

$$\left.\begin{aligned}\sigma_{yy}\Big|_{\left(x_0+b>x>x_0-b;\ y=\frac{h_1}{2},h_2-\frac{h_1}{2}\right)}&=0\\ \tau_{xy}\Big|_{\left(x_0+b>x>x_0-b;\ y=\frac{h_1}{2},h_2-\frac{h_1}{2}\right)}&=0\end{aligned}\right\}(\text{Region 3});\qquad \left.\begin{aligned}\sigma_{yy}\Big|_{\left(x>x_0+b;\ y=\pm\frac{h_1}{2}\right)}&=0\\ \tau_{xy}\Big|_{\left(x>x_0+b;\ y=\pm\frac{h_1}{2}\right)}&=0\end{aligned}\right\}(\text{Region 4}) \tag{4.30}$$

The stress and displacement field vectors associated with these wave fields are expressed as

$$\vec{\sigma}=\begin{bmatrix}\sigma_{xx}\\ \tau_{xy}\end{bmatrix};\qquad \vec{u}=\begin{bmatrix}u_x\\ u_y\end{bmatrix} \tag{4.31}$$

The boundary conditions at the horizontal crack are illustrated in Figure 4.7. The boundary conditions at the interface at $x=x_0-b$ are,

$$\left(\vec{\sigma}_0+\vec{\sigma}_1\right)=\begin{cases}\vec{\sigma}_3, & x=x_0-b, \quad h_2-h_1/2\le y\le h_1/2\\ \vec{\sigma}_2, & x=x_0-b, \quad -h_1/2\le y\le h_2-h_1/2\end{cases} \tag{4.32}$$

$$\vec{u}_0+\vec{u}_1=\begin{cases}\vec{u}_3, & x=x_0-b, \quad h_2-h_1/2\le y\le h_1/2\\ \vec{u}_2, & x=x_0-b, \quad -h_1/2\le y\le h_2-h_1/2\end{cases} \tag{4.33}$$

The boundary conditions at the interface at $x=x_0+b$ are,

$$\vec{\sigma}_4=\begin{cases}\vec{\sigma}_3, & x=x_0+b, \quad h_2-h_1/2\le y\le h_1/2\\ \vec{\sigma}_2, & x=x_0+b, \quad -h_1/2\le y\le h_2-h_1/2\end{cases} \tag{4.34}$$

$$\vec{u}_4 = \begin{cases} \vec{u}_3, & x = x_0 + b, \quad h_2 - h_1/2 \le y \le h_1/2 \\ \vec{u}_2, & x = x_0 + b, \quad -h_1/2 \le y \le h_2 - h_1/2 \end{cases} \tag{4.35}$$

The subscript 0 stands for incident waves in Region 1, subscript 1 stands for reflected waves in Region 1, subscripts 2 and 3 stand for the trapped waves in Regions 2 and 3, respectively. The subscript 4 stands for transmitted waves in Region 4. Let us assume the incident wave field in Region 1to be harmonic of the form

$$\Phi_0 = f_0(y)e^{i(\xi_0 x - \omega t)} \qquad H_0 = ih_0(y)e^{i(\xi_0 x - \omega t)} \tag{4.36}$$

where, ξ_0 satisfies the Rayleigh-Lamb equation for Region 1, and $f_0(y)$, $h_0(y)$ are the corresponding wave modes.

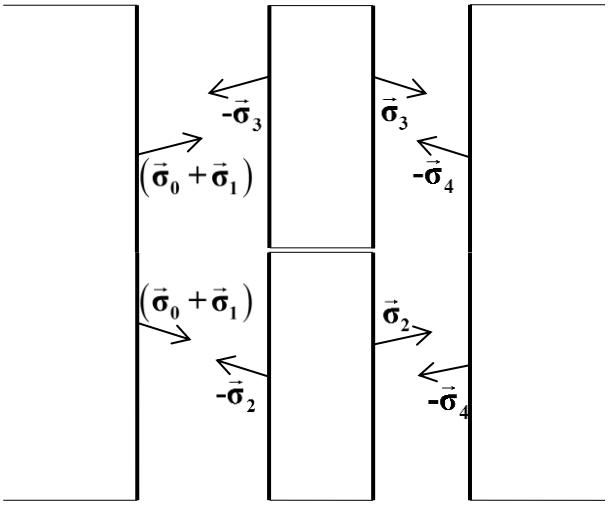

Figure 4.7: Boundary conditions at the horizontal crack

4.2.3.2 Complex Modes Expansion of the Scattered Wave Field for a Horizontal Crack

In this section, we present the general concept of our CMEP algorithm. We assume that the transmitted, reflected, and trapped wave fields to have harmonic expressions similar to the incident wave field (Φ_0, H_0) given by equation (4.8). Since the boundary conditions at the horizontal crack cannot be satisfied by assuming any finite number of Lamb wave modes (Torvik 1966), we expand these transmitted, reflected, and trapped wave fields in terms of all possible complex Lamb wave modes corresponding to

the complex roots of Rayleigh-Lamb frequency equation with unknown complex amplitudes. Therefore, the scattered wave fields are expressed as

$$
\begin{aligned}
\Phi_1 &= \sum_{n_1=1}^{\infty} C_{1B,n_1}\Phi_{1B,n_1} = \sum_{n_1=1}^{\infty} C_{1B,n_1} f_{n_1}\left(y_1\right) e^{i\left(\xi_{1B,n_1}x-\omega t\right)} \\
H_1 &= \sum_{n_1=1}^{\infty} C_{1B,n_1} H_{1B,n_1} = \sum_{n_1=1}^{\infty} C_{1B,n_1} i h_{n_1}\left(y_1\right) e^{i\left(\xi_{1B,n_1}x-\omega t\right)} \\
\Phi_2 &= \sum_{n_2=1}^{\infty}\left(C_{2F,n_2}\Phi_{2F,n_2} + C_{2B,n_2}\Phi_{2B,n_2}\right) \\
&= \sum_{n_2=1}^{\infty}\left(C_{2F,n_2} f_{n_2}\left(y_2\right) e^{i\left(\xi_{2F,n_2}x-\omega t\right)} + C_{2B,n_2} f_{n_2}\left(y_2\right) e^{i\left(\xi_{2B,n_2}x-\omega t\right)}\right) \\
H_2 &= \sum_{n_2=1}^{\infty}\left(C_{2F,n_2}H_{2F,n_2} + C_{2B,n_2}H_{2B,n_2}\right) \\
&= \sum_{n_2=1}^{\infty}\left(C_{2F,n_2} i h_{n_2}\left(y_2\right) e^{i\left(\xi_{2F,n_2}x-\omega t\right)} + C_{2B,n_2} i h_{n_2}\left(y_2\right) e^{i\left(\xi_{2B,n_2}x-\omega t\right)}\right) \\
\Phi_3 &= \sum_{n_3=1}^{\infty}\left(C_{3F,n_3}\Phi_{3F,n_3} + C_{3B,n_3}\Phi_{3B,n_3}\right) \\
&= \sum_{n_3=1}^{\infty}\left(C_{3F,n_3} f_{n_3}\left(y_3\right) e^{i\left(\xi_{3F,n_3}x-\omega t\right)} + C_{3B,n_3} f_{n_3}\left(y_3\right) e^{i\left(\xi_{3B,n_3}x-\omega t\right)}\right) \\
H_3 &= \sum_{n_3=1}^{\infty}\left(C_{3F,n_3}H_{3F,n_3} + C_{3B,n_3}H_{3B,n_3}\right) \\
&= \sum_{n_3=1}^{\infty}\left(C_{3F,n_3} i h_{n_3}\left(y_3\right) e^{i\left(\xi_{3F,n_3}x-\omega t\right)} + C_{3B,n_3} i h_{n_3}\left(y_3\right) e^{i\left(\xi_{3B,n_3}x-\omega t\right)}\right) \\
\Phi_4 &= \sum_{n_4=1}^{\infty} C_{4F,n_4}\Phi_{4F,n_4} = \sum_{n_4=1}^{\infty} C_{4F,n_4} f_{n_4}\left(y_4\right) e^{i\left(\xi_{4F,n_4}x-\omega t\right)} \\
H_4 &= \sum_{n_4=1}^{\infty} C_{4F,n_4} H_{4F,n_4} = \sum_{n_4=1}^{\infty} C_{4F,n_4} i h_{n_4}\left(y_4\right) e^{i\left(\xi_{4F,n_4}x-\omega t\right)}
\end{aligned}
\tag{4.37}
$$

where, subscripts B and F stand for backward and forward propagating wave, y_1, y_2, y_3 are connected by the expressions $y_2 = y_1 + a_2$ and $y_3 = y_1 + a_3$ with $a_2 = \left(h_1 - h_2\right)/2$ and $a_3 = -h_2/2$ being the eccentricities of Region 2 and Region 3 from Region 1 and $y_1 = y_4$. The wavenumber ξ_{1B,n_1} is the n_1th complex root of the Rayleigh-Lamb equation corresponding to backward propagating Lamb waves in Region 1 and the wavenumbers

ξ_{2F,n_2} and ξ_{2B,n_2} are n_2th complex root of the Rayleigh-Lamb equation corresponding to forward and backward propagating waves in Region 2, respectively. Similarly, wavenumber ξ_{4F,n_4} is the n_4th complex root of the Rayleigh-Lamb equation corresponding to forward propagating waves in Region 4 and the wavenumbers ξ_{3F,n_3} and ξ_{3B,n_3} are n_3th complex root of the Rayleigh-Lamb equation corresponding to forward and backward propagating waves in Region 3, respectively. The coefficient C_{1B,n_1} is the unknown amplitude of the n_1th mode of backward propagating Lamb waves in Region 1 whereas C_{2F,n_2} and C_{2B,n_2} are the unknown amplitudes of the n_2th mode of forward and backward propagating Lamb waves in Region 2, respectively. Similarly, the coefficient C_{4F,n_4} is the unknown amplitude of the n_4th mode of forward propagating Lamb waves in Region 4 whereas C_{3F,n_3} and C_{3B,n_3} are the unknown amplitudes of the n_3th mode of forward and backward propagating Lamb waves in Region 3, respectively. Equation (4.37) expresses the scattered wave field as the summation of all possible complex Lamb wave modes at a given frequency. The amplitudes C_{1B,n_1}, C_{2F,n_2}, C_{2B,n_2}, C_{3F,n_3}, C_{3B,n_3} and C_{4F,n_4} of these modes have to be determined through the boundary matching process. Recall the boundary conditions at the interfaces at $x = x_0 - b$ and $x = x_0 + b$ are given by equations (4.32), (4.33), (4.34), and.(4.35). Also, note that the wave equations and the plate boundary conditions given by equations (4.1) and (4.30) are satisfied by the definition of Lamb waves. We express the stress and displacement fields of equations (4.32), (4.33), (4.34), and.(4.35) using the complex Lamb wave mode expansion of equation (4.37), i.e.,

$$\vec{u}_1 = \sum_{n_1=1}^{\infty} C_{1B,n_1} \begin{bmatrix} u_x \\ u_y \end{bmatrix}_{1B,n_1} ; \vec{\sigma}_1 = \sum_{n_1=1}^{\infty} C_{1B,n_1} \begin{bmatrix} \sigma_{xx} \\ \tau_{xy} \end{bmatrix}_{1B,n_1}$$

$$\vec{u}_2 = \sum_{n_2=1}^{\infty} \left(C_{2F,n_2} \begin{bmatrix} u_x \\ u_y \end{bmatrix}_{2F,n_2} + C_{2B,n_2} \begin{bmatrix} u_x \\ u_y \end{bmatrix}_{2F,n_2} \right); \vec{\sigma}_2 = \sum_{n_2=1}^{\infty} \left(C_{2F,n_2} \begin{bmatrix} \sigma_{xx} \\ \tau_{xy} \end{bmatrix}_{2F,n_2} + C_{2B,n_2} \begin{bmatrix} \sigma_{xx} \\ \tau_{xy} \end{bmatrix}_{2F,n_2} \right)$$

$$\vec{u}_3 = \sum_{n_3=1}^{\infty} \left(C_{3F,n_3} \begin{bmatrix} u_x \\ u_y \end{bmatrix}_{3F,n_3} + C_{3B,n_3} \begin{bmatrix} u_x \\ u_y \end{bmatrix}_{3F,n_3} \right); \vec{\sigma}_3 = \sum_{n_3=1}^{\infty} \left(C_{3F,n_3} \begin{bmatrix} \sigma_{xx} \\ \tau_{xy} \end{bmatrix}_{3F,n_3} + C_{3B,n_3} \begin{bmatrix} \sigma_{xx} \\ \tau_{xy} \end{bmatrix}_{3F,n_3} \right)$$

$$\vec{u}_4 = \sum_{n_4=1}^{\infty} C_{4F,n_4} \begin{bmatrix} u_x \\ u_y \end{bmatrix}_{4F,n_4} ; \vec{\sigma}_4 = \sum_{n_4=1}^{\infty} C_{4F,n_4} \begin{bmatrix} \sigma_{xx} \\ \tau_{xy} \end{bmatrix}_{4F,n_4} \tag{4.38}$$

In the same vein, the incident wave field uses subscript 0, i.e.,

$$\vec{u}_0 = \begin{bmatrix} u_x \\ u_y \end{bmatrix}_0 \qquad \vec{\sigma}_0 = \begin{bmatrix} \sigma_{xx} \\ \tau_{xy} \end{bmatrix}_0 \tag{4.39}$$

Using equations(4.10), (4.11) into equations (4.4), (4.5), (4.6) and (4.7) yields

$$\vec{\sigma}_0 + \vec{\sigma}_1 = \begin{cases} \vec{\sigma}_3, & x = x_0 - b, \quad h_2 - h_1/2 \le y \le h_1/2 \\ \vec{\sigma}_2, & x = x_0 - b, \quad -h_1/2 \le y \le h_2 - h_1/2 \end{cases} \tag{4.40}$$

$$\vec{u}_0 + \vec{u}_1 = \vec{u}_3, \qquad x = x_0 - b, \quad h_2 - h_1/2 \le y \le h_1/2 \tag{4.41}$$

$$\vec{u}_0 + \vec{u}_1 = \vec{u}_2, \qquad x = x_0 - b, \quad -h_1/2 \le y \le h_2 - h_1/2 \tag{4.42}$$

$$\vec{\sigma}_4 = \begin{cases} \vec{\sigma}_3, & x = x_0 + b, \quad h_2 - h_1/2 \le y \le h_1/2 \\ \vec{\sigma}_2, & x = x_0 + b, \quad -h_1/2 \le y \le h_2 - h_1/2 \end{cases} \tag{4.43}$$

$$\vec{u}_4 = \vec{u}_3, \qquad x = x_0 + b, \quad h_2 - h_1/2 \le y \le h_1/2 \tag{4.44}$$

$$\vec{u}_4 = \vec{u}_2, \qquad x = x_0 + b, \quad -h_1/2 \le y \le h_2 - h_1/2 \tag{4.45}$$

Therefore, equations (4.40), (4.41), (4.42), (4.43), (4.44) and (4.45) represent the thickness dependent boundary conditions at the horizontal crack.

4.2.3.3 Vector Projection of the Boundary Conditions for a Horizontal Crack

To make equations (4.40), (4.41), (4.42), (4.43), (4.44) and (4.45) independent of y, we follow Grahn (Grahn 2003) and project them onto appropriate complete orthogonal vector spaces. But, different from (Grahn 2003), we do not use generic sine and cosine functions, instead, we use the time averaged power flow expression which uses the stress-velocity product (Auld 1973). Thus, in Region 1, we project the stress

boundary conditions (4.40), onto the conjugate displacement vector space of the complex Lamb wave modes; in Region 2 and 3, we project the displacement boundary conditions (4.41), (4.42),(4.44), and (4.45), onto the conjugate stress vector space of the complex Lamb wave modes. By the same token, in Region 4, we project the stress boundary conditions (4.43), onto the conjugate displacement vector space of the complex Lamb wave modes. By doing so, the CMEP formulation incorporates the average power flow associated with the reflected, transmitted, and trapped wave fields. This approach has two main advantages: first, by following the time averages power flow associated with the modes, it creates dominant diagonal terms in the final matrix equation which leads to fast convergence; second, it transforms the stress and displacement equations at the interface into the equations representing the power flow balance across the interface between separate wave fields. In short, this approach incorporates the balance of power flow across the interface which ensures fast convergence.

The projection vector space for equation (4.40) is

$$\vec{\bar{u}}_{1B} = \text{conj}\begin{bmatrix} u_x \\ u_y \end{bmatrix}_{1B,\bar{n}_1} = \begin{bmatrix} \bar{u}_x \\ \bar{u}_y \end{bmatrix}_{1B,\bar{n}_1}, \quad \bar{n}_1 = 1,2,3,... \tag{4.46}$$

After projecting equation (4.40) onto equation (4.16), the stress boundary conditions in equation (4.40) take the form,

$$\int_{-h_1/2}^{h_1/2}\left(\vec{\sigma}_0+\vec{\sigma}_1\right)\cdot\vec{\bar{u}}_{1B}dy=\int_{-h_1/2}^{h_2-h_1/2}\vec{\sigma}_2\cdot\vec{\bar{u}}_{1B}dy+\int_{h_2-h_1/2}^{h_1/2}\vec{\sigma}_3\cdot\vec{\bar{u}}_{1B}dy$$

$$\Rightarrow\sum_{n_2=1}^{\infty}\left(C_{2F,n_2}\left\langle\begin{bmatrix}\sigma_{xx}\\ \tau_{xy}\end{bmatrix}_{2F,n_2},\begin{bmatrix}\bar{u}_x\\ \bar{u}_y\end{bmatrix}_{1B,\bar{n}_1}\right\rangle_{-h_1/2}^{h_2-h_1/2}+C_{2B,n_2}\left\langle\begin{bmatrix}\sigma_{xx}\\ \tau_{xy}\end{bmatrix}_{2B,n_2},\begin{bmatrix}\bar{u}_x\\ \bar{u}_y\end{bmatrix}_{1B,\bar{n}_1}\right\rangle_{-h_1/2}^{h_2-h_1/2}\right)$$

$$+\sum_{n_3=1}^{\infty}\left(C_{3F,n_3}\left\langle\begin{bmatrix}\sigma_{xx}\\ \tau_{xy}\end{bmatrix}_{3F,n_3},\begin{bmatrix}\bar{u}_x\\ \bar{u}_y\end{bmatrix}_{1B,\bar{n}_1}\right\rangle_{h_2-h_1/2}^{h_1/2}+C_{3B,n_3}\left\langle\begin{bmatrix}\sigma_{xx}\\ \tau_{xy}\end{bmatrix}_{3B,n_3},\begin{bmatrix}\bar{u}_x\\ \bar{u}_y\end{bmatrix}_{1B,\bar{n}_1}\right\rangle_{h_2-h_1/2}^{h_1/2}\right)\qquad(4.47)$$

$$-\sum_{n_1=1}^{\infty}C_{1B,n_1}\left\langle\begin{bmatrix}\sigma_{xx}\\ \tau_{xy}\end{bmatrix}_{1B,n_1},\begin{bmatrix}\bar{u}_x\\ \bar{u}_y\end{bmatrix}_{1B,\bar{n}_1}\right\rangle_{-h_1/2}^{h_1/2}=\left\langle\begin{bmatrix}\sigma_{xx}\\ \tau_{xy}\end{bmatrix}_{0},\begin{bmatrix}\bar{u}_x\\ \bar{u}_y\end{bmatrix}_{1B,\bar{n}_1}\right\rangle_{-h_1/2}^{h_1/2};\ n_1,\ n_2,\ n_3=1,2,3,...$$

where, $\int_a^b P\cdot Qdy=\langle P,Q\rangle_a^b$ represents the inner product. Similarly, the projection vector space for equation (4.14) is

$$\vec{\bar{u}}_{4F}=\text{conj}\begin{bmatrix}u_x\\ u_y\end{bmatrix}_{4F,\bar{n}_4}=\begin{bmatrix}\bar{u}_x\\ \bar{u}_y\end{bmatrix}_{4F,\bar{n}_4},\quad \bar{n}_4=1,2,3,...\qquad(4.48)$$

Upon projecting equation (4.14) onto equation (4.18), the stress boundary conditions in equation (4.14) take the form

$$\int_{-h_1/2}^{h_1/2}\vec{\sigma}_4\cdot\vec{\bar{u}}_{4F}dy=\int_{-h_1/2}^{h_2-h_1/2}\vec{\sigma}_2\cdot\vec{\bar{u}}_{4F}dy+\int_{h_2-h_1/2}^{h_1/2}\vec{\sigma}_3\cdot\vec{\bar{u}}_{4F}dy$$

$$\Rightarrow\sum_{n_2=1}^{\infty}\left(C_{2F,n_2}\left\langle\begin{bmatrix}\sigma_{xx}\\ \tau_{xy}\end{bmatrix}_{2F,n_2},\begin{bmatrix}\bar{u}_x\\ \bar{u}_y\end{bmatrix}_{4F,\bar{n}_4}\right\rangle_{-h_1/2}^{h_2-h_1/2}+C_{2B,n_2}\left\langle\begin{bmatrix}\sigma_{xx}\\ \tau_{xy}\end{bmatrix}_{2B,n_2},\begin{bmatrix}\bar{u}_x\\ \bar{u}_y\end{bmatrix}_{4F,\bar{n}_4}\right\rangle_{-h_1/2}^{h_2-h_1/2}\right)$$

$$+\sum_{n_3=1}^{\infty}\left(C_{3F,n_3}\left\langle\begin{bmatrix}\sigma_{xx}\\ \tau_{xy}\end{bmatrix}_{3F,n_3},\begin{bmatrix}\bar{u}_x\\ \bar{u}_y\end{bmatrix}_{4F,\bar{n}_4}\right\rangle_{h_2-h_1/2}^{h_1/2}+C_{3B,n_3}\left\langle\begin{bmatrix}\sigma_{xx}\\ \tau_{xy}\end{bmatrix}_{3B,n_3},\begin{bmatrix}\bar{u}_x\\ \bar{u}_y\end{bmatrix}_{4F,\bar{n}_4}\right\rangle_{h_2-h_1/2}^{h_1/2}\right)\qquad(4.49)$$

$$=\sum_{n_4=1}^{\infty}C_{4F,n_4}\left\langle\begin{bmatrix}\sigma_{xx}\\ \tau_{xy}\end{bmatrix}_{4F,n_4},\begin{bmatrix}\bar{u}_x\\ \bar{u}_y\end{bmatrix}_{4F,\bar{n}_4}\right\rangle_{-h_1/2}^{h_1/2};\ n_2,\ n_3,\ n_4=1,2,3,...$$

The projection vector space for equation (4.13) is

$$\vec{\bar{\sigma}}_{3F}=\text{conj}\begin{bmatrix}\sigma_{xx}\\ \tau_{xy}\end{bmatrix}_{3F,\bar{n}_3}=\begin{bmatrix}\bar{\sigma}_{xx}\\ \bar{\tau}_{xy}\end{bmatrix}_{3F,\bar{n}_3},\quad \bar{n}_3=1,2,3,...\qquad(4.50)$$

After projecting equation (4.13) onto equation(4.20), the displacement boundary conditions in equation(4.13), take the form

$$\int_{h_2-h_1/2}^{h_1/2}\left(\vec{u}_0+\vec{u}_1\right)\cdot\bar{\bar{\sigma}}_{3F}dy=\int_{h_2-h_1/2}^{h_1/2}\vec{u}_3\cdot\bar{\bar{\sigma}}_{3F}dy$$

$$\Rightarrow\sum_{n_3=1}^{\infty}\left(C_{3F,n_3}\left\langle\begin{bmatrix}u_x\\u_y\end{bmatrix}_{3F,n_3},\begin{bmatrix}\bar{\sigma}_{xx}\\\bar{\tau}_{xy}\end{bmatrix}_{3F,\bar{n}_3}\right\rangle_{h_2-h_1/2}^{h_1/2}+C_{3B,n_3}\left\langle\begin{bmatrix}u_x\\u_y\end{bmatrix}_{3B,n_3},\begin{bmatrix}\bar{\sigma}_{xx}\\\bar{\tau}_{xy}\end{bmatrix}_{3F,\bar{n}_3}\right\rangle_{h_2-h_1/2}^{h_1/2}\right) \tag{4.51}$$

$$-\sum_{n_1=1}^{\infty}C_{1B,n_1}\left\langle\begin{bmatrix}u_x\\u_y\end{bmatrix}_{1B,n_1},\begin{bmatrix}\bar{\sigma}_{xx}\\\bar{\tau}_{xy}\end{bmatrix}_{3F,\bar{n}_3}\right\rangle_{h_2-h_1/2}^{h_1/2}=\left\langle\begin{bmatrix}u_x\\u_y\end{bmatrix}_{0},\begin{bmatrix}\bar{\sigma}_{xx}\\\bar{\tau}_{xy}\end{bmatrix}_{3F,\bar{n}_3}\right\rangle_{h_2-h_1/2}^{h_1/2}$$

$$n_1,\ n_3=1,2,3,...$$

The projection vector space for equation (4.42) is

$$\bar{\bar{\sigma}}_{2F}=\text{conj}\begin{bmatrix}\sigma_{xx}\\\tau_{xy}\end{bmatrix}_{2F,\bar{n}_2}=\begin{bmatrix}\bar{\sigma}_{xx}\\\bar{\tau}_{xy}\end{bmatrix}_{2F,\bar{n}_2},\quad \bar{n}_2=1,2,3,... \tag{4.52}$$

After projecting equation (4.42) onto equation(4.20), the displacement boundary conditions in equation(4.42), take the form

$$\int_{-h_1/2}^{h_2-h_1/2}\left(\vec{u}_0+\vec{u}_1\right)\cdot\bar{\bar{\sigma}}_{2F}dy=\int_{-h_1/2}^{h_2-h_1/2}\vec{u}_2\cdot\bar{\bar{\sigma}}_{2F}dy$$

$$\Rightarrow\sum_{n_2=1}^{\infty}\left(C_{2F,n_2}\left\langle\begin{bmatrix}u_x\\u_y\end{bmatrix}_{2F,n_2},\begin{bmatrix}\bar{\sigma}_{xx}\\\bar{\tau}_{xy}\end{bmatrix}_{2F,\bar{n}_2}\right\rangle_{-h_1/2}^{h_2-h_1/2}+C_{2B,n_2}\left\langle\begin{bmatrix}u_x\\u_y\end{bmatrix}_{2B,n_2},\begin{bmatrix}\bar{\sigma}_{xx}\\\bar{\tau}_{xy}\end{bmatrix}_{2F,\bar{n}_2}\right\rangle_{-h_1/2}^{h_2-h_1/2}\right) \tag{4.53}$$

$$-\sum_{n_1=1}^{\infty}C_{1B,n_1}\left\langle\begin{bmatrix}u_x\\u_y\end{bmatrix}_{1B,n_1},\begin{bmatrix}\bar{\sigma}_{xx}\\\bar{\tau}_{xy}\end{bmatrix}_{2F,\bar{n}_2}\right\rangle_{-h_1/2}^{h_2-h_1/2}=\left\langle\begin{bmatrix}u_x\\u_y\end{bmatrix}_{0},\begin{bmatrix}\bar{\sigma}_{xx}\\\bar{\tau}_{xy}\end{bmatrix}_{2F,\bar{n}_2}\right\rangle_{-h_1/2}^{h_2-h_1/2}$$

$$n_1,\ n_2=1,2,3,...$$

The projection vector space for equation (4.15) is

$$\bar{\bar{\sigma}}_{3B}=\text{conj}\begin{bmatrix}\sigma_{xx}\\\tau_{xy}\end{bmatrix}_{3B,\bar{n}_3}=\begin{bmatrix}\bar{\sigma}_{xx}\\\bar{\tau}_{xy}\end{bmatrix}_{3B,\bar{n}_3},\quad \bar{n}_3=1,2,3,... \tag{4.54}$$

Upon projecting equation (4.15) onto equation (4.22), the displacement boundary conditions in equation (4.15) take the form

$$\int_{h_2-h_1/2}^{h_1/2} \vec{u}_4 \cdot \vec{\bar{\sigma}}_{3B} dy = \int_{h_2-h_1/2}^{h_1/2} \vec{u}_3 \cdot \vec{\bar{\sigma}}_{3B} dy$$

$$\Rightarrow \sum_{n_3=1}^{\infty} \left(C_{3F,n_3} \left\langle \begin{bmatrix} u_x \\ u_y \end{bmatrix}_{3F,n_3}, \begin{bmatrix} \bar{\sigma}_{xx} \\ \bar{\tau}_{xy} \end{bmatrix}_{3B,\bar{n}_3} \right\rangle_{h_2-h_1/2}^{h_1/2} + C_{3B,n_3} \left\langle \begin{bmatrix} u_x \\ u_y \end{bmatrix}_{3B,n_3}, \begin{bmatrix} \bar{\sigma}_{xx} \\ \bar{\tau}_{xy} \end{bmatrix}_{3B,\bar{n}_3} \right\rangle_{h_2-h_1/2}^{h_1/2} \right) \quad (4.55)$$

$$= \sum_{n_4=1}^{\infty} C_{4F,n_4} \left\langle \begin{bmatrix} u_x \\ u_y \end{bmatrix}_{4F,n_4}, \begin{bmatrix} \bar{\sigma}_{xx} \\ \bar{\tau}_{xy} \end{bmatrix}_{3B,\bar{n}_3} \right\rangle_{h_2-h_1/2}^{h_1/2}$$

$$n_3,\ n_4 = 1,2,3,...$$

The projection vector space for equation (4.45) is

$$\vec{\bar{\sigma}}_{2B} = \text{conj} \begin{bmatrix} \sigma_{xx} \\ \tau_{xy} \end{bmatrix}_{2B,\bar{n}_2} = \begin{bmatrix} \bar{\sigma}_{xx} \\ \bar{\tau}_{xy} \end{bmatrix}_{2B,\bar{n}_2}, \quad \bar{n}_2 = 1,2,3,... \quad (4.56)$$

Upon projecting equation (4.45) onto equation (4.22), the displacement boundary conditions in equation (4.45) take the form

$$\int_{-h_1/2}^{h_2-h_1/2} \vec{u}_4 \cdot \vec{\bar{\sigma}}_{2B} dy = \int_{-h_1/2}^{h_2-h_1/2} \vec{u}_2 \cdot \vec{\bar{\sigma}}_{2B} dy$$

$$\Rightarrow \sum_{n_2=1}^{\infty} \left(C_{2F,n_2} \left\langle \begin{bmatrix} u_x \\ u_y \end{bmatrix}_{2F,n_2}, \begin{bmatrix} \bar{\sigma}_{xx} \\ \bar{\tau}_{xy} \end{bmatrix}_{2B,\bar{n}_2} \right\rangle_{-h_1/2}^{h_2-h_1/2} + C_{2B,n_2} \left\langle \begin{bmatrix} u_x \\ u_y \end{bmatrix}_{2B,n_2}, \begin{bmatrix} \bar{\sigma}_{xx} \\ \bar{\tau}_{xy} \end{bmatrix}_{2B,\bar{n}_2} \right\rangle_{-h_1/2}^{h_2-h_1/2} \right) \quad (4.57)$$

$$= \sum_{n_4=1}^{\infty} C_{4F,n_4} \left\langle \begin{bmatrix} u_x \\ u_y \end{bmatrix}_{4F,n_4}, \begin{bmatrix} \bar{\sigma}_{xx} \\ \bar{\tau}_{xy} \end{bmatrix}_{2B,\bar{n}_2} \right\rangle_{-h_1/2}^{h_2-h_1/2}$$

$$n_2,\ n_4 = 1,2,3,...$$

4.2.3.4 Numerical Solution for a Horizontal Crack

For numerical calculation we consider finite values for the indices $n_1, n_2, n_3, n_4, \bar{n}_1, \bar{n}_2, \bar{n}_3, \bar{n}_4$. We assume, $n_1 = 1,2,3,...,N_1$, $n_2 = 1,2,3,...,N_2$, $n_3 = 1,2,3,...,N_3$, $n_4 = 1,2,3,...,N_4$, $\bar{n}_1 = 1,2,3,...,\bar{N}_1$, $\bar{n}_2 = 1,2,3,...,\bar{N}_2$, $\bar{n}_3 = 1,2,3,...,\bar{N}_3$, $\bar{n}_4 = 1,2,3,...,\bar{N}_4$. Then, equation (4.17) contains $\bar{N}_1$ linear equations with $(N_1 + 2N_2 + 2N_3)$ unknowns and equation (4.19) contains $\bar{N}_4$ linear equations with

$\left(N_4+2N_2+2N_3\right)$ unknowns. Also, equation (4.51) contains $\bar{N}_3$ linear equations with $\left(N_1+2N_3\right)$ unknowns, equation (4.21) contains $\bar{N}_2$ linear equations with $\left(N_1+2N_2\right)$ unknowns, equation (4.55) contains $\bar{N}_3$ linear equations with $\left(N_4+2N_3\right)$ unknowns, and equation (4.23) contains $\bar{N}_2$ linear equations with $\left(N_4+2N_2\right)$ unknowns. Recall that the $\left(N_1+2N_2+2N_3+N_4\right)$ unknowns are the complex Lamb wave mode amplitudes $\left(C_{1B,n_1}, C_{2F,n_2}, C_{2B,n_2}, C_{3F,n_3}, C_{3B,n_3}, C_{4F,n_4}\right)$. Thus, equations (4.17), (4.19), (4.51), (4.21), (4.55), (4.23) combine to form a set of $\left(\bar{N}_1+2\bar{N}_2+2\bar{N}_3+\bar{N}_4\right)$ linear algebraic equations in $\left(N_1+2N_2+2N_3+N_4\right)$ unknowns C_{1B,n_1}, C_{2F,n_2}, C_{2B,n_2}, C_{3F,n_3}, C_{3B,n_3}, C_{4F,n_4}. By assuming $N_1=N_2=N_3=N_4=\bar{N}_1=\bar{N}_2=\bar{N}_3=\bar{N}_4=N$, we get $6N$ equations in $6N$ unknowns. Then, equations (4.17), (4.19) can be written as

$$\begin{aligned}[A]_{N\times N}\{C_{2F}\}_{N\times 1}+[B]_{N\times N}\{C_{2B}\}_{N\times 1}+[D]_{N\times N}\{C_{3F}\}_{N\times 1}+[E]_{N\times N}\{C_{3B}\}_{N\times 1}\\ -[F]_{N\times N}\{C_{1B}\}_{N\times 1}-[0]_{N\times N}\{C_{4F}\}_{N\times 1}=\{G\}_{N\times 1}\end{aligned} \tag{4.58}$$

$$\begin{aligned}[H]_{N\times N}\{C_{2F}\}_{N\times 1}+[J]_{N\times N}\{C_{2B}\}_{N\times 1}+[K]_{N\times N}\{C_{3F}\}_{N\times 1}+[L]_{N\times N}\{C_{3B}\}_{N\times 1}\\ -[0]_{N\times N}\{C_{1B}\}_{N\times 1}-[M]_{N\times N}\{C_{4F}\}_{N\times 1}=\{0\}_{N\times 1}\end{aligned} \tag{4.59}$$

Similarly equations (4.21) through (4.23) can be written as

$$\begin{aligned}[0]_{N\times N}\{C_{2F}\}_{N\times 1}+[0]_{N\times N}\{C_{2B}\}_{N\times 1}+[N]_{N\times N}\{C_{3F}\}_{N\times 1}+[O]_{N\times N}\{C_{3B}\}_{N\times 1}\\ -[P]_{N\times N}\{C_{1B}\}_{N\times 1}-[0]_{N\times N}\{C_{4F}\}_{N\times 1}=\{Q\}_{N\times 1}\end{aligned} \tag{4.60}$$

$$\begin{aligned}[R]_{N\times N}\{C_{2F}\}_{N\times 1}+[S]_{N\times N}\{C_{2B}\}_{N\times 1}+[0]_{N\times N}\{C_{3F}\}_{N\times 1}+[0]_{N\times N}\{C_{3B}\}_{N\times 1}\\ -[T]_{N\times N}\{C_{1B}\}_{N\times 1}-[0]_{N\times N}\{C_{4F}\}_{N\times 1}=\{U\}_{N\times 1}\end{aligned} \tag{4.61}$$

$$\begin{aligned}[0]_{N\times N}\{C_{2F}\}_{N\times 1}+[0]_{N\times N}\{C_{2B}\}_{N\times 1}+[V]_{N\times N}\{C_{3F}\}_{N\times 1}+[W]_{N\times N}\{C_{3B}\}_{N\times 1}\\ -[0]_{N\times N}\{C_{1B}\}_{N\times 1}-[X]_{N\times N}\{C_{4F}\}_{N\times 1}=\{0\}_{N\times 1}\end{aligned} \tag{4.62}$$

$$\begin{aligned}[Y]_{N\times N}\{C_{2F}\}_{N\times 1}+[Z]_{N\times N}\{C_{2B}\}_{N\times 1}+[0]_{N\times N}\{C_{3F}\}_{N\times 1}+[0]_{N\times N}\{C_{3B}\}_{N\times 1}\\ -[0]_{N\times N}\{C_{1B}\}_{N\times 1}-[\Gamma]_{N\times N}\{C_{4F}\}_{N\times 1}=\{0\}_{N\times 1}\end{aligned} \tag{4.63}$$

In equations (4.24), (4.25), (4.26), (4.27), (4.62), (4.63) the coefficient matrices $[A]$, $[B]$, $[D]$, $[E]$, $[F]$, $[G]$, $[H]$, $[J]$, $[K]$, $[L]$, $[M]$, $[N]$, $[O]$, $[P]$, $[Q]$, $[R]$, $[S]$, $[T]$, $[U]$, $[V]$, $[W]$, $[X]$, $[Y]$, $[Z]$, $[\Gamma]$ are known matrices containing the vector-projected boundary conditions; the vectors $\{C_{2F}\}$, $\{C_{2B}\}$, $\{C_{3F}\}$, $\{C_{3B}\}$, $\{C_{1B}\}$ and $\{C_{4F}\}$ contain the unknown coefficients. Combining equations (4.24) through (4.63) yields them we get

$$\begin{bmatrix} A & B & D & E & -F & 0 \\ H & J & K & L & 0 & -M \\ 0 & 0 & N & O & -P & 0 \\ R & S & 0 & 0 & -T & 0 \\ 0 & 0 & V & W & 0 & -X \\ Y & Z & 0 & 0 & 0 & -\Gamma \end{bmatrix}_{6N\times 6N} \begin{Bmatrix} C_{2F} \\ C_{2B} \\ C_{3F} \\ C_{3B} \\ C_{1B} \\ C_{4F} \end{Bmatrix}_{6N\times 1} = \begin{Bmatrix} G \\ 0 \\ Q \\ U \\ 0 \\ 0 \end{Bmatrix}_{6N\times 1} \tag{4.64}$$

$$\Rightarrow [\Upsilon]_{6N\times 6N} \{C\}_{6N\times 1} = \{\Lambda\}_{6N\times 1}$$

Equation (4.28) can be solved for the unknown amplitudes of the reflected and transmitted Lamb wave modes as

$$\{C\}_{6N\times 1} = [\Upsilon]^{-1}_{6N\times 6N} [\Lambda]_{6N\times 1} \tag{4.65}$$

As a test case we consider a horizontal crack in an aluminum plate with $E = 70$ GPa, $\rho = 2780$ kg/m^3, $\nu = 0.33$, $h_1 = 2$ mm, $h_2 = 1.5$ mm, and $b = 5$ mm. This results in depth ratio $R_d = (h_1 - h_2)/h_1 = 0.25$, and width ratio $R_w = 2b/h_1 = 5$. We also consider S0 as the incident Lamb wave mode. We use a frequency range of up to 1.5 MHz-mm for its relevance to practical applications. We perform convergence studies to determine the maximum number of complex roots of the Rayleigh-Lamb equation needed to calculate the first two scattered Lamb wave modes with high accuracy. Figure 4.8 shows the convergence study for the amplitudes of the first two modes of Lamb waves, S0 and A0. Considering 39 modes in the expansion ensured convergence to about 0.5% error.

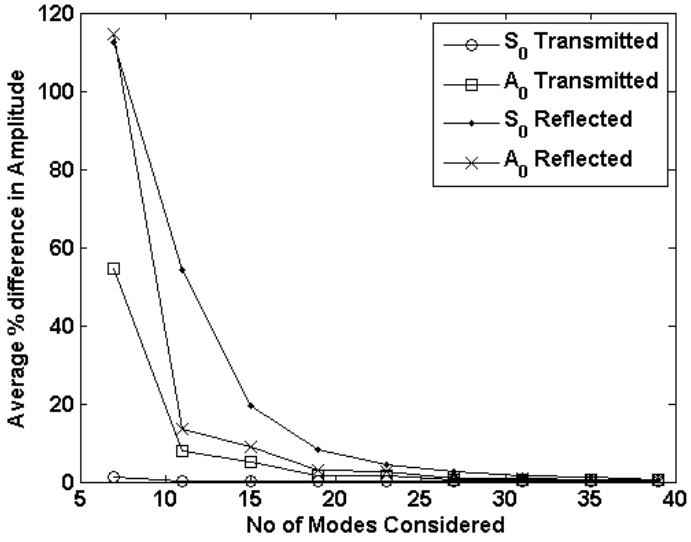

(a)

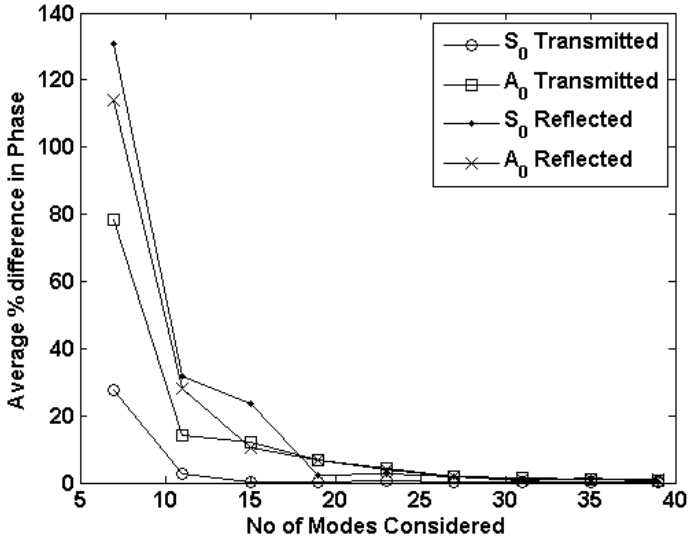

(b)

Figure 4.8: Convergence of (a) amplitudes, (b) phases of scattered Lamb wave modes for S0 mode incident on a horizontal crack with R_d=0.25 and R_w=5; results are averaged over a wide frequency range, 200 kHz.mm to 1.5 MHz.mm

Another important verification of convergence is the power flow balance. Figure 4.9 shows that a 39-mode expansion gave a balanced average power flow though the horizontal cracks over the whole frequency range of up to 750 kHz. It is apparent that power flow balance requirements are met since the "P_{av} incident" line exactly overlaps

with the "P_{av} Scattered (Reflected + Transmitted)" line. Also, Figure 4.9 shows that at certain frequencies the power flow associated with reflected and transmitted waves show sharp spikes. This is because the forward and backward propagating trapped Lamb wave modes in Region 2 and 3 form standing wave fields between the two geometric interfaces of the horizontal crack and at these frequencies the standing wave modes resonates and increases scattered wave amplitudes as well. Similar behavior was also shown by Glushkov et al. for notch type damages(Y. V. Glushkov et al. 2009).

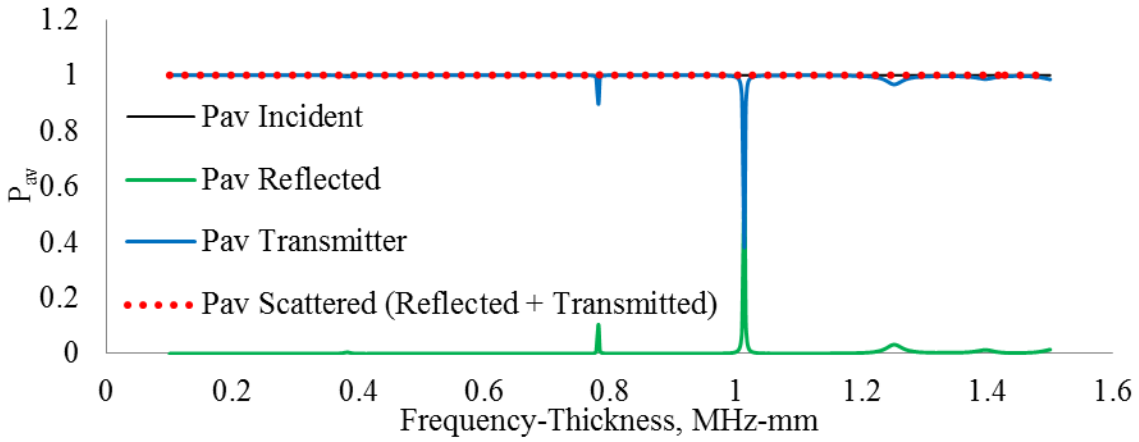

Figure 4.9: Variation of time average power flow P_{av} through the horizontal crack as calculated by CMEP with a 39-mode expansion (S0 mode incident on a horizontal crack with R_d = 0.25 and R_w = 5)

4.2.4 Verification of CMEP for A Horizontal Crack Using FEM

For the validation of the results from CMEP for a notch, we made finite element models (FEM) using the commercial software ANSYS. The dimensions and the material properties were chosen as described in section 4.2.3.4 with $R_d = 0.25$ and $R_w = 5$.

4.2.4.1 FEM Modeling Strategy

The modeling strategy was same as described in section 3.4.1 for a step. The element size and the model sizes were same except, instead of a step, a horizontal crack

was modeled in the 2D FEM model. The range of frequencies was also same along with the thickness of the plate modeled.

4.2.4.2 CMEP vs. FEM for A Horizontal Crack

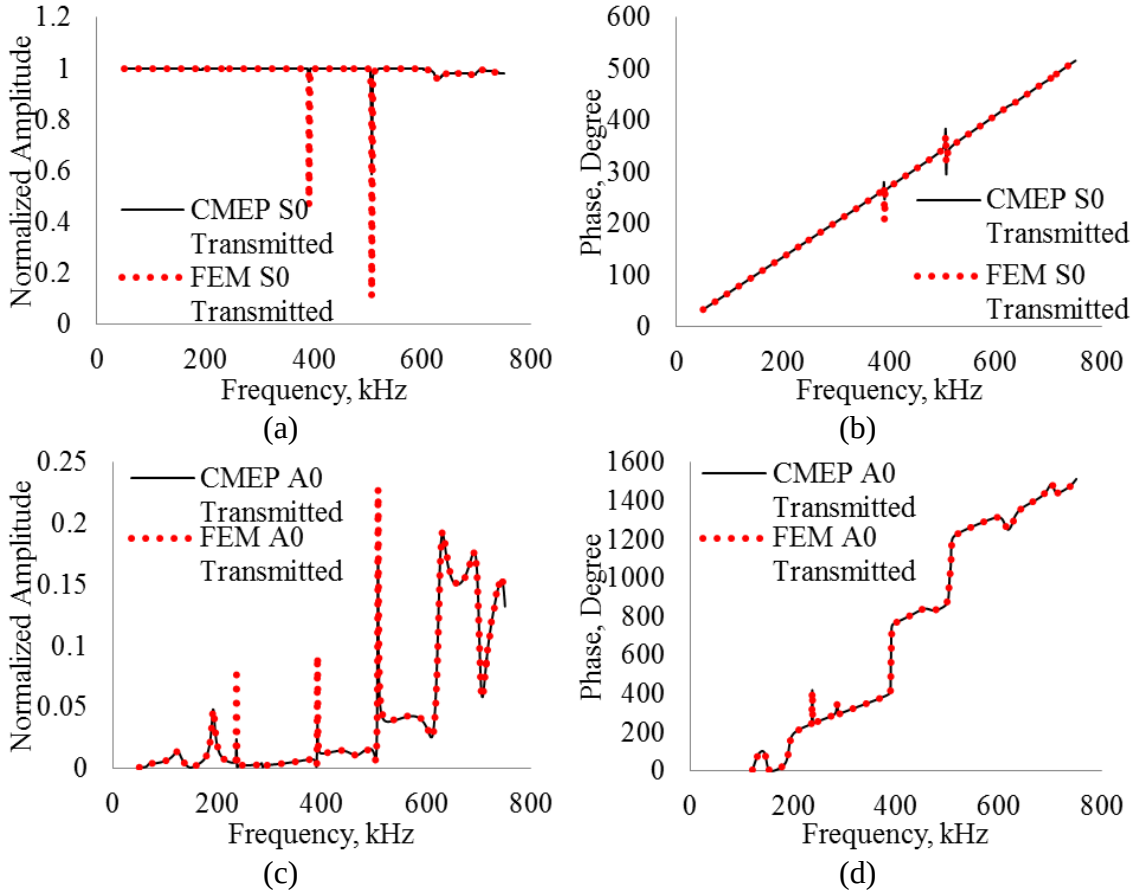

Figure 4.10: Comparison of u_x displacement of transmitted modes; (a) S0 amplitude, (b) S0 phase, (c) A0 amplitude, (d) A0 phase for incident S0 mode scattered from a horizontal crack with R_d = 0.25 and R_w = 5

Figure 4.10 and Figure 4.11 shows the comparison of results from CMEP and FEM; we can see that the amplitudes and phases of the reflected and transmitted waves obtained from FEM are convergent with the CMEP results for a wide range of frequencies. Both CMEP and FEM results show characteristic resonances of the horizontal crack at certain frequencies due to the standing wave field created by trapped Lamb wave modes. These resonance frequencies depend on the width and depth rations

of the horizontal crack. Therefore these frequencies can be used to estimate the horizontal crack dimensions. Since a disbond is also a horizontal crack, similar approach can also be taken to model a disbond between two plates or laminas.

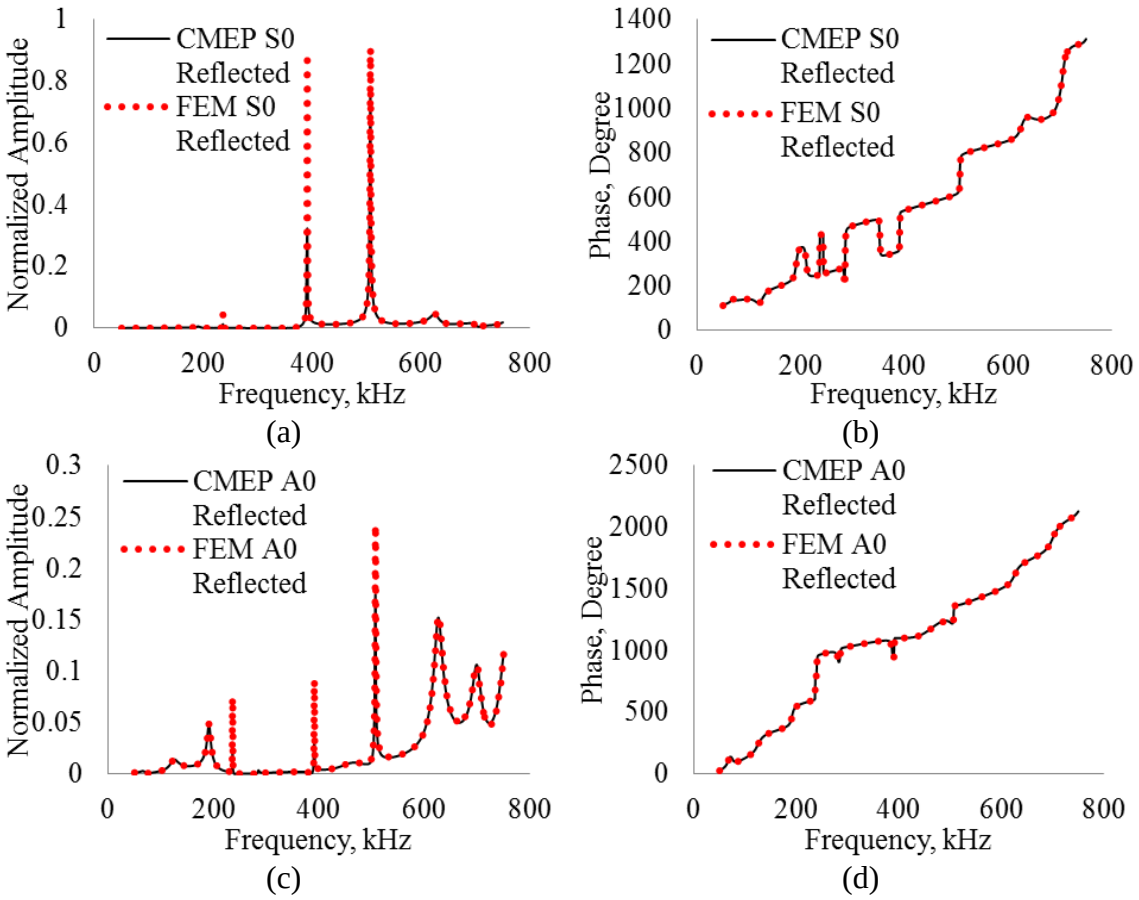

Figure 4.11: Comparison of u_x displacement of reflected modes; (a) S0 amplitude, (b) S0 phase, (c) A0 amplitude, (d) A0 phase for incident S0 mode scattered from a horizontal crack with R_d = 0.25 and R_w = 5

However, the convergence of FE models is quite expensive in terms of computational time; FEM takes about 200 times more computational time than CMEP to compute the same results. This disparity in computational time is due to the fact that FEM requires very fine discretization for convergence of both phase and amplitude. It is very important to obtain correct scatter coefficients quickly for NDE and SHM. Therefore, with fast, accurate, and reliable prediction of the scatter field, CMEP can be an

important tool to solve the inverse problem of detection and characterization of horizontal cracks and disbonds.

4.3 ANALYTICAL MODEL OF SCATTERING FROM NON-RESONANT TYPE DAMAGE

If the damage has zero width, then there is no finite geometric effect due to its presence. Therefore, there is no standing wave field along the width of this damage, and no resonance due to this damage. This type of damage includes a vertical crack, a step in plate thickness, etc. In this section we will present a vertical crack as non-resonating type damage.

4.3.1 CMEP FOR A CRACK

4.3.1.1 Problem Setup for a Crack

To begin our analysis, let us consider a plate with a cross section as shown in Figure 4.1. We assume that there is an incident straight-crested Lamb wave mode travelling from the left towards a vertical surface breaking crack. Upon interacting with the vertical crack, it will result in reflected wave modes, transmitted wave modes, and wave modes trapped in the crack. As shown in Figure 4.1, the crack is located at a distance $x = x_0$ with the thickness of the plate being h_1. At the crack, the plate has a thickness h_2 with the width of the crack being zero. At the crack, we define depth ration as, $R_d = (h_1 - h_2)/h_1$. Also, let us imagine that the incident wave field is represented by (Φ_0, H_0), travelling in *+ve* x direction in the Region 1. We define the reflected wave field as (Φ_1, H_1) and the transmitted wave field in Region 3 as (Φ_3, H_3). We also define the trapped wave field inside the crack in Region 2 as (Φ_2, H_2). The incident and scattered wave fields satisfy the generic wave equations

$$\frac{\partial^2 \Phi}{\partial x^2} + \frac{\partial^2 \Phi}{\partial y^2} = \frac{1}{C_P^2} \ddot{\Phi}$$
$$\frac{\partial^2 H}{\partial x^2} + \frac{\partial^2 H}{\partial y^2} = \frac{1}{C_S^2} \ddot{H} \tag{4.66}$$

where, C_P and C_S are the wave speeds of pressure wave and shear waves, respectively.

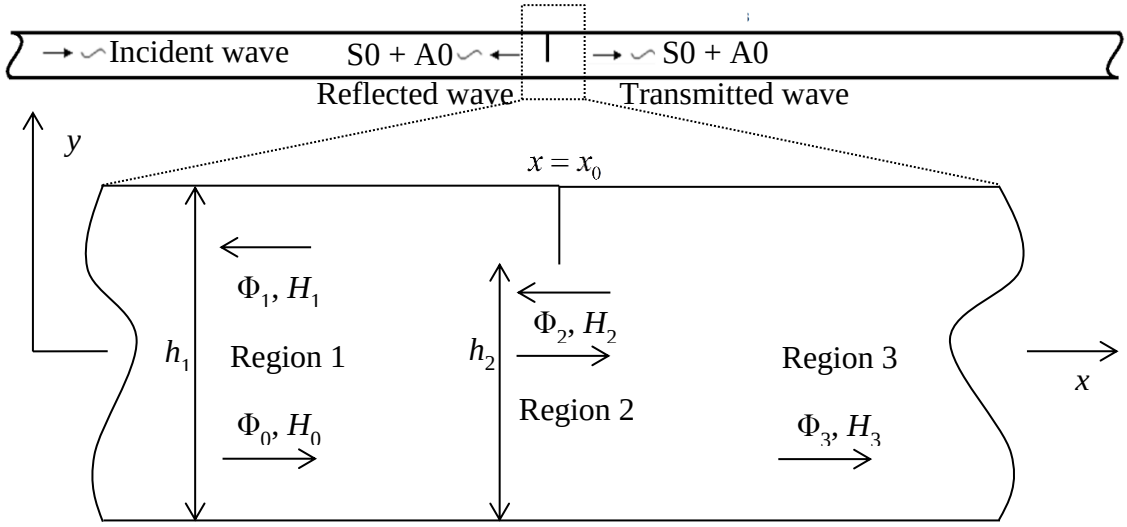

Figure 4.12: Schematic of Lamb waves interacting with a notch

These must satisfy the zero-stress boundary condition at the top and bottom of the plate,

$$\sigma_{yy}\Big|_{\left(x<x_0;\ y=\pm\frac{h_1}{2}\right),\ \left(x>x_0;\ y=\pm\frac{h_1}{2}\right),\ \left(x=x_0;\ y=h_2-\frac{h_1}{2},-\frac{h_1}{2}\right)} = 0$$
$$\tau_{xy}\Big|_{\left(x<x_0;\ y=\pm\frac{h_1}{2}\right),\ \left(x>x_0;\ y=\pm\frac{h_1}{2}\right),\ \left(x=x_0;\ y=h_2-\frac{h_1}{2},-\frac{h_1}{2}\right)} = 0 \tag{4.67}$$

The stress and displacement fields associated with the wave fields are expressed as

$$\boldsymbol{\sigma} = \begin{bmatrix} \sigma_{xx} & \tau_{xx} \\ \tau_{xy} & \sigma_{yy} \end{bmatrix}; \quad \vec{\sigma} = \begin{bmatrix} \sigma_{xx} \\ \tau_{xy} \end{bmatrix}; \quad \vec{u} = \begin{bmatrix} u_x \\ u_y \end{bmatrix} \tag{4.68}$$

where, $\boldsymbol{\sigma}$ is stress tensor, $\vec{\boldsymbol{\sigma}}$ is stress vector, and $\vec{\mathbf{u}}$ is displacement vector. For the displacements, subscripts x and y indicate the directions of the displacement. For stresses, the subscripts xx, yy stand for the normal stress in x, y directions, respectively

and the subscript xy stands for the shear stress. The boundary conditions at the notch are illustrated in Figure 4.2. The boundary conditions at the interface at $x = x_0$ are,

$$\left(\boldsymbol{\sigma_0} + \boldsymbol{\sigma_1}\right) \cdot \hat{n}_{x_1} = \begin{cases} 0, & x_1(y) = x_0, \quad h_2 - h_1/2 \le y \le h_1/2 \\ \boldsymbol{\sigma_2} \cdot -\hat{n}_x, & x = x_0, \quad -h_1/2 \le y \le h_2 - h_1/2 \end{cases} \tag{4.69}$$

$$\vec{u}_0 + \vec{u}_1 = \vec{u}_2, \qquad x = x_0, \quad -h_1/2 \le y \le h_2 - h_1/2 \tag{4.70}$$

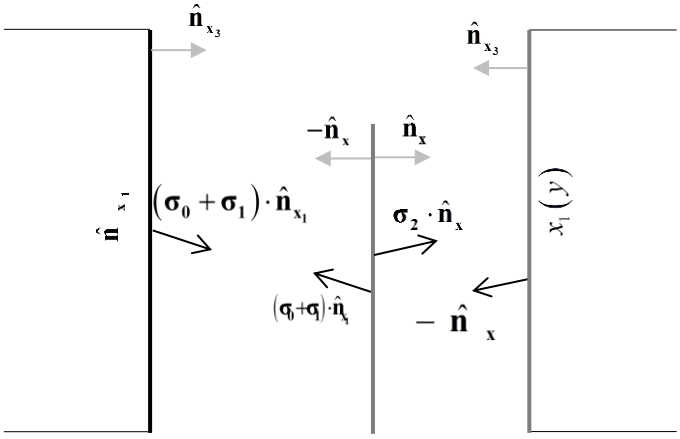

Figure 4.13: Boundary conditions at the crack

The boundary conditions at the interface at $x = x_0 + b$ are,

$$\boldsymbol{\sigma_3} \cdot \hat{n}_{x_3} = \begin{cases} 0, & x_3(y) = x_0, \quad h_2 - h_1/2 \le y \le h_1/2 \\ \boldsymbol{\sigma_2} \cdot \hat{n}_x, & x = x_0, \quad -h_1/2 \le y \le h_2 - h_1/2 \end{cases} \tag{4.71}$$

$$\vec{u}_3 = \vec{u}_2, \qquad x = x_0, \quad -h_1/2 \le y \le h_2 - h_1/2 \tag{4.72}$$

where $\hat{n}_{x_1}$, $\hat{n}_{x_3}$ are the unit surface normal vectors of the interface surfaces represented by $x_1(y)$, $x_3(y)$ and $\hat{n}_x$ is the unit vector in +ve x direction as shown in Figure 4.2. Also, note that for a vertical crack, $\hat{n}_{x_1} = \hat{n}_x$ and $\hat{n}_{x_3} = -\hat{n}_x$. The subscript 0 stands for incident waves in Region 1, subscript 1 stands for reflected waves in Region 1, subscript 2 stands for the trapped waves in Region 2 and subscript 3 stands for transmitted waves in Region 3. Let us assume the incident wave field to be a harmonic wave field of the form

$$\Phi_0 = f_0(y) e^{i(\xi_0 x - \omega t)} \qquad H_0 = i h_0(y) e^{i(\xi_0 x - \omega t)} \tag{4.73}$$

Assuming ξ_0 to be one of the roots of Rayleigh-Lamb equation for the plate in Region 1, Eq. (4.1) and (4.2) are satisfied by definition of Lamb waves and the incident wave becomes one of the modes of Lamb waves.

From the problem setup we can see that the case of a crack is a special case of a notch with vanishing width. Therefore, in CMEP, a the crack problem can be solved by the CMEP by assuming it to be a notch with zero width. Therefore, the complex modes expansion and vector projection of complex Lamb wave modes for the crack problem are identical to the notch problem.

4.3.1.2 Numerical Solution for a Crack

As a test case we consider a vertical crack in an aluminum plate with $E = 70$ GPa, $\rho = 2780$ kg/m^3, $\nu = 0.33$, $h_1 = 2$ mm, $h_2 = 1$ mm, and $b = 0$ mm. This results in depth ratio $R_d = (h_1 - h_2)/h_1 = 0.5$, and width ratio $R_w = 2b/h_1 = 0$. We also consider S0 as the incident Lamb wave mode. We use a frequency-thickness range of up to 1.5 MHz-mm for its relevance to practical applications. We perform convergence studies to determine the maximum number of complex roots of the Rayleigh-Lamb equation needed to calculate the first two scattered Lamb wave modes S0 and A0 with high accuracy. Figure 4.14 shows the convergence study for the amplitudes of the first two modes of Lamb waves, S0 and A0. Unlike Figure 4.4 (a) which shows a monotonic convergence with increased number of modes for a finite width of the notch, Figure 4.14 show an initial monotonic behavior but around 50 modes it show a jump in the calculated amplitudes for zero width of the notch. Later it goes down to about 4% error around 75 modes.

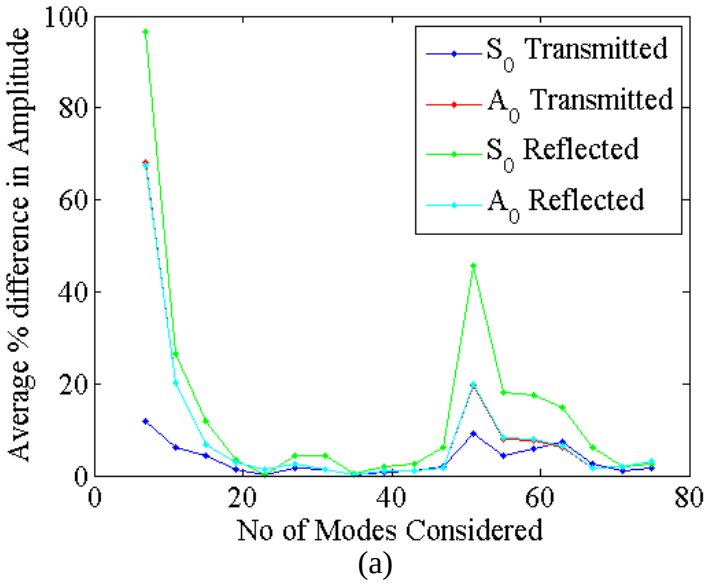

(a)

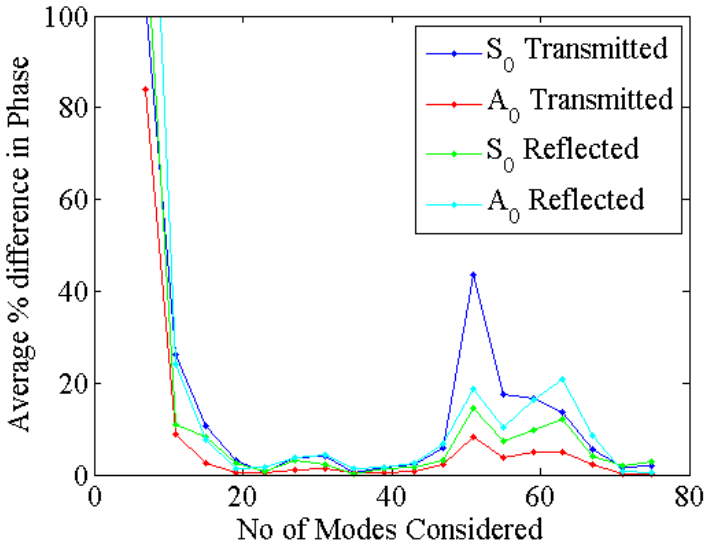

(b)

Figure 4.14: Convergence of (a) amplitudes, (b) phases of scattered Lamb wave modes for S0 mode incident on a vertical crack with R_d=0.5 over a wide frequency range of 200 kHz.mm to 1.5 MHz.mm.

However, Figure 4.15 shows that a 75-mode expansion gave a balanced average power flow though the vertical notches over the whole frequency-thickness range up to 1.5 MHz. It is apparent that power flow balance requirements are met since the "P_{av} incident" line exactly overlaps with the "P_{av} Scattered (Reflected + Transmitted)" line.

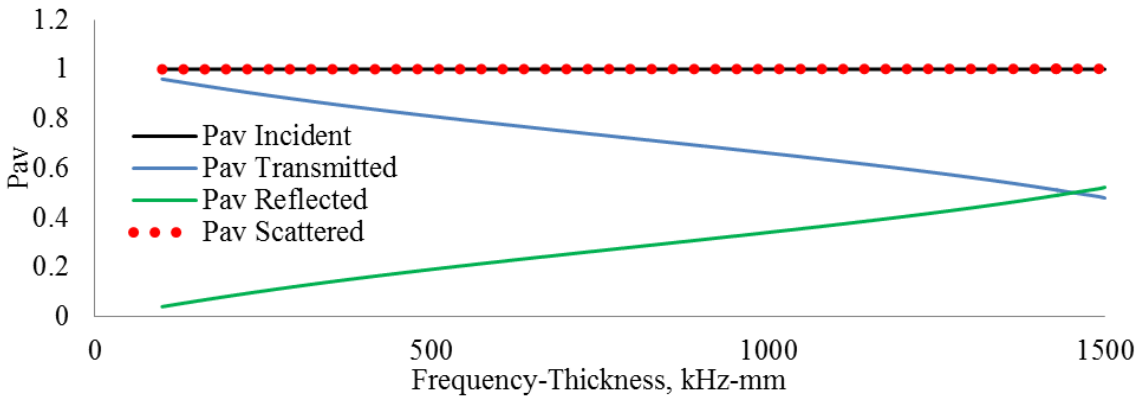

Figure 4.15: Variation of time average power flow P_{av} through the crack as calculated using CMEP with a 75-mode expansion for S0 mode incident on a notch with R_d=0.5 and R_w=0.

4.3.2 Verification of CMEP for A Crack Using FEM

For the validation of the results from CMEP for a crack, we made finite element models (FEM) using the commercial software ANSYS. The dimensions and the material properties were chosen as described in section 4.3.1.2 with $R_d = 0.5$ and $R_w = 0$.

4.3.2.1 FEM Modeling Strategy

The modeling strategy was same as described in section 4.2.2.1 for a notch. The element size was chosen to be 0.001 mm and the model size was kept same except, instead of a notch, a crack was modeled in the 2D FEM model. The increase in the mesh density was to capture the stress singularity at the crack tip. The range of frequencies was kept same along with the thickness of the plate modeled.

4.3.2.2 CMEP vs. FEM for A Notch

Figure 4.5 shows that the amplitudes and phases of the scattered waves obtained from FEM are convergent with the CMEP results for a wide range of frequencies for a half thickness vertical crack. However, unlike the case of notch with finite width we do not see any resonance phenomenon. This is because the resonance is associated with the width of the notch and in this particular case the width is zero. Therefore, there is no

resonance associated with this type of damage. In terms of efficiency, due to the slow convergence for a crack it took about 600 seconds of computational time which is 20 times more than a usual notch problem. However, due to increase in the mesh density the reported FE analysis took about 25000 seconds, 4 times that of a notch problem.

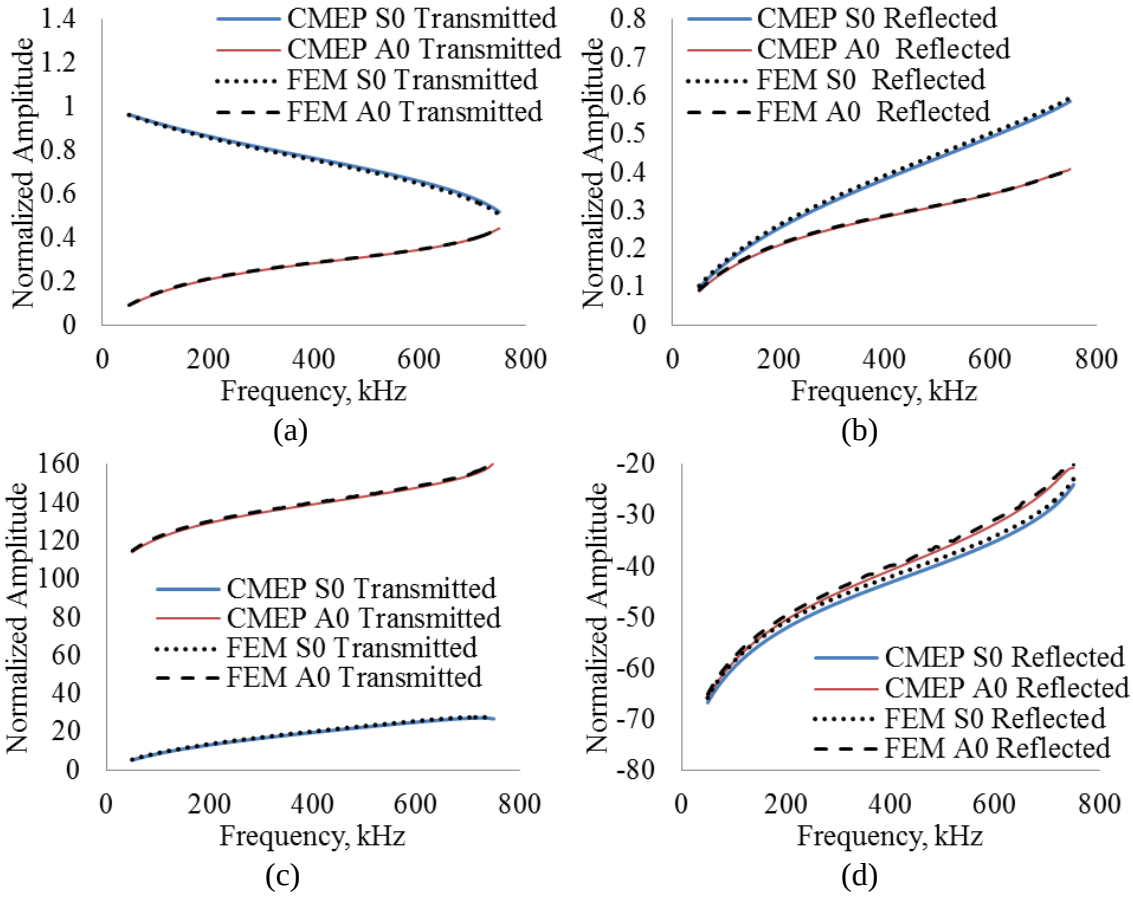

Figure 4.16: Comparison of u_x displacement of scattered waves for incident S0 mode, (a) amplitude of transmitted modes; (b) amplitude of reflected modes; (c) phase of transmitted modes and (b) phase of reflected modes

4.4 CONCLUSION AND FUTURE WORK

In this chapter we have demonstrated the use of complex Lamb wave modes and their application in analytical modeling of Lamb wave scattering from various types of damage. We have demonstrated the method complex modes expansion and vector projections (CMEP) for this purpose. We have applied CMEP to a horizontal cark, a

vertical crack and a notch to demonstrate its capability in predicting scattered Lamb wave field. We have also verified the predictions with FEM models and confirmed that CMEP is orders of magnitude faster than the FEM code we used and it is as accurate as FEM. However, there are some convergence issues in the case of a vertical crack for CMEP. The convergence required 75 complex Lamb wave modes for a vertical crack; this is much higher compared to only 27 for a vertical notch, despite the fact that we used the same CMEP code for both of these damages. In our opinion this could be due to the nature of discontinuity that a vertical crack creates. Farther study needs to be performed for better understanding. Also, the CMEP method that we demonstrated assumes straight crested Lamb wave modes in plate strain condition. However, similar approach of using complex modes expansion with the projection of thickness dependent boundary conditions onto the vector space of complex wave modes using power flow associated with the wave guides can be used for non-straight crested plate guided waves. One needs to keep in mind that shear horizontal waves should also be considered along with Lamb waves for such analysis.

CHAPTER 5
EXPERIMENTAL VALIDATION OF CMEP

5.1 STATE OF THE ART

As mentioned in previous chapters, methods of predicting the scattered Lamb wave modes from different types of damage has been an interesting research topic for decades due to its possible application in SHM and NDE. Researchers have developed predictive models based on numerical techniques such as FEM, BEM (Cho and Rose 2000; Galán and Abascal 2005; Mackerle 2004; Moser, Jacobs, and Qu 1999), and semi analytical techniques (Cho and Rose 2000; Galán and Abascal 2005; Gunawan and Hirose 2004; Terrien et al. 2007). However, validation of these models is of importance when it comes to application of them in predicting real life phenomenon. One of the earliest work was done by Alleyne et al.(Alleyne and Cawley 1992) where, they studied interaction of various types of notches with a straight crested Lamb waves using FEM and compared it with experiments. The FEM analysis was done in 2D assuming straight crested waves in plane strain condition. However, for experimental verification they assumed a circular crested wave front as straight crested at a distance from the transducer. Similar study was also performed by Lowe et al. (Lowe et al. 2000) where the prediction was done assuming a straight crested Lamb wave but the experiments did not involve straight crested waves. In other studies, Benmeddour et al. studies the mode conversion of S0 and A0 modes at symmetric and antisymmetric notches in a plate (Benmeddour et al. 2008a)(Benmeddour et al. 2008b). To excite a straight crested wave they used long transduces. However, it was not reported if it resulted in straight crested

Lamb waves. In another study Santhanam et al. (Santhanam and Demirli 2013) have attempted to validate their analytical model to predict oblique reflection of straight crested Lamb waves with experiments using circular crested Lamb waves. In many cases, building predictive models of Lamb wave scattering require experimental generation of straight crested Lamb for validation. The studies mentioned approximated cuved wave fronts to straight crested waves by placing the transducer at a distance or by using long transducers or simply ignoring the curvature of the wave front. However, creation of straight crested Lamb waves in a finite plate using finite transducers is quite challenging and has not been reported in literature. In this chapter, we present our technique to generate a straight crested Lamb waves in a finite plate with finite transducers. The aim of this experiment is to validate the predictions of CMEP, particularly for a Lamb wave mode interacting with a step in plate thickness

5.2 GENERAL EXPERIMENTAL PROCEDURE

There are several major challenges any researcher faces when attempting to generate a straight crested Lamb waves. These challenges and the challenges in experimentally determining the scatter coefficients of a straight crested Lamb wave mode are

- Determining specimen geometry
- Eliminating the boundary reflections
- Creating a straight crested Lamb wave mode
- Tuning symmetric or antisymmetric Lamb wave mode selectively
- Measuring the scatter wave field with sufficient accuracy

5.2.1 DETERMINING THE SPECIMEN GEOMETRY

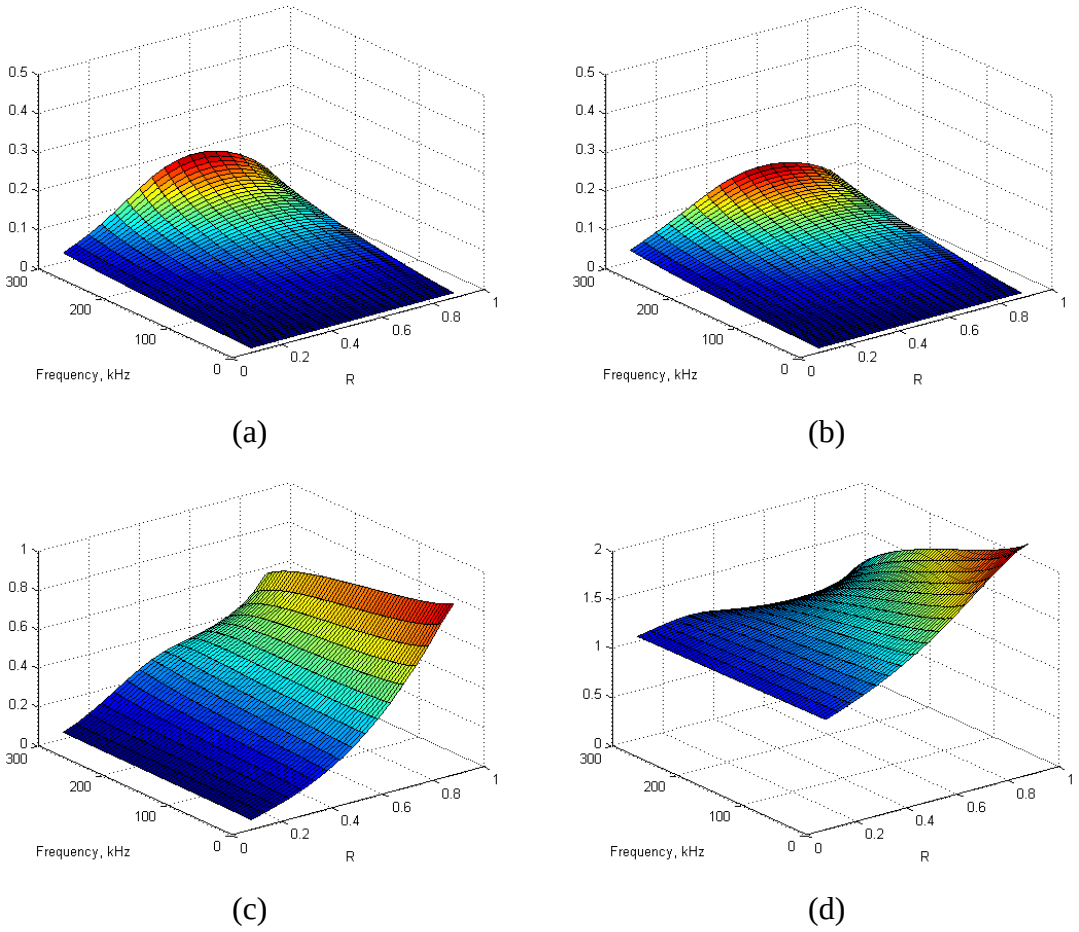

Figure 5.1: CMEP results for variation of scattering coefficients of Lamb wave modes with frequency and depth-ratio for incident A0 mode (a) reflected S0 (b) transmitted S0 (c) reflected A0 (d) transmitted A0

To optimize the specimen geometry we used CMEP predictions for our experiments. We focused on capturing the mode conversion aspect of the step. We predicted the scattered wave amplitudes at various depth rations using CMEP. In Figure 5.1 (a) and (b) we can see that for incident A0 at depth ratio of 0.6 the scatter coefficients of reflected and transmitted S0 modes mode are maximum. Therefore we chose this depth ration for our experiment. For safe handling, we avoided small plate thickness after the

step; we considered a plate of thickness 4.86 mm. We chose aluminum 6061 as the material for the plate for good machinability.

In a pitch-catch type wave propagation experiment, for reliable measurement of scattered waves, the receiver should be at a sufficient distance from the source for separation of symmetric and antisymmetric modes. To predict the required distance, we used existing analytical tool WFR1D for straight crested Lamb waves (Figure 5.2). This suggested us to place the sensor at 300 mm away from the step to detect the reflected wave modes and 250 mm for the transmitted wave modes. We also needed sufficient distance between the edge of the plate and the actuator and sensors. Considering these requirement we selected 1220 mm × 305 mm × 4.86 mm plate. Figure 5.5 (a) shows the design of the plate geometry after considering all the dimensional criteria. Figure 5.3 shows the plate after machining a step using a vertical milling machine.

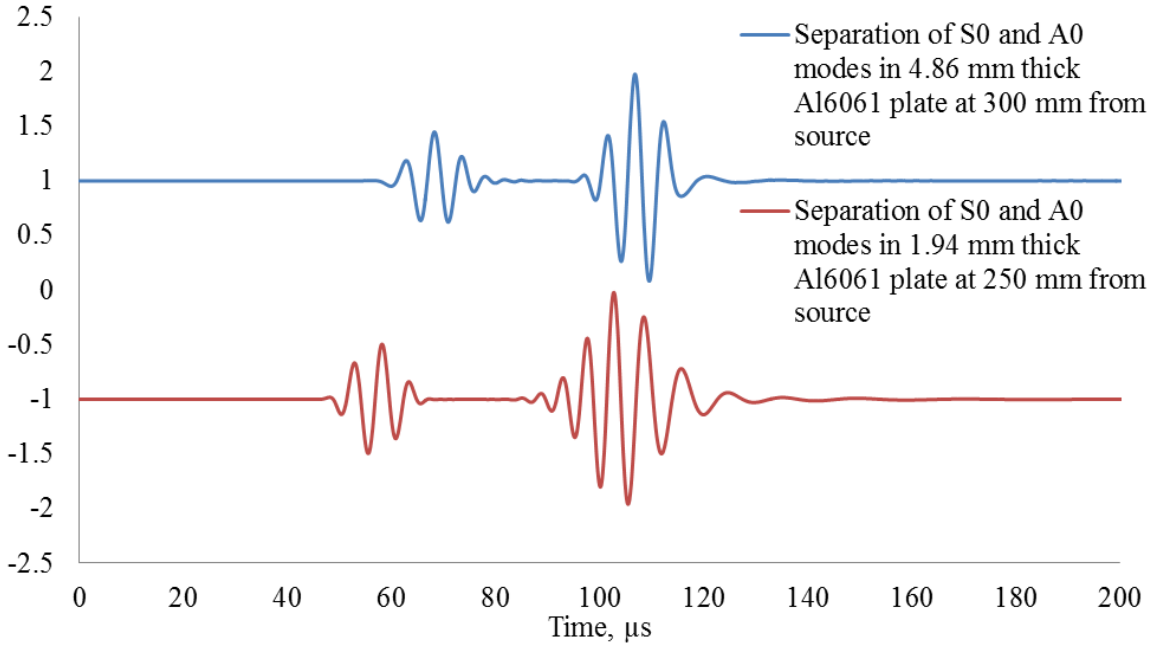

Figure 5.2: Separation of S0 and A0 modea predicted by WFR1D

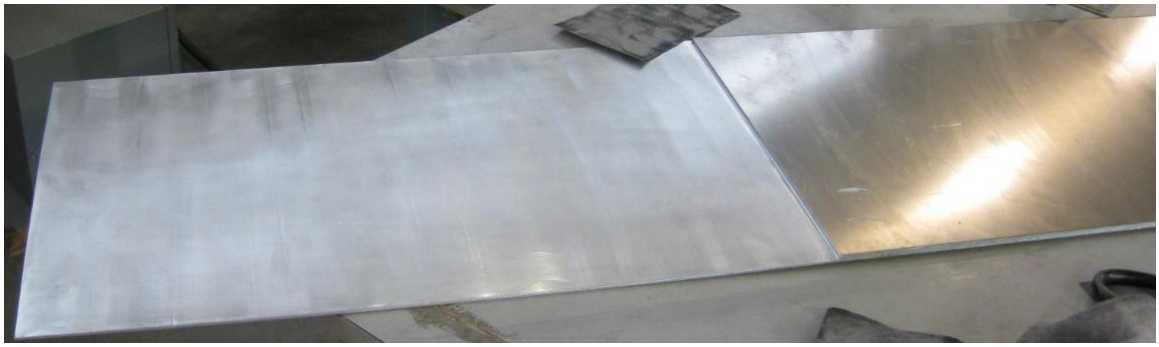

Figure 5.3: Aluminum plate after machining the step

5.2.2 Eliminating Boundary Reflections

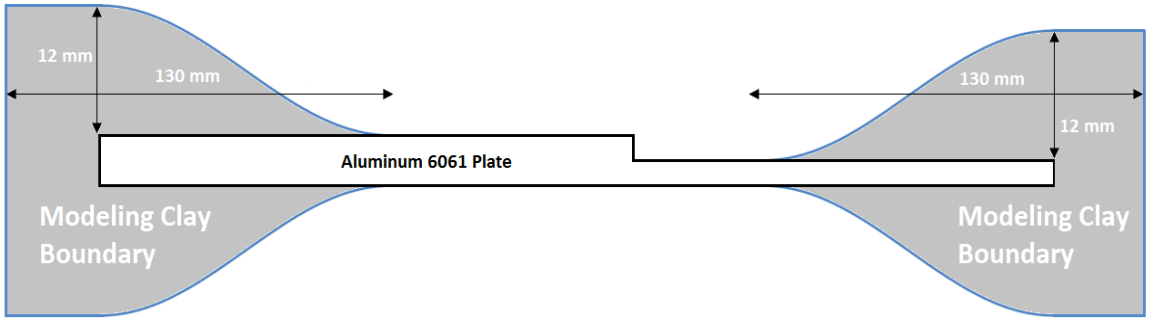

(a)

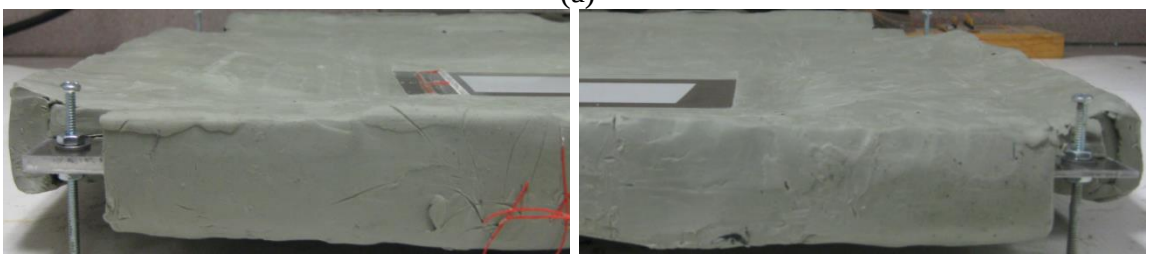

(b) (c)

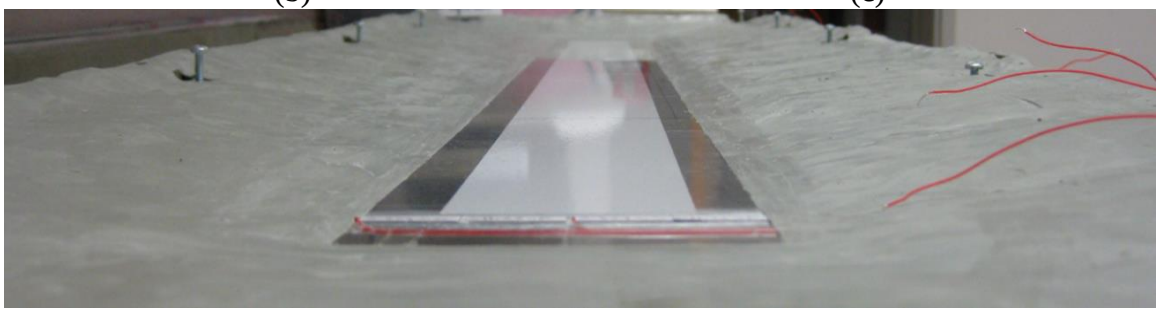

(d)

Figure 5.4: Creating absorbing boundary with modeling clay (a) schematic diagram (b) left end of the plate after application of clay (c) right end of the plate after application of clay (d) absorbing boundary around the plate

To eliminate boundary reflections we took inspiration from our FEM model. As mentioned in section 3.4.1, in FE models we used non-reflecting boundaries (NRB) to absorb edge reflection. To create NRBs, we introduced surface damping in the form of spring damping elements to damp out reflected waves in a finite geometric model. Similarly we chose to use damping material on the surface of the plate around the edge.

We considered modeling clay as the damping material as it is easy to apply and gives a very good surface adhesion after melting at 85°C. As shown in Figure 5.4 (a), we varied the thickness of the modeling clay, starting from zero thickness to about 12 mm thick at the edge. This was done so that the waves do not reflect from the beginning of the clay boundary due to sudden change in boundary conditions. Figure 5.4 (b), (c) and (d) shows the variation of the absorbing clay boundary thickness in the real specimen. Figure 5.5 (b) shows the entire plate after application of the absorbing boundaries all around the specimen.

5.2.3 Creating a Straight Crested Wave Front

We used three 40 mm × 5 mm × 0.2 mm piezoelectric wafer active sensor (PWAS) and bonded them in a line to create a long line source. However, due to the edge effect, the wave crest does not stay straight at the ends of a line source. We created a 3D FE model of a similar plate for understanding. In Figure 5.6 (a) we can see FEM simulation of a similar setup where PWAS of the same size was used with 40 mm wide non-reflecting boundary. The non-reflecting boundary absorbed the curved crested waves produced around the corners of the PWAS. This results in a straight crested wave front after propagating less than 100 mm distance. In experiment we excited the three PWAS transducers in phase and measured the wave field using scanning LASER Doppler

velocimeter (SLDV). Figure 5.6 (b) shows that we were successful in generating straight crested A0 Lamb wave mode experimentally with absorbing clay boundaries.

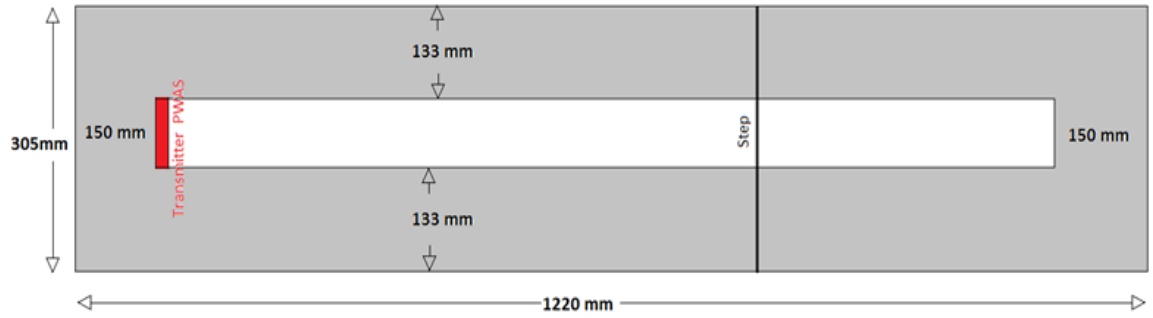

(a)

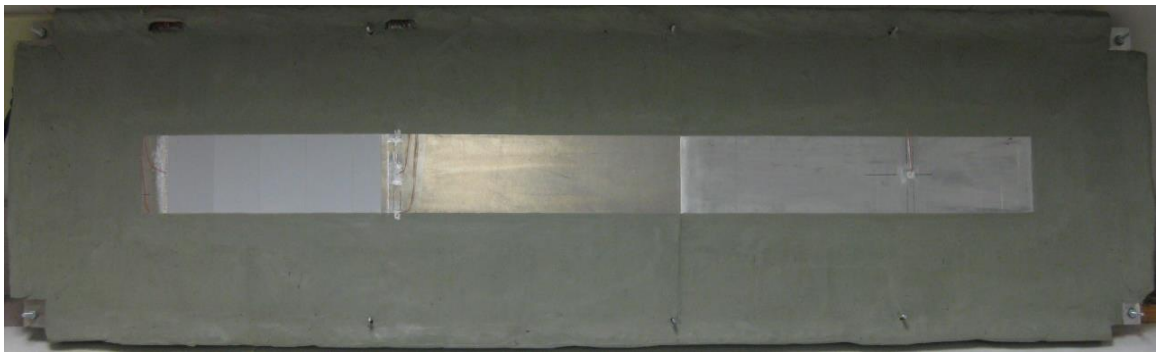

(b)

Figure 5.5: Top view of the specimen (a) schematic diagram (b) actual specimen

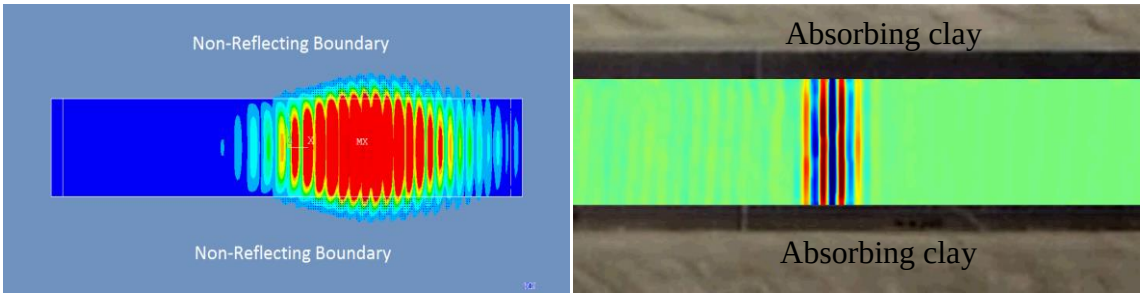

(a) (b)

Figure 5.6: Creating straight crested waves using non-reflecting boundary (a) FEM simulation (b) experimental result

In Figure 5.7 (b) we can see the signal corresponding to generated A0 mode after travelling different distances. We can see that the wave amplitude does not change much proving that we were successful in generating a straight crested Lamb wave mode

channeled by absorbing clay boundary. This also shows that the clay boundary does not really damp the channeled wave. the little differences that we can see between two signals in Figure 5.7 (b) are due to low dispersion of the A0 mode at 200 kHz evident from Figure 5.7 (a).

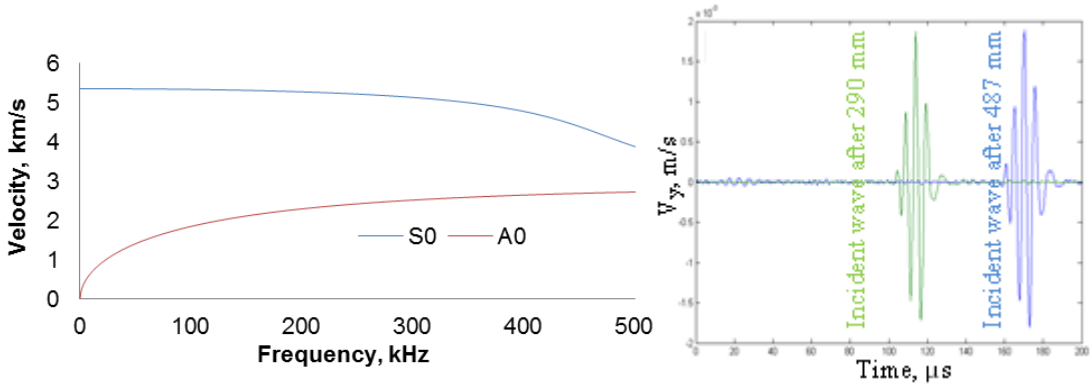

(a) (b)

Figure 5.7: (a) Dispersion curve for 4.86 mm thick aluminum plate (b) experimental incident wave after travelling different distances

5.2.4 TUNING S0 AND A0 MODE SEPARATELY

To actuate a symmetric or an antisymmetric mode selectively we used PWAS transducers on both top and bottom surfaces for the plate with careful alignment. Since PWAS transfer function is sensitive to the bonding condition (Giurgiutiu 2014), we may never get the exact same transfer function for both top and bottom PWAS. For this reason we excited both the PWAS with amplitude and phase adjustment. To achieve this we used Tektronics AFG3052C dual channel signal generator to tune A0 mode using 175 kHz 3.5 count tone burs signal. In Figure 5.9 we can see the above mentioned procedure resulted in excitation of only A0 mode and no S0 mode.

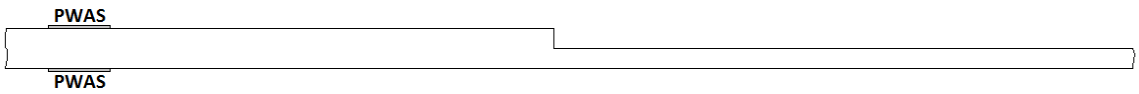

Figure 5.8: Tuning S0 and A0 mode using top and bottom PWAS

Figure 5.9: Tuned A0 mode using top and bottom PWAS

5.2.5 MEASURING SCATTERED WAVE FIELD

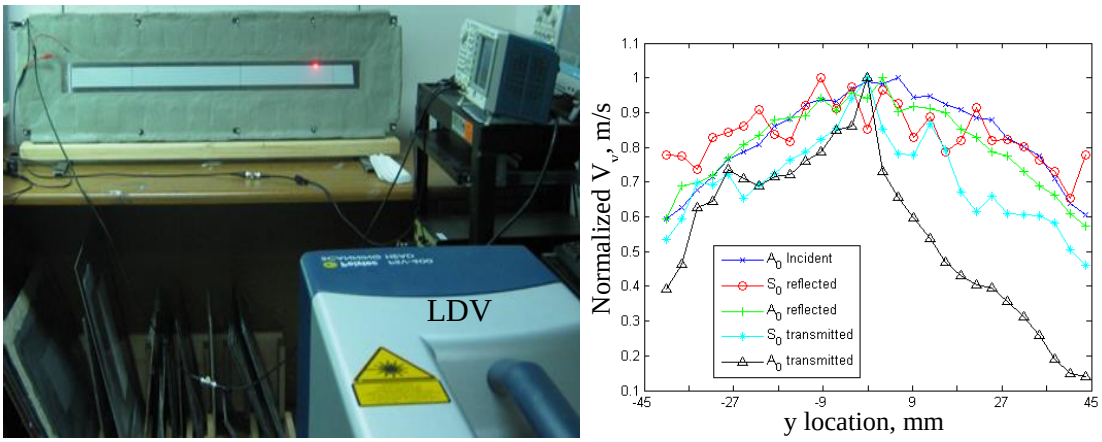

(a) (b)

Figure 5.10: Out of plane velocity measurement using laser doppler velocimeter (LDV) (a) experimental setup (b) variation of measurement across width

To measure the scattered wave field we used single laser scanning LASER Doppler velocimeter (SLDV) to measure the out of plane velocity (v_y) at the surface of the plate (Figure 5.10). This also gave us the opportunity to visualize the wave modes scattered by the step. In Figure 5.11 we can see that the scattered wave modes are easily visible in the recorded wave field data. Also it is important to note that the amplitude of the scattered symmetric mode is much smaller than the amplitude of the antisymmetric mode. This is because the antisymmetric modes have much higher out of plane velocity than the symmetric mode. It is very difficult to measure symmetric modes accurately using single laser LADV as they have very low out of plane velocity.

$$C^s = \frac{v_y^s(\omega)}{v_y^{in}(\omega)} = \frac{\omega u_y^s(\omega)}{\omega u_y^{in}(\omega)} = \frac{u_y^s(\omega)}{u_y^{in}(\omega)} \tag{5.1}$$

For incident, reflected, and transmitter modes we used wave field data recorded at 87 mm, 365 mm, and 264 mm, respectively, from the step. First, we separate the portions of the signal corresponding to different modes and converted the time domain signal to frequency domain using FFT algorithm. Then, we used equation (5.1) to calculate the scatter coefficient C^s were indices s and in stand for scattered and incident wave modes, respectively. Also from equation (5.1), we can see that either the velocity (v_y) or displacement (u_y) will result in the same scatter coefficient.

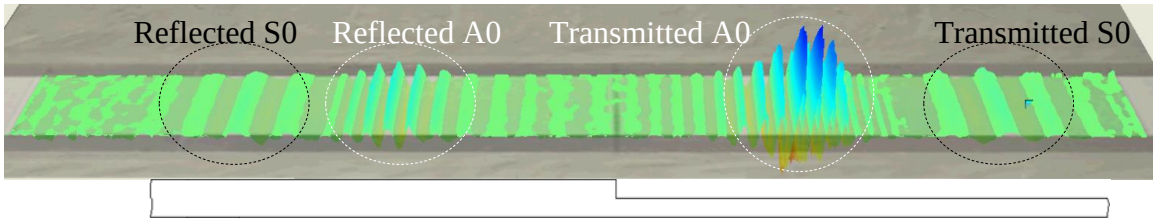

Figure 5.11: Experimentally measured scattered straigh crested Lamb wave modes using scanning LDV

At this point it is worthwhile to mention that, as we used a scanning laser beam to measure the out of plane velocity the laser was not always perpendicular to the place surface. Also, since the plate was a rolled aluminum sheet the portion of the plate that was machined developed a curvature after machining. These two factors gave rise to experimental error. As we can see from Figure 5.10 (b), the measured wave amplitudes varied rather abruptly along the width of the wave field. To minimize the effects of these errors we have calculated the mean scatter coefficients across the width of the wave field.

5.3 CMEP VS EXPERIMENT FOR A STEP

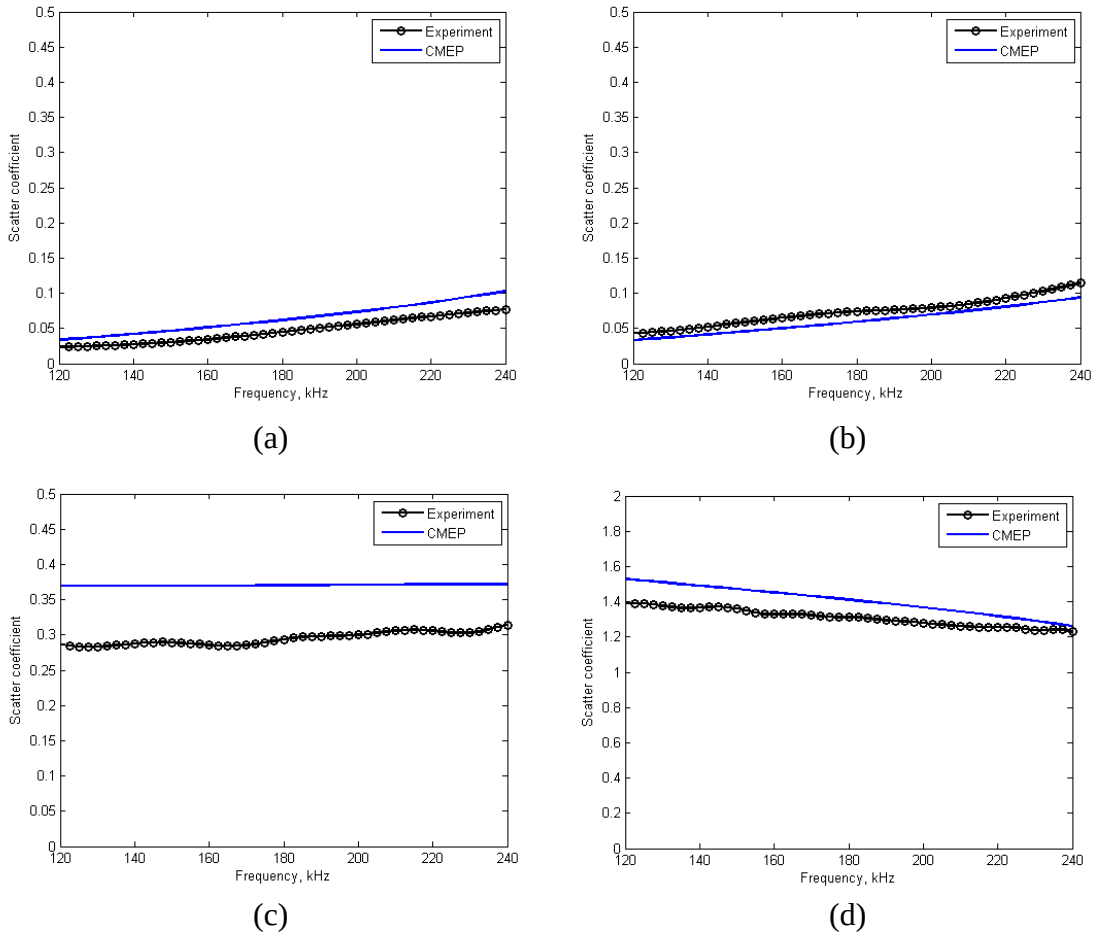

Figure 5.12: Experiment vs CMEP result for variation of scatter coefficients of differen Lamb wave modes for incident A0 mode (a) reflected S0(b) transmitted S0 (c) reflected A0 (d) transmitted A0

From Figure 5.12 we can see that the experimental results are in agreement with the CMEP results. From these figures we can also notice that the experimentally obtained scatter coefficients for reflected and transmitted A0 modes were consistently lower than the predicted ones. The CMEP predictions assumed no material damping. Whereas, in reality, there is material damping and its effect is higher on A0 mode than S0 mode. Since we are measuring the scattered waves at a significant distance away from the step,

this effect of damping may result in lower than predicted amplitude of the reflected and transmitted modes, particularly for A0 mode.

However, all the four plots show the trends of the scatter coefficient predicted by CMEP are same as that of the experimentally obtained results. The values of the scatter coefficients are also sufficiently close to the predicted values from CMEP. This shows that CMEP is a reliable tool to predict the scattering of the Lamb waves from geometric discontinuities. The experimental results may also be obtained for a larger frequency domain.

5.4 CONCLUSION AND FUTURE WORK

In this chapter we demonstrated a method to create straight crested Lamb wave modes using inspirations from FE analysis. We showed that it is possible to create straight crested Lamb wave modes using absorbing boundary along with long transducers. This method of generating straight crested Lamb waves is useful for many experimental investigation and validation of predictive models. We used this method to validate the predictions from CMEP for a step in plate thickness. We used analytical models like CMEP and WFR1D to design our experiment successfully. The obtained experimental results agree with the CMEP predictions well. The major sources of errors were in specimen geometry and in the use of SLDV for measurement. Also, the reflective tape used on the entire wave guide for wave field measurement contributed to deviation of the experimental results from CMEP predictions.

For better agreement of experimental results with predictions, one must control the specimen and damage geometry precisely. Also, the use of single point LDV instead of SLDV may result in more accurate measurement of scattered waves.

CHAPTER 6

PASSIVE DETECTION AND CHARACTERIZATION OF FATIGUE CRACK

6.1 STATE OF THE ART

Passive detection of fatigue crack by sensing acoustic emission has attracted attention of many researchers for decades. The fundamental problem with passive sensing is its susceptibility to various sources of noise. There are various acoustic and non-acoustic sources that contribute to the signals recorded during passive detection. Apart from the white noise, it contains signals from natural vibrations, impact, other types of sources along with acoustic emissions due to cracks and other structural damages. The fundamental challenge is to identify the crack related acoustic emission data from the sensed signal. Researchers have applied data driven methods ((Roberts and Talebzadeh 2003), (Chang et al. 2009), (Gagar, Foote, and Irving 2014), (Cuadra et al. 2015)) to tackle this problem. However to successfully identify acoustic emission in passive sensing mode it is important to develop the science and understanding of how crack-generated acoustic emission (AE) wave signals can be extracted from non-crack wave signals during AE monitoring under actual operational conditions. To develop this understanding researchers have studied acoustic emission (AE) due to crack propagation in elastic medium (Paris and Erdogan 1963) (Nemati, Metrovich, and Nanni 2015). Ceranogliu and Yih-Hsing (Ceranogliu and Yih-Hsing 1981) have analyzed how transient waves are generated by variety of dynamic nuclei of strains based on generalized ray theory. Chung and Kannatey-Asibu (Chung and Kannatey-Asibu 1992) have studied how acoustic emission occurs during plastic deformation for a pure crystal considering

acceleration of a moving dislocation. Lysak (Lysak 1996) investigated acoustic emission from a growing crack by formulating non-stationary dynamic problems of crack theory. Lysak obtained variety of new analytical relationship between crack parameters and AE signal parameters. Andreykiv et al. (O. Y. Andreykiv et al. 2001; O. Andreykiv et al. 2010) have studied acoustic emission caused by internal crack growth. Sause and Horn (Sause and Horn 2010) have proposed a microscopic source model to simulate AE in CFRP. In another study, González and LLorca (Gonzalez and LLorca 2006) have used multiscale modeling to capture the fracture behavior of fiber reinforced composite. Other researchers have used peridynamic formulation based on homogenization and mapping between elastic and fracture parameters of the micro-scale peridynamic bonds and the macro-scale parameters of the composite (Hu, Ha, and Bobaru 2011). Several studies were done to understand the emission of guided waves such as, Lamb waves, due to crack growth in plate like structures (Gorman and Ziola 1991). Gorman and Prosser (Gorman and Prosser 1996) suggested the application of normal mode expansion to address the issue. Maji, et al. (Maji, Satpathi, and Kratochvil 1997) have demonstrated the use of NDE technique based on Lamb wave propagation to locate the source of acoustic emissions. Prosser et al. (Prosser et al. 1999) used Mindlin plate theory and finite element analysis to model acoustic emissions. Zhou and Zhang (Zhou and Zhang 2014) have studied how phase difference of the received signal at two different sensor locations can be used to locate AE source in a thick plate. Use of acoustic emission for detecting and locating fatigue cracks in metallic structures is widely reported but studies to estimate crack length from acoustic emission are rare. Gagar et al. (Gagar, Foote, and Irving 2014) have developed a method for deducing crack length based on correlations

between AE signals generated during fatigue crack growth and corresponding cyclic loads. However, this method was based on an experiment driven model. In this dissertation we present our work aimed towards identifying crack related acoustic emissions; our focus is on estimation of crack length based on physics of wave propagation in plate structures.

6.2 ACOUSTIC EMISSION DUE TO FATIGUE CRACK GROWTH

The aim of this research is to develop a predictive simulation method for acoustic emission (AE) from cracks in plate structures. This methodology will help identifying crack related acoustic emission signals from non-crack related acoustic emission signals and help characterize cracks. Our approach is different from most other approaches in the use of Lamb wave theory. Therefore, to use acoustic emission for damage detection and identification, we will use physics of material based approach. However, to identify and characterize cracks using acoustic emission signal we need to use experimental methods to generate acoustic emissions from cracks.

6.2.1 EXPERIMENTAL PROCEDURE

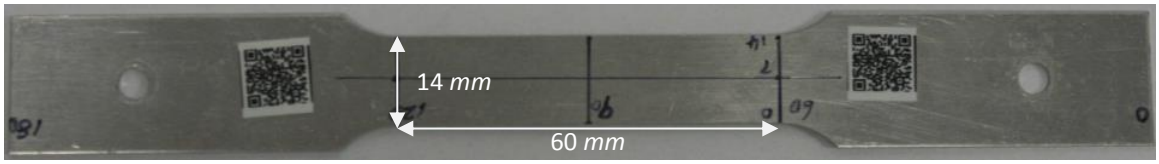

Figure 6.1: Specimen for fatigue test

We performed fatigue tests on a 1 mm thick dog bone specimen of Al2024 as shown in Figure 6.1. We drilled a 1 mm hole at the center of the specimen to initiate crack growth from that particular location. Four PICO AE sensors were placed close to the hole, two of them being 5 mm away from the hole and other two were 20 mm away from the hole (Figure 6.2 (b)). To minimize reflections of the acoustic emission wave from the boundaries we used clay padding at the boundaries Figure 6.2 (a).

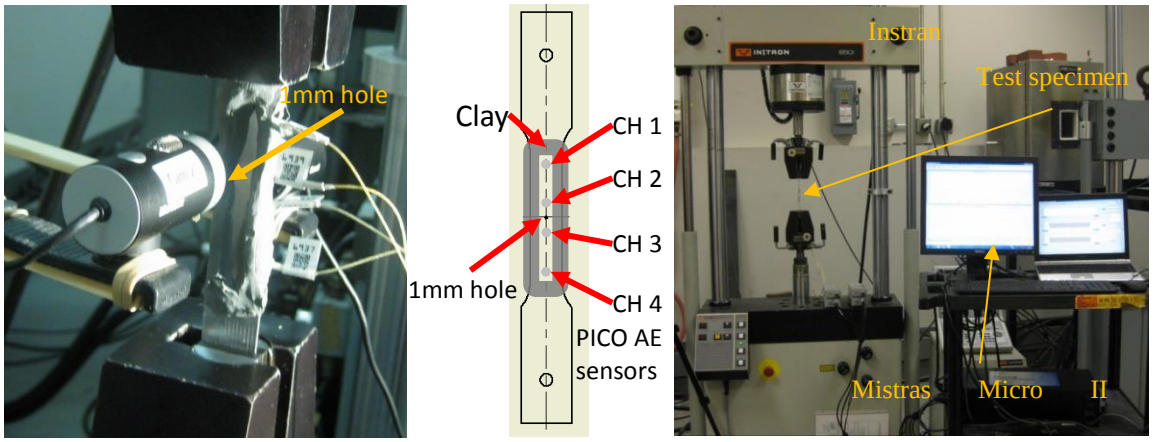

(a) (b) (c)

Figure 6.2: Fatigue test of the specimen (a) actual specimen (b) schematic of the specimen (c) experimental setup

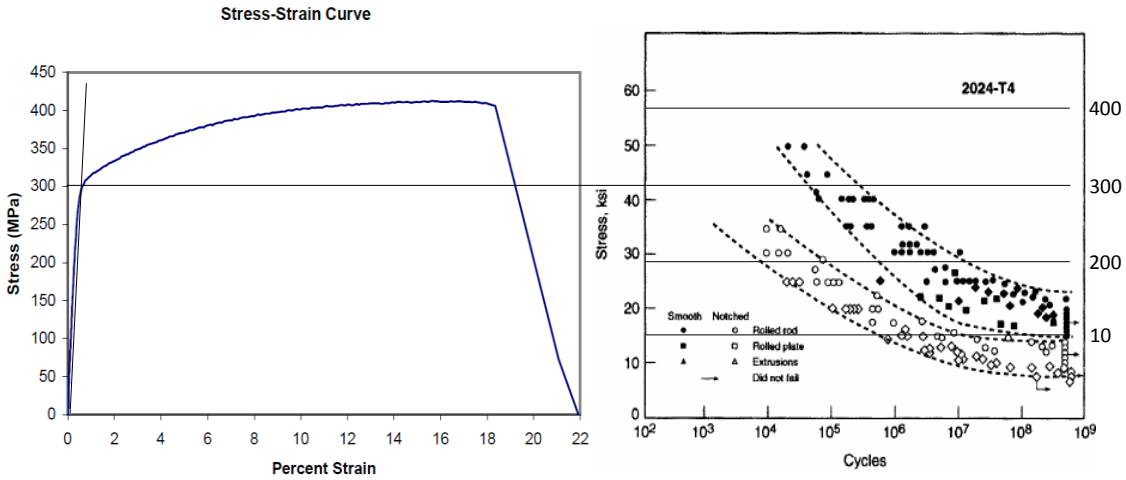

(a) (b)

Figure 6.3: Fatigue loading of the specimen (a) $Y = \sigma$ for 0.2% permanent strain after unloading (b) S-N curve for the material of the specimen

The fatigue test was performed using Instron 8501 fatigue test machine. The stress range was chosen to be 30 MPa to 300 MPa using a load range of 0.4 kN to 4.2 kN. This meant that we were loading the specimen up to the yield stress of the material (Figure 6.3 (a)). From Figure 6.3 (b) we estimated the expected fatigue life for the specimen under these loading conditions to be about 5000 cycles. The actual specimen ruptured at about 6000 cycles. Figure 6.4 shows a picture of butterfly cracks at the hole.

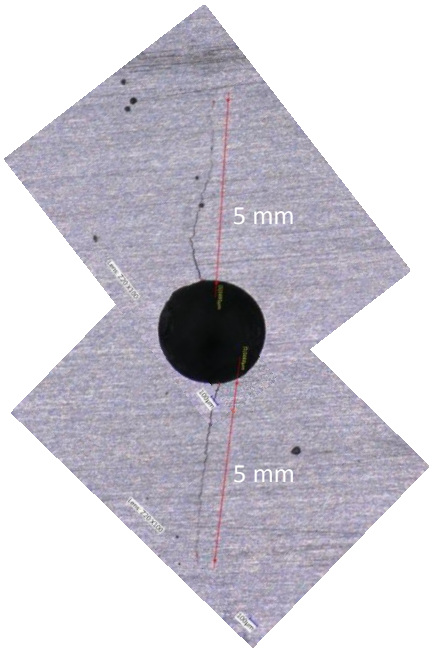

Figure 6.4: Butterfly crack at the hole after fatigue loading at yield stress

From Figure 6.5(a) we can see that the acoustic emission signal has trailing train of pulses which is unlike an acoustic emission signal with shorter time durations. Upon analysis of the acoustic emission signal, we found that these acoustic emission signals consist of two main bands of frequencies, around 50 kHz and 200 kHz. From the frequency vs. wavelength plot (Figure 6.5 (b)) we can see that at 196 kHz the wavelength of S0 Lamb wave mode is about 28 mm and for the A0 Lamb wave mode the wavelength at 50 kHz is about 14 mm. For standing waves in a plate with free boundaries the wavelengths should follow the relation

$$w = n\lambda/2 \Rightarrow \lambda = 2w/n; \qquad n = 1, 2, 3, \ldots \tag{6.1}$$

where w is the width of the specimen and λ is the wavelength of the standing wave. Thus, for $n = 1, 2$, we get $\lambda = 28\,\text{mm}\,\text{and}\,14\,\text{mm}$, respectively. Therefore, the acoustic emission signal is obscured by standing Lamb wave modes across the width of

the specimen. To identify features of a crack from acoustic emission, it is important to minimize the effects of the boundary reflections on acoustic emission signals.

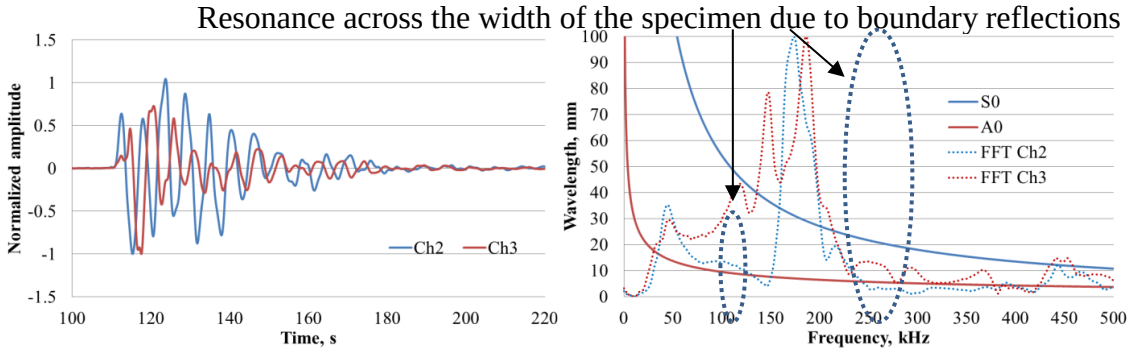

(a) (b)

Figure 6.5: (a) Typical acoustic emission signal received during fatigue test (b) wavelength vs. frequency plot of Lamb waves and acoustic emission signal received in frequency domain

6.2.2 Prediction of Acoustic Emission Signals Using Simulation

For initial analysis, we used analytical wave propagation simulation in plates to predict acoustic emission signals. For the simulation, we assumed that the specimen is under pure tension and the crack growth is symmetric with respect to the thickness of the plate. Therefore we also assumed symmetric emission of acoustic energy across the plate thickness (Figure 6.6).

We modified an existing analytical tool, Wave Form Revealer 2D (WFR2D), to predict acoustic emission events (Figure 6.7 (a)). To simplify the problem, we further assumed that there is only one source of acoustic emission at the center of the hole and we neglected the effects of boundary reflections. We also considered only S0 mode of Lamb waves to represent acoustic emission signal. We added several different wave sources in WFR2D such as square pulse, rectangular pulse, and modulated/unmodulated

sinusoidal pulse as the choice of the excitation. The duration of the pulse is also controllable as the duration of the acoustic emission event may vary.

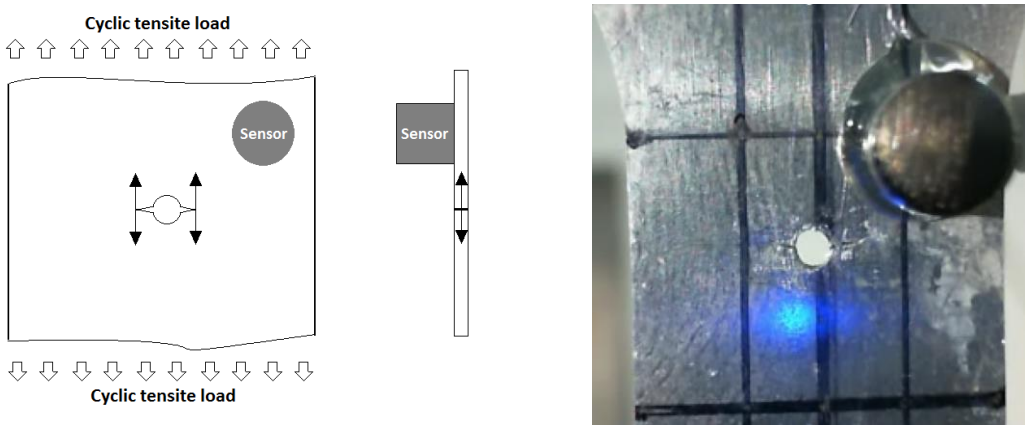

(a) (b)

Figure 6.6: (a) Schematic of the fatigue crack growth (b) fatigue crack growth in the actual specimen

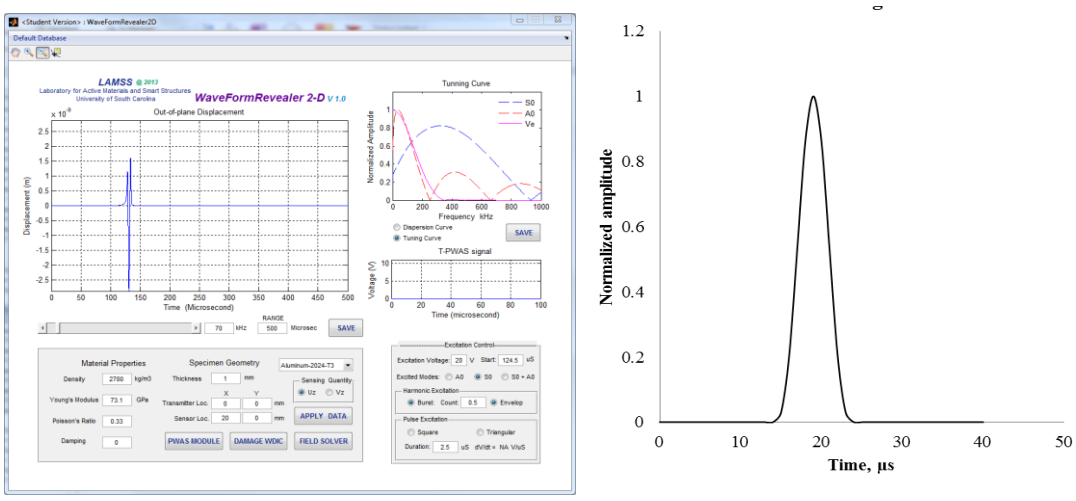

(a) (b)

Figure 6.7: (a) Analytical tool, acoustic emission predictor (b) chosen excitation pulse

As discussed earlier, due to the boundary reflections, we considered only the first pulse in the recorded acoustic emission signal for comparison with our analytical simulation. We chose the excitation pulse to be Hanning window modulated half cycle sine wave and compared the out of plane displacement with the signal recorded during

experimental. Figure 6.8 shows that the assumption of this pulse type gave us a good estimation of the initial part of the acoustic emission signal received.

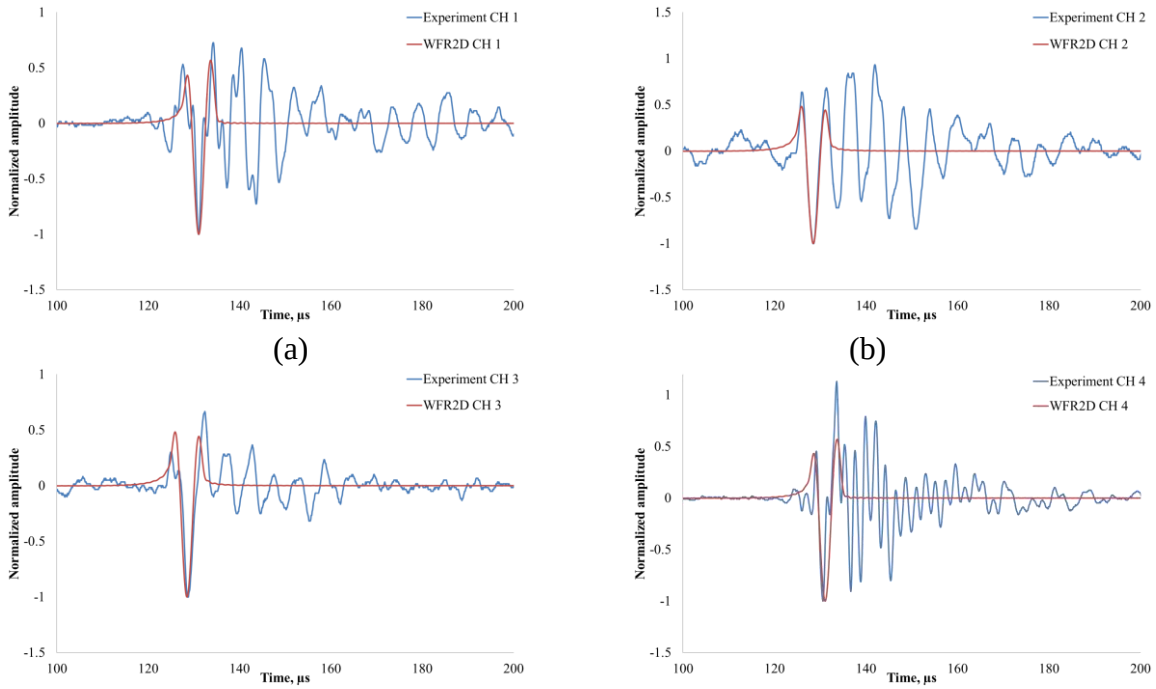

Figure 6.8: Comparison of out of plane displacement predicted by acoustic emission predictor and experimental result

However, this simulation is not sufficient to capture the source characteristics because it involved some major assumptions about the source of acoustic emissions and the recorded signal. Assumptions about the recorded signals are: only the first pulse contains the acoustic emission related information from the source and the sensor is a point sensor. Since our aim is to predict acoustic emission as a source of wave propagation in plate structure, we need more detailed modelling of the acoustic emission source. Therefore, we used FE analysis to understand various types of acoustic emission sources in plate structure.

6.2.3 FEM Modeling of Acoustic Emission Source

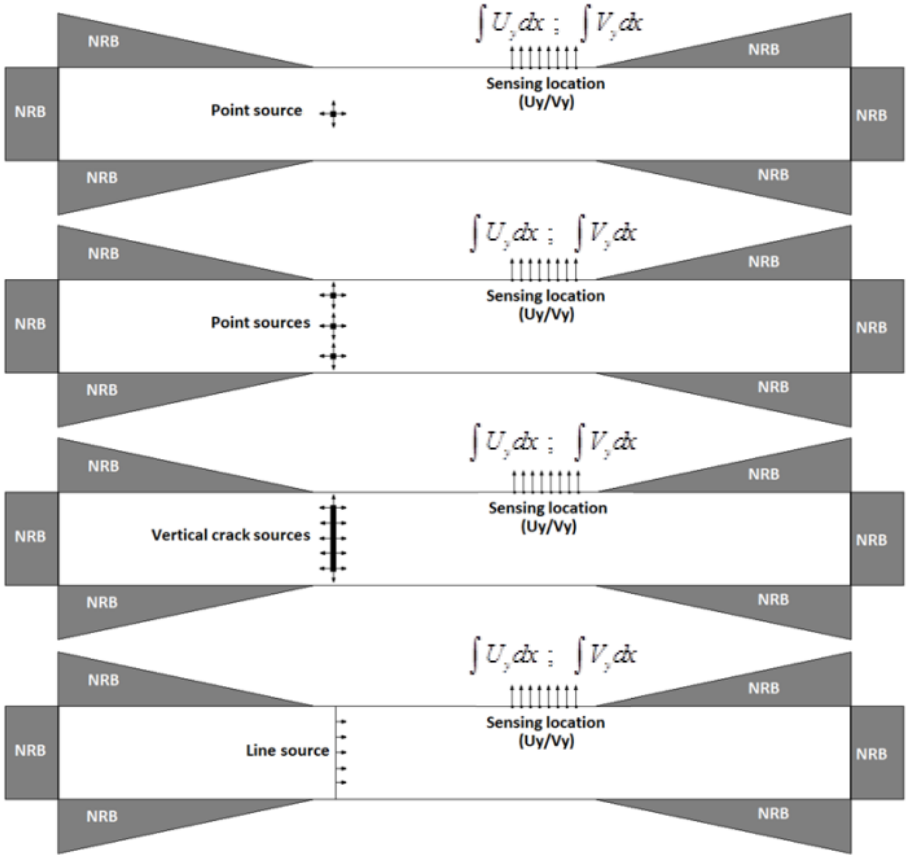

Figure 6.9: Different FE models for different types of acoustic emission sources

In this study, we modeled several different types of acoustic emission sources using FE analysis as show in Figure 6.9. We used 2D FE model to develop our understanding. To achieve a transient response without boundary reflections from a finite dimensional model, we used non reflective boundary (NRB) at both ends of the model and eliminated the boundary reflections. The NRBs were created using COMBIN14 spring damper element. These elements were arranged at the top and bottom surfaces of the NRBs and also at both the ends. The damping coefficients of the elements were varied gradually in a sinusoidal pattern starting from zero (Figure 1.12). This eliminated all reflections from the edge of the NRB itself. We simulated emission of acoustic energy

due to nucleation of cracks. We modeled different types of cavities to represent the gradual formation of a crack (Figure 6.9). To simulate an acoustic emission event, we induced nodal displacements around the cavities symmetrically as shown in Figure 6.9. To incorporate the finite sensor effects we integrated the sensed parameter over the sensor area (Figure 6.9).

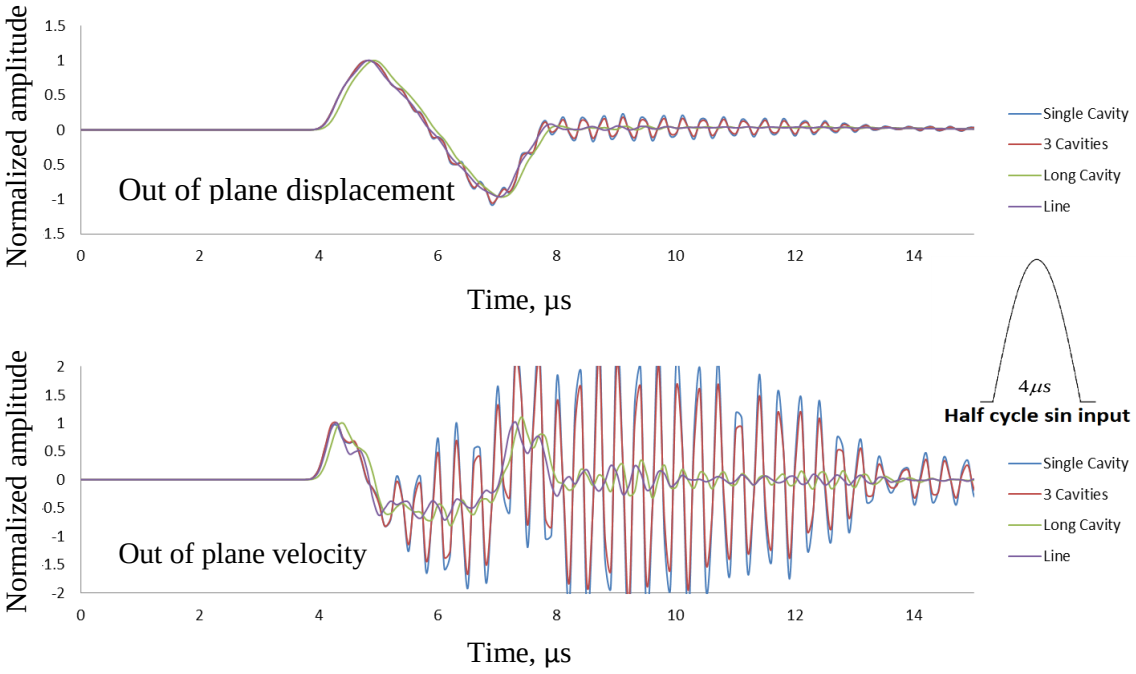

Figure 6.10: Comparison of different types of acoustic emission sources at 26 mm from sensor

From Figure 6.10, we can see that the single cavities create lot of ripples after the initial pulse. This is due to multiple reflections from many sources between the two plate surfaces. As the number of single cavities increases these ripples coalesces; for a long cavity, as we can see in Figure 6.10, these ripples are absent. Therefore as the damage forms from single cavity to multiple single cavities across the thickness coalescing into a long cavity and eventually into a through thickness crack, the acoustic emission from these sources will also coalesce. Since the transition of a single cavity to a through

thickness crack will happen in a time scale much shorter than the time scale of the acoustic emission detection, we can assume the acoustic emission source to be a through thickness crack. We can also see that for a through thickness type source we do not see ripples.

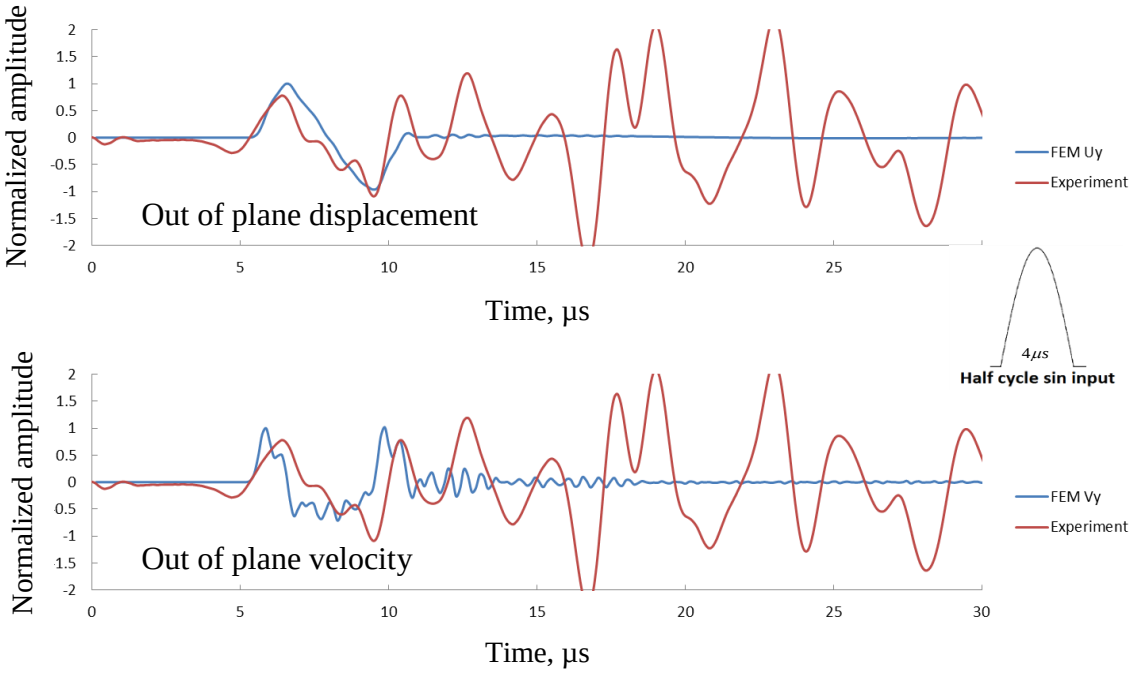

Figure 6.11: Comparison of FEM and experiment assuming a line source at 26 mm from sensor

Assuming a line source, we compared the out of plane displacement and velocity obtained from FE analysis with the experimentally recorded acoustic emission signal. From Figure 6.11, we can see that the out plate velocity for a line source assumption gives a closer estimate of the shape of the signal for first couple of pulses than out of plane displacement. However, none of them truly represent the experimentally obtained signal. One of the reasons for this is that in our 2D FEM model we ignored the fact that the acoustic emission source is located at the tip of a crack. The presence of the crack will modify characteristics of the acoustic emission source which cannot be captured with a

2D FEM. The acoustic emission source will also produce non-propagating Lamb wave modes which cannot be predicted by WFR2D as it assumes propagating Lamb wave modes only. Though WFR2D predicts wave propagation in a 3D plate assuming a point source, it cannot capture the effect of the crack

As shown in Figure 6.12, the displacement field near the source will contain both propagating and non-propagating Lamb wave modes. The non-propagating modes will die out away from the source and only the propagating modes will exist. For a long cavity type source with thickness wise symmetric excitation and frequencies below 1.5 MHz, the propagating Lamb wave mode away from the source will be S0 mode. The mode shape for 500 kHz will be as shown in Figure 6.13.

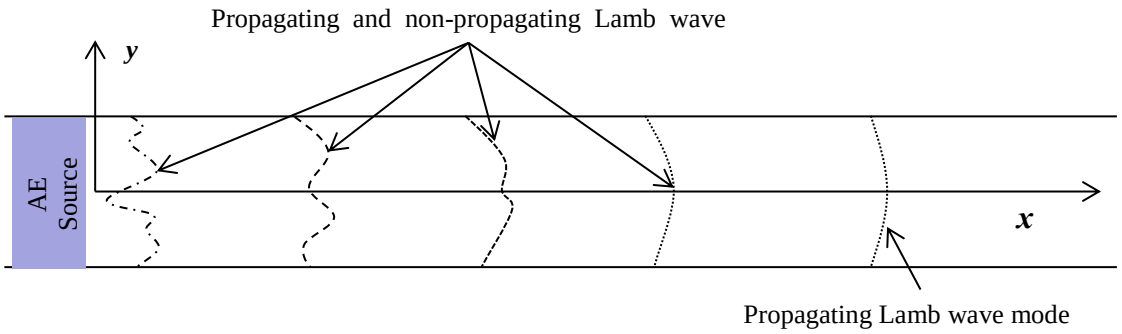

Figure 6.12: Schematic diagram of acoustic emission converging into a propagating Lamb wave mode

To understand how the displacement pulse converges into Lamb wave modes we studied mode shape convergence across thickness using FEM for a long cavity type source.

Based on the mode shape of S0 Lamb wave mode shown in Figure 6.13, we can see from Figure 6.14 that the displacement field across the thickness of the plate converges to that of the S0 Lamb wave mode after about 100 mm. So, if the sensor is less

than 100 mm away from the source of acoustic emission, then the received signal will have significant contribution from the non-propagating Lamb wave modes; therefore cannot be simulated using WFR2D without the inclusion of non-propagating modes.

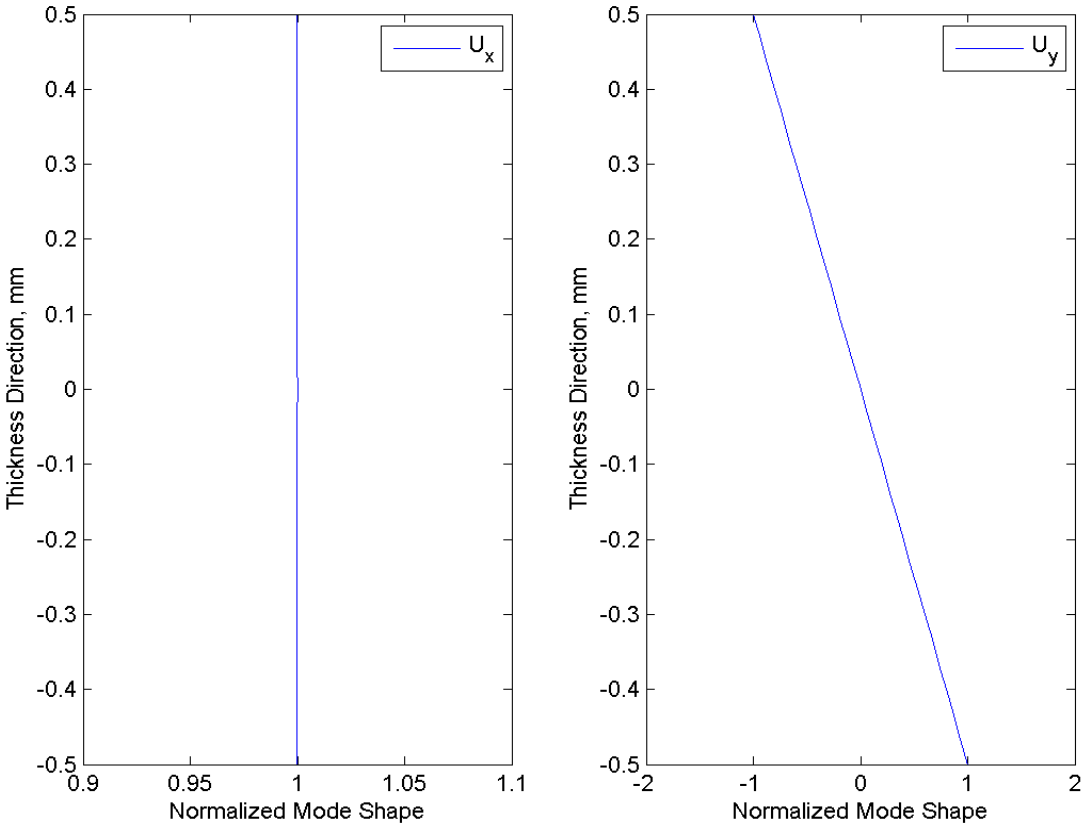

(a) (b)

Figure 6.13: (a) In plane and (b) out of plane displacement mode shape of S0 Lamb wave mode at 500 kHz for 1 mm thick Aluminum

For analytical simulation of acoustic emission source for prediction of resulting wave field (both near field and far field), we need to use CMEP which can capture the effects of the non-propagating complex modes. However, for successful implementation of CMEP we need to incorporate the boundary conditions at the crack tip as the crack propagates. This approach has two main hurdles: first, it requires us to extend CMEP formulation for circular crested Lamb waves and their interactions with cracks; second, simulation of acoustic emission due to crack propagation will require in depth

understanding of the changing boundary condition at the moving crack tip and its implementation in CMEP. This study is beyond the scope of this dissertation. Since this dissertation is focused on crack identification and characterization from acoustic emission, we used 3D FE analysis instead of CMEP to simulate acoustic emission.

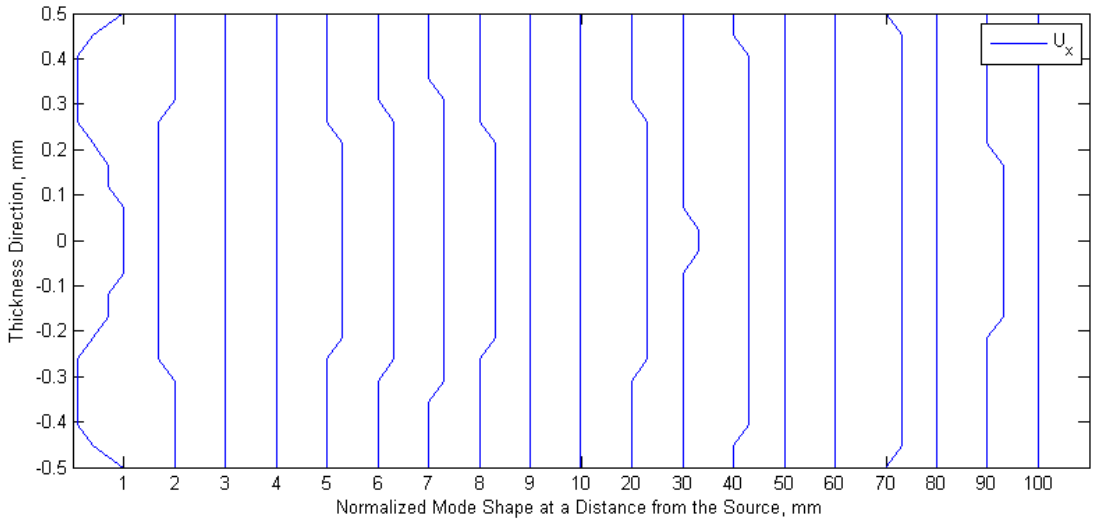

(a)

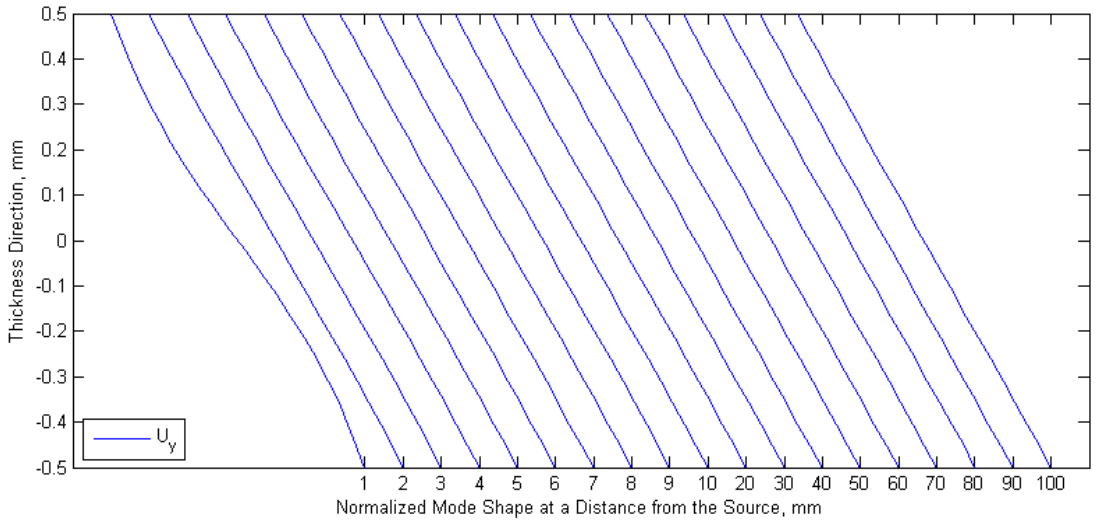

(b)

Figure 6.14: Convergence of mode shape in to S0 Lamb wave mode shape for long cavity type source; (a) in-plane displacement and (b) out of plane displacement

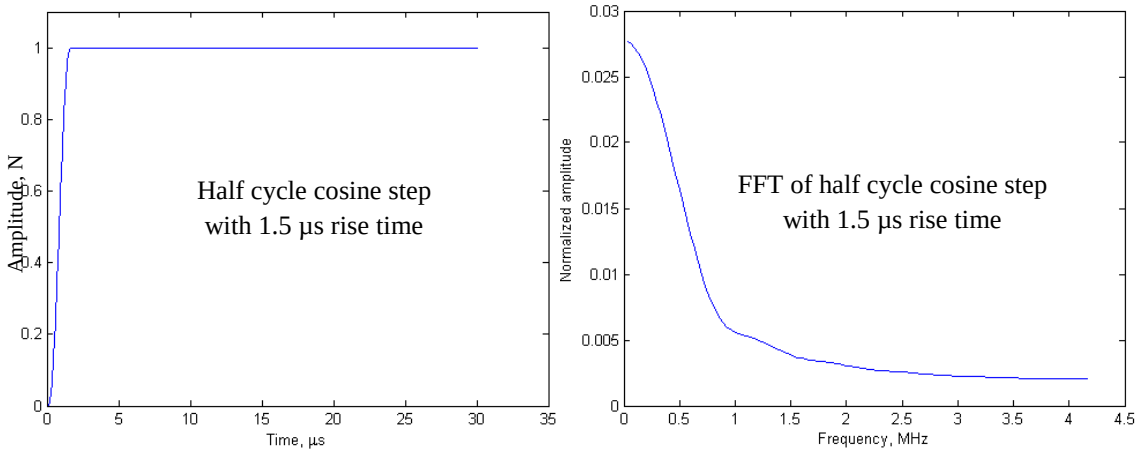

(a) (b)

Figure 6.15: (a) Time and (b) frequency characteristics of dipole as acoustic emission source

Dynamic finite-element modeling requires that the element size must be smaller than the smallest wavelength of interest, and the time step must satisfy a stability condition called the Courant-Friedrichs-Lewy (CFL) condition. In our case the CFL condition required the time step to be less than the time required for the bulk longitudinal wave to traverse a single element. This means smaller element size will require smaller the time step.

Due to limitation on simulation capability, we chose element size of 0.25 mm for our simulation. For AL2024T4 with bulk longitudinal wave speed of 6.2 mm/µs, we needed a time step of 40 ns or less to satisfy the CFL condition. But, because of limitation on computational resources, we were able to simulate at $\mathrm{CFL} = 3$ for the source rise time of 1.5 µs with half cycle cosine (Figure 6.15). Following Hamstad et al.(Hamstad, O'Gallagher, and Gary 1999), this also gave us minimum wavelength $\lambda_m = 4.71$ mm. We used $\lambda/s = 9.4$, $\lambda/cs = 18.8$, $D/s = 40$ (where, *s*, *cs*, and *D* are element size, dipole size and the distance between the source and sensor) which

according to Hamstad et al. (Hamstad, O'Gallagher, and Gary 1999) should give satisfactory result for acoustic emission simulation.

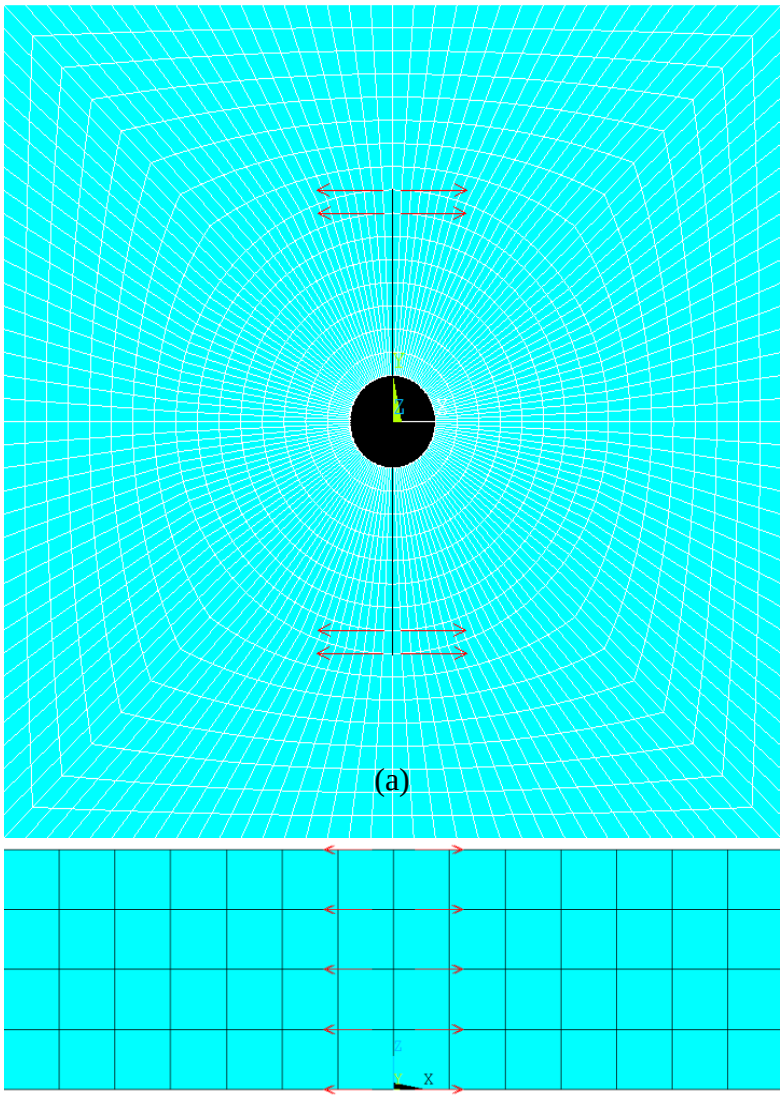

Figure 6.16: (a) Dipoles at crack tips for simulation of acoustic emission due to crack growth; (b) distribution of dipoles across the thickness of the plate

To create a 3D FEM model of a fatigue crack in a plate, we idealized a fatigue butterfly-crack in our specimen shown in Figure 6.4. We assumed crack surfaces to be perpendicular to the plate surface and radiating outwards from the hole. We have also assumed crack surfaces to be stress free. We placed the acoustic emission sources at the

tips of the cracks. We modelled the acoustic emission source as equal strength dipoles distributed across the thickness of the plate (Figure 6.16).

By incorporating a temporal variation of the dipole strength, we simulated generation of acoustic emission from the crack tips. As mentioned earlier, following Hamstad et al.(Hamstad, O'Gallagher, and Gary 1999), we used the temporal variation of the dipole strength as a cosine bell curve with 1.5 μs rise time.

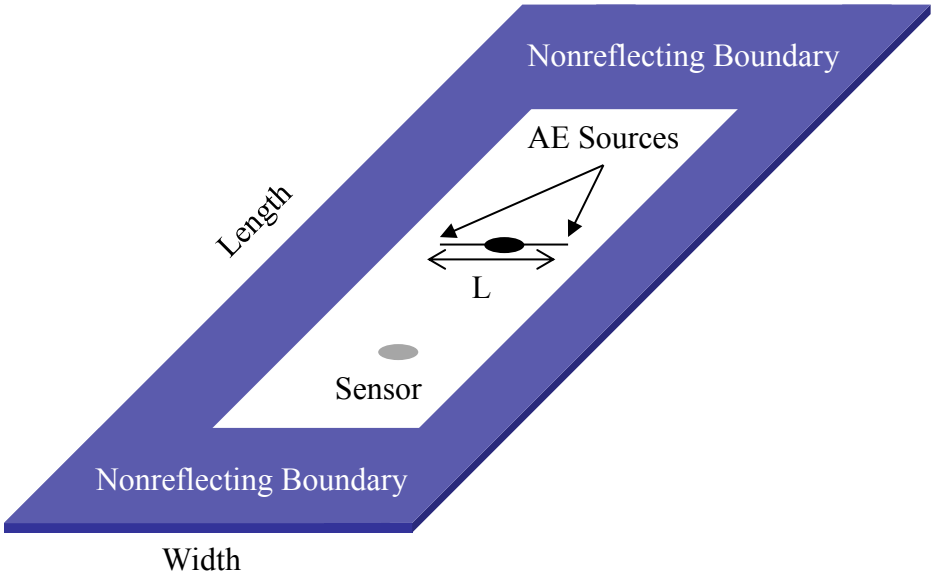

Figure 6.17: Schematic diagram of 3D FE model for AE from crack tips

Figure 6.17 shows a schematic diagram of the FEM model created for simulation of acoustic emission in 3D. To minimize boundary reflections from the edges of the FE model, we used non-reflecting boundary (NRB) around the edges. The NRBs were created by adding damping elements on top and bottom surfaces of the plate around the edges along with damping elements at the edge of the boundaries (Shen and Giurgiutiu 2015). The purpose of NRBs is to absorb the incident and reflected wave energies to minimize boundary reflections. Figure 6.18 (a) and (b) show out of plane displacements at 20 mm from the hole along the length of the specimen from FE model without NRB

and with NRB. We can see that the boundary reflections are almost eliminated by the use of NRB. The usefulness of NRB is also clear from Figure 6.19 (a) and (b) which show the time frequency analysis of the displacement plots shown in Figure 6.18.

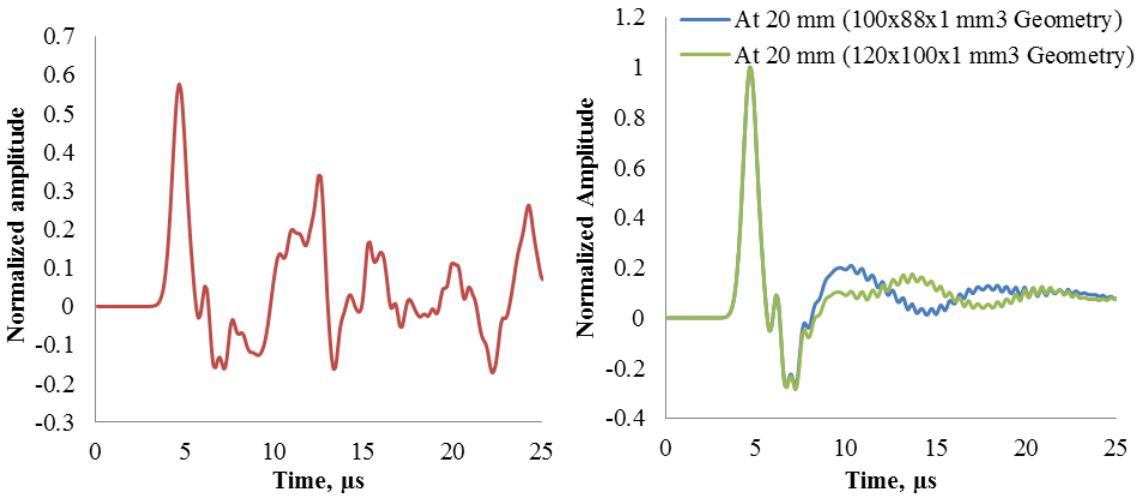

(a) (b)

Figure 6.18: Out of plane displacement at 20 mm from hole (a) without NRB, (b) with NRB

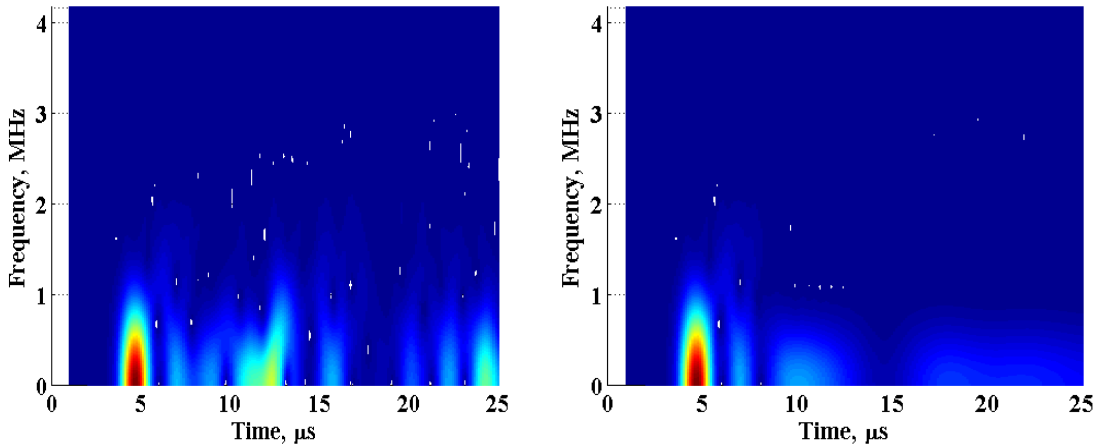

(a) (b)

Figure 6.19: Time-frequency analysis of out of plane displacement at 20 mm from hole (a) without NRB, (b) with NRB

However, the NRBs do not eliminate boundary reflections completely. From Figure 6.18 (b), we can see that the ripples after the arrival of the first acoustic emission

changes as the specimen dimensions are changed. This is the effect of specimen geometry on the acoustic emission signal due to reminiscent boundary reflections. But, these reflections are much smaller than the direct acoustic emission signal and contain only very low frequencies as shown in Figure 6.19 (b). Therefore, we conclude that, even though not perfect, NRBs are very effective in simulating acoustic emission using FE analysis.

To investigate effects of the presence of the butterfly crack, we created another FE model with the identical geometry with no crack as shown in Figure 6.20. We placed the dipoles at the same locations relative to the hole. The purpose of this study was to understand if there is a difference in the acoustic emission signal due to the presence of the crack and if this difference is related to the crack geometry or not.

Figure 6.21 shows the comparison between the out of plane displacement calculated by the two FE models; one is with butterfly cracks and the other is without. From the time variation of the displacements, we can clearly see that there is a significant difference due to the presence of the crack.

Figure 6.22 shows the calculated displacements in frequency domain. We can see that the presence of the butterfly cracks modifies the frequency content of the acoustic emission signal significantly. Therefore, the crack acts as a frequency filter to the acoustic emission. It is apparent that, at least theoretically, a significant difference exists between the crack related acoustic emission and non-crack related acoustic emission.

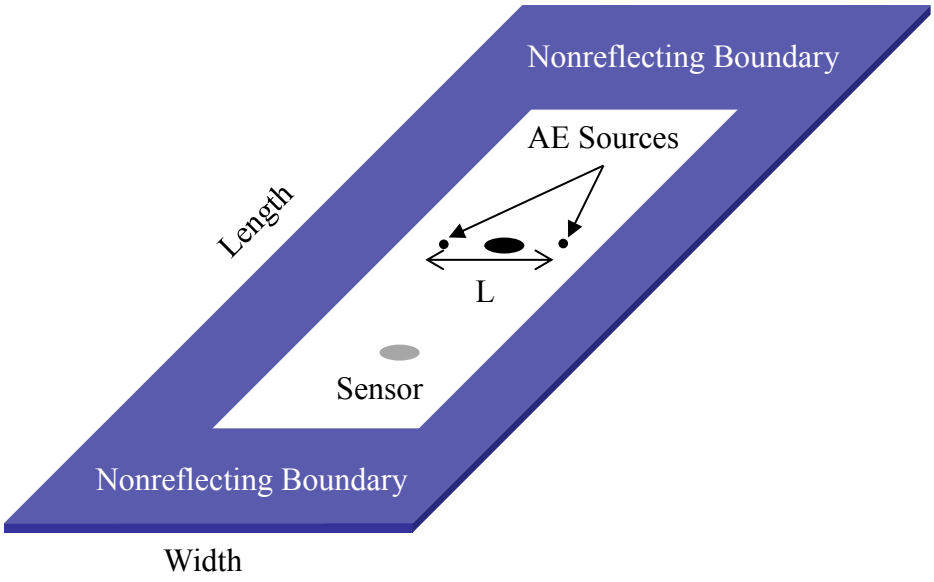

Figure 6.20: Schematic diagram of 3D FE model for acoustic emission from point sources next to a hole

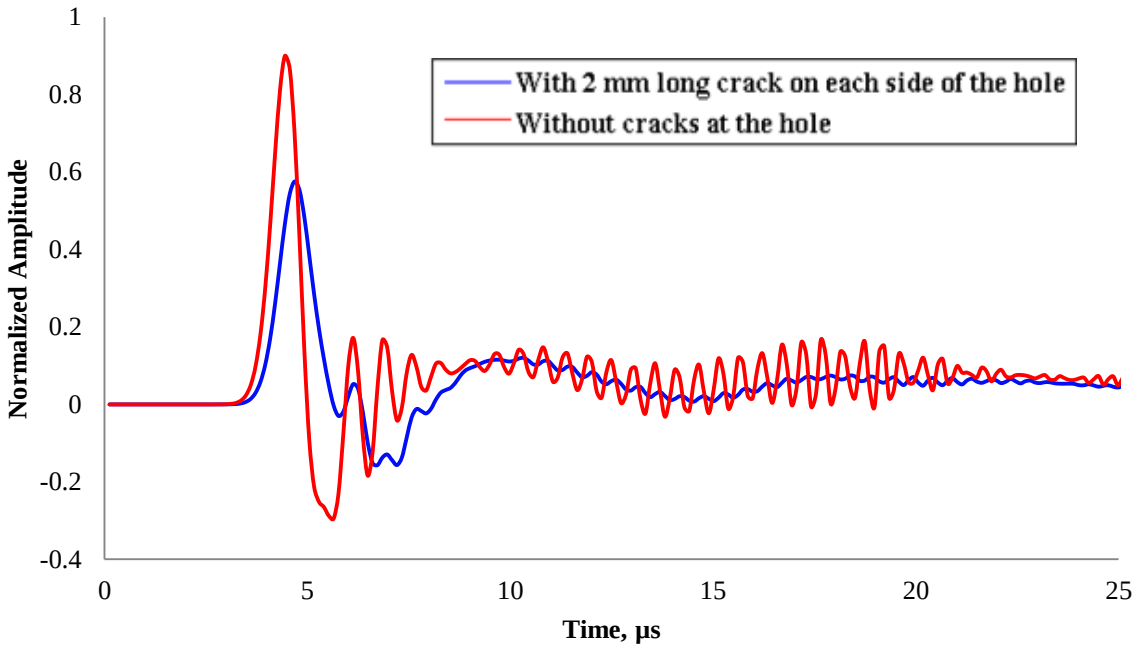

Figure 6.21: Out of plane displacement at 20 mm from hole

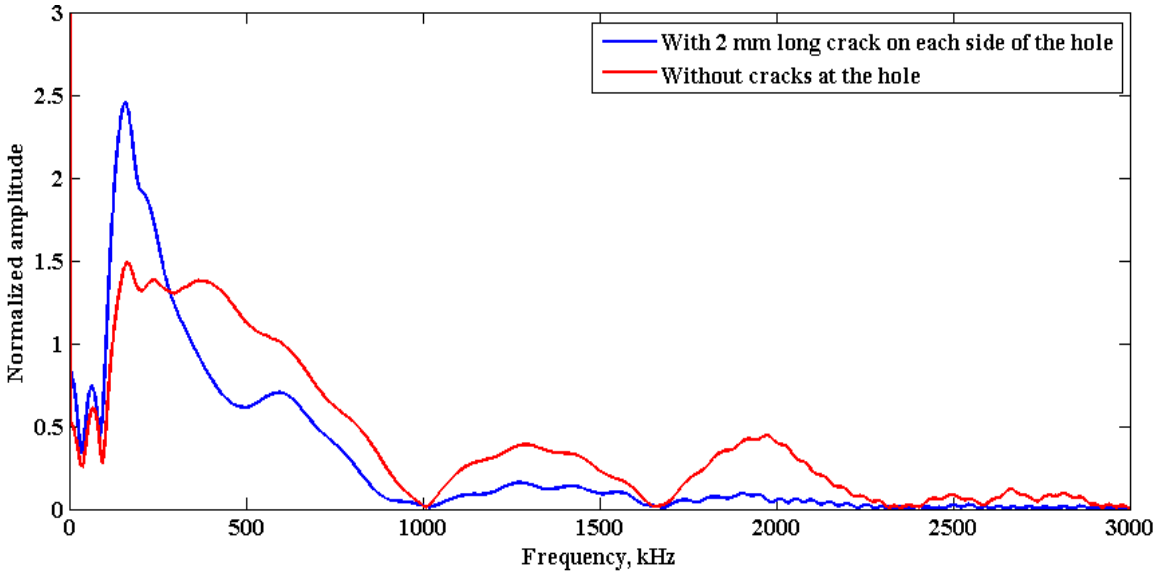

Figure 6.22: Frequency content pf out of plane displacement at 20 mm from hole

6.2.4 Resonance of Fatigue Crack Due to Fatigue Crack Growth

We have seen that the presence of the crack modifies the frequency content to the acoustic emission signal received. Next, we want to investigate if we can extract any crack feature from crack related acoustic emission. We first performed harmonic analysis on our FE models. On the model with crack, instead applying the dipole with time varying dipole strength, we applied frequency varying dipole strength. The aim was to understand the frequency characteristics of the crack vibration. Figure 6.23 shows that due to a harmonic source the crack will undergo resonances in crack-opening type motion. Also, it shows that this resonance frequency will depend on the length of the crack. For example, the fundamental resonance frequency of a 2 mm long crack will be higher than that of a 5 mm long crack; as the crack length increases, the fundamental resonance frequency will decrease.

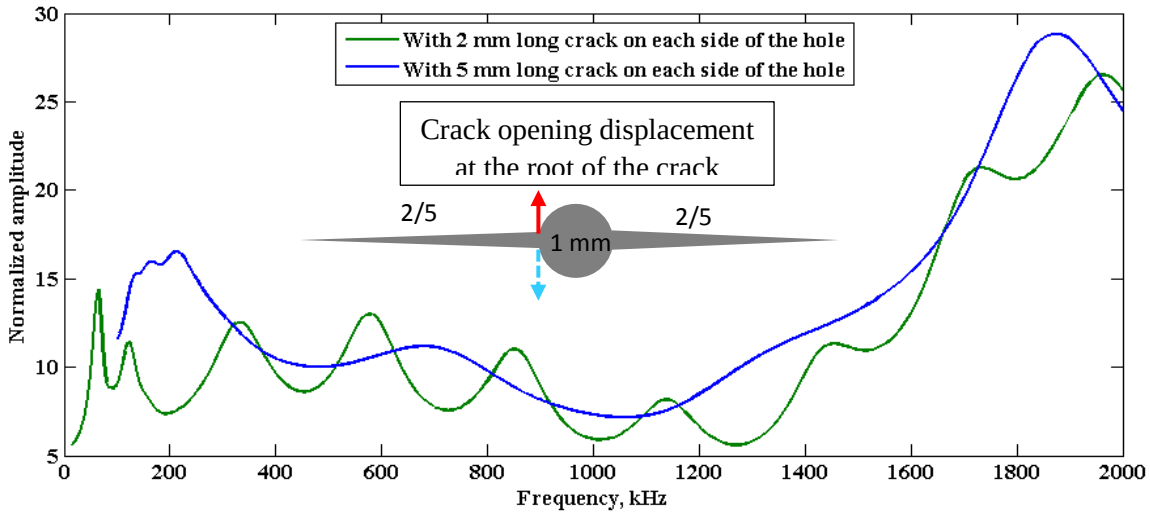

Figure 6.23: Crack opening resonance frequencies from harmonic analysis

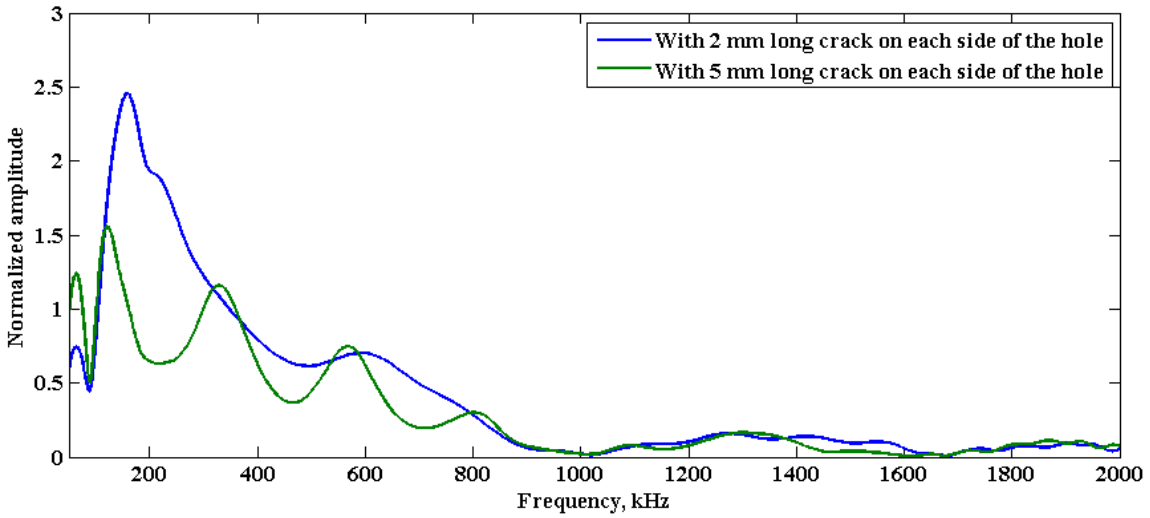

Figure 6.24: Crack resonance captured from an acoustic emission signal measured at a distance

Figure 6.24 shows the frequency content of the simulated acoustic emission in terms of out of plane displacement measured 20 mm away from the hole. We can clearly see multiple resonances from the simulated acoustic emission signal. Upon comparing Figure 6.23 and Figure 6.24, we can see that these resonance frequencies are same as the resonance frequencies associated with the crack opening motion. Therefore, we

confirmed through simulation that a wideband acoustic source located at the tip of a crack causes the crack to resonate and this resonance can be detected from the acoustic emission signal. Since the crack resonance frequency depends on the crack length, theoretically it is possible to detect crack length from this acoustic emission signal.

6.2.5 Experimental Validation of the Resonance Phenomenon

Our aim was to validate the simulation results with a fatigue test experiment. In our fatigue test, when the crack grows, the plate causes acoustic emissions from one of the crack tips. In our simulation, the crack surfaces was assumed to be stress free which is not the case in a fatigue crack. Therefore, to confirm the phenomenon of crack resonance due an acoustic emission source at the tip, we used a slit instead of a fatigue crack. We started with a 1.6 mm thick aluminum plate with 1220 mm in length and 1220 mm in width. We cut a through thickness slit in the plate with diamond cutting disc of 0.25 mm in thickness as shown in Figure 6.25. Then, piezoelectric wafer active sensors (PWAS) were bonded at one of the tips of the slit to emulate an acoustic source.

Two PWAS transducers were bonded at the slit tip on the top and bottom surfaces of the plate. The advantage of using a PWAS in this configuration is in its excitability. We could excite the PWAS transducers in-phase or out-of-phase. However, in our fatigue test, we load the plate under uniform tension which, in our understanding, will cause symmetric type excitation at the crack when the crack grows. Therefore, we excited the PWAS transducers simultaneously in-phase to cause a symmetric excitation. To create a wideband acoustic emission, we excited the PWAS transducers with a voltage pulse as shown in Figure 6.26 (b) and (c).

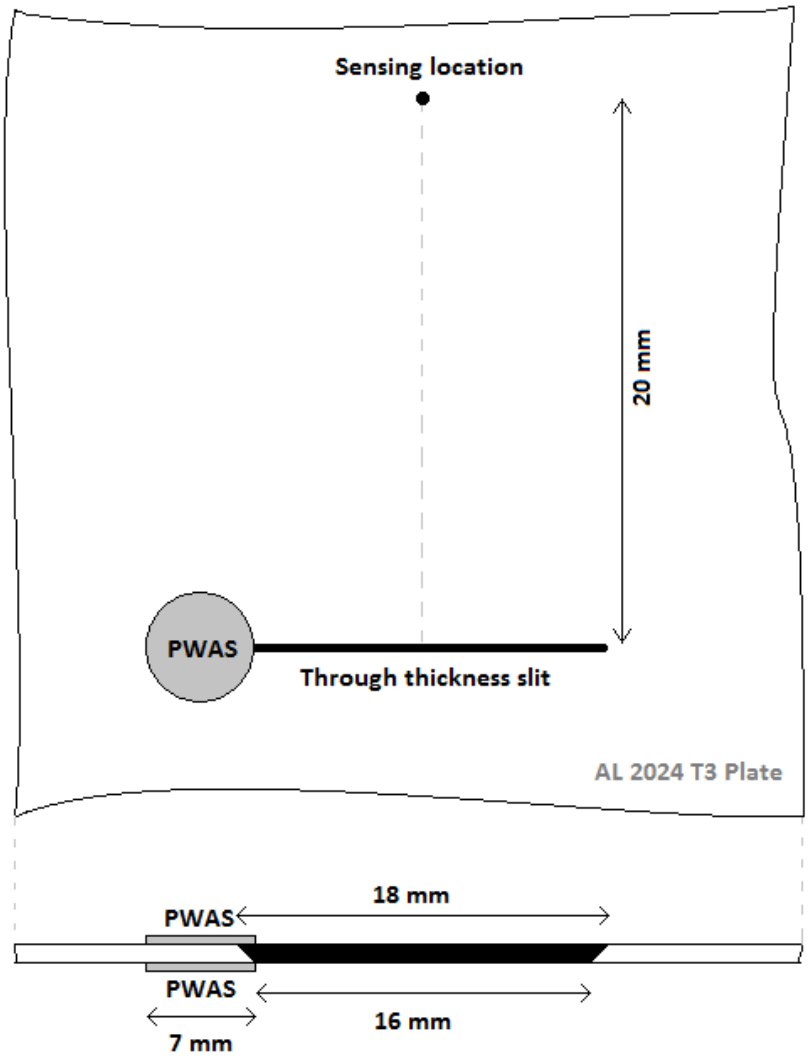

Figure 6.25: Schematic diagram of experiment to detect resonance of a slit caused by an acoustic source at tip

The resulted acoustic emission was measured 20 mm from the slit with a LASER Doppler Velocimeter (LDV). Figure 6.27 (a) shows the frequency domain plot of the measured acoustic emission at 20 mm from the slit; in this figure, we can see multiple peaks which look like resonances. To verify these peaks, we also scanned the area around crack using LDV to visualize the wave field around the crack. This was done by using chirp excitation with synchronized LDV measurement at a large number of points around the slit. This measurement made it possible to visualize resonances of the slit due to the

acoustic emission from PWAS. Figure 6.27 (b)-(e) show the plate surface velocity around the slit measured by LDV at various resonance frequencies. Upon comparison with Figure 6.27 (a), we can clearly understand that the resonance peaks in Figure 6.27 (a) correspond to the resonance at the through thickness slit. This experiment confirms the crack resonance due to acoustic emission from its tip and validates our FE analysis.

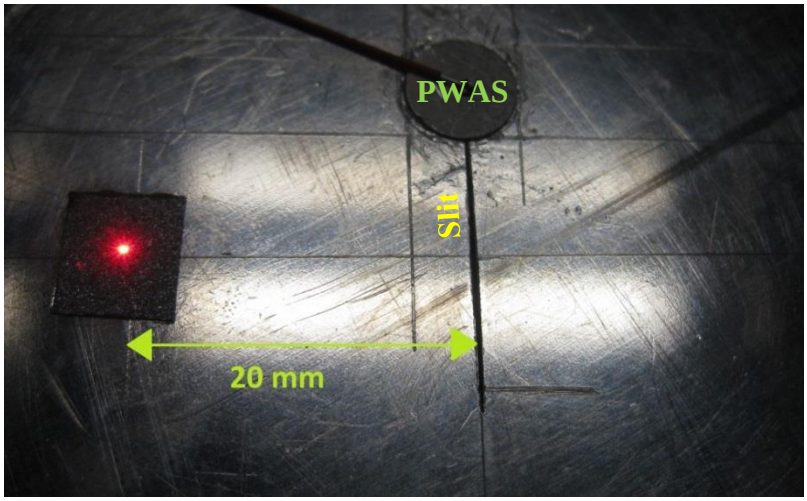

(a)

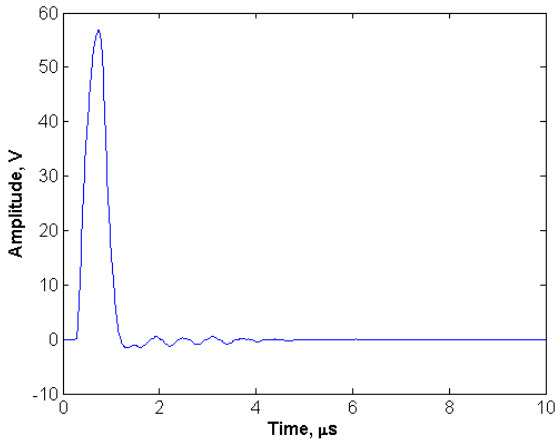

(b)

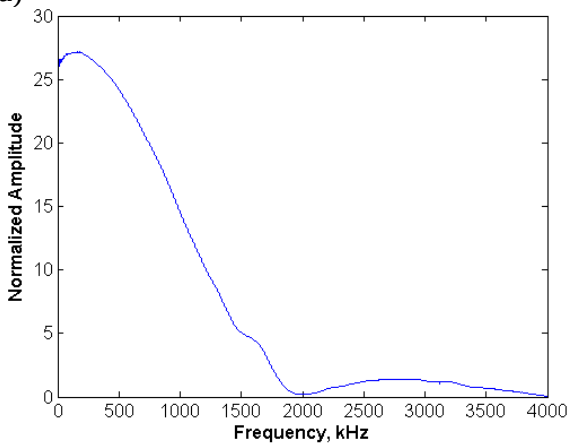

(c)

Figure 6.26: (a) Picture of the specimen with a slit; (b) excitation signal in time domain; (c) excitation signal in frequency domain

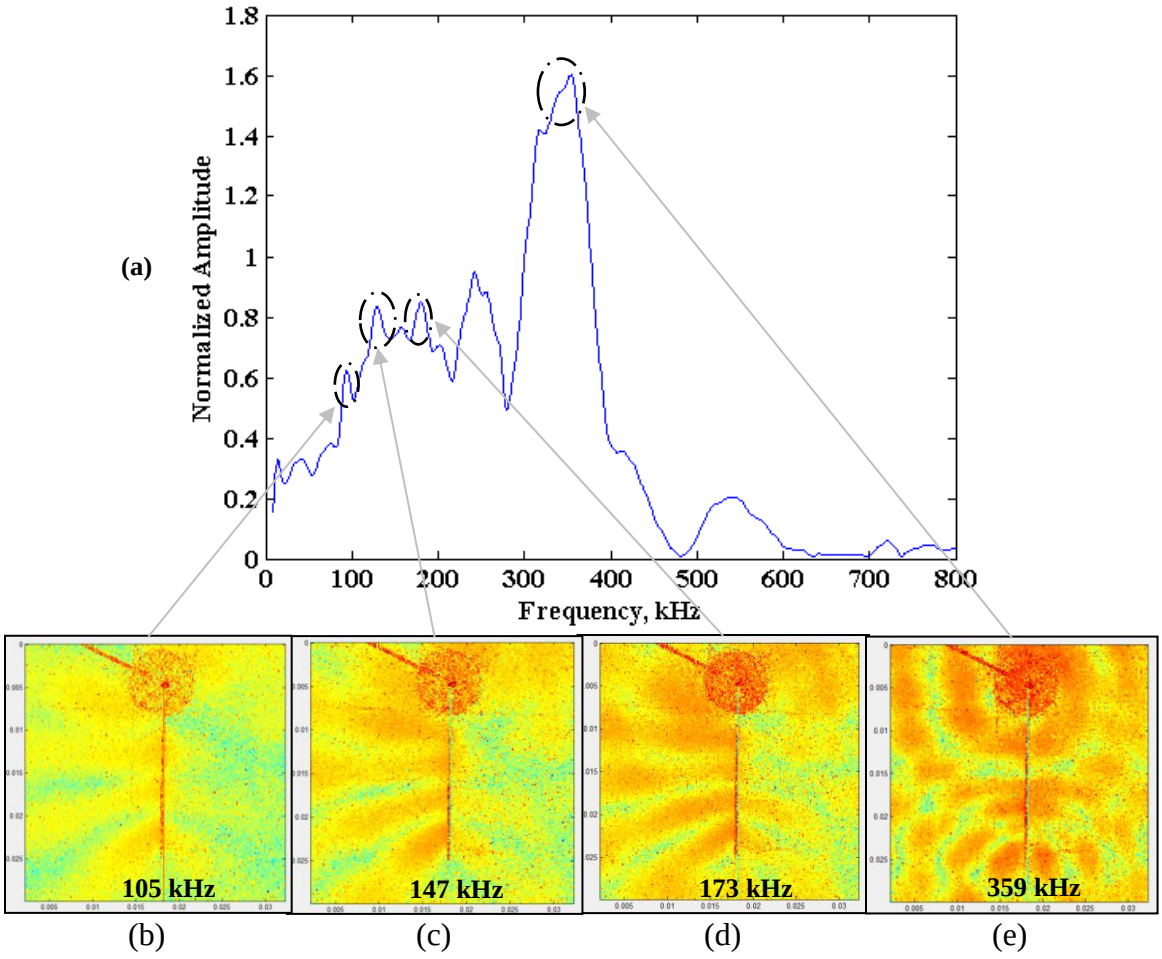

Figure 6.27: Resonance of the slit at multiple frequencies due to acoustic emission from PWAS (a) measured at 20 mm from the slit (b)-(e) area scan results showing standing wave field around the slit

6.3 DETECTION OF FATIGUE CRACK LENGTH FROM ACOUSTIC EMISSION SIGNALS

Section 6.2 proposed and validated the phenomenon of crack vibration due the presence of a wideband acoustic source at the crack tip using FE analysis and experimentation. As acoustic emission is a wideband excitation generally at the crack tip, our aim is to use this phenomenon to detect fatigue crack length from recorded acoustic emission signal. There are two main mechanisms for generation of acoustic emission from a fatigue crack as shown in Figure 6.28. As shown on the left branch of Figure 6.28, one mechanism is when the crack grows and some of the energy at the crack tip is

released in the form of acoustic emission (Moorthy, Jayakumar, and Raj 1996). The other mechanism is depicted on the right branch of Figure 6.28; when the crack resonated due to ambient vibration, the rubbing of the crack surfaces create acoustic emissions (Meriaux et al. 2010). Our main challenge is to detect these acoustic emissions and identify crack resonance from them. We follow the left branch in Figure 6.28.

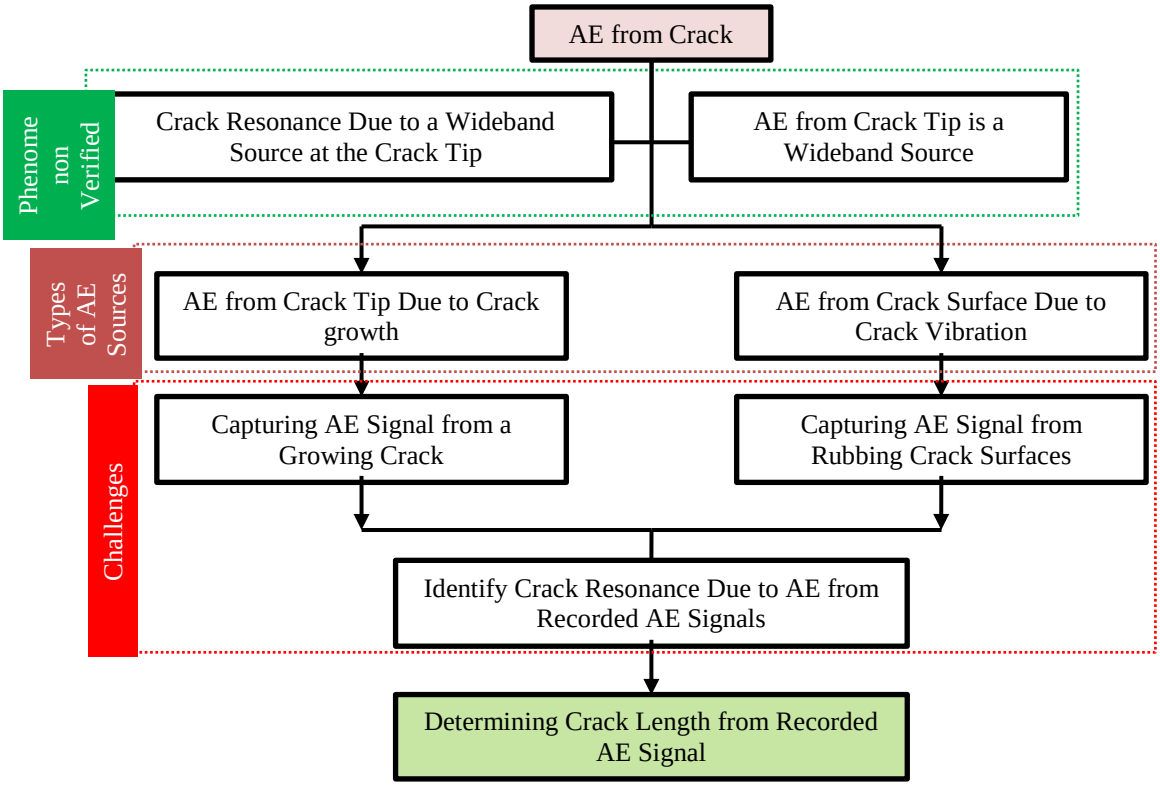

Figure 6.28: Flow chart diagram for detection of fatigue crack length from acoustic emission

6.3.1 Identification of Crack Length from Acoustic Emission Due to Crack Growth

As discussed in section 6.2.1, it is important to minimize the boundary reflections to successfully extract crack information from acoustic emission. We have considered two methods to minimize the effects of boundary reflections: one is by using a wide specimen such that the reflections are farther apart; the other one is by using absorbing material at the boundary to absorb the boundary reflections. Therefore, we used a wider

specimen of 100 mm width with absorbing clay around the boundary (Figure 6.29(a) and (b)).The length of the specimens were 300 mm; a 1 mm diameter hole was drilled at the center for the crack initiation. To minimize the sensor effect on acoustic emission, we used smallest possible sensors available, i.e. the PICO AE sensor from MISTRAS Corp.

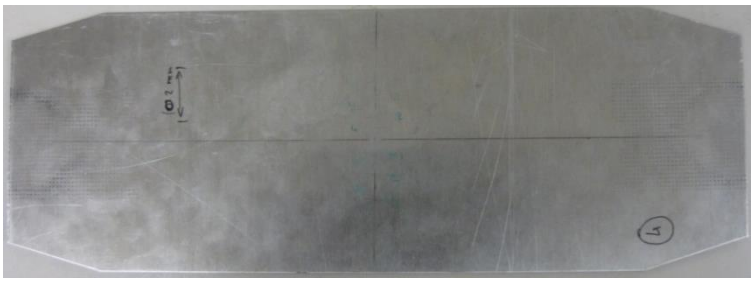

(a)

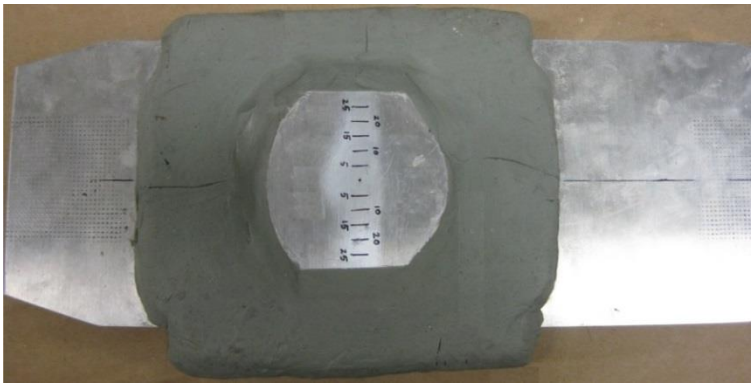

(b)

Figure 6.29: (a) 100 mm wide, 300 mm long, and 1 mm thick specimen (b) absorbing clay boundary to minimize boundary reflections

Conventional acoustic emission sensors such as the PICO sensor are fundamentally resonant sensors. This implies that these sensors have strong resonances around the frequency it is designed for. This is good in general for detection of acoustic emissions even for low energy acoustic emissions. However, these resonating sensors may not be best to detect crack resonances as the signals detected by these sensors are modified by their own dynamics. Therefore, we have used PICO AE sensors along with PWAS sensors for detection of acoustic emissions during fatigue tests.

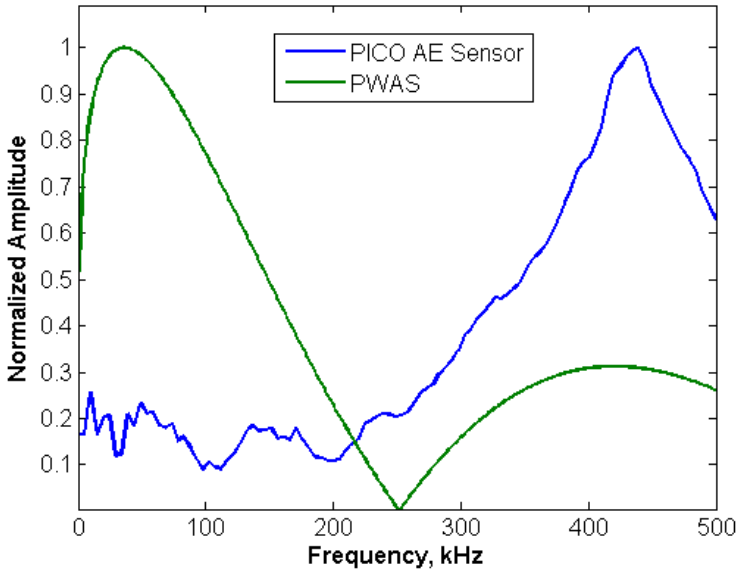

Figure 6.30: Tuning curve of sensors

One advantage of using PWAS is that it senses both in plane and out of plane motion, whereas PICO is predominantly sensitive to out of plane motion. Realistically, any contact type sensors will have its own dynamics which will influence the wave field that it senses. However, from Figure 6.30 we can see that, for out of plane type motion, PWAS is much more sensitive to lower frequencies than PICO because PICO resonated at around 450 kHz. This is advantageous for detection of crack resonances at lower frequencies. However, to verify PWAS as acoustic emission sensor, we used both PICO and PWAS and compared results.

We used pencil lead break (PLB) to emulate acoustic emission in a plate. We bonded a PWAS and PICO on top and bottom surfaces of the plate at the same location in the plate as shown in Figure 6.31 (a). The pencil lead break signals received by the sensors are shown in Figure 6.31 (b). We can see that the frequency content of both signals are quite similar but PWAS has better detection at low frequency. Next, we

bonded two PWAS sensors on top and bottom surfaces of the plate at 20 mm from the hole as shown in Figure 6.32 (a).

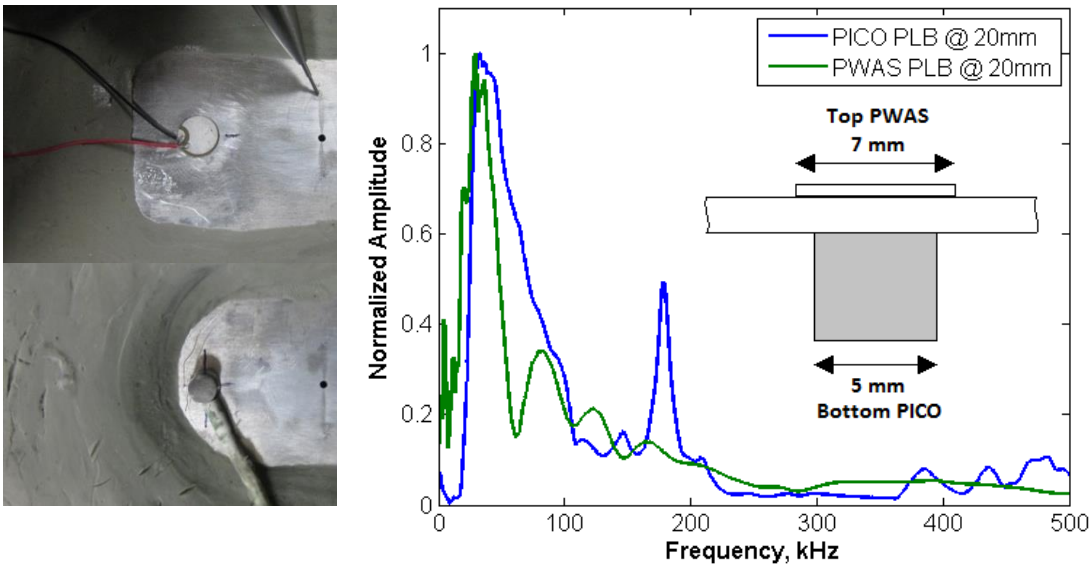

(a) (b)

Figure 6.31: Pencil lead break test for sensor comparison; (a) location of sensors and (b) plots of pencil lead break signals received by both the sensors

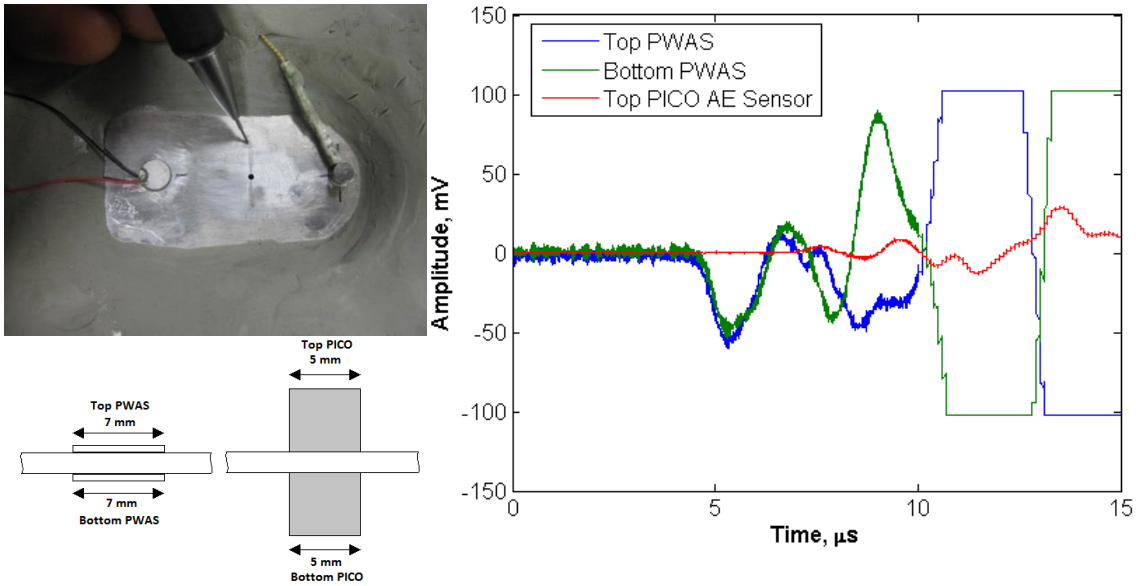

(a) (b)

Figure 6.32: Detection of symmetric and antisymmetric modes in PLB; (a) location of sensors and (b) plots of pencil lead break signals received by both the sensors

Similarly, we bonded two PICO sensors at 20 mm from the hole on the opposite side of PWAS as shown in Figure 6.32 (a). Form Figure 6.32 (b) we can see that the initial part of the pencil lead break signal shows the same response for both the PWAS sensors. This shows that this initial part of the signal corresponds to symmetric Lamb wave modes. However, we do not see this behavior for PICO sensors. This proves that PICO sensors only detect the antisymmetric modes. We should keep in mind that we need both symmetric and antisymmetric modes to successfully detect crack resonances. Therefore, in fatigue tests we relied on the PWAS sensor signal.

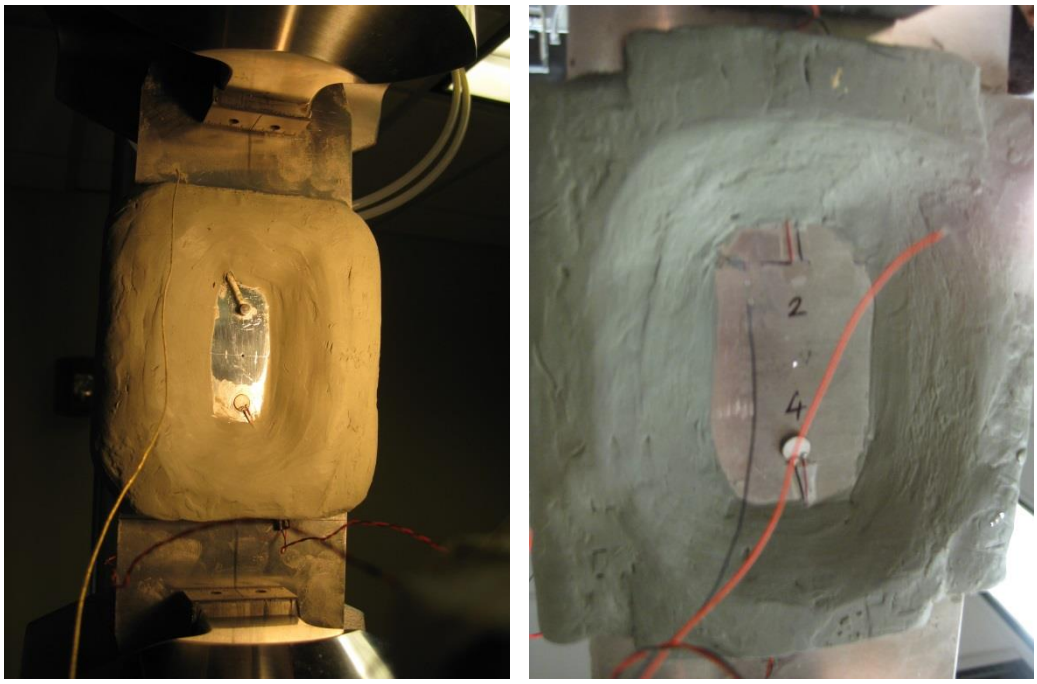

(a) (b)

Figure 6.33: (a)Specimen with PICO and PWAS sensor undergoing fatigue test; (b) PWAS disbonded under high fatigue loading

We mounted the specimen in MTS machine for fatigue testing (Figure 6.33 (a)) and applied cyclic loading between 6.5% and 65% of the yield stress of the material (AL2024T4) to shorten the test duration. First, we bonded PICO AE sensor and PWAS sensors at 20 mm from the center of the hole. Several specimens were tested. On average,

the cracks started growing from the hole after about 23000 cycles and grew to a size of about 10 mm on each side after 30000 cycles (Figure 6.34). However, due to high surface strain, the bonding layer between the plate and the PWAS sensors started cracking from the beginning of the experiment and the PWAS sensors peeled off the plate surface (Figure 6.33(b)). So, most of the acoustic emission received by PWAS in this configuration was due to the bonding layer cracking rather than crack growth in the plate.

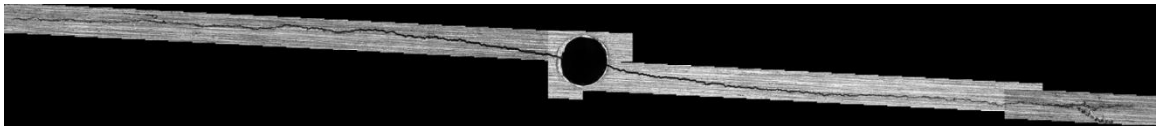

Figure 6.34: 20 mm long fatigue crack after 30000 cycles of loading

To resolve this issue, we conducted the next test in two stages. In the first stage we did not use any sensor or clay boundary on the specimen. Because of which we could use higher frequency (10 Hz to 12 Hz) of fatigue loading to shorten the duration of the test. In the second stage we used absorbing clay to absorb boundary reflections. Because of the fast first stage we could use very low frequency fatigue loading (0.25 Hz) for higher degree of control over the crack growth and still save time. First we grew a long crack in the specimen (Figure 6.34) and then we mounted the PWAS very close to the crack (Figure 6.35). Then, the crack was grown further under low frequency fatigue loading. The reason for such proximity of the PWAS was the surface strains being very low close to a long crack. This ensured that the PWAS bonding on the plate surface did not break and the acoustic emissions detected by the PWAS corresponded to the crack growth.

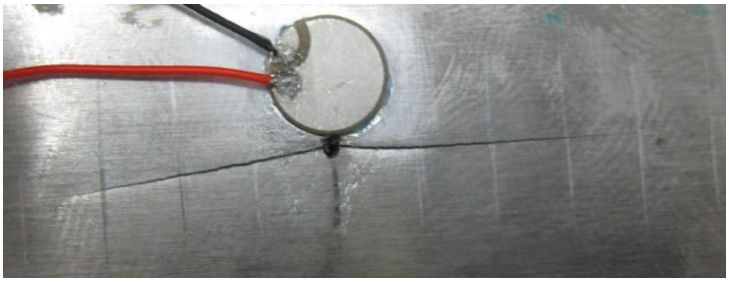

Figure 6.35: PWAS bonded next to a 20 mm long fatigue crack

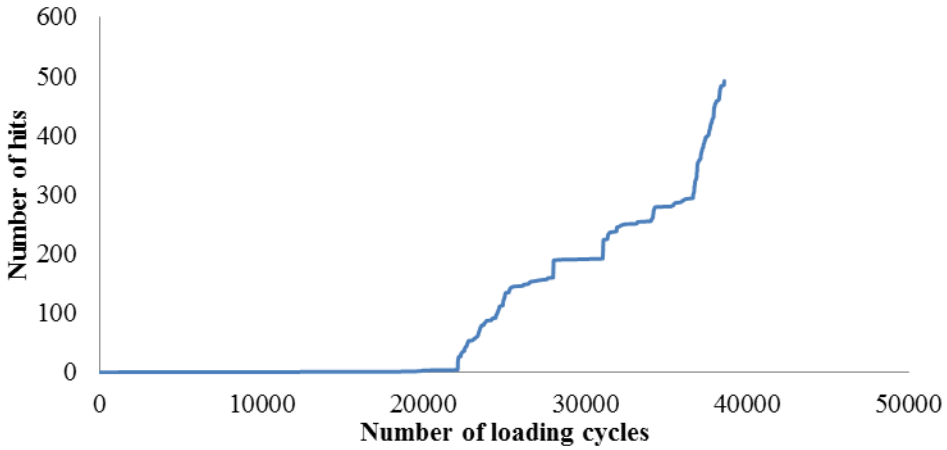

Figure 6.36: Cumulative number of acoustic emission recorded

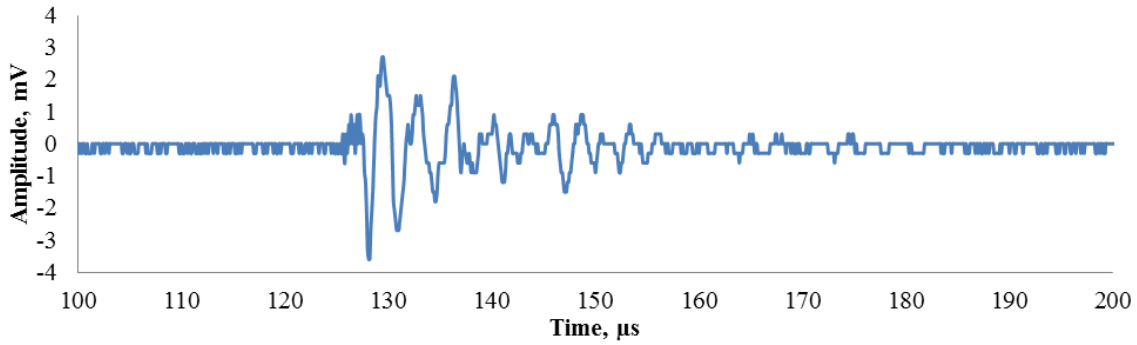

Figure 6.37: acoustic emission detected using PWAS without preamplifier

Figure 6.36 shows accumulative number of acoustic emissions detected by the PWAS. This is consistent with the crack growth rate. As the crack grows longer, the growth rate increases resulting in higher rate of emissions. This can be easily understood from Figure 6.36. However, the recorded signals were very low in amplitude as shown in

Figure 6.37. Since the signal strength is in the same range of the lower limit of the hardware we were not successful in extracting any meaningful frequency information from the recorded signals.

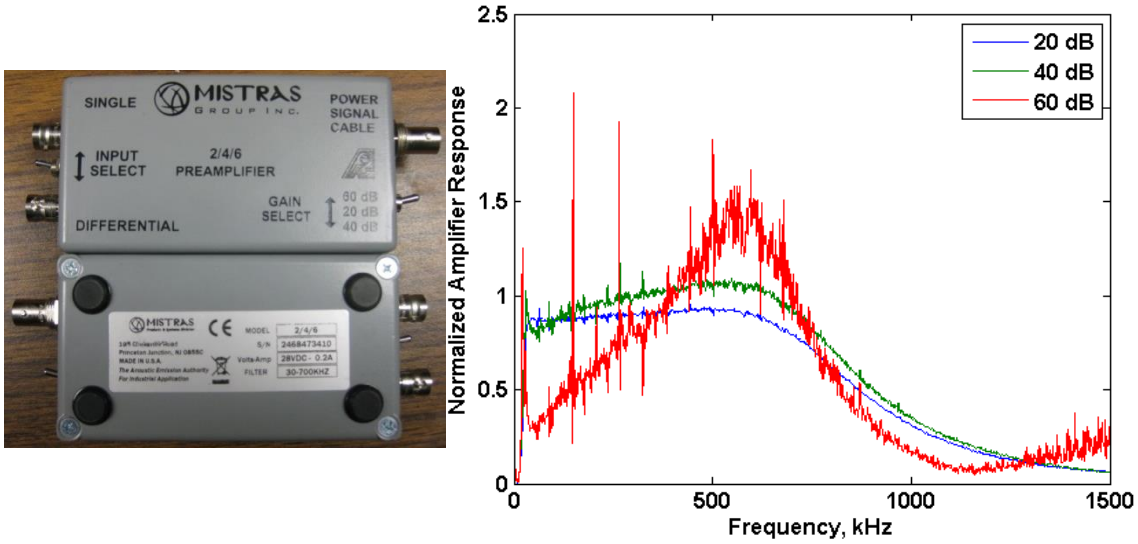

(a) (b)

Figure 6.38: (a) Picture of preamplifiers, (b) frequency characteristics of preamplifier

To alleviate this issue, we used preamplifiers (Figure 6.38 (a)) to amplify the signal detected by PWAS before recording. To ensure the suitability of these amplifiers for our method we determined the frequency characteristics of these amplifiers. We used a wideband input signal (Figure 6.39) to record the response of these amplifiers and compared the response with the input signal in frequency domain to obtain the frequency characteristics of Figure 6.38 (b). From the plot we can see that at 40 dB gain the amplifier response is relatively flat up to about 700 kHz. Therefore, we used these amplifiers at 40 dB gain to amplify the PWAS signal.

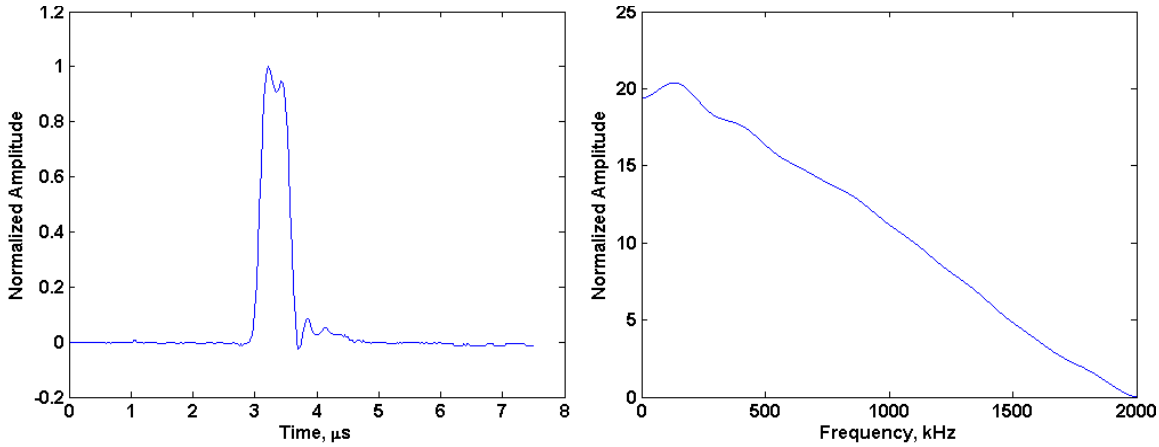

(a) (b)

Figure 6.39: Input signal in (a) time domain and (b) frequency domain

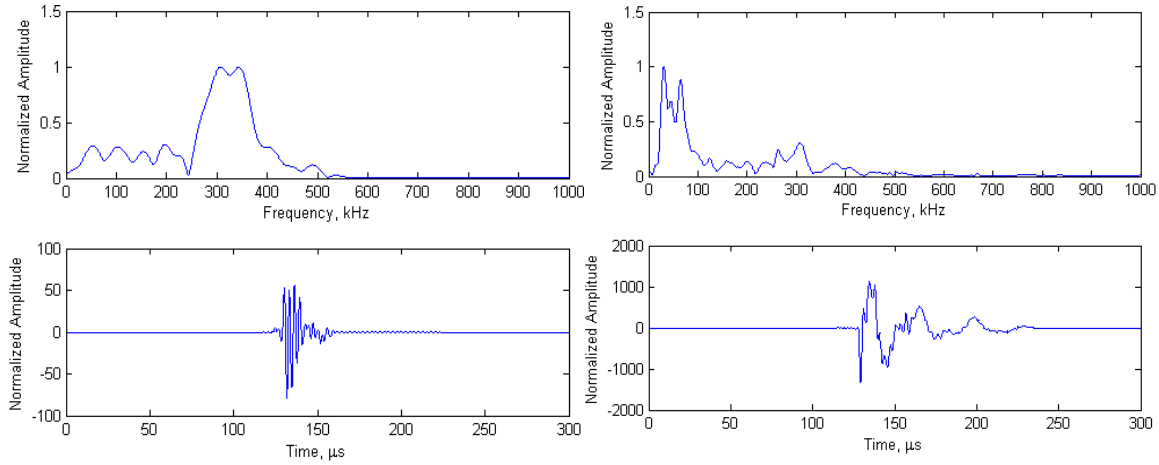

(a) (b)

Figure 6.40: acoustic emission signals received by PWAS: (a) type 1 and (b) type 2

Figure 6.40 shows typical signals received by PWAS related to crack growth. Predominantly we recorded two types of acoustic emission signals type 1 and type 2. If we compare type 1 signals with type 2 signals as shown in Figure 6.40 (a) and (b), we can see that the type 1 signals appears to be non-dispersive and type 2 signals appear to be dispersive. Upon inspecting the tuning curves of PWAS in Figure 6.41 (a) and (b) we realize that the frequency contents of type 1 and type 2 signals are very similar to the tuning curves of PWAS for S0 and A0 modes respectively. Also it is well known fact that

S0 mode is non-dispersive and A0 mode is dispersive at relatively low frequencies. Therefore, we conclude that the type 1 and type 2 signals correspond to the S0 and A0 Lamb wave modes respectively.

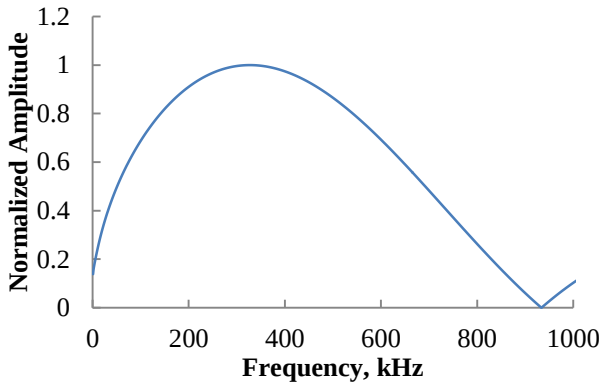

(a)

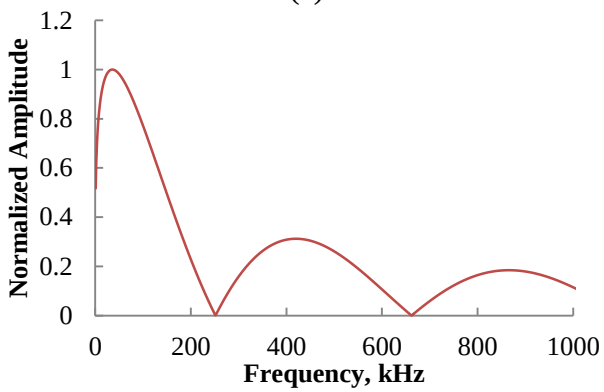

(b)

Figure 6.41: PWAS tuning curve: (a) S0 and (b) A0 Lamb wave mode

A small percentage of signals appeared to contain both S0 and A0 modes (Figure 6.42). However, type 1 and type 2 signals accounted for more than 90% of acoustic emissions recorded with both of these types being present in equal proportions.

All the signals recorded contain noise of specific frequencies appearing as spikes in the frequency plots of the signals. This may be due to the electromagnetic noise generated by the servo-actuators in the MTS fatigue testing machine. This is clearly understood if the analyze the frequency content of the noise in the signal as shown in Figure 6.43. These are received by PWAS sensors as they are not shielded from

electromagnetic noise. We used Hanning window to isolate the meaningful part of the signal from the noise floor then filtered the noise using 8 order low pass Butterworth filter of 800 kHz.

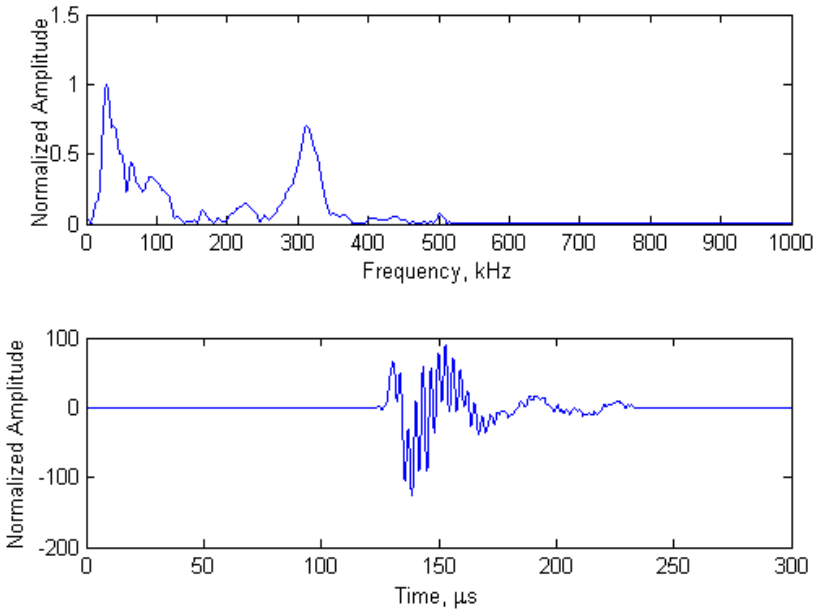

Figure 6.42: PWAS signal of mixed type

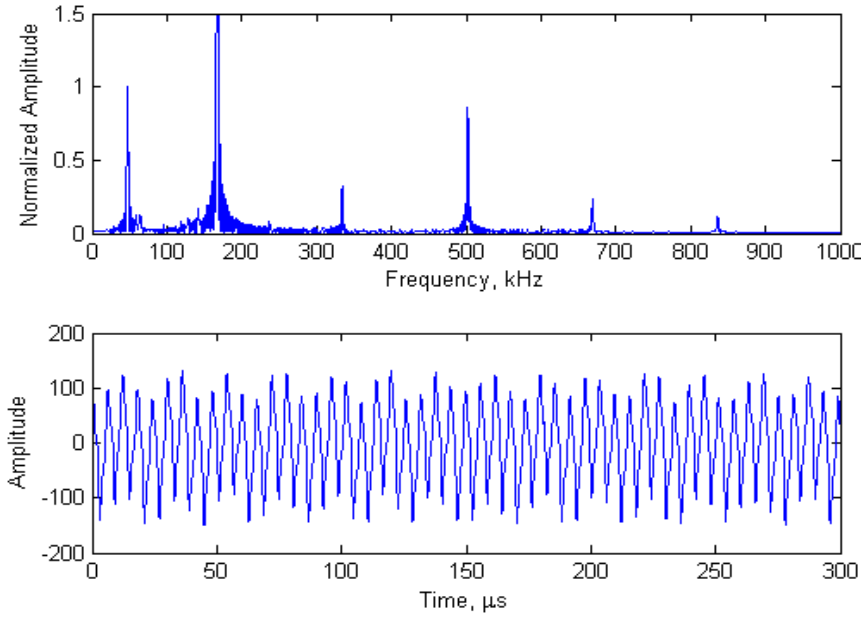

Figure 6.43: Noise due to servo actuation system in MTS machine

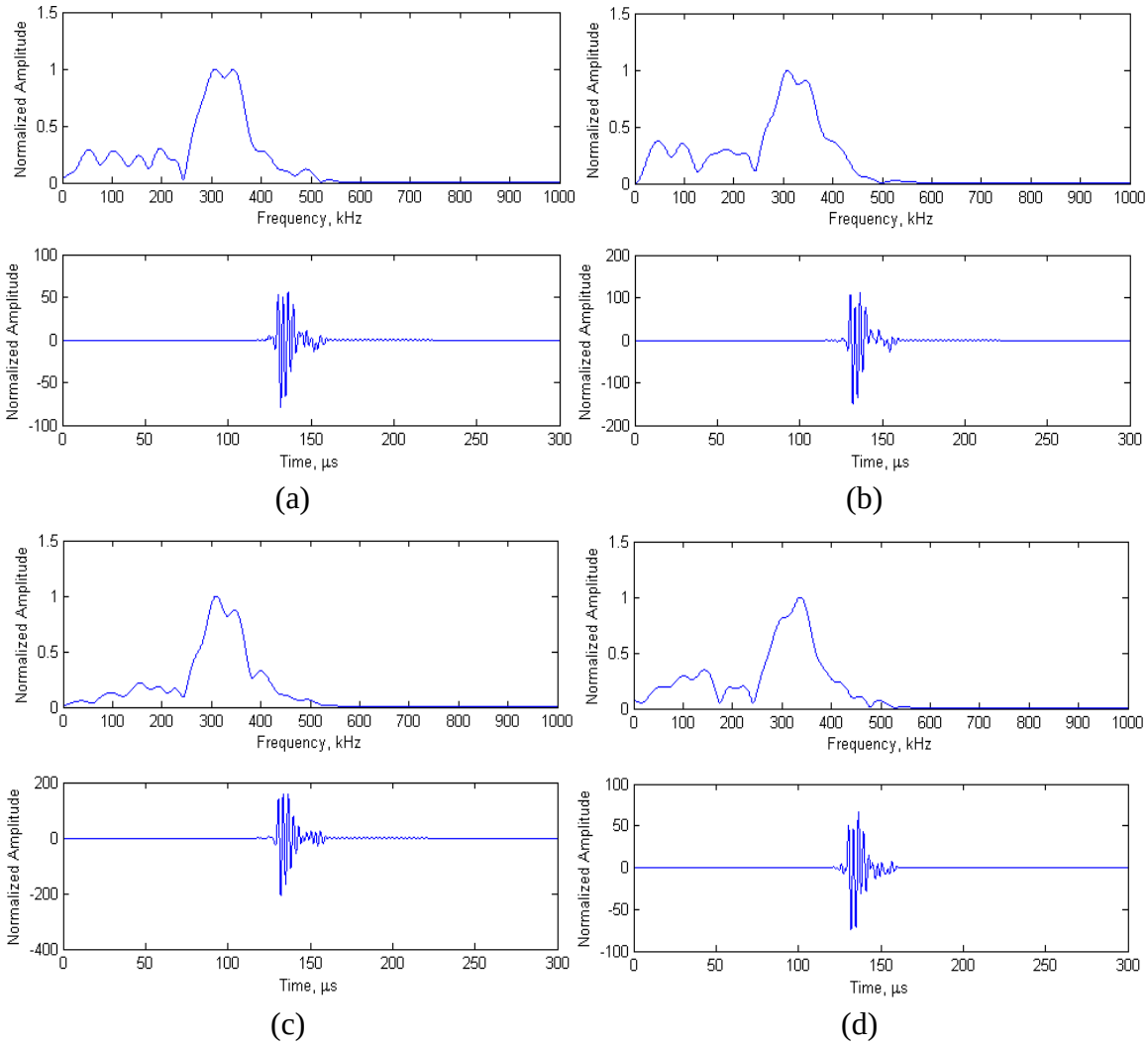

Figure 6.44: PWAS signal of type 1 at crack length of (a) 20 mm; (b) intermediate length 1; (c) intermediate length 2; (d) 37 mm

Since acoustic emissions due to fatigue crack growth occur within a very short time interval, the source should contain a wide frequency band. Therefore, based on the recorded acoustic emission signals, distinctive type 1 or type 2 signals are possible when the acoustic emission source is emitting either symmetric or antisymmetric modes respectively. So, there are two distinctive behaviors of the acoustic emission source represented by type 1 and type 2 signals. One possible explanation of this is, during the crack growth at the top of the loading cycle, the acoustic energy is released

predominantly in S0 Lamb wave mode; subsequently, when the loading cycle is decreasing, the inclined crack surfaces rub against each other near the crack tip and emits A0 Lamb wave mode.

Figure 6.44 (a) to (d) and Figure 6.45 (a) to (d) show samples of type 1 and type 2 signals at different stages of the test with different lengths of the fatigue crack. However, in the frequency plots of either of these two types of signals, we do not see any obvious crack resonance peak decreasing in frequency as the crack increased in length.

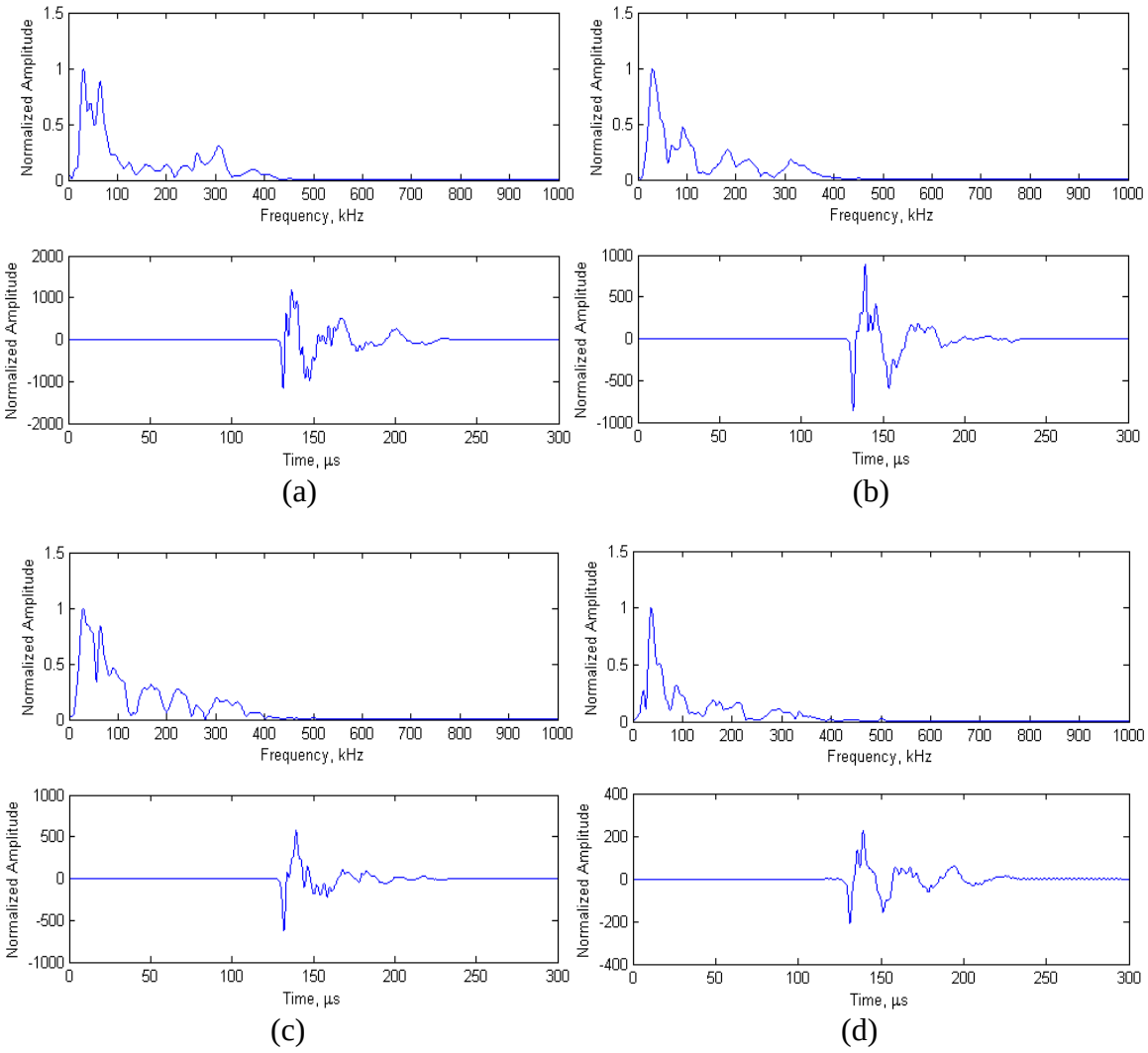

Figure 6.45: PWAS signal of type 2 at crack length of (a) 20 mm; (b) intermediate length 1; (c) intermediate length 2; (d) 37 mm

If our explanation is correct, then the crack surfaces are not stress free when the A0 mode is emitted. So the boundary conditions are not stress free and are unpredictable at the crack surfaces during this type of acoustic emissions. Therefore, using type 2 signals, we may not be able to predict crack length based on our crack resonance phenomenon which assumed stress free crack surfaces. At the top of the loading cycles, as the crack grows, the crack surfaces are stress free and, based on our hypothesis, this emits S0 mode. Therefore, using the crack resonance phenomenon we should be able to identify crack resonances from type 1 signals under ideal circumstances. However, to be successful in detecting crack resonance from type 1 signals, the lower frequency contents of the recorded signals should be noise free.

There is also a possibility that our explanation is not correct because the proximity of the PWAS to the crack changes the crack resonance. This may also be the reason for the type 1 and 2 signals being very similar to the PWAS tuning curves.

6.4 CONCLUSION AND FUTURE WORK

In this chapter we have presented our efforts to understand the behavior of source of acoustic emission due to fatigue crack growth based on physics of materials. We used FE analysis to develop our understanding. A CMEP type approach could also be used to develop an analytical model for acoustic emission due to crack growth; the initial deformation field at the crack tip could be expressed as modal expansion of only the non-propagating Lamb wave modes which will result into propagating Lamb wave modes due to the change in boundary conditions as the crack grows. However, detailed study needs to be performed to develop this type of analytical models.

One of the main focuses of this study was to apply this physical understanding of the source characteristics to extract the length information of a growing crack from

acoustic emissions. We have invented a method to detect the crack length from the recorded acoustic emission signals and experimentally demonstrated its validity. However, detecting crack length of a growing fatigue crack during a fatigue test remains challenging.

To obtain better results one should perform displacement controlled crack growth. In this method one should follow the first stage of the testing method as described earlier. But in the second stage, one should bond the PWAS farther away from the crack to minimize its effect on crack resonance. Also, in the second stage, instead of using low frequency fatigue loading one should use displacement controlled loading to ensure stable crack growth. This will also ensure no rubbing between the crack surfaces. In this method, in future, one should obtain acoustic emission signal related to the crack growth events only. This will also give opportunity to verify our explanation for two types of acoustic emission signals.

One should also use coaxial cable to connect the PWAS along with grounding the plate to instrument grounds. This will minimize the noise received by the PWAS. Also, better post processing technique to eliminate noise from the recorded signals would be helpful.

CHAPTER 7
CONCLUSION AND FUTURE WORK

7.1 RESEARCH CONCLUSIONS

This dissertation has presented the theoretical background of plate guided waves. Along with that, it has illustrated an algorithm to solve for complex roots of a transcendental equation in a large complex domain. It has also presented an application of this algorithm to obtain all complex roots of the Rayleigh-Lamb equations in a large complex domain containing several hundreds of complex Lamb wave modes. It has explained the physical behaviors of these Lamb wave modes and how they appear in an elastodynamic field in a plate. It has illustrated the physical behavior of Lamb wave modes in terms of fundamental pressure wave and shear wave. It has illustrated an efficient method using of Lamb wave complex eigen space to project the thickness dependent boundary conditions encountered in the Lamb wave scatter problem. The presented method is called complex modes expansion and vector projection (CMEP).

This dissertation has also presented convergence and accuracy of this method over a wide range of frequency-thickness values up to 1.5 MHz-mm. It was found that the CMEP method is more than two orders of magnitude faster than FEM for the same accuracy. As a byproduct, the CMEP method also yields the local vibration field near the damage which is dominated by the evanescent and complex wave modes. The CMEP method is different from other methods (Feng, Shen, and Lin 2012), (Feng, Shen, and Shen 2016) which use the orthogonality between modal stresses and displacements. Unlike these methods, CMEP does not need to assume virtual wave guides and vertical

free-ends to implement the orthogonality relations. We applied CMEP to a horizontal cark, a vertical crack and a notch to demonstrate its capability in predicting scattered Lamb wave field. We also verified the predictions with FEM models and confirmed that CMEP is orders of magnitude faster than the FEM code we used and it is as accurate as FEM. However, there were some convergence issues in the case of a vertical crack for CMEP. The convergence required 75 complex Lamb wave modes for a vertical crack; this is much higher compared to only 27 for a vertical notch, despite the fact that we used the same CMEP code for both of these damages. In our opinion this could be due to the nature of discontinuity that a vertical crack creates.

For experimental verifications, this dissertation has demonstrated a method to create straight crested Lamb wave modes using inspirations from FE analysis. It has showed that it is possible to create straight crested Lamb wave modes using absorbing boundary along with long transducers. This method of generating straight crested Lamb waves is useful for many experimental investigation and validation of predictive models. We used this method to validate the predictions from CMEP for a step in plate thickness. We used analytical models like CMEP and WFR1D to design our experiment successfully. The obtained experimental results agree with the CMEP predictions well. The major sources of errors were in specimen geometry and in the use of SLDV for measurement. Also, the reflective tape used on the entire wave guide for wave field measurement contributed to deviation of the experimental results from CMEP predictions.

This dissertation continued to present our efforts to understand the behavior of source of acoustic emission due to fatigue crack growth based on physics of materials.

We used FE analysis to develop our understanding. One of the main focuses of this study was to apply this physical understanding of the source characteristics to extract the length information of a growing crack from acoustic emissions. We invented a method to detect the crack length from the recorded acoustic emission signals and experimentally demonstrated its validity. However, detecting crack length of a growing fatigue crack during a fatigue test remains challenging.

7.2 MAJOR CONTRIBUTIONS

This dissertation has contributed to the state of the art in various ways. The major contributions are listed below:

1. A novel approach was developed to solve for complex roots of generic transcendental equations and was applied to obtain complete solution of Rayleigh-Lamb equations in a very large complex domain.
2. Using the complex solution of Rayleigh-Lamb equations, a complex modes expansion and vector projection method (CMEP) was developed to predict Lamb wave scattering from a step in plate thickness and validated by FEM results.
3. An analytical model to predict scattering of axial-flexural waves from a step in plate thickness was developed using simplified Kirchhoff plate theory and, after comparison with CMEP, was found to be useful only at low frequencies.
4. Using the complex solution of Rayleigh-Lamb equations, a complex modes expansion and vector projection method (CMEP) was developed to predict Lamb wave scattering from a notch in plate thickness and validated by FEM results.
5. Using the complex solution of Rayleigh-Lamb equations, a complex modes expansion and vector projection method (CMEP) was developed to predict Lamb wave scattering from a crack in plate and validated by FEM results.

6. Using the complex solution of Rayleigh-Lamb equations, a complex modes expansion and vector projection method (CMEP) was developed to predict Lamb wave scattering from a horizontal crack in plate and validated by FEM results.
7. The developed CMEP method is orders of magnitude faster than conventional numerical techniques like FEM
8. A unique experimental technique was developed to create straight crested Lamb wave modes in a finite plate for verification of predictive models.
9. The developed experimental technique was used to verify CMEP predictions.
10. A unique phenomenon of crack vibration due to a wide band excitation at the crack tip was identified.
11. A method was invented to detect crack length from acoustic emission signals recorded during fatigue crack growth.

7.3 RECOMMENDATION FOR FUTURE WORK

The algorithm described in this dissertation to solve for complex roots of transcendental equations uses modified bracketing method for the entire complex domain. However, this method can be improved; based on the roots already obtained, we can predict the roots along the direction of increasing Ω. This will improve the speed by narrowing the region for root search and follow the modes as they appear (Gregory and Gladwell 1983).

The CMEP method that we demonstrated assumes straight crested Lamb wave modes in plate strain condition. However, similar approach of using complex modes expansion with the projection of thickness dependent boundary conditions onto the vector space of complex wave modes using power flow associated with the wave guides can be used for non-straight crested plate guided waves. One needs to keep in mind that shear

horizontal waves should also be considered along with Lamb waves for such analysis. Also, some convergence issues have been identified for the case of a surface breaking crack and farther study needs to be performed for better understanding.

For better agreement between theoretical predictions and experimental results obtained using the proposed method, one must control the specimen and damage geometry precisely. Also, the use of single point LDV instead of SLDV may result in more accurate measurement of scattered waves.

To capture crack resonance due to acoustic emission during fatigue crack growth, one should perform displacement controlled crack growth. In this method one should follow the first stage of the testing method as described in section 6.3.1. But in the second stage, one should bond the PWAS farther away from the crack to minimize its effect on crack resonance. Also, in the second stage, instead of using low frequency fatigue loading one should use displacement controlled loading to ensure stable crack growth. This will also ensure no rubbing between the crack surfaces. In this method, in future, one should obtain acoustic emission signal related to the crack growth events only. This will also give opportunity to verify our hypothesis.

One should also use coaxial cable to connect the PWAS along with grounding the plate to instrument grounds. This will minimize the noise received by the PWAS. Also, better post processing technique to eliminate noise from the recorded signals would be helpful.

For fast and accurate predictive simulation of acoustic emission due to fatigue crack growth, a CMEP type complex modes expansion approach could also be used; the initial deformation field at the crack tip could be expressed as modal expansion of the

non-propagating Lamb wave modes which will result into propagating Lamb wave modes due to the change in boundary conditions as the crack grows. However, detailed study needs to be performed to develop this type of analytical models.

REFERENCES

Achenbach, J.D. 1973. *Wave Propagation in Elastic Solids*. Amsterdam, Londan, New York: North-Holland-American Elsevier.

Alleyne, D N, and P Cawley. 1992. "The Interaction of Lamb Waves with Defects." *IEEE Transactions on Ultrasonics, Ferroelectrics, and Frequency Control* 39(3): 381–97.

Andreykiv, Olexander, Valentyn Skalsky, Oleh Serhiyenko, and Denys Rudavskyy. 2010. "Acoustic Emission Estimation of Crack Formation in Aluminium Alloys." *Engineering Fracture Mechanics* 77(5): 759–67.

Andreykiv, Olexandr Ye, Mykola V. Lysak, Oleh M. Serhiyenko, and Valentyn R. Skalsky. 2001. "Analysis of Acoustic Emission Caused by Internal Cracks." *Engineering Fracture Mechanics* 68(11): 1317–33.

Auld, B.A. 1973. *Acoustic Fields and Waves in Solids, Volume II*. New York: Wiley.

Benmeddour, Farouk, Sébastien Grondel, Jamal Assaad, and Emmanuel Moulin. 2008a. "Study of the Fundamental Lamb Modes Interaction with Asymmetrical Discontinuities." *NDT & E International* 41(5): 330–40.

———. 2008b. "Study of the Fundamental Lamb Modes Interaction with Symmetrical Notches." *NDT & E International* 41(1): 1–9.

Burden, Richard L., and John Douglas Faires. 2011. Cengage Learning *Numerical Analysis*.

Castaings, Michel, Emmanuel Le Clezio, and Bernard Hosten. 2002. "Modal

Decomposition Method for Modeling the Interaction of Lamb Waves with Cracks." *The Journal of the Acoustical Society of America* 112(6): 2567–82.

Ceranogliu, A. N., and Pao Yih-Hsing. 1981. "Propagation of Elastic Pulses and Acoustic Emission in a Plate." *Jounal of Applied Mechanics* 48: 125–47.

Chang, H., E. H. Han, J. Q. Wang, and W. Ke. 2009. "Acoustic Emission Study of Fatigue Crack Closure of Physical Short and Long Cracks for Aluminum Alloy LY12CZ." *International Journal of Fatigue* 31(3): 403–7.

Cho, Younho, and Joseph L Rose. 2000. "An Elastodynamic Hybrid Boundary Element Study for Elastic Guided Wave Interactions with a Surface Breaking Defect." *International Journal of Solids and Structures* 37(30): 4103–24.

Chung, Jin-Bok, and Elijah Kannatey-Asibu. 1992. "Acoustic Emission from Plastic Deformation of a Pure Single Crystal." *Journal of Applied Physics* 72(5): 1812.

Cuadra, J., P.a. Vanniamparambil, D. Servansky, I. Bartoli, and A. Kontsos. 2015. "Acoustic Emission Source Modeling Using a Data-Driven Approach." *Journal of Sound and Vibration* 341: 222–36.

Feng, Feilong, Jianzhong Shen, and Shuyu Lin. 2012. "Scattering Matrices of Lamb Waves at Irregular Surface and Void Defects." *Ultrasonics* 52(6): 760–66.

Feng, Feilong, Zhuangzhi Shen, and Jianzhong Shen. 2016. "Scattering of Obliquely Incident Waves by Straight Features in a Plate." *Wave Motion* 60: 84–94.

Flores-López, Miguel A., and R. Douglas Gregory. 2006. "Scattering of Rayleigh-Lamb Waves by a Surface Breaking Crack in an Elastic Plate." *The Journal of the Acoustical Society of America* 119(4): 2041–49.

Gagar, Daniel, Peter Foote, and Philip Irving. 2014. "A Novel Closure Based Approach

for Fatigue Crack Length Estimation Using the Acoustic Emission Technique in Structural Health Monitoring Applications." *Smart Materials and Structures* 23(10): 105033.

Galán, José M, and Ramón Abascal. 2005. "Lamb Mode Conversion at Edges. A Hybrid Boundary Element-Finite-Element Solution." *The Journal of the Acoustical Society of America* 117(4): 1777–84.

Giurgiutiu, Victor. 2014. *Structural Health Monitoring With Piezoelectric Wafer Active Sensors*. Second Edi. Amsterdam, Boston, Heidelberg, London, New York, Oxford, Paris, San Diego, San Francisco, Singapore, Sydney, Tokyo: Elsevier.

Glushkov, E., N. Glushkova, A. Eremin, and V. Giurgiutiu. 2015. "Low-Cost Simulation of Guided Wave Propagation in Notched Plate-Like Structures." *Journal of Sound and Vibration* 352: 80–91.

Glushkov, Ye.V., N.V. Glushkova, A.a. Yeremin, and V.V. Mikhas'kiv. 2009. "The Layered Element Method in the Dynamic Theory of Elasticity." *Journal of Applied Mathematics and Mechanics* 73(4): 449–56.

Gonzalez, Carlos, and Javier LLorca. 2006. "Multiscale Modeling of Fracture in Fiber-Reinforced Composites." *Acta Materialia* 54(16): 4171–81.

Gorman, M. R., and W. H. Prosser. 1996. "Application of Normal Mode Expansion to Accoustic Emission Waves in Finite Plates." *Journal of Applied Mechanics* 63(2): 555–57.

Gorman, M.R., and S.M. Ziola. 1991. "Plate Waves Produced by Transverse Matrix Cracking." *Ultrasonics* 29(3): 245–51.

Graff, Karl F. 1991. *Wave Motion in Elastic Solids*. New York: Dover Publications, Inc.

Grahn, Tomas. 2003. “Lamb Wave Scattering from a Circular Partly Through-Thickness Hole in a Plate.” *Wave Motion* 37(1): 63–80.

Gregory, R. Douglas, and I Gladwell. 1982. “The Cantilever Beam Under Tension, Bending or Flexure at Infinity.” *Journal of Elasticity* 12(4): 317–43.

———. 1983. “The Reflection of a Symmetric Rayleigh-Lamb Wave at the Fixed or Free Edge of a Plate.” *Journal of Elasticity* 13: 185–206.

Gunawan, Arief, and Sohichi Hirose. 2004. “Mode-Exciting Method for Lamb Wave-Scattering Analysis.” *The Journal of the Acoustical Society of America* 115(3): 996–1005.

———. 2007. “Reflection of Obliquely Incident Guided Waves by an Edge of a Plate.” *Materials Transactions* 48(6): 1236–43.

Hamstad, M. A., A. O’Gallagher, and J. Gary. 1999. “Modeling of Buried Monopole and Dipole Sources of Acoustic Emission with a Finite ELement Technique.” *Journal of Acoustic Emission* 17: 97–110.

Helmholtz, Hermann Von. 1867. “On Integrals of the Hydrodynamic Equations That Correspond to Vortex Motions.” *Philosophical Magazine and Journal of Science* 33(226): 485–512.

Hernando Quintanilla, F., M. J S Lowe, and R. V. Craster. 2015. “Full 3D Dispersion Curve Solutions for Guided Waves in Generally Anisotropic Media.” *Journal of Sound and Vibration* 363: 545–59.

Hu, Wenke, Youn Doh Ha, and Florin Bobaru. 2011. “Modeling Dynamic Facture and Damage in a Fiber-Reinforced Composite Lamina with Peridynamics.” *Journal for Multiscale Computational Engineering* 9(6): 707–26.

Karim, M. R., M. A. Awal, and T. Kundu. 1992. “Elastic Wave Scattering by Cracks and Inclusions in Plates: In-Plane Case.” *International Journal of Solids Structures* 29(19): 2355–67.

Kreyszig, Erwin. 1997. *Advanced Engineering Mathematics*. 8th ed. Delhi: Wiley-India.

Lampman, Steven R., Theodore B. Zorc, and Alice W. Ronke, eds. 1992. *ASM Handbook, Volume 17*. The Materials Information Society: ASM International.

Lowe, M J S, P Cawley, J-y Kao, and O Diligent. 2000. “Prediction and Measurement of the Reflection of the Fundamental Anti- Symmetric Lamb Wave from Cracks and Notches.” In *AIP Conference Proceedings*,.

Lysak, M. V. 1996. “Development of the Theory of Acoustic Emission by Propagating Cracks in Terms of Fracture Mechanics.” *Engineering Fracture Mechanics* 55(3): 443–52.

Mackerle, Jaroslav. 2004. “Finite-Element Modelling of Non-Destructive Material Evaluation, an Addendum: A Bibliography (1997-2003).” *Modelling and Simulation in Materials Science and Engineering* 12: 799–834.

Maji, A. K., D. Satpathi, and T. Kratochvil. 1997. “Acoustic Emission Source Location Using Lamb Wave Modes.” *Journal of Engineering Mechanics* 123: 154–61.

Meeker, T. R., and A. H. Meitzler. 1964. “Guided Wave Propagation in Elongated Cylinders and Plates.” *Physical Acoustics* 1(B): 111–67.

Meriaux, J., M. Boinet, S. Fouvry, and J. C. Lenain. 2010. “Identification of Fretting Fatigue Crack Propagation Mechanisms Using Acoustic Emission.” *Tribology International* 43(11): 2166–74.

Mindlin, R. D. 1957. “Mathematical Theory of Vibration of Elastic Plates.” In

Proceedings of Eleventh Annual Symposium of Frequency Control, , 1–40.

Moorthy, V., T. Jayakumar, and Baldev Raj. 1996. "Influence of Microstructure on Acoustic Emission Behavior During Stage 2 Fatigue Crack Growth in Solution Annealed, Thermally Aged and Weld Specimens of AISI Type 316 Stainless Steel." *Materials Science and Engineering A* 212(2): 273–80.

Moreau, L., M. Caleap, A. Velichko, and P.D. Wilcox. 2011. "Scattering of Guided Waves by Through-Thickness Cavities with Irregular Shapes." *Wave Motion* 48(7): 586–602.

———. 2012. "Scattering of Guided Waves by Flat-Bottomed Cavities with Irregular Shapes." *Wave Motion* 49(2): 375–87.

Moser, Friedrich, Laurence J. Jacobs, and Jianmin Qu. 1999. "Modeling Elastic Wave Propagation in Waveguides with the Finite Element Method." *NDT & E International* 32(4): 225–34.

Nemati, Navid, Brian Metrovich, and Antonio Nanni. 2015. "Acoustic Emission Assessment of Through-Thickness Fatigue Crack Growth in Steel Members." *Advances in Structural Engineering* 18(2): 269–83.

Pagneux, V, and A Maurel. 2001. "Determination of Lamb Mode Eigenvalues." *The Journal of the Acoustical Society of America* 110(3 Pt 1): 1307–14.

Paris, P, and F Erdogan. 1963. "A Critical Analysis of Crack Propagation Laws." *Journal of Fluids Engineering* 85(4): 528–34.

Press, William, Saul Teukolsky, William Vetterling, and Brian Flannery. 1987. 29 Technometrics *Numerical Recipes: The Art of Scientific Computing*. Cambridge, New York, Port Chester, Melbourne, Sydney: Cambridge University Press.

Prosser, W. H., M. A. Hamstad, J. Gary, and A. O'Gallagher. 1999. "Finite Element and Plate Theory Modeling of Acoustic Emission Waveforms." *Journal of Nondestructive Evaluation* 18(3): 83–90.

Roberts, T. M., and M. Talebzadeh. 2003. "Acoustic Emission Monitoring of Fatigue Crack Propagation." *Journal of Constructional Steel Research* 59(6): 695–712.

Rokhlin, S. 1980. "Diffraction of Lamb Waves by a Finite Crack in an Elastic Layer." *The Journal of the Acoustical Society of America* 67(4): 1157–65.

Santhanam, Sridhar, and Ramazan Demirli. 2013. "Reflection of Lamb Waves Obliquely Incident On the Free Edge of a Plate." *Ultrasonics* 53(1): 271–82.

Sause, M. G R, and S. Horn. 2010. "Simulation of Acoustic Emission in Planar Carbon Fiber Reinforced Plastic Specimens." *Journal of Nondestructive Evaluation* 29(2): 123–42.

Scandrett, C., and N. Vasudevan. 1991. "The Propagation of Time Harmonic Rayleigh-Lamb Waves in a Bimaterial Plate." *J. Acoust. Soc. Am.* 89(4): 1606–14.

Shen, Yanfeng, and Victor Giurgiutiu. 2015. "Effective Non-Reflective Boundary for Lamb Waves: Theory, Finite Element Implementation, and Applications." *Wave Motion* 58: 22–41.

Terrien, N, D Osmont, D Royer, F Lepoutre, and A Déom. 2007. "A Combined Finite Element and Modal Decomposition Method to Study the Interaction of Lamb Modes with Micro-Defects." *Ultrasonics* 46(1): 74–88.

Torvik, P. J. 1966. "Reflection of Wave Trains in Semi Infinite Plates." *The Journal of the Acoustical Society of America* 41(2): 346–53.

Viktorov, Igor Aleksandrovich. 1967. *Rayleigh and Lamb Waves: Physical Theory and*

Applications. New York: Plenum Press.

Wang, C.H., and L.R.F. Rose. 2003. "Wave Reflection and Transmission in Beams Containing Delamination and Inhomogeneity." *Journal of Sound and Vibration* 264(4): 851–72.

Zhou, C., and Y. Zhang. 2014. "Acoustic Emission Source Localization Using Coupled Piezoelectric Film Strain Sensors." *Journal of Intelligent Material Systems and Structures* 25(16): 2082–92.